UNIVERSIDADE DE LISBOA
FACULDADE DE CIÊNCIAS

Improving the estimation of fire danger, fire propagation and fire monitoring: new insights using remote sensing data and statistical methods

" Documento Definitivo"

Doutoramento em Ciências Geofísicas e da Geoinformação
Especialidade de Meteorologia

Miguel Neves Mota Pinto

Tese orientada por:
Professor Doutor Ricardo Trigo, Doutora Isabel Trigo

Documento especialmente elaborado para a obtenção do grau de doutor

2022

UNIVERSIDADE DE LISBOA
FACULDADE DE CIÊNCIAS

Improving the estimation of fire danger, fire propagation and fire monitoring: new insights using remote sensing data and statistical methods

Doutoramento em Ciências Geofísicas e da Geoinformação
Especialidade de Meteorologia

Miguel Neves Mota Pinto

Tese orientada por:
Professor Doutor Ricardo Trigo, Doutora Isabel Trigo

Júri:

Presidente:

- João Manuel de Almeida Serra, Professor Catedrático e Presidente do Departamento de Engenharia Geográfica, Geofísica e Energia da Faculdade de Ciências da Universidade de Lisboa.

Vogais:

- Doutor Martin John Wooster, Professor da Faculty of Social Science & Public Policy do King’s College London (Reino Unido);
- Doutor Mário Jorge Modesto Gonzalez Pereira, Professor Auxiliar do Departamento de Física da Universidade de Trás-os-Montes e Alto Douro;
- Doutor Manuel Lameiras de Figueiredo Campagnolo, Professor Associado do Instituto Superior de Agronomia da Universidade de Lisboa;
- Doutor Ricardo Machado Trigo, Professor Associado da Faculdade de Ciências da Universidade de Lisboa (orientador).

Documento especialmente elaborado para a obtenção do grau de doutor
Doutoramento financiado pela Fundação para a Ciência e a Tecnologia
(PD/BD/142779/2018)

2022

Acknowledgements

I would like to thank my supervisors, Ricardo Trigo and Isabel Trigo, for all the guidance and support throughout this process. I would also like to thank Carlos da Camara that, despite not being officially a supervisor, followed all the work closely, provided additional insight and ideas and made discussions more fun with his great sense of humour. A special thanks to Renata Libonati for joining as co-author in the article described in section 3.2, providing important additional guidance during the discussion of the results and preparation of the manuscript. A special thanks as well to Alexandra Hurduc, co-author of the published works described in sections 2.2 and 2.3, for the friendship and all the brainstorming sessions that led to great ideas and made the process more enjoyable. Also, I would like to thank my family for their support during these past years and a very special thanks to Nina for all the motivation and support over the past two years.

This work was in part supported by national funds through Fundação para a Ciência e a Tecnologia, Portugal (FCT) under project FireCast (PCIF/GRF/0204/2017). Research by Miguel M. Pinto was supported by FCT through the PhD grant PD/BD/142779/2018.

Abstract

This thesis covers three major topics related to wildfires, remote sensing and meteorology: (i) quantifying and forecasting fire danger combining numerical weather forecasts and satellite observations of fire intensity; (ii) mapping burned areas from satellite observations with multiple spatial and spectral resolution; and (iii) modelling fire progression taking into account weather conditions and fuel (vegetation) availability. Regarding the first topic, an enhanced Fire Weather Index (FWI) is proposed by using statistical methods to combine the classical FWI with an atmospheric instability index with the aim of better forecasting the fire danger conditions favourable to the development of convective fires. Furthermore, the daily definition of the classical FWI was extended to an hourly timescale, allowing for assessment of the variability of the fire danger conditions throughout the day. For the second topic, a method is proposed to map and date burned areas using sequences of daily satellite data. This method, tested over several regions around the globe, provide burned area maps that outperform other existing methods for the task, particularly regarding the consistency and accuracy of the date of burning. Furthermore, a method is proposed for fast assessment of burned areas using 10-meter resolution satellite data and making use of Google Earth Engine (GEE) as a tool for pre-processing and downloading of data that is then used as input to a deep learning model that combines a coarse burned area map with the medium resolution data to provide a refined burned area map with 10-meter resolution at event level and with low computational requirements. Finally, for the third topic, a method is proposed to estimate the fire progression over a 12-hour period with resource to an ensemble of models trained based on the reconstruction of past events. Overall, I am confident that the results obtained and presented in this thesis provide a significant contribution to the remote sensing and wildfires scientific community while opening interesting paths for future research on the topics described.

Keywords: fire weather index, burned areas, fire progression, remote sensing, machine learning.

Resumo

A presente tese de doutoramento tem como foco três tópicos importantes na área de interseção entre os incêndios florestais, a deteção remota e a meteorologia, fazendo uso de técnicas estatísticas e de aprendizagem automática e com um foco adicional na utilidade prática dos métodos desenvolvidos. Os três tópicos principais nesta tese apresentados são: (i) a quantificação e previsão do perigo de incêndio combinando previsões numéricas do estado do tempo e observações de satélite de intensidade dos fogos; (ii) o mapeamento de áreas queimadas usando observações de satélite com várias resoluções espaciais e temporais; (iii) a modelação da progressão de incêndios tendo em conta as condições meteorológicas e características do terreno e vegetação.

A questão da quantificação e previsão do perigo de incêndio é abordada no capítulo 2 desta tese onde são identificadas limitações e propostas melhorias para o *Fire Weather Index* (FWI) – um índice de perigo meteorológico de incêndio usado a nível global. Na secção 2.2, o estudo de dois eventos extremos em Portugal permitiu avaliar como a utilização de um índice de instabilidade atmosférica permite em certos casos uma melhor análise das condições de perigo meteorológico de incêndio. Resultante desta observação, a primeira melhoria apresentada, descrita na secção 2.3, combina o FWI com um índice de instabilidade atmosférica denominado *Continuous Haines Index* (CHI). O objetivo é tornar o FWI mais sensível a condições propícias à ocorrência de fogos com uma pluma com características convectivas que pode resultar em comportamento imprevisível do desenvolvimento do fogo. Esta melhoria do FWI é obtida combinando os dois índices mencionados por meio de modelos estatísticos que garantem que a interpretação do novo índice é equivalente à do original em termos de probabilidade de exceder um limiar pré-definido de energia libertada pelos incêndios. A segunda melhoria do FWI, apresentada na secção 2.4, corresponde a uma extensão da definição diária do índice original para uma definição horária, de forma a melhor capturar as características do ciclo diurno da perigosidade de incêndio. Este resultado é obtido utilizando uma interpolação linear das componentes de memória que estão na base do algoritmo do FWI, de forma a que o valor do FWI horário à hora de referência (usada para o FWI diário) seja idêntico ao valor do FWI diário. A análise da climatologia dos ciclos diários do novo FWI sugere que este é uma mais-valia para diversas aplicações como a modelação da energia libertada pelos incêndios. A contribuição principal deste capítulo é então um novo e melhorado FWI que é fácil de integrar em sistemas

e aplicações existentes que façam uso do FWI clássico e simultaneamente de simples compreensão para os utilizadores deste índice.

O tópico do mapeamento de áreas queimadas usando observações de satélite é abordado em parte do capítulo 3 desta tese, em particular nas secções 3.2 – 3.4. Nestas secções, são abordadas algumas limitações importantes dos métodos existentes para o mapeamento de áreas ardidas. Em particular, na secção 3.2, um método com base em redes neuronais para processamento de sequências de imagens (BA-Net) foi desenvolvido para gerar mapas diários de áreas queimadas utilizando o sensor *VIIRS* e testado para várias regiões no mundo. Este método utiliza como *input* sequências de imagens para um período de 64 dias, correspondentes às refletâncias no vermelho, infravermelho-próximo, infravermelho-médio e adicionalmente informação relativa aos fogos ativos também com base nos dados do sensor *VIIRS*. Os resultados mostram que o método proposto permite melhorar o estado da arte para esta tarefa, em particular no que diz respeito à precisão da datação das áreas queimadas. Esta melhoria tem bastante importância para, por exemplo, o desenvolvimento de produtos que procuram analisar a progressão dos fogos ou derivar estatísticas relativas às características dos fogos individuais. A metodologia proposta nesta secção (3.2) tem a vantagem de ser facilmente aplicável a dados de outros sensores, com características semelhantes, podendo ser feito um *fine-tuning* com base nos parâmetros obtidos para o *VIIRS*. Note-se também que este método não necessita de qualquer filtro de nuvens ou pré-selecionamento de imagens. Ainda neste capítulo da tese, na secção 3.3, uma metodologia foi desenvolvida para uma monitorização rápida das áreas ardidas com dados de média resolução espacial (10 m). Isto foi possível utilizando a ferramenta *Google Earth Engine* (GEE) para pré-processamento e *download* de compósitos pré-fogo e pós-fogo, e combinando esta informação com um mapa de baixa resolução utilizando um modelo com base em redes neuronais para processamento de imagens. Os resultados mostram que os mapas de áreas ardidas gerados com 10 m de resolução espacial para 6 casos de estudo em Portugal, França e Grécia se aproximam dos mapeamentos de referência obtidos do serviço de emergência Copernicus. Na secção 3.4 um caso de estudo é apresentado, correspondendo aos grandes fogos no sudoeste da Australia em 2019–2020. Neste caso de estudo é feito o mapeamento das áreas ardidas usando dados *VIIRS* a diferentes resoluções espaciais (750 m e 375 m), demonstrando a aplicação do método descrito na secção 3.2 aos dados de melhor resolução. É feita também a comparação com um produto operacional de áreas ardidas global usando como referência um mapeamento com base em imagens de média resolução. Os resultados mostram que o modelo BA-Net generaliza bem para as bandas de mais fina resolução

espacial do sensor *VIIRS* e que apresenta alguma vantagem em comparação com o produto operacional mencionado, particularmente para regiões que arderam com menor severidade.

O tema relativo à modelação da progressão de incêndios tendo em conta as condições meteorológicas e características do terreno e vegetação é apresentado na última secção do capítulo 3 (secção 3.5). A abordagem proposta baseia-se na utilização de técnicas de aprendizagem automática para gerar um conjunto de modelos otimizados individualmente com base em reconstruções da progressão de eventos significativos na região de Portugal continental no período de 2012 a 2020. A reconstrução dos eventos históricos é feita com base nas observações de fogos ativos pelo sensor *VIIRS*, utilizando um método de interpolação para preencher os locais dentro da área ardida para os quais observações não estão disponíveis. É então considerado um modelo com seis parâmetros cujos inputs consistem em dados do campo do vento, declive do terreno, localização do fogo, condições meteorológicas avaliadas por meio do FWI horário melhorado (de acordo com o método descrito na secção 2.3) e classes de coberto vegetal/uso do solo. Para cada cenário de previsão a 12h os parâmetros ótimos são então obtidos utilizando um método de otimização que consiste em gerar vários modelos com parâmetros gerados aleatoriamente, avaliar a sua performance e usar as estatísticas dos melhores modelos para sucessivamente gerar novos modelos que se aproximam da solução ótima dentro dos constrangimentos definidos. O conjunto de modelos resultantes é depois utilizado para gerar um ensemble de previsões apresentado como um mapa probabilístico indicando as regiões previstas para a progressão de um incêndio nas 12 horas seguintes. Esta metodologia foi desenvolvida e testada com dados meteorológicos da reanálise ERA5-Land e faz uso de várias das metodologias anteriormente apresentadas nesta tese, nomeadamente, os métodos para o mapeamento de áreas ardidas e as modificações do FWI propostas.

As metodologias desenvolvidas no âmbito deste programa doutoral e descritas na presente tese representam uma contribuição significativa para as comunidades científicas de deteção remota e incêndios florestais, abrindo caminhos interessantes para futuros desenvolvimentos dos tópicos descritos. No capítulo 4 desta tese, são apresentadas conclusões e ideias ou direções a explorar para trabalho futuro.

Palavras-chave: índice de perigo de incêndio, áreas queimadas, propagação do fogo, deteção remota, aprendizagem automática.

Contents

List of Figures

List of Tables

List of Acronyms

API	Application Programming Interface
AUS GEEBAM	Australian Google Earth Engine Burnt Area Map
AVHRR	Advanced Very-High-Resolution Radiometer
BA-Net	Burned Areas Neural Network
BUI	Build-Up Index
CAMS	Copernicus Atmosphere Monitoring Service
CDF	Cumulative Distribution Function
CE	Commission Error
CEMS	Copernicus Emergency Management System
CEOS CalVal	Committee on Earth Observation Satellites Calibration and Validation
CFFWIS	Canadian Forest Fire Weather Index System
CHI	Continuous Haines Index
CI	Confidence Interval
CNPQ	Brazilian National Council for Scientific and Technological Development (in Portuguese: Conselho Nacional de Desenvolvimento Científico e Tecnológico, earlier Conselho Nacional de Pesquisas)
COMS	Communication, Ocean and Meteorological Satellite
CORINE	Coordination of information on the environment
CPU	Central Processing Unit
CV	Cross-Validation
DC	Drought Code
DJF	December January February
DMC	Duff Moisture Code
DSR	Daily Severity Rating
ECMWF	European Centre for Medium-Range Weather Forecasts
EFFIS	European Forest Fire Information System
EGU	European Geosciences Union
ENVISAT	Environmental Satellite
ERA	ECMWF Re-Analysis
ERA5	ECMWF Re-Analysis 5th Generation
ETM+	Enhanced Thematic Mapper Plus
EU	European Union
EUMETSAT	European Organisation for the Exploitation of Meteorological Satellites
FARSITE	Fire Area Simulator–model development and evaluation
FCT	Portuguese Foundation for Science and Technology
FFDI	Forest Fire Danger Index
FN	False Negatives
FP	False Positives
FFMC	Fine Fuel Moisture Code
FRP	Fire Radiative Power
FWI	Fire Weather Index
FWIe	Enhanced Fire Weather Index
FY	Feng Yun Satellite
GB	Gigabyte
GEE	Google Earth Engine

GJ	Gigajoule
GOES	Geostationary Operational Environmental Satellite
GP	Generalized Pareto
GPU	Graphics Processing Unit
GTX	Giga Texel Shader eXtreme
HRG	High-Resolution Geometric
HRV	High-Resolution Visible
HRVIR	Visible & Infrared High-Resolution
ICNF	Portuguese Institute for Nature Conservation and Forests (in Portuguese: Instituto da Conservação da Natureza e das Florestas)
INSAT	Indian National Satellite System
IPCC	Intergovernmental Panel on Climate Change
IPMA	Portuguese Institute for Sea and Atmosphere (in Portuguese: Instituto Português do Mar e da Atmosfera)
ISI	Initial Spread Index
ISPRS	International Society for Photogrammetry and Remote Sensing
JJA	June July August
JPSS	Joint Polar Satellite System
LIDAR	Light Detection and Ranging
LSA SAF	Satellite Application Facility on Land Surface Analysis
LSTM	Long Short-Term Memory
MAE	Mean Absolute Error
MAM	March April May
MB	Megabyte
MERIS	Medium Resolution Imaging Spectrometer
MIR	Middle-Infrared
MLE	Maximum Likelihood Estimation
MODIS	Moderate Resolution Imaging Spectroradiometer
MSG	Meteosat Second Generation
MSI	Multispectral Instrument
MSS	Multispectral Scanner
MTBS	Monitoring Trends in Burn Severity
NAOMI	New AstroSat Optical Modular Instrument
NBR	Normalized Burned Ratio
NDVI	Normalized Difference Vegetation Index
NFDRS	National Fire Danger Rating System
NIAFED	Australian National Indicative Aggregated Fire Extent Dataset
NIR	Near-Infrared
NLL	Negative Log-Likelihood
NOAA	National Oceanic and Atmospheric Administration
NPP	National Polar-orbiting Partnership
NRT	Near Real-Time
OA	Overall Accuracy
OE	Omission Error
OLCI	Ocean and Land Colour Instrument
OLI	Operational Land Imager
OOF	Out-Of-Fold
RAM	Random Access Memory

ReLU	Rectified Linear Unit
RNNs	Recurrent Neural Networks
SAR	Synthetic Aperture Radar
SLSTR	Sea and Land Surface Temperature Radiometer
SON	September October November
SPOT	Satellite Pour l'Observation de la Terre
SRTM	Shuttle Radar Topography Mission
SWIR	Shortwave-Infrared
TERN	Australian Terrestrial Ecosystem Research Network
TIROS	Television Infrared Observation Satellite
TM	Thematic Mapper
TN	True Negatives
TP	True Positives
UTC	Universal Time Coordinated
VIIRS	Visible Infrared Imaging Radiometer Suite
VGT	Vegetation
WIGOS	WMO Integrated Global Observing System
WMO	World Meteorological Organization
WRF	Weather Research and Forecasting

1 Introduction

Wildland fires and humans have long coexisted on planet Earth. Naturally occurring fires are an important component of many ecosystems, such as those found in the Mediterranean Region (Pausas et al. 1999). Changes in the frequency, extent and severity of the wildfires can however lead to nefarious consequences. As land-use evolves and climate changes, some regions become more vulnerable to unprecedented wildfires (e.g.: Kumar et al. 2022), leading to serious negative impacts at social, economic, and environmental levels (Patz et al., 2000, Bowman and Johnston, 2005, Driscoll et al., 2010). Over just the past few years, tragic fire events have often been making news around the world. In 2017, about 500,000 hectares burned in Portugal leading to 119 casualties and extensive damages (Molina-Terrén et al. 2019). In 2018, Greece was struck by two tragic fires that led to 102 deaths and thousands of buildings destroyed (Haynes et al. 2020). In the same year, the Camp Fire was the deadliest and most destructive fire in California, with 85 deaths and over 18,000 buildings destroyed (Maranghides et al. 2021). In the 2019–2020 Australia fire season, the south-eastern region of the country was devastated by a series of wildfires burning about 7 million hectares, destroying nearly 6000 buildings, and causing the direct death of 34 people and hundreds more due to smoke inhalation (Graham et al. 2021).

In face of unprecedented events, it is more important than ever to adopt measures to mitigate the negative impacts of the wildfires. In order to achieve that goal, it is fundamental to have a good understanding of how fire patterns are distributed and change over time. Mapping the extent and progression of burned areas accurately is, therefore, an important topic of research that has been studied for many decades, particularly since Earth observation satellites started to provide consistent data for the entire planet (Chuvieco et al. 2019). If burned areas and active fire location data allow us to study how wildfire patterns are changing, another fundamental aspect is to understand why they are changing and what can be expected in future climate scenarios. The onset of a fire event requires an ignition and the availability of dry fuels to burn. However, its severity and progression will be strongly conditioned by the weather conditions (Di Giuseppe et al. 2016). Estimating the meteorological fire danger is, therefore, extremely important for planning of fire-fighting operations and forest management in general, being another topic of extensive research (e.g.: Castro and Chuvieco 1998, Viegas et al. 1999, Vasilakos et al. 2007, Fernandes 2019). The proper calibration of fire danger models requires historical data, providing information on fire intensity or spread (burned areas) under different weather conditions and for different vegetation types. Satellite-based data records of burned areas or energy released are good candidates for that purpose, given their growing time periods and wide and diverse areas that are covered (DaCamara et al. 2014, Pinto et al. 2018a, Chuvieco et al. 2020). This work addresses the three intimately related topics referred above, namely: (i) quantifying and forecasting fire danger combining numerical weather forecasts and satellite observations of fire intensity; (ii) mapping burned areas from satellite observations with multiple spatial and spectral resolution; and (iii) modelling fire progression taking into account weather conditions and fuel (vegetation) availability.

To identify the patterns and calibrate the models for fire danger or burned area monitoring in a robust and accurate way, statistical methods are a powerful tool that enables the extraction of refined information from large volumes of data. This thesis makes, therefore, extensive use of statistical methods such as extreme value theory (De Haan et al. 2006) and modern machine learning techniques for pattern recognition (LeCun et al. 2015) aiming to develop state-of-the-art methods and products that can ultimately have a practical utility by helping to understand and mitigate the risks posed by the changes in wildfire patterns. For most of the work presented in this thesis, Python code has been made publicly available, in line with the goal of facilitating their use and their further development.

The next sections of this introduction briefly describe the satellite data available to address the research topics described above the weather reanalysis data, the statistical methods that will be used throughout the next chapters, and the historical background of the three topics that will be the object of study of this thesis.

1.1 Earth Observation Satellites

The first artificial satellite to orbit Earth was launched in 1957 and operated for three weeks until the batteries failed (Sinelnikov et al. 2014). The first weather satellite was launched two years later but problems in the axis of rotation and orbit made it unusable (Schnapf 1982). Later, in 1960, the first weather satellite to be launched with success, TIROS-1, operated for over two months and finally provided some images of the cloud tops from space (Vaughan and Johnson 1994). Fast forward 60 years and nowadays there are thousands of satellites orbiting the Earth, a number that is quickly growing, which includes dozens of operational weather satellites (see **Figure 1.1**). The lifetime of the satellites also increased by orders of magnitude since the early experiments. Landsat-5, the current record holder, operated for almost 29 years from 1984 to 2013, despite being designed for a 3-year lifetime (Showstack et al. 2013). As technology evolves, every new iteration of satellites can provide higher quality data than the previous generations. Together with the quickly lowering costs to launch a satellite into orbit, it is expected that in the future the volume of satellite data available will continue to increase at a rapid pace.

Earth observation satellites most commonly operate in either geostationary or polar orbits. Geostationary satellites orbit at a point above the equator line at an altitude of nearly 36,000 km and remain stationary over the same point providing a view of the entire hemisphere (Li 2014). Polar-orbiting satellites for Earth observation applications orbit at altitudes that usually lie between 600 and 850 km, scanning a portion of the surface as the satellite moves, resulting in elongated images called swaths (Maini and Agrawal 2014). A particularly important subclass of polar orbits for meteorological applications is the Sun-synchronous orbit, in which the satellite visits the same spot at the same local time, allowing to have comparable images from one visit to the next (Zayan and Eltohamy 2008). This is particularly important for the monitoring of surface variables including burned areas, one of the main subjects of this thesis.

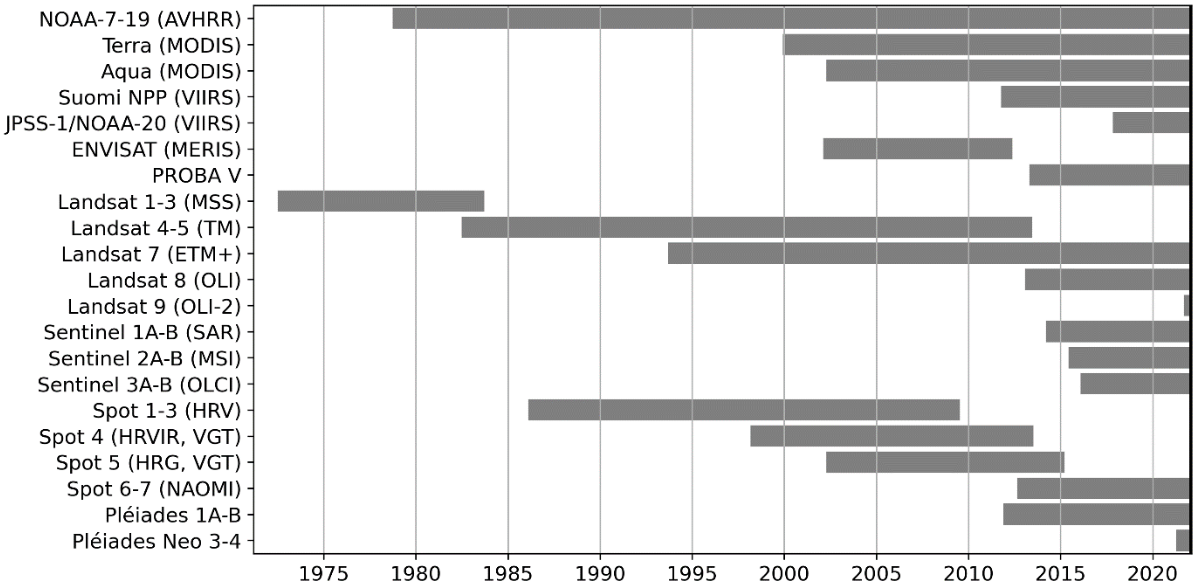

Figure 1.1. Operation timeline for the main satellites used for mapping burned areas.

The main satellites used for observation of variables such as vegetation and burned areas are listed in **Figure 1.1**. Different satellites have different characteristics in terms of equator crossing time, revisit time, spectral bands, width of the swath and image resolution of the data captured. **Table 1.1** summarizes some of these characteristics for the satellites shown in **Figure 1.1** (information compiled from several sources: Chuvieco et al. 2019; eumetsat.int/avhrr; modis.gsfc.nasa.gov/about/specifications.php; lpdaac.usgs.gov/data/get-started-data/collection-overview/missions/s-npp-nasa-viirs-overview; sentinels.copernicus.eu/web/sentinel/missions;

earth.esa.int/eogateway/missions. Last access on 2022-02-23). In chapter 3 of this thesis, the use of VIIRS and Sentinel-2 for mapping burned areas will be discussed in detail.

Table 1.1. Equator crossing time, revisit time and resolution of visible and near-infrared bands (or SAR in case of Sentinel-1) at nadir for the satellites/sensors shown in **Figure 1.1**. *Pléiades 5 and 6 to be launched in 2022.

Satellite	**Equator Crossing Time**	**Revisit time (days)**	**Resolution (m)**
NOAA 7-19 (AVHRR)	10:00 (17) 13:30 – 14:30 (7,9,11,14,16,18,19) 19:30 (8,10,12,15)	1	1100
Terra-Aqua (MODIS)	10:30 (Terra); 13:30 (Aqua)	1 (constellation)	250
Suomi NPP / JPSS (VIIRS)	13:30 (Suomi); 14:30 (JPSS)	1	375
ENVISAT (MERIS)	10:00	3	300
PROBA V	10:30	1; 5	300; 100
Landsat 1-3 (MSS)	9:30	18	60
Landsat 4-5 (TM)	9:45	16	30
Landsat 7 (ETM+)	10:00	16	30
Landsat 8-9 (OLI)	10:00	16	30
Sentinel 1A-B (SAR)	18:00	3 (constellation)	10
Sentinel 2A-B (MSI)	10:30	5 (constellation)	10
Sentinel 3A-B (OLCI)	10:00	1 (constellation)	300
Spot 1-3 (HRV)	10:30	3	20
Spot 4 (HRVIR, VGT)	10:30	3; 1 (VGT)	20; 1000 (VGT)
Spot 5 (HRG, VGT)	10:30	3; 1 (VGT)	10; 1000 (VGT)
Spot 6-7 (NAOMI)	10:00	1 (constellation)	6
Pléiades 1A-B	10:30	1 (constellation)	2
Pléiades Neo 3-6*	10:30	0.5 (constellation)	1.2

Regarding geostationary satellites, there are several operational satellites forming a ring around the globe that provide high-frequency observations crucial for weather surveillance and forecast. The main operational geostationary satellites over the years are listed in **Figure 1.2** (information compiled from several sources: directory.eoportal.org/web/eoportal/satellite-missions/m/meteosat-first-generation, goes-r.gov/mission/history, en.wikipedia.org/wiki/Elektro%E2%80%93L#Launches, earth.esa.int/web/eoportal/satellite-missions/i/insat-3d, jma.go.jp/jma/jma-eng/satellite/introduction/history, directory.eoportal.org/web/eoportal/satellite-missions/content/-/article/geo-kompsat-2. Last access on 2022-03-19). For the purpose of this thesis, the series of Meteosat Second Generation (MSG) cover the area and period of interest, namely the Iberian Peninsula where the enhancements of the Fire Weather Index are evaluated. This satellite series is operated by EUMETSAT, providing observations every 15 minutes for a geostationary disk centred at 0°E above the equator, with a spatial resolution of 3 km at nadir. MSG observations are processed resulting in various products such as the Fire Radiative Power product (Wooster et al. 2015), disseminated by LSA SAF (Trigo et al. 2011), which is extremely useful to assess fire intensity and calibrate models of fire danger as it will be discussed to greater detail in chapter 2.

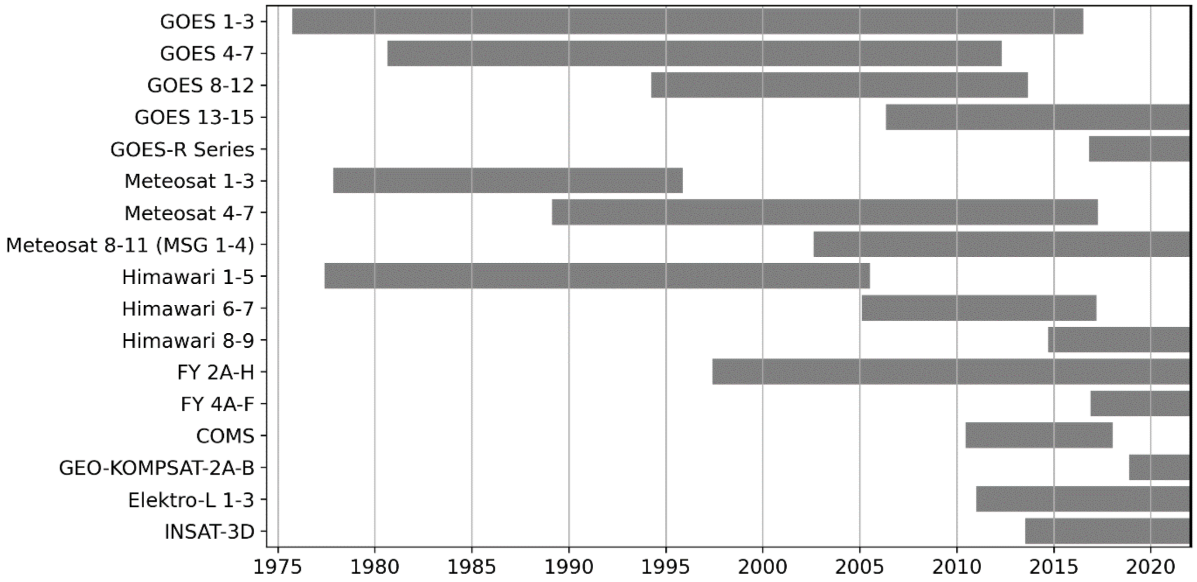

Figure 1.2. Operation timeline for geostationary weather satellites.

1.2 Atmospheric Reanalysis

Atmospheric, land and ocean observations are a fundamental aspect for monitoring Earth climate. Weather stations around the world monitor variables such as the temperature, relative humidity, wind speed and direction and atmospheric pressure near the surface. Weather balloons regularly launched in many locations allow us to retrieve the vertical profile of the atmosphere up to about 30 to 35 km height. Furthermore, aircraft and ships collect atmospheric and oceanic data. The nature of observation data is however subject to several problems. For instance, the density of stations is highly variable around the world (**Figure 1.3**), and they can also be subjected to errors and interruptions in the time-series. Satellite data, on the other hand, provide consistent observations around the globe but these data can only provide indirect estimates of surface or atmospheric variables based on the signal detected by the sensors aboard the satellites.

Figure 1.3. Observation and model differences for 2 m temperature comparing weather stations with ECMWF reference model on 17th of January of 2022. Image from WIGOS Data Quality Monitoring System (wdqms.wmo.int/nwp/land_surface/daily/quality/temperature/ECMWF/2022-01-17, last access on 2022-01-19).

Data assimilation techniques and dynamical models allow us to generate an analysis of global weather conditions based on the observations of multiple sources and on the physical equations in the model, which is consistent over space and time and corresponds to our best estimate of the true conditions (Navon 2009). Reanalyses are analyses for past weather conditions that provide continuous global datasets of an extensive list of atmospheric, land and oceanic climate variables. Among the many reanalyses datasets released in the last two decades (Uppala et al. 2008, Baatz et al. 2021) it is important to stress that the ERA5 is the most up-to-date (and robust) global reanalysis produced by the ECMWF, covering the period from 1950 to the present with a 30 km spatial resolution, hourly timesteps, and 137 pressure levels up to a height of 80 km (Hersbach et al. 2020). ECMWF also provides ERA5-Land reanalysis that is computed with a native resolution of 9 km, providing more detailed data for surface variables over land (Muñoz-Sabater et al. 2021).

1.3 Statistical Methods and Machine Learning

Extreme value theory is a branch of statistics that studies the occurrence of rare events. The wildfires that cause more concern are often large or very intense fires that are unusual for a given region (Ribeiro et al. 2020). To assess the fire danger in a robust way it is therefore important to study the tail of these extreme value distributions to get a good understanding of the fire risk. The modelling of wildfires intensity, size or duration distributions is often done using a peak over threshold approach (Pickands 1975) in which a Generalized Pareto distribution is considered the model to assign probabilities of exceedance of some variable x above a predefined threshold x_{min} (de Zea Bermudez and Kotz 2010). The variable x can be the size of the fire, the duration or even the energy released by the fire as estimated by satellite observations (DaCamara et al. 2014, Pinto et al. 2018a).

The cumulative distribution function of exceedances $\Delta x = x - x_{min}$ is then given by

$$G(\Delta x|\alpha, \sigma) = 1 - \left(1 + \frac{\alpha}{\sigma}\Delta x\right)^{-\frac{1}{\alpha}} \tag{1.1}$$

where α and σ are the shape and scale parameters of the Generalized Pareto distribution that can be estimated for a given set of independent and identically distributed samples of x using the maximum-likelihood method (Grimshaw 1993). The result is a model that allows to compute the probability that a fire event that exceeded x_{min} will exceed some value x. These models can be made more useful by incorporating fire weather indexes as covariates of the parameters of the distribution as will be further discussed in **section 2.3** of this thesis that extends ideas proposed previously by DaCamara et al. (2014) and Pinto et al. (2018a).

While classical statistical methods are extremely useful in the context described before, in which the most important (i.e. extreme) events are rare, for mapping burned areas, insights from different domains and applications (e.g.: Ronneberger et al. 2015, Zhang et al. 2016, Kussul et al. 2017) suggest that the task could be better addressed by state-of-the-art machine learning techniques, in particular multilayer neural network-based models falling into the category referred to as Deep Learning (LeCun et al. 2015) that have seen an exponential increase in adoption over the past years. This recent resurgence of neural networks is in part associated to the increasing computation capabilities made possible by modern GPUs that allow to accelerate the learning time for deep learning models. On the other hand, improved techniques for regularization of the models have been developed to overcome gradient instability problems, which would otherwise make the use of neural networks with many layers very challenging (Nusrat and Jang 2018).

Convolutional neural networks have shown state-of-the-art results for image classification and segmentation in many different areas of knowledge from the classification of regular pictures to medical applications, including 3-dimensional medical data segmentation to assist diagnosis (Milletari et al. 2016, De Fauw et al. 2018). Burned areas mapping is a problem that falls in this category of pattern identification in volumetric data as it will be discussed in more depth in chapter 3 of this thesis. However, one important challenge of burned area mapping is that the temporal component of the data (i.e., the satellite scenes of a region over a period of time) is often very noisy; for instance, clouds can often obstruct the surface view. As such, a simple application of pre-existing model architectures used to solve other problems, such as 3d segmentation of medical data, is not ideal for this case. Another class of neural networks, the recurrent neural networks, is often used to address problems with time-series and natural language processing as some of these model architectures can “remember” longer-term dependencies in the sequence of data (Hochreiter and Schmidhuber 1997). Combining these two model structures can easily yield very large models that can be difficult to handle with limited hardware requirements. The task of designing a model architecture for burned areas mapping is, therefore, one that needs to be optimized to reach a balance between the model size and complexity and the model capability to detect the patterns that characterize burned areas using noisy data, a task that is addressed in chapter 3 of this thesis.

1.4 Historical Background and Proposed Innovations

Forecasting the fire danger is a problem historically addressed at local or national scales, often using indices combining long-term changing variables, such as land cover, or short-term changing variables as it is the case for meteorological parameters such as wind, temperature, and relative humidity (San-Miguel-Ayanz et al. 2003). Some early examples of indices include the Nesterov index (Nesterov 1949) used in the former Soviet Union, the Forest Fire Danger Index (FFDI, McArthur 1967) developed to measure fire danger in Australian forests, the National Fire Danger Rating System (NFDRS, Deeming et al. 1977) used in the United States, and the Canadian Forest Fire Weather Index System (CFFWIS), proposed to assess fire danger over the Canadian forests (Van Wagner 1974 and 1987). Notably, the use of the CFFWIS system has been extended to regions across the world and nowadays it is used on a global scale as a general methodology to assess fire danger (Field et al. 2015, Vitolo et al. 2019, McElhinny et al. 2020). Despite its widespread use, the Fire Weather Index (FWI) has some limitations that often are addressed by combining additional sources of data. For instance, the FWI does not account for atmospheric instability information, which has been shown to play an important role in convective fires, nor does it consider the variability of the weather conditions along the day, since it is defined for a daily time scale. Regarding the fire danger topic, two important innovations proposed in this thesis are the generalisation of the FWI itself to account for these factors in a way that the interpretation of the final index values remains close to that of the original FWI. This is extremely important as it allows for users of the original FWI to easily understand and appreciate the added value of the improved versions. For the case of the variability of weather conditions along the day, it is necessary to interpolate the reference values of the previous days in a way that the resulting hourly index is identical to the daily index at the reference time chosen. For the case of including atmospheric instability information, addressing this problem requires the combination of two indices and a fire metric to consider as the reference point. The metric chosen was the Fire Radiative Power (FRP) detected by the Meteosat Second Generation satellite as it is available at 15-min steps and has shown to be useful for the calibration of models for predicting classes of fire danger based on probabilities of exceedance of predefined thresholds of FRP (Pinto et al. 2018a). Other metrics such as burned area or duration of the fire would not be an option for this problem as they do not reflect the intensity of the fire along the day, considering that burned areas are usually not available with temporal resolutions finer than 1 day.

Mapping the daily progression of burned areas is a challenge in itself, as traditionally more attention is given to the spatial accuracy of burned area maps. The task of mapping burned areas using satellite images has its origins back in the 1970s (Hitchcock and Hoffer 1974) using Landsat multispectral scanner. Over the years an extensive range of burned areas methods have been proposed, using a growing set of satellites (see **Figure 1.1** and **Table 1.1**). Burned area products are often subdivided into three groups based on the spatial resolution of the sensors, namely coarse resolution (≥250 m), medium resolution (10–80 m) and high resolution (<10 m). Regarding coarse-resolution products, some notable up-to-date products include: the MCD64A1 Collection 6 (Giglio et al. 2018a), available from 2000 to the present; the FireCCI51 (Chuvieco et al. 2018) available for the 2001–2017 period; the Global Fire Emission Database (van der Werf et al. 2017) available from 1997 onwards; and the FireCCILT10 (Otón and Pettinari 2019), covering the period of 1982–2017. As for the medium resolution sensors, a continuous global coverage is very challenging due to the high volumes of data and computation required. Long et al. (2019) addressed this problem by using Google Earth Engine to propose an annual global burned area product with Landsat data. Other notable efforts include the FireCCISFD11 (Roteta et al. 2019) developed for sub-Saharan Africa for the year 2016. High-resolution data is often used for case studies or emergency response systems like the Copernicus Emergency Management System (CEMS) which provides a quick analysis of notable fires in Europe, making use of several data sources including SPOT 6-7 and Pléiades 1A-B that provide multispectral data with resolutions of 6 m and 2 m, respectively. Another type of data used for mapping burned areas is Synthetic Aperture Radar (SAR) which has the advantage of penetrating clouds and working day and night-time (Ban et al. 2020). To convert satellite data to burned area maps, several methods have been used over the years such as logistic regression (Koutsias and Karteris 1998), random forests (Collins et al. 2018), support vector machines (Pereira et al. 2017), and rule-based algorithms based in physical considerations (e.g.: Giglio et al. 2018a, Chuvieco et al. 2018). Some of these methods make use of the active fires to identify initial candidates for burned pixels or to train machine learning classifiers. A more in-depth review of the historical background for burned area mapping can be found at Chuvieco et al. (2019). A newer class of methods for burned area mapping involving Deep Learning techniques have recently started to emerge along with important advancements in other computer vision problems such as segmentation of biomedical images (Ronneberger et al. 2015). Some recent applications to burned areas mapping have been focusing on medium resolution data (e.g.: Knopp et al. 2020, Zhang et al. 2021). Regarding the topic of mapping the daily progression of burned areas, two important innovations proposed in this thesis are: (1) the development of a deep learning neural network architecture for mapping burned areas using sequences of satellite images applied to daily data from VIIRS to provide robust maps of the daily progression of the fires; (2) leveraging a coarse burned area map and the cloud computation capabilities of Google Earth engine, for downloading and pre-processing data, to generate 10 m resolution burned area maps at an event level with a low computational requirement. These innovations also allow to create more accurate reconstructions of the fire progression for large fires, that in turn can be the basis for applications such as forecasting the fire progression.

Over the years, many techniques have been developed and used to study and simulate fire progression (Sullivan 2009a, 2009b and 2009c). These methods can be categorized into physical deterministic models and probabilistic models. The former type of model works by solving a set of equations and parametrizations that represent the physical processes involved in fire progression, including the interactions with the atmosphere. A good example is WRF-Fire (Coen et al. 2013) which runs as a module of the Weather Research and Forecasting (WRF) model widely used for mesoscale numerical weather prediction (Skamarock et al. 2019). A disadvantage of these models is the very high computational costs to resolve the simulation in a fine spatial grid (Peace et al. 2020). Regarding the probabilistic models, they can be subcategorized as vector-based or raster-based (Sullivan 2009c). Usually, vector-based approaches achieve better results trading off with an increased computational cost. Raster-based approaches, cellular automata being one of the most important, are very computationally efficient (Sousa et al. 2012, Gregorio et al. 2013) and it has been shown that improvements to the simpler formulation can lead to results that are similar to vector-based approaches (Ghisu et al. 2015). These models discretize the space in grid cells and the propagation of the fire to neighbouring cells is given as a probability that accounts for the states of the cells and the factors that drive the fire. Besides computational efficiency, these models have the ability to easily incorporate all types of information like allocation of firefighting resources (Freire et al. 2019) and fuel-breaks (Cohen and Etienne 2002). In this thesis, it is proposed an approach inspired by cellular automata but with some key differences, namely, the task is framed as a machine learning problem and the rules for the fire spread are learned based on observations and reconstructions of past large fire events. Furthermore, the forecasts are presented as probability maps resulting from an ensemble of predictors that in a sense give an estimate of fire danger in a neighbourhood of an active fire.

Besides the domain interconnections of the three topics described in the previous paragraphs, there is an overlap in some of the data and methods used. For instance, the fire radiative power (derived from MSG) is used in the first topic for calibrating and evaluating the FWI enhancements. The fire radiative power (derived from VIIRS) is also used as an input layer for mapping the daily progression of burned areas and for the reconstruction of the fire events in the topic of fire progression. Also, the hourly FWI and burned area maps produced within topics one and two are a core component of the dataset used for developing fire progression models in topic three. Furthermore, in future work, results of the fire progression models can likely provide feedback to be used as inputs for new fire danger classifications aware of landscape shape and active fire locations.

1.5 Objectives and Structure

To better understand past fires and to mitigate the impacts of fires in years to come it is of major importance to: (i) quantify and forecast fire danger combining numerical weather forecasts and satellite observations of fire intensity; (ii) map burned areas from satellite observations with multiple spatial and spectral resolution; and (iii) model fire progression taking into account weather conditions and fuel (vegetation) availability.

The main objectives for this thesis are the following:

- Improve the widely used FWI to incorporate atmospheric instability data and to extend its application to an hourly time basis. This allows for better discrimination of intraday weather variability and better risk assessment of atmospheric conditions favourable to convective fires that the traditional FWI may overlook.

- Develop a general methodology for mapping and dating burned areas and test it with VIIRS imagery. This methodology should also improve the pixel-level accuracy of dates of burning and be generalizable to sensors with similar characteristics.
- Develop a computationally efficient automatic method to map burned areas for large fires, using Sentinel-2 data at a 10-meter spatial resolution. This allows for a quick response for fire monitoring or a detailed study of past events.
- Develop a machine learning environment for short-term forecasting of fire progression based on the atmospheric conditions and the land characteristics in the fire location. This method will allow for a quick risk assessment for ongoing fires as well as pave the way to landscape aware fire danger products.
- Create and release Python libraries for most of the methodologies presented, so that interested researchers or institutions around the world can easily use or improve the methodologies proposed.

The structure of this thesis is as follows:

- In **chapter 2**, the main topic of fire weather danger is addressed. **Section 2.1** introduces the topic of fire weather danger. **Section 2.2** presents a case study, published in a conference book, of two large fires that occurred in Portugal in 2017 where the meteorological context is evaluated and discussed. **Section 2.3** presents a published paper describing an enhanced Fire Weather Index that combines the widely used FWI with a fire weather instability index. **Section 2.4** presents new unpublished research where an extension of the Fire Weather Index to an hourly basis is proposed, evaluated, and discussed.
- In **chapter 3**, the main topic of fire propagation and monitoring is addressed. **Section 3.1** introduces the topic. **Section 3.2** presents a published paper that proposes a new deep learning model architecture designed and trained to map the daily progression of burned areas using VIIRS data, tested for several regions around the globe. **Section 3.3** presents a published paper where a methodology is proposed for quick monitoring of burned areas using Sentinel-2 data and leveraging the capability of Google Earth Engine to pre-process and download the imagery required for the task. **Section 3.4** presents a case study, not published yet, regarding the large fires of south-eastern Australia where the method described in **section 3.2** is used and extended to the higher resolution bands

of VIIRS sensor. **Section 3.5** presents new work consisting of an ensemble approach to estimate short-term probability maps for fire progression.

- In **chapter 4**, the conclusions and final remarks are presented, as well as a vision for future research in this area.

2 Forecasting the Meteorological Fire Danger

2.1 Introduction

Forecasting the meteorological fire danger is an important topic of research, particularly in a climate change scenario where in many regions the risks posed by wildfires to society and the environment are increasing (Jones et al. 2020, Ellis et al. 2021, Jain et al. 2021). These risks can be particularly striking in regions not used to significant wildfires in the past but that may face fires with higher severity in the future (e.g.: Arnell et al. 2021, Krikken et al. 2021). For a fire to start, an ignition is needed either from natural or human causes. For the fire to grow to unmanageable dimensions, there are two additional conditions that need to be met, the availability of dry fuels and weather conditions favourable to the fire to develop and expand. The human-caused ignitions can in part be managed through education, regulation and law enforcement to avoid risk behaviours on days with higher fire risk. The distribution of fuels can, to some extent, be controlled by forest management and cleaning activities. The weather conditions, on the contrary, cannot, in general, be controlled by humans but they can be predicted. Forecasting the weather and in turn assessing the meteorological fire danger is therefore a key component for short term risk mitigation, allocation of resources and a better understanding of the fire dynamics for active firefighting planning.

Several indices have been proposed over the years to assess the meteorological fire danger or fire severity. Some early examples include the Nesterov index (Nesterov 1949) used in the former Soviet Union, the Forest Fire Danger Index (FFDI, McArthur 1967) developed to measure the fire danger in Australian forests, and the National Fire Danger Rating System (NFDRS, Deeming et al. 1977) used in the United States. However, the most widely used index is the Canadian Forest Fire Weather Index System (CFFWIS), initially developed to assess the fire danger over the Canadian forests (Van Wagner 1974 and 1987). The CFFWIS, used in the vast majority of regional and global scale studies, comprises six components, three fuel moisture codes and three fire behaviour indices. The fuel moisture codes are the Fine Fuel Moisture Code (FFMC), that indicates the dryness of the top fine fuels that are responsible for an easy ignition; the Duff Moisture Code (DMC) that indicates the dryness of the medium-size fuel materials; and the Drought Code (DC) that is a good indicator of seasonal drought and dryness of large fuels and deep compact organic layers. The fire behaviour indices are the Initial Spread Index (ISI) that indicates how fast a fire could spread based on the wind speed and the

FFMC; the Build-up Index (BUI) that combines the DMC and DC into a single numerical rating for the fuel available for combustion; and the Fire Weather Index (FWI) that is based on ISI and BUI and used as a general rating for the fire weather danger. There is an additional component often used, the Daily Severity Rating (DSR) that is a direct function of the FWI. The FWI has shown to be very useful in Mediterranean Europe (Viegas et al. 1999, DaCamara et al. 2014, Pinto et al. 2018a), and currently it operates on the Fire Danger Forecast module of the European Forest Fire Information System (EFFIS, San-Miguel-Ayanz et al. 2012). Additionally, it is also the basis for the Fire Risk Map product (Pinto et al. 2018a) disseminated by the Satellite Application Facility for the Land Surface Analysis (LSA SAF, Trigo et al. 2011).

The FWI, nevertheless, has some limitations. In particular, it does not consider the land cover type or the atmospheric instability that is known to play an important role in convective fires (Pinto et al. 2020b). The FWI does also ignore the variability of the weather throughout the day as it considers only the conditions at a reference hour that usually is selected as the synoptic hour closest to the solar noon. Calibrating fire risk models based on the FWI and including information of the land cover directly or indirectly is a usual solution for the first problem (DaCamara et al. 2014, Pinto et al. 2018a). As for the atmospheric instability information, the Haines Index (Haines 1988) has been developed for the United States and more recently an improved version, the Continuous Haines Index (CHI, Mills and McCaw 2010), has been proposed and is often used in conjunction with other fire danger indices, particularly in Australia (Ndalila et al. 2020). Regarding the weather variability, the extension of the FWI to an hourly timescale is not straightforward as the computation of the index each day depends on the values of the moisture codes of the previous day.

In this chapter two of the mentioned limitations of the FWI are addressed, first by combining the FWI and CHI into a single index - the enhanced FWI - by using statistical models to ensure that the interpretation of the new enhanced FWI is equivalent to the daily FWI in terms of the fire intensity to expect. Secondly, a method to extend the FWI computation to an hourly time-step is proposed while ensuring the FWI value at the reference time corresponds exactly to the daily FWI and once again allowing for easy integration and interpretability of the new index.

The structure of this chapter is as follows:

- In **section 2.2** a detailed description of the weather conditions associated with two extreme fire events that occurred in Portugal in 2017 is presented. The FWI and CHI are evaluated, and it is discussed how these indices together can provide a better picture of these extreme events, from a meteorological standpoint. This work corresponds to the conference paper “The extreme weather conditions behind the destructive fires of June and October 2017 in Portugal” published in **Advances in forest fire research 2018** by *Imprensa da Universidade de Coimbra*.

- In **section 2.3** a method is proposed to improve the FWI by incorporating atmospheric instability information. This is achieved by defining an enhanced FWI that is a combination of the FWI and CHI. The method uses statistical techniques to make the interpretation of the new index equivalent to the traditional FWI in terms of the energy released by fires as observed by satellite. This work corresponds to the paper “Enhancing the fire weather index with atmospheric instability information” published in **Environmental Research Letters** 15, no. 9.
- In **section 2.4** a method is proposed to compute the FWI at an hourly time-step as a generalization of the daily FWI ensuring that the value at the reference time is identical to the daily FWI. Comparisons of the hourly FWI with the evolution of the fire radiative power observed by satellite are then performed to demonstrate some of the potential utility of the hourly FWI. While the method described in this section has been previously presented at the EGU 2018 international conference, the analysis and results of this section are new material not published or presented before.

The main contribution of this chapter is a newly enhanced FWI that should be easy to integrate into existing FWI based applications and simple to understand by users of the traditional FWI.

2.2 The extreme weather conditions behind the destructive fires of June and October 2017 in Portugal

This section presents the results published in the following conference book chapter: Pinto, M. M., Hurduc, A., Trigo, R. M., Trigo, I. F., and DaCamara, C. C., 2018: The extreme weather conditions behind the destructive fires of June and October 2017 in Portugal, in Advances in Forest Fire Research 2018, Ed. Imprensa da Universidade de Coimbra.

The 2017 fire season in Portugal was marked by two tragic events leading to a toll of 116 fatalities and serious impacts at social, economic, and ecological levels. The first of the two events started on June 17 and the second on October 15. With the aim to better understand and predict future similar situations, we conducted an analysis of the meteorological conditions in which the two fire events took place. First, we analysed the events in a high-resolution meteorological context, using simulations by the Weather Research and Forecasting Model (WRF) and then within a climatic context with resource to ERA-Interim reanalysis. Fire Weather Index (FWI) was used to evaluate the meteorological conditions at the surface level while the Continuous Haines Index (CHI) was employed to assess the atmospheric instability conditions. WRF simulations show high temperature and low relative humidity for both fire events. Conversely, the October 15 event presents strong winds whereas the June 17 event shows weak winds at synoptic level. However, for the June event, the model simulates several downburst phenomena, associated with a mesoscale convective system, in agreement with the Doppler radar observations that show several gust fronts associated to the convective system that developed during the evening, reinforcing the need for the CHI to assess the vertical instability conditions. Monthly climatology of daily FWI and CHI were computed for the period spanning 1979–2016. Results show that for October 15, FWI is the new absolute maximum in the daily time-series, and CHI is at the percentile 90 for the extended fire season (June to September). On the other hand, for June 17, FWI is near the percentile 75 for the extended fire season and CHI is close to the percentile 99. We conclude that both fire events were associated to extreme meteorological conditions, however, their characteristics are very distinct. For the June 17 event, the atmospheric instability played the main role in the fast spread of the fire, whereas for the October 15 the strong winds associated with the close passage of hurricane Ophelia, together with extreme drought conditions were the main drivers.

2.2.1 Introduction

Forest fires are an important characteristic of the Mediterranean climate. Portugal is regularly affected by large and destructive wildfires leading to serious impacts at social, economic, and ecological levels (Amraoui et al. 2015). The 2017 fire season was particularly conspicuous in several ways, with a record total burned area of about 500 000 hectares and a tragic toll of 116 fatalities. Furthermore, the unusual extent of the 2017 fire season implied that the two most tragic events occurred prior (17–20 June) and after (15–17 October) the official fire season window used by the Portuguese authorities.

The case of June was marked by a heat wave that affected western and central Europe leading to very unusual conditions for that month (Sánchez-Benítez et al. 2018). The largest fires in central Portugal (Pedrogão-Grande and Gois) started on June 17, a day characterised by anomalously high temperatures and low relative humidity, associated to very unstable atmospheric conditions that favoured the formation of convective cells and thunderstorms. According to the report from the Portuguese Weather Service (IPMA) this instability, further strengthened by local fires, also led to several downburst events and associated gust fronts that played an important role in the fast spread of the fire (Moreira et al. 2017).

The case of October was marked by strong and persistent southerly winds caused by the close passage of hurricane Ophelia moving northward. The winds and the very dry vegetation due to the extreme drought situation were the main ingredients for the tragic events of October 15.

In this study we explore the two events, first in a high-resolution meteorological context using simulations by the Weather Research and Forecasting Model (WRF) initialized with ERA5 reanalysis and running on a grid covering Portugal with a spatial resolution of 4 km and then within a climatic context with resource to ERA-Interim reanalysis (Dee et al. 2011) for the period 1979–2017. Both ERA-Interim and ERA5 reanalysis are produced by the European Centre for Medium-Range Weather Forecasts (ECMWF), being the ERA5 the most recent state-of-the-art dataset, featuring hourly analysis fields with 0.25º spatial resolution.

2.2.2 Data and Methods

This study focuses on the region comprising mainland Portugal paying close attention to the sub-region delimited by the green box in **Figure 2.1**.

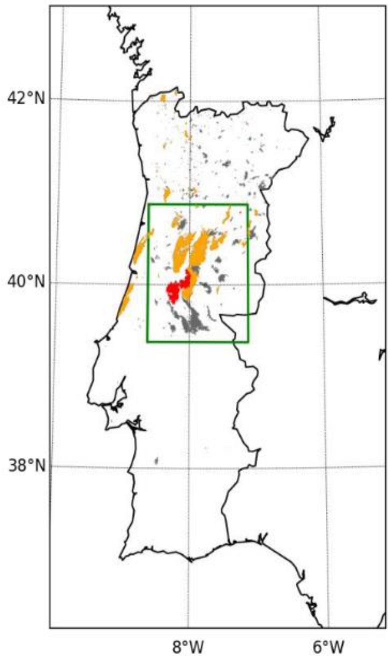

Figure 2.1. The map shows the burned areas for 2017 in mainland Portugal for the October case (orange), the June case (red) and the remaining period (gray). The green rectangle delimits the sub-region of study.

To assess the mesoscale weather conditions, we used WRF version 3.9.1 simulations on a 4 km spatial resolution grid, covering mainland Portugal, initialized with ERA5 reanalysis data as boundary conditions, with 64 vertical levels.

Meteorological fire danger conditions at the surface level were evaluated using the Fire Weather Index (FWI) that is part of the Canadian Fire Weather Index System (CFFWIS, Van Wagner 1974; Van Wagner 1987) and is a widely used fire danger rating system in Mediterranean Europe (e.g.: San-Miguel-Ayanz et al. 2012; DaCamara et al. 2014; Pinto et al. 2018a). This index measures the severity due to the present meteorological conditions but has also a memory from the past conditions based on a measure of fuel moisture. The Continuous Haines Index (CHI) is an extension of a discrete index proposed by Haines (1988) to measure atmospheric instability conditions that may allow for erratic fire behaviour (Mills and McCaw 2010).

The climatology of both FWI and CHI was computed using data from ERA-Interim reanalysis for the period spanning 1979–2017. Average FWI values for the defined sub-region are computed using 2-metre temperature and relative humidity, 10-metre wind speed and 24h accumulated precipitation all referring to the 12h UTC. Average CHI for the sub-region is also computed at 12h UTC using the temperature in degrees Celsius at 850 and 700 hPa and the dew point temperature at 850 hPa (Mills and McCaw, 2010).

In order to evaluate the sensitivity of FWI to meteorological variables, the average of each input variable is calculated for the respective month during the study period and FWI is then computed replacing each variable by the climatology of the month, one at the time. This allows evaluating how much FWI increases or decreases due to the positive or negative anomalies observed for each variable and to accordingly rank the contribution of each meteorological variable.

2.2.3 Results and Discussion

High-resolution simulations produced by the WRF model at a 4 km spatial and hourly temporal resolutions allow for a better understanding of mesoscale characteristics that are not neither represented in the coarser grids of reanalyses nor in global circulation models. **Figure 2.2** shows the WRF forecasts for 2-metre temperature, relative humidity and wind speed (left to right panels) valid at 15 UTC of 17 June (top panels) and 15 October, 2017 (bottom panels).

We can see that for June 17 (**Figure 2.2**, top panels) values of temperature were very high in most of the region, reaching anomalies of more than +12ºC (as marked by black contours) when comparing to the average for June for the period 1979–2017. As for relative humidity, very dry conditions were observed, with values more than 20% below average over most of the country. For wind speed, the picture is quite distinct, with negative anomalies being observed in most of the study region although the WRF shows several round-shaped regions of strong winds, up to 70 km/h at the considered hour. These concentric diverging strong wind regions are consistent with phenomena of downbursts and convective gust fronts that are simulated by the model in association with a convective system (Fujita 1985). Moreover, the location, spatial extent and wind velocity achieved are fairly in agreement with satellite and radar observations that show the development of strong convective storms and the occurrence of multiple convective gust fronts during the afternoon (Moreira et al. 2017). **Figure 2.3** (left panel) presents the average vertical profile for the sub-region of study as simulated by the WRF model at 15 UTC. Dry conditions at the lower atmospheric levels are observed followed by a more humid region that became saturated in places where the convective system developed. Rain or ice droplets falling start to evaporate when passing through the dry region, leading to evaporative cooling that results in downwards acceleration until the air mass reaches the ground and spreads horizontally with strong, sometimes damaging, wind gusts (Fujita 1985).

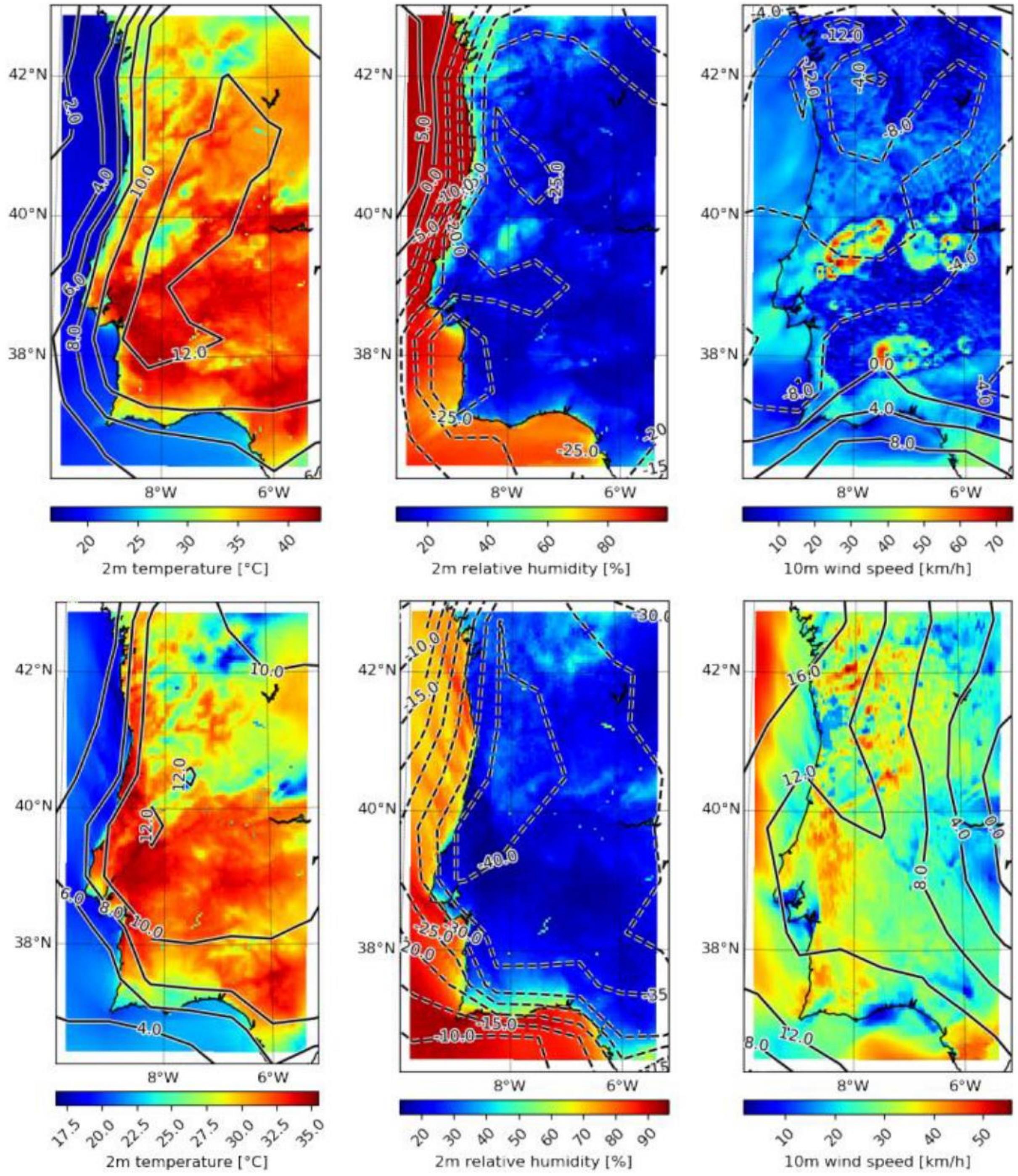

Figure 2.2. 15 UTC fields of 2-metre temperature and relative humidity and of wind speed (left to right panels) as simulated by the WRF model for June 17 (top panels) and October 15, 2017 (bottom panels). Fields are coloured according to the respective colour bars and black contours represent ERA-Interim anomalies, with dashed lines indicating negative anomalies.

As shown in the bottom panels of **Figure 2.2**, the October 15 event is characterized by high temperatures, with anomalies above +10ºC and very low relative humidity values, more than 40% below average in a large part of central and north Portugal. However, it must be stressed that wind was the main driver of this event. The last panel of **Figure 2.2** shows strong winds with anomalies greater than 10 km/h. These strong winds with southerly orientation were mainly caused by the nearby passage of hurricane Ophelia which was centred at about 485 km from Viana do Castelo (41.7ºN, 8.82ºW) on the considered day (IPMA, 2017). As shown in **Figure 2.3** a dry region at the lower layers of the atmosphere is present in both June and October cases, superimposed by a more humid layer (at about 500 hPa), the main difference being the presence of a drier layer above 400 hPa in the October event. It is also important to notice that, in October, besides the strong wind, the ongoing extreme drought conditions were a major key ingredient for the unprecedented dimension of burned area observed in Portugal in a single day.

It is also worth mentioning that while the October case is very well characterized by means of large-scale conditions, in the case of June, high-resolution information provided by the mesoscale model is fundamental to resolving the mesoscale convective storms and better understand the situation. This predisposition of the atmosphere for instability conditions can be measured by CHI (Mills and McCaw 2010). For that, we computed both CHI and FWI for each day since 1979 using ERA-Interim reanalysis data. Results (**Figure 2.4**) show that the October case was indeed an absolute extreme in FWI while the June case was characterised by values above percentile 75 for the month of June and just below percentile 75 when considering the extended fire season (from June to September). However, when looking for CHI we see that the June case shows a CHI above 10, very close to percentile 99 for the extended fire season, while the October case corresponds to percentile 90. This reinforces the idea that looking to the vertical instability conditions provides additional information that is necessary in order to obtain a more in-depth characterization of the extreme event at the local to regional scales.

Moreover, instability indices such as CHI that are fairly simple to compute can be used for a more complete information about fire danger. According to Mills and McCaw (2010), values of CHI above 10 imply an extremely difficult setting to extinguish fires and a high risk of under-predicted behaviour. This is in agreement with the observations for June 17 where fast fire spread was observed with the development of pyrocumulonimbus (Moreira et al. 2017).

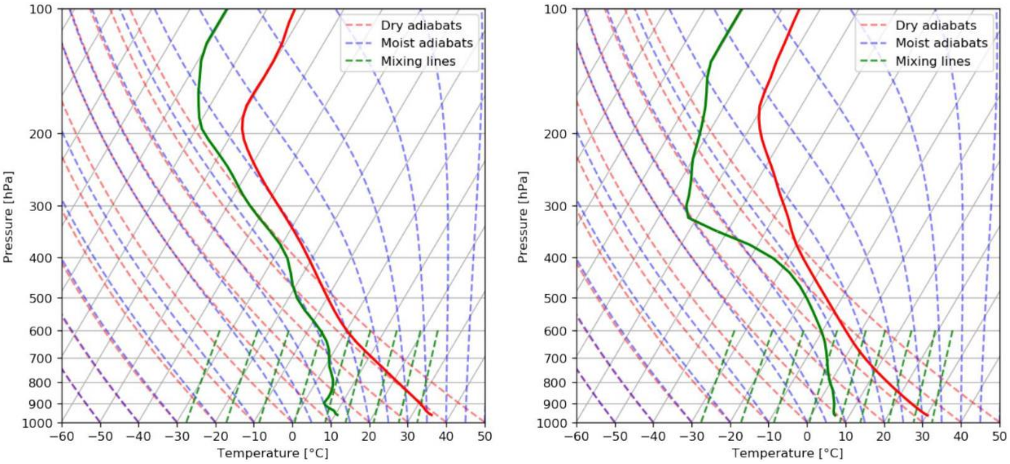

Figure 2.3. Vertical profiles of temperature (red line) and dew point temperature (green line) in °C, as simulated by the WRF model, at 15 UTC of June 17 (left panel) and October 15 (right panel). Dashed red, blue and green lines respectively represent the dry adiabats, moist adiabats and saturating mixing ratio.

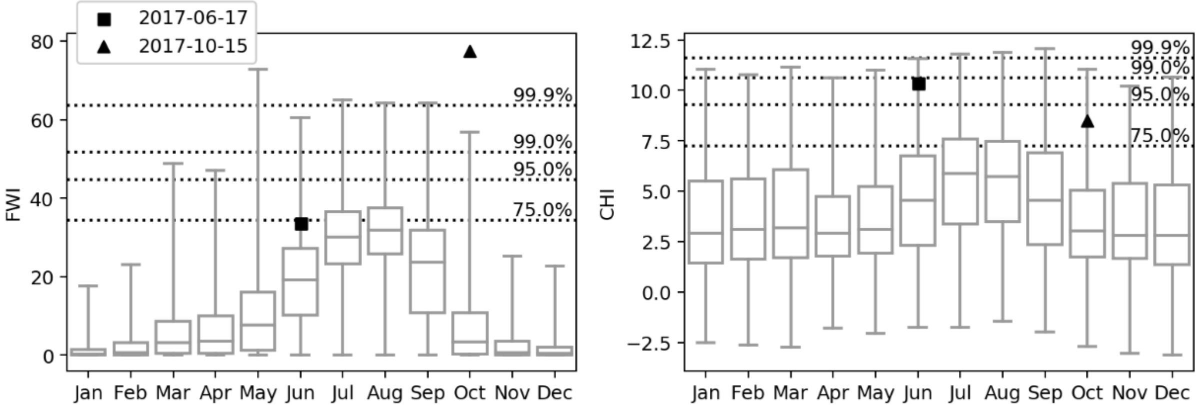

Figure 2.4. Boxplots of monthly distributions of FWI (left panel) and CHI (right panel) for the period 1979–2016). The horizontal dashed lines indicate percentiles for the extended fire season (June to September) whereas the black squares and triangles refer to the values for June 17 and October 15, 2017.

Table 2.1 presents a comparison of values of FWI for June 17 and October 15 with values of the same index computed with temperature, relative humidity, and wind intensity, respectively replaced by the respective monthly means over the period 1979–2017.

Considering the case of June 17, when replacing the wind speed by the climatological mean there is a small increase of 3% of FWI (from 34 to 35) whereas decreases of 18% and 24%, (from 34 to 28 and from 34 to 26) are obtained when replacing temperature and relative humidity by climatological means. This is to be expected since the large-scale wind speed is below average whereas the other two variables are above average (**Figure 2.2**). Relative humidity was accordingly the most important factor contributing to the observed value of FWI, closely followed by temperature. However, as discussed earlier, the mesoscale wind associated with the convective system has played a main role that is not captured by FWI at such coarse scale and the effect is better quantified by CHI.

Table 2.1. FWI observed and modelled (replacing observed temperature, wind and relative humidity by respective monthly means in 1979–2017) for June 17 and October 15, 2017. In brackets, the relative change (%) of each modelled value from the respective observed value.

		FWI	
		17 Jun	**15 Oct**
Observed		**34**	**78**
Modelled	**Wind**	**35 [+3%]**	**41 [-47%]**
	Temperature	**28 [-18%]**	**66 [-15%]**
	Relative humidity	**26 [-24%]**	**46 [-41%]**

Analysing the case of October 15, it may be noted that FWI reached a value of 78 (more than double of June 17). In this case, all parameters present a positive contribution. The most notorious change occurs when considering the average wind speed, followed by relative humidity. When modelling FWI replacing wind speed by the monthly average for October, the resulting FWI value drops to 41, almost half of the observed value. The contribution of relative humidity closely follows that of wind whereas temperature has the smallest contribution.

2.2.4 Conclusions

Analysis of FWI and CHI in a climate context shows that both June and October fire events were associated to extreme meteorological conditions. However, the characteristics of these two events are very distinct. The June event happened very early in the fire season in the context of a heat wave and a very unstable atmosphere that allowed for a fast and unpredictable spread of the fires. The October case, in turn, took place late in the fire season in a situation of extreme drought and in a day marked by strong winds associated with the close passage of hurricane Ophelia that led to a very fast fire spread.

A closer look at the sensitivity of FWI to meteorological conditions shows that for the June 17 case temperature and relative humidity were the main contributors, the large-scale wind speed being below average. For the October 15 case, all meteorological variables considered show a positive contribution. Wind speed and relative humidity were the most relevant contributing variables that led to a record FWI value of 78 for the considered region, indicating an extreme potential fire intensity associated with a high rate of fire spread due to the strong winds.

It is also shown that the WRF model initialized with boundary conditions given by state-of-the-art reanalyses, in this case ERA5, can reasonably well simulate the development of the convective systems and the atmospheric instability. Furthermore, the incorporation of CHI as a measure of atmospheric instability can represent an added value when rating fire danger, a topic that is currently being addressed in our research.

2.2.5 Acknowledgements

Research by Miguel M. Pinto was supported by the Portuguese Science Foundation (FCT) through PhD grant PD/BD/142779/2018. Research by Alexandra Hurduc was supported by a grant in the framework of Project “Reabilitação das Áreas Queimadas na Freguesia de Alvares”, financed by donation of Observador on time SA.

2.2.6 Author Contributions

Miguel M. Pinto (MMP) wrote the paper. MMP and Alexandra Hurduc (AH) organized the data, developed the algorithms, and validated the results. Ricardo M. Trigo (RMT), Isabel F. Trigo (IFT) and Carlos C. DaCamara (CCD) contributed with constructive criticism and suggestions. RMT, IFT, CCD and AH revised and edited the manuscript.

2.3 Enhancing the fire weather index with atmospheric instability information

This section presents the results published in the following article: Pinto, M. M., DaCamara, C. C., Hurduc, A., Trigo, R. M., & Trigo, I. F. (2020). Enhancing the fire weather index with atmospheric instability information. Environmental Research Letters, 15(9), 0940b7.

The Fire Weather Index (FWI) is widely used to assess the meteorological fire danger in several ecosystems worldwide. One shortcoming of the FWI is that only surface weather conditions are considered, despite the important role often played by atmospheric instability in the development of very large wildfires. In this work, we focus on the Iberian Peninsula for the period spanning 2004–2018. We show that atmospheric instability, assessed by the Continuous Haines Index (CHI), can be used to improve estimates of the probability of exceedance of energy released by fires. To achieve this, we consider a Generalized Pareto (GP) model and we show that by stepwisely introducing the FWI and then the CHI as covariates of the GP parameters, the model is improved at each stage. A comprehensive comparison of results using the GP with the FWI as a covariate and the GP with both the FWI and CHI as covariates allowed us to then define a correction to the FWI, dependent on the CHI, that we coined enhanced FWI (FWIe). Besides ensuring a better performance of this improved FWI version, it is important to stress that the proposed FWIe incorporates efficiently the effect of atmospheric instability into an estimation of fire weather danger and can be easily incorporated into existing systems.

2.3.1 Introduction

Wildfires are an important natural hazard with significant impact on ecosystems and human populations (Amraoui et al. 2015). The Iberian Peninsula, and in particular Portugal and the northwestern Spanish province of Galicia, are the regions in Southern Europe most affected by wildfires (Pereira et al. 2011). According to the European Forest Fire Information System (EFFIS, San-Miguel-Ayanz et al. 2012), Portugal and Spain rank in 1st and 2nd place, respectively, for the European countries with the highest burned area during the period of 2008–2018. Portugal with a figure of 115 736 ha yr^{-1}, corresponding to 1.2% of the country area, and Spain with 62 844 ha yr^{-1}, corresponding to about 0.1% of the country area. Together, Portugal and Spain account for about 44% of the total burned area in Europe. Furthermore, future climate scenarios predict an increase in fire-prone weather conditions making this problem even more relevant (Amatulli et al. 2013, Pereira et al. 2013, Bedia et al. 2014, Abatzoglou et al. 2019).

Wildfires can be categorized into three types: convective, wind-driven and topographic (Lecina-Diaz et al. 2014). Atmospheric instability plays an important role in convective fires in which the hot air rising above the fire can, in the right conditions, generate pyrocumulonimbus and result in extreme fire intensity and unpredictable fire behaviour, particularly if high amounts of dry fuel are available. In the case of wind-driven fires, the strong wind is the main factor driving the fire propagation that occurs in the direction of the wind. For the topographic fires, slope winds are the main force and fire progression will be strongly dependent on the topography.

Over the years, several methods have been proposed to assess the meteorological fire danger over Europe (e.g. San-Miguel-Ayanz et al. 2012, Dacamara et al. 2014, Pinto et al. 2018a). These methods are usually based on the Fire Weather Index (FWI), one of the components of the Canadian Fire Weather Index (CFWIS, van Wagner 1974, 1987), and, therefore, the limitations of the FWI may affect the accuracy of fire danger estimates. Other indices exist for similar purposes, for example, the Forest Fire Danger Index (FFDI, Mcarthur 1967) is commonly used over Australia. These indices are based on surface meteorological information and drought/fuel moisture, without taking into consideration atmospheric instability conditions that can play an important role in the development of very large fires (Fernandes et al. 2016). The Haines Index (Haines 1988) has been proposed to measure fire-prone atmospheric instability conditions over the United States of America and has since then been used over several regions of the globe such as the United States (e.g. Werth and Ochoa 1993, Trouet et al. 2009), New Zealand (Simpson et al. 2014), the Mediterranean basin (Tatli and Turkes 2014) and Australia (Mccaw et al. 2007). However, the original formulation of the Haines Index presents some limitations that need to be addressed (Potter 2018). The Continuous Haines Index (CHI, Mills and McCaw 2010) has been proposed to address some of these limitations and has been used mainly over Australia (e.g. McRae et al. 2013, Sharples et al. 2016).

The main goal of this work is to provide an enhanced version of the widely used FWI to take into account atmospheric instability. We choose the CHI as it provides a simple large-scale measure of instability that has been shown to be useful to evaluate extreme convective fires in conjunction with the FWI (e.g. Pinto et al. 2018b) or with the FFDI over Australia (e.g. Ndalila et al. 2020). We first show that the logarithm of energies released by fires, as derived from remote sensing observations, follows a Generalized Pareto (GP) distribution. Then, we show that by incorporating the FWI and CHI as covariates of the GP parameters, the model is better at explaining the observations of released energy. The resulting model allows us to estimate the probability of exceedance of a predefined energy threshold, dependent on the FWI and CHI. Moreover, this probability of exceedance may be expressed in terms of an enhanced FWI, i.e. FWIe, which incorporates the effect of atmospheric instability into an estimation of fire weather danger. Finally, we show two case studies to exemplify the practical use of the FWIe.

2.3.2 Data and Methods

This study focuses on the Iberian Peninsula, spanning the period of 2004–2018. The data to compute the FWI and CHI were obtained from ERA5 reanalysis, available at https://cds.climate.copernicus.eu. ERA5 is the latest reanalysis produced by the European Center for Medium-range Weather Forecast (ECMWF), featuring a spatial resolution of 0.25º and 37 pressure levels. The data obtained for the period and region of study comprise temperature and dew point at 2 m, 700 hPa and 850 hPa, U and V components of the wind at 10 m and 24 h accumulated precipitation; all fields are daily, referring to 12 h UTC.

2.3.2.1 Fire Weather Index (FWI)

The CFWIS consists of six indices: three fuel moisture codes that have a memory component, allowing us to capture the effect of drought; and three behaviour indices, including the FWI. The weather inputs required to compute the CFWIS indices are 2 m temperature and relative humidity, 10 m wind speed and 24 h accumulated rain. The relative humidity is computed using the temperature and dew-point temperature according to the Magnus expression (Lawrence 2005). The code for the computation of the CFWIS indices can be found in Wang et al. (2015) and an in-depth interpretation of the CFWIS indices can be found in Wotton (Wotton 2009). The CFWIS indices are therefore computed for each ERA5 grid cell covering the study region and for each day of the study period (2004–2018).

2.3.2.2 Continuous Haines Index (CHI)

The CHI is designed to assess the instability that favours convective fires and is composed of two terms: (1) an instability term that is based on the difference in temperature at two atmospheric levels (CA), and (2) a moisture term that is given by the difference between temperature and dew point at the lower level (CB). This is an important feature since a very high CHI requires a dry atmosphere at the lower level and a steep lapse rate. If instead, the air is moist at the lower level, a rising parcel of air will result in a low lifting condensation level that is favourable to the development of storms with heavy rainfall. A dry atmosphere and high cloud base are favourable to dry thunderstorms and severe wind phenomena such as downbursts that can also play a role in the ignition and spread of fire. In this sense, the CHI is, by design, more suitable for measuring conditions favourable to convective fires in comparison to the traditional instability indices. Furthermore, the CHI can be computed at different height levels depending on the average topography of the region (Haines 1988, Mills and McCaw 2010). We selected the level 850–700 hPa, referred to as the middle level, which is more suitable for the average topography over the Iberian Peninsula (Winkler et al. 2007). The CHI is then defined as

$$CA = \frac{T_{850} - T_{700}}{2} - 2 \tag{2.1}$$

$$CB = \frac{min(T_{850} - DP_{850}, 30)}{3} - 1 \tag{2.2}$$

$$if\ CB > 5, then\ CB = 5 + \frac{CB - 5}{2}$$

$$CHI = CA + CB \tag{2.3}$$

where the T_{700} and T_{850} are the temperatures at 700 and 850 hPa, DP_{850} is the dew-point temperature at 850 hPa and the min $(T_{850} - DP_{850}, 30)$ term in equation (2.2) indicates that an upper bound of 30 °C is set to the difference between the temperature and dewpoint at 850 hPa. Using equations (2.1)–(2.3), the CHI is then computed for each ERA5 grid pixel covering the study region and for each day during the study period (2004–2018).

2.3.2.3 Daily Energy Released by Fires

Daily energy values were derived from Fire Radiative Power (FRP) product produced and disseminated by the Satellite Application Facility for Land Surface Analysis (LSA SAF) (Trigo et al. 2011, Wooster et al. 2015). To derive the daily energy values from the FRP data with a periodicity of 15 min, we convert the radiative power to energy by assuming a constant power over the 15 min period (Pinto et al. 2018a) and limiting to FRP events with fire confidence (Roberts and Wooster 2014, Wooster et al. 2015) greater than 70%. We then sum the energy values for each day over each ERA5 grid cell in order to have triplets of (FWI, CHI, energy) for each day and each ERA5 cell covering the study region.

2.3.2.4 Generalized Pareto Models and FWIe

The GP distribution has been shown to be useful for modelling fire duration (DaCamara et al. 2014) and fire released energy (Pinto et al. 2018a). The cumulative distribution function (CDF) of the GP for an exceedance of x above a predefined minimum threshold is defined as

$$G(x|\alpha,\sigma) = 1 - \left(1 + \frac{\alpha}{\sigma}x\right)^{-\frac{1}{\alpha}} \tag{2.4}$$

where α and σ are the shape and scale parameters of the distribution, respectively.

To test for the goodness of fit of the samples to the GP distribution, the A^2 test is used (Anderson and Darling 1952) and the confidence level is obtained by generating 5000 data samples from the GP distribution with the estimated shape and scale parameters (DaCamara et al. 2014, Pinto et al. 2018a).

We then consider two models, one with the FWI as a covariate of shape and scale parameters of the GP and another with both the FWI and CHI as covariates. The shape and scale parameters for the first model ($GP_{(FWI)}$) are defined as

$$\alpha(FWI) = a + b \times FWI \tag{2.5}$$

$$\sigma(FWI) = c + d \times FWI \tag{2.6}$$

where a, b, c and d are the new model parameters. For the $GP_{(FWI,CHI)}$ model, the shape and scale parameters are defined as

$$\alpha(FWI,CHI) = e + f \times FWI + g \times CHI + h \times FWI \times CHI \tag{2.7}$$

$$\sigma(FWI,CHI) = i + j \times FWI + k \times CHI + l \times FWI \times CHI \tag{2.8}$$

where e, f, g, h, i, j, k and l are the new parameters.

We find the parameters for each model using maximum likelihood estimation (MLE) and we test if the more complex models are better than the previous one using the likelihood ratio test (Neyman and Pearson 1933). We implement this procedure in Python using the SciPy library (Virtanen et al. 2020).

As the use of the FWI in practical applications is more widespread than the concept of probabilities of exceedance of energy released by fires, we then determine the FWI value, i.e. FWIe, that yields $GP_{(FWIe)} = GP_{(FWI,CHI)}$ for a given threshold. The FWIe is therefore a function of the FWI and CHI, calibrated so that the probability of exceedance of a predefined threshold of released energy on the $GP_{(FWI)}$ model is identical to the one given by the more complex $GP_{(FWI,CHI)}$ model.

In order to test for the generalization of the method for years not used to estimate the parameters, we use a 15-fold cross-validation (CV) scheme, leaving one year out for validation on each fold and estimating the parameters with the remaining years (Wilks 2011). To present the results, we then consider the average of the 15 models. The standard deviation of the 15 models is used to assess the uncertainty of the estimates.

2.3.3 Results and Discussion

2.3.3.1 GP Model for all Data

In order to show that the GP model is appropriate to model the distribution of the natural logarithm of energy (ln(E)) released by fires, we consider all ERA5 grid cells, over the study region and period, for which the natural logarithm of daily released energy is greater than 5 (about 150 GJ) and we subtract 5 to have values starting at zero. The threshold of 5 is chosen empirically based on visual inspection of the histogram of the natural logarithm of energy (**Figure 2.5**, left panel) as the start of the right tail of the distribution. **Figure 2.5** also shows the histograms for the FWI and CHI where the histograms in grey correspond to all 28 709 events, whereas the histograms in blue represent the corresponding distributions for events with ln(E) > 5, resulting in 17573 events. It is worth noting that for the FWI histograms (**Figure 2.5**, central panel) the distribution is bimodal, the lower mode corresponding to a smaller peak of fire activity usually occurring in March, more prominent in the north of the Iberian Peninsula (Trigo et al. 2016).

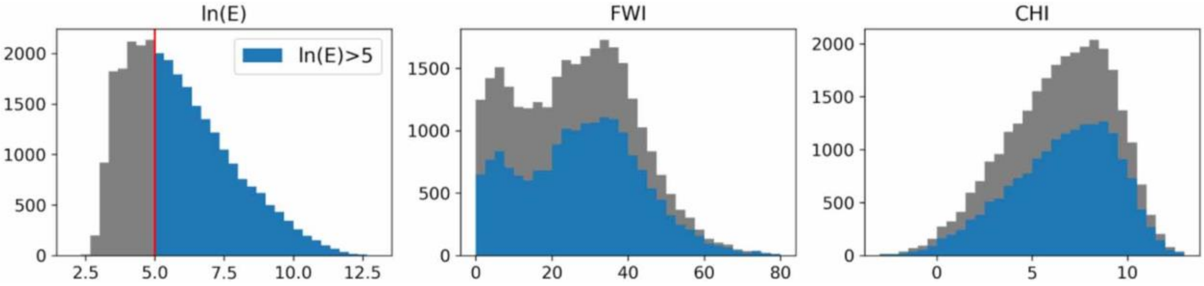

Figure 2.5. Histograms for the natural logarithm of energy, with the FWI and CHI for all 28709 fire events and for $ln(E) > 5$ (blue) overlayed. Red vertical line represents the threshold of $ln(E) = 5$.

The optimal shape and scale parameters of the GP are then obtained for the given distribution of $ln(E)$ using MLE, resulting in a shape parameter of -0.33 and a scale parameter of 2.62. The quantile-quantile plot (**Figure 2.6**, left panel) provides an indication of the goodness of fit of the model, revealing that observed quantiles plotted against theoretical ones are very close to the 1:1 line. Following the Anderson–Darling test and corresponding computation of the A^2 statistic, we can conclude that samples follow a GP distribution with a confidence level above 97%. The GP model with the obtained shape and scale parameters provides the probability of an event exceeding any given threshold, assuming that it has already exceeded the threshold of 5 as mentioned above (i.e. that its total released energy is higher than e^5 GJ). As an example, an exceedance of 2.6 corresponds to the probability of exceeding 5 + 2.6 (about 2000 GJ) given that 5 (about 150 GJ) was already surpassed. We represent this conditional probability as P(2000|150).

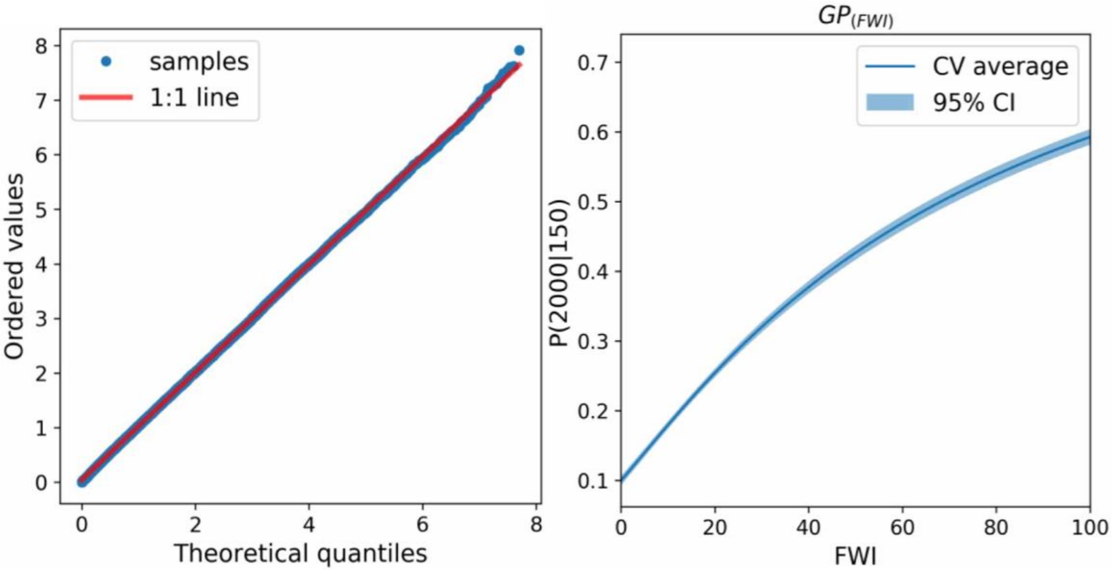

Figure 2.6. Quantile-quantile plot for the GP distribution fitted to the natural logarithm of energy released by fires (left panel) and probability of exceedance of 2000 GJ given 150 GJ for successive values of the FWI (right panel). The blue line in the right panel corresponds to the average of the 15 CV folds and the shaded blue region the 95% CI.

2.3.3.2 GP Model Dependent on FWI

Following the procedure described in **section 2.3.2.4**, we now define the shape and scale of the GP as functions of the FWI according to equations (2.5) and (2.6) and we find the parameters a, b, c and d, using MLE. **Table A.1** in the annexes shows the average and standard deviation of the four parameters for the 15 CV folds. Using an exceedance threshold of 2000 GJ we can now compute the probability of exceedance of 2000 GJ given 150 GJ - P(2000|150) - for successive values of the FWI. We repeat this procedure for each of the 15 CV folds. **Figure 2.6** (right panel) shows the average of the CV folds and the 95% confidence interval (95% CI), given by the range −2 to 2 times the standard deviation, represented by the shaded region. We can see that as expected the P(2000|150) increases with the FWI, starting at about 0.1 for FWI of 0 and rising to almost 0.6 for an FWI of 100. This result is in line with results obtained by Pinto et al. 2018a for the Mediterranean Europe, although it should be noted that here we also introduce the FWI as a covariate of the shape parameter. This differs from previous works where the FWI was only used as a covariate of the scale parameter (Dacamara et al. 2014, Pinto et al. 2018a). To assess the statistical significance of introducing the FWI also as a covariate of the shape parameter, we compared a model with the FWI as the covariate of the scale parameter with the one with the FWI as the covariate of both shape and scale parameters, using the negative log-likelihood (NLL) ratio test. We obtained a p-value < 0.0001 suggesting that including the covariate in the shape parameter improves the performance of the model. Furthermore, the small spread of the model (even for high values of the FWI), as depicted by the small difference between the 15 CV folds, is a good indication of the robustness of the approach.

2.3.3.3 GP Model Dependent on FWI and CHI

Following the same procedure as the one adopted in the previous section, we now consider both the FWI and CHI as covariates of the shape and scale parameters according to equations (2.7) and (2.8) and the eight parameters are again obtained using MLE. **Table A.2** in the annexes shows the average and standard deviation of the parameters. Using the 15 CV models and fixing an exceedance of 2.6, similar to **section 2.3.3.2**, we now compute P(2000|150) for successive values of the FWI and CHI for each model and we show the mean (**Figure 2.7**, left panel) and twice the standard deviation (**Figure 2.7**, right panel) of the 15 models. As mentioned before, the P(2000|150) increases significantly for higher values of the FWI. This increment, however, is not constant as it depends on the magnitude of the CHI. Indeed, higher (lower) values of the CHI translate to an increase (decrease) in the probability of exceedance. Finally, considering the amplitude of values depicted on the right panel of **Figure 2.7**, we can confirm that the variation among the 15 models is in general small, being the highest for very low CHI and very high FWI. This corresponds to a region of the (FWI, CHI) domain with a low number of fire events, as shown by the black contours in **Figure 2.7** right panel, corresponding to the Gaussian kernel density estimation for all fire events, scaled to the interval (0, 1).

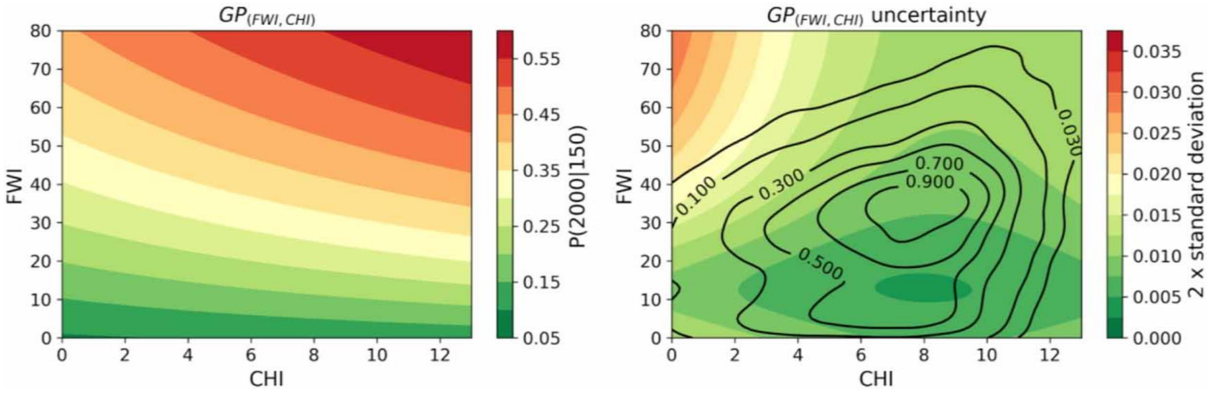

Figure 2.7. P(2000|150) for successive values of the FWI and CHI (left panel) and twice the standard deviation of the 15 CV models (right panel). Black contours in the right panel correspond to the gaussian kernel density estimation for all fire events scaled to the interval (0, 1).

In order to evaluate the GP model with FWI and CHI as covariates in respect to the GP model with only FWI as the covariate, the NLL ratio test is used. Once again, the obtained p-value < 0.0001 is a good indication that including the CHI translates to a model that explains better the observed values of released energies by the fires.

2.3.3.4 FWIe

Comparing the CDF for low/high values of the FWI and CHI (**Figure 2.8**, left panel), it can be seen that for an FWI of 10 (grey dashed line, disregarding in this case the CHI), fires with lower energy are more common whereas for an FWI of 80 (black dashed line, also disregarding the CHI) the CDF increases at a slower pace, meaning that large fires are much more likely. When evaluating the results for the same values of the FWI, but considering the model of **section 2.3.3.3**, i.e. with both the FWI and CHI as covariates, and selecting extreme values for the CHI (1 and 12, respectively), we see that for a CHI of 12 (1), the CDFs shift downwards (upwards), meaning that, as discussed before, the probability of large fires increases (decreases) for higher (lower) CHI. Furthermore, it is worth noting that the effect is more prominent for higher values of the FWI.

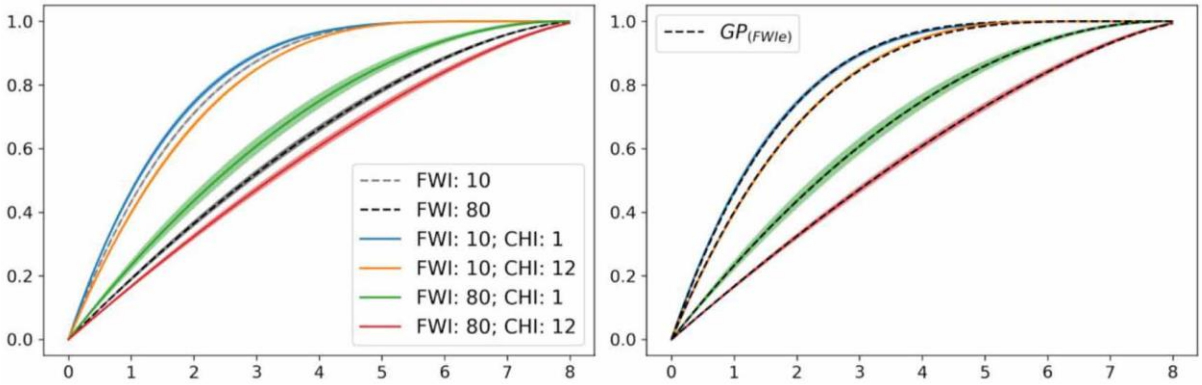

Figure 2.8. Cumulative distribution functions for several values of the FWI and CHI (left panel) and comparison of CDFs of the $GP_{(FWI,CHI)}$ model and $GP_{(FWI_e)}$ model (right panel).

Using the $GP_{(FWI)}$ model and $GP_{(FWI,CHI)}$ model, we can now use the threshold of exceedance of 2.6 (i.e. the P(2000|150)) to find the FWI value in the $GP_{(FWI)}$ model, i.e. the FWIe, which yields $GP_{(FWI_e)} = GP_{(FWI,CHI)}$ for the selected threshold of 2.6. **Figure 2.8** (right panel) shows that the CDFs for the $GP_{(FWI)}$ model using the FWIe (represented by the dashed black lines), hereafter referred to as $GP_{(FWI_e)}$, are very close to the ones of the $GP_{(FWI,CHI)}$ model. Note that by the definition of FWIe, they must be equal for an exceedance of 2.6 (~2000 GJ). One advantage of using the FWIe instead of a model with the FWI and CHI is that the FWI is widely used and, for practical applications, it is usually easier to introduce a modification to an already widespread index.

Figure 2.9 shows the values of the FWIe for each (FWI, CHI) pair (left panel) and their respective differences with respect to the baseline FWI (right panel). **Table A.3** in the annexes shows the FWIe values for fixed values of the FWI and CHI. It can be observed (**Figure 2.9**, right panel) that for higher values of the FWI, the contribution of the CHI is stronger, translating into differences exceeding ± 20. This suggests that the fire danger based only on the FWI underestimates (overestimates) the probability of large fires for the CHI values above (below) about 7, being the effect less pronounced when the FWI is low.

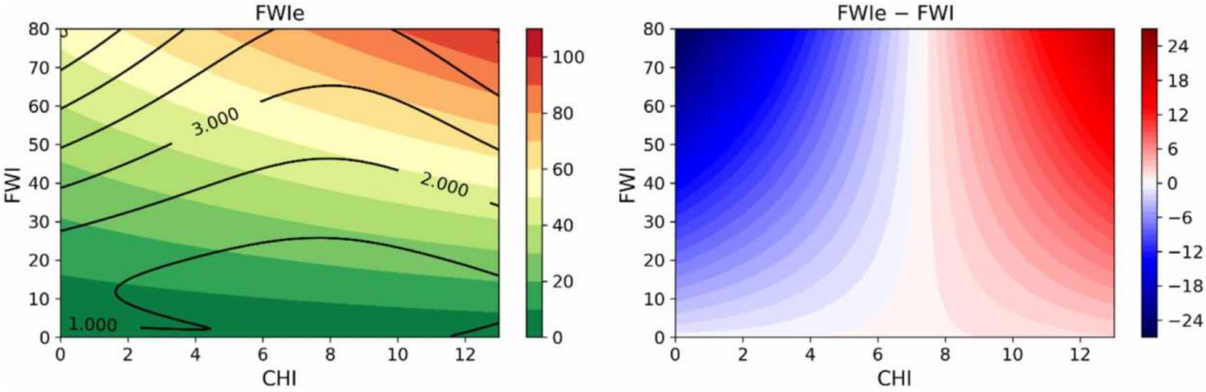

Figure 2.9. FWIe for successive values of the FWI and CHI (left panel) and differences with respect to the FWI. Black contours in the left panel correspond to twice the standard deviation of the 15 CV models.

To further validate the model and understand how well it generalizes to years not used for the estimation of the parameters, we compare probabilities of exceedance provided by the two GP models ($GP_{(FWI)}$ and $GP_{(FWI_e)}$) with actually observed fire released energy, as computed from the LSA SAF FRP product (see **section 2.3.2.3**). We consider a sliding window of probabilities estimated by the model (for the threshold of 2.6), starting at the probability interval (0–0.2) and then increasing in steps of 0.05, considering only the windows that include at least 200 observations. Then, for each window, we plot the average model estimates against the fraction of events exceeding 2.6. The procedure is repeated for the $GP_{(FWI)}$ and $GP_{(FWI_e)}$ models both for the mean of the 15 CV models and for out-of-fold (OOF) prediction, i.e. the probability for each event is assigned using the model that did not used that year for the estimation of the parameters. The results (**Figure 2.10**) indicate that the model estimates agree on average with the observed fractions of exceedance. Most importantly, the difference between the 15 CV mean and the OOF estimates is very small, indicating that the model generalizes well for 'unseen' years, giving therefore some confidence to use the model for forecasting over the next few years.

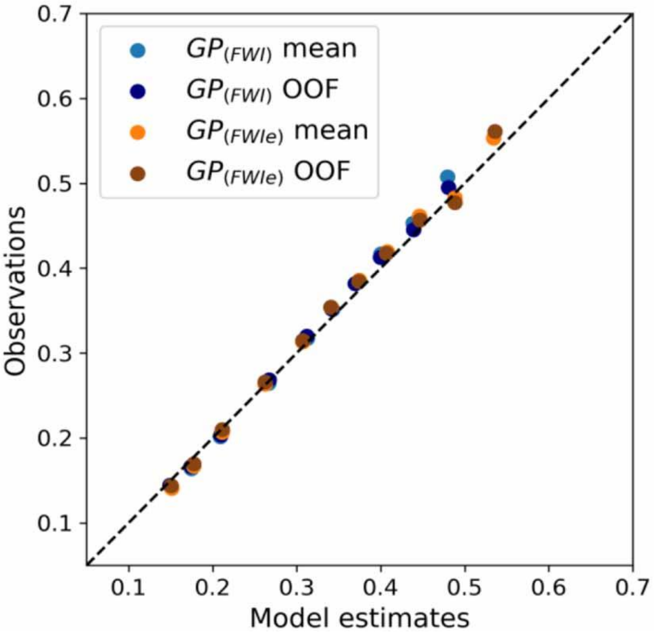

Figure 2.10. Model estimates of P(2000|150) versus observed fractions of exceedance.

Table 2.2. Number of occurrences for groups of released energy (E) and FWI. For table cells with two rows, the top row corresponds to FWI and the bottom row to FWIe. Values in square brackets show the percentage of occurrences with respect to the total of each group of released energy.

E (GJ)	0–10 (%)	10–30 (%)	30–50 (%)	50–70 (%)	> 70 (%)	Total
148–2000	2577 (21.0) 2633 (21.4)	4877 (39.7) 5155 (41.9)	4142 (33.7) 3613 (29.4)	664 (5.4) 792 (6.4)	40 (0.3) 107 (0.9)	12300 (100)
2000–10000	349 (9.9) 341 (9.7)	1284 (36.6) 1355 (38.6)	1568 (44.7) 1406 (40.1)	273 (7.8) 345 (9.8)	35 (1.0) 62 (1.8)	3509 (100)
>10000	49 (2.8) 50 (2.8)	429 (24.3) 456 (25.9)	989 (56.1) 862 (48.9)	262 (14.9) 325 (18.4)	35 (2.0) 71 (4.0)	1764 (100)
Total	2975 (16.2) 3024 (17.2)	6590 (37.5) 6966 (39.6)	6699 (38.1) 5881 (33.5)	1199 (6.8) 1462 (8.3)	110 (0.6) 240 (1.4)	17573

To better discuss the effect of the FWIe, **Table 2.2** shows the number of events for groups of released energy and FWI/FWIe (top and bottom row on each cell, respectively). Comparing the FWI with the FWIe rows, we can see that for the FWIe there is an overall decrease in the number of events for the FWIe in the range 30–50 and an increase for other groups of the FWIe. However, if we look for the individual groups of fire-released energy, we can see that for values below 2000 GJ, 60.7% (63.3%) of the events occur with an FWI (FWIe) of less than 30. Conversely, for energy values above 10 000 GJ, 16.9% (22.4%) of the events occur with an FWI (FWIe) greater than 50. This difference is even more noticeable for FWI and FWIe greater than 70 where the fraction of events with released energy greater than 10 000 GJ doubles from

2% to 4%. This is a good indication that the FWIe can discriminate better the conditions favouring large fires, which especially in the case of extreme fire events, are often enhanced by atmospheric instability.

2.3.4 Case Studies

2.3.4.1 Monchique Fire - August 2018

The fire of Monchique 2018 took place during 3–10 of August in the southwest of the Iberian Peninsula, leading to a burned area of about 27 000 hectares (DaCamara et al. 2019). The left panel of **Figure 2.11** shows the evolution of the FWI, FWIe and CHI, for the month of August, considering for each day the maximum value over the two ERA5 grid cells where the fire was severe. The coloured bars in the same panel correspond to the natural logarithm of the total energy released by the fire on each day, with colours corresponding to the legend in **Figure 2.11** (right panel) where a high-resolution reference map of the burned area is shown (Rego et al 2019). It is interesting to note that on day 5 when the fire reached extreme values of released energy and was burning an extensive region, the FWI was 51.9. However, the CHI was 11.8, indicating a high level of instability that can translate into extreme fire behaviour. The resulting FWIe of 61.9 is significantly higher than the corresponding FWI. This is a good example of a case where the FWIe provides more insight into the meteorological conditions affecting the behaviour of the fire. After four consecutive days of extreme fire activity, on 9 August the FWIe, FWI and CHI start to decline to milder levels and as can be observed in **Figure 2.11** (right panel), the burned area was already very small on day 9. Note that on days 9 and 10 the natural logarithm of released energy is below 7.6, corresponding to less than 2000 GJ.

2.3.4.2 Guadalajara Fire - July 2005

The Guadalajara fire that took place during 16–19 July 2005 led to a burned area of more than 8000 ha and with a high cost in human lives, being responsible for the death of 11 forest agents (Cardil and Molina 2015). The analysis of the FWI, FWIe and CHI together with the natural logarithm of released energy (**Figure 2.12**) shows that the fire started on 16 July, a day with an extreme FWI value of 74.0. However, we argue that the fire risk for that day was not entirely encapsulated by the FWI metric alone, as the associated CHI value reached 12.8, translating to an extreme FWIe of 92.6. The fire was only extinguished 3 days later when the FWI/FWIe were both close to a milder value of 40. Once again, this is a good example of how the use of the CHI provides additional relevant information that is well incorporated in the FWIe.

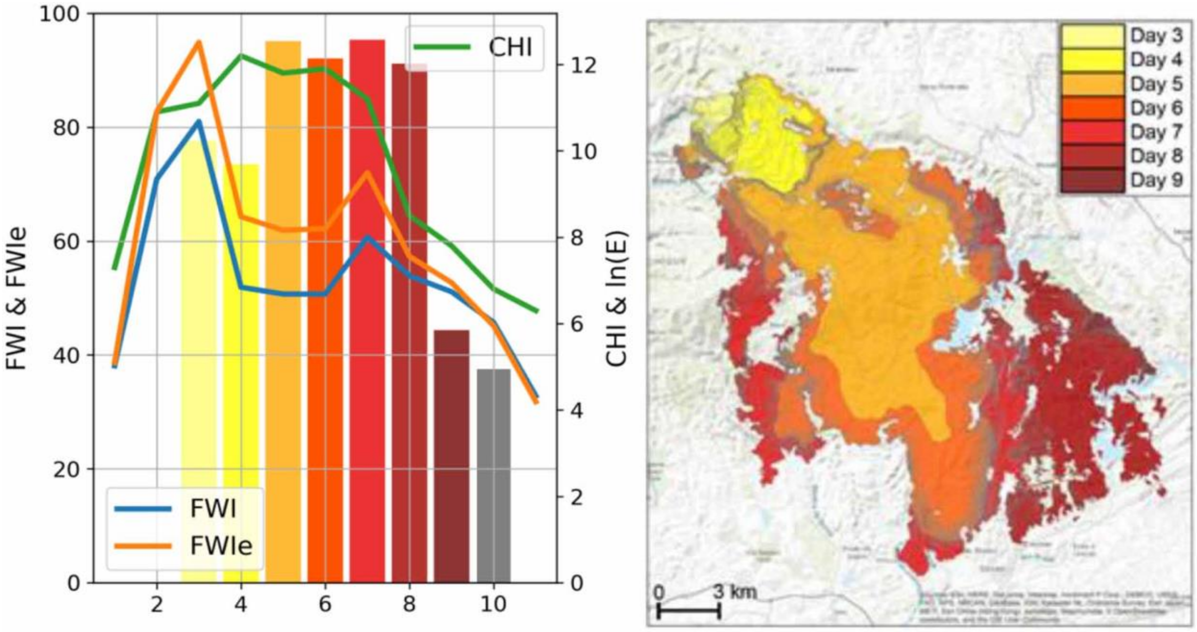

Figure 2.11. Left panel: blue, orange and green lines show the daily evolution between 1 and 11 August 2018 of the FWI, FWIe and CHI, respectively, for the Monchique fire. Coloured bars indicate the natural logarithm of the energy released by the fire for each day, matching the colours in the right panel. Right panel: high-resolution map of the burned area and fire progression adapted from Rego et al. (2019). High-resolution map reproduced with permission from the authors.

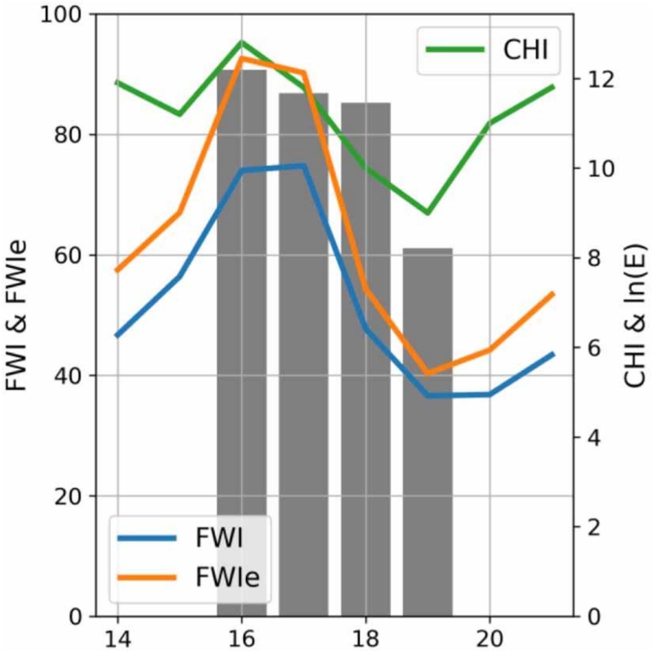

Figure 2.12. Similar to Figure 2.11 (left panel), but for the case study of Guadalajara in July 2005.

2.3.5 Conclusions

Understanding and assessing the meteorological fire danger is of paramount importance to fire management. To this end, the FWI is widely used, being the basis for several operational fire danger rating systems. The FWI, however, does not account for the atmospheric instability, assessed by the CHI, which is shown to play a role in the energy released by fires. The use of the CHI alone is not straightforward, since atmospheric instability conditions can be observed throughout the year, even when the fire danger, as measured by the FWI, is low. Therefore, to address these problems, we demonstrated that the FWI can be improved by incorporating relevant information related to vertical instability through the CHI. It is worth noting that we are not suggesting that one disregard the historical know-how associated with the FWI metric, but basically an upgraded version be adopted, as the proposed FWIe can be easily incorporated into existing FWI-based systems.

The analysis of two case studies shows the practical application of the FWIe aiming towards an improved reliability of fire danger estimates that can be particularly important for days with a mild FWI but a very high CHI, where the fire danger can be underestimated. The opposite situation can also be true, i.e. days that present a very high FWI value can be in fact associated to a more moderate fire risk due to the presence of a very stable atmosphere (CHI values close to zero), leading to lower values of the FWIe, which in some cases can be significantly smaller than the original FWI.

Climate change in recent decades has warmed continents faster than the ocean and such asymmetric trends are bound to continue in the coming decades (IPCC 2014). In semi-arid regions already prone to wildfires, such as the Mediterranean, the rise of temperature must be considered together with the increasing dryness, both concurring to increasing values of sensible heat fluxes at the surface. In fact, some of the most recent notorious events, with a significant number of human casualties, have been amplified by vertical atmospheric instability, such as the Portugal event in June 2017 (Viegas 2018, Turco et al. 2019), California 2018 (Brown et al. 2020), Greece 2018 (Lagouvardos et al. 2019) and Australia 2019 (Bureau of Meteorology 2019). In this context, we argue that our enhanced FWI scale is particularly suitable to account for the likely increase in dry vertical instability of such continental areas.

Code to compute the FWIe is available at https://github.com/mnpinto/FWIe.

2.3.6 Acknowledgements

This work was in part supported by national funds through Fundação para a Ciência e a Tecnologia, Portugal (FCT) under project FireCast (PCIF/GRF/0204/2017) and by a contract with The Navigator Company. Research by Miguel M. Pinto was supported by FCT through a PhD grant PD/BD/142779/2018.

2.3.7 Author Contributions

Miguel M. Pinto (MMP) wrote the paper, developed the algorithms and validated the results. MMP and Alexandra Hurduc (AH) organized the data. Ricardo M. Trigo (RMT), Isabel F. Trigo (IFT) and Carlos C. DaCamara (CCD) contributed with constructive criticism and suggestions. RMT, IFT, CCD and AH revised and edited the manuscript.

2.4 An Hourly Fire Weather Index

2.4.1 Introduction

The Fire Weather Index (FWI) is traditionally defined daily using the weather conditions at solar noon or at the closest synoptic hour (12 UTC over Portugal). The daily FWI value is then used as a representation of the daily fire weather danger or as input to fire danger classification models (e.g.: Pinto et al. 2018a). However, the daily definition of FWI can underestimate the real fire danger due to the variability of the weather conditions throughout the day. For instance, if the wind increases during the afternoon the FWI calculated at noon will meaningfully underestimate the severity of the fire danger conditions as the wind plays a key role in the value of the FWI (Cheney and Sullivan 2008). Also, local weather conditions may result in different hours for the maximum fire weather danger that are not captured if the FWI is defined at a single hour for an extended region. Another important aspect is the nighttime conditions that often provide an opportunity to slowdown or extinguish fires. In a recent study, Balch et al. (2022) showed that the warming conditions during nighttime translated into an increase of nighttime fires intensity by 7.2% globally over the period of 2003 to 2020, further reinforcing the need for a fire weather index that captures the variations along the day.

To address this limitation of the daily FWI, a methodology is proposed to generalize the index to an hourly basis while ensuring that the value at the reference hour is identical to the traditionally defined daily FWI. This aspect is important to facilitate comparison to existing studies, as well as to allow users of the traditional index to easily adapt to the interpretation of the hourly index. To achieve this, a linear interpolation of the memory components of the FWI (the moisture codes) of the previous two days is used, instead of using the value of the previous day as it is the case for the daily FWI. As for the weather inputs, the values of the respective hour are always used to reflect the severity of the weather conditions at the respective hour. The advantage of using a linear interpolation is that the input values for the memory components will be smooth over the time dimension. If instead, only the values of the previous day were used, there would be a discontinuity in the FWI components when changing to the next day.

The proposed approach is tested using hourly data from ERA5-Land reanalysis for a region centred in continental Portugal, spanning the full reanalysis period of 1950 to 2020. A comparison between the hourly FWI and the satellite-derived Fire Radiative Power (FRP) is then performed to assess the correlation of the two quantities for 175 selected fire events during the period 2012 to 2019.

The main goal of this work is to define the hourly FWI and to show how it can be useful to local authorities and civil protection as an enhanced tool for planning as well as for future research and models of fire danger and fire progression that may benefit from the use of hourly information aggregated as a single index.

2.4.2 Data and Methods

The region defined for this study covers continental Portugal and parts of western Spain, spanning from -10 to -6 degrees of longitude and from 36 to 44 degrees of latitude (see **Figure 2.15**). The weather variables to compute the FWI were obtained from ERA5-Land reanalysis, available at Copernicus Climate Data Store (https://cds.climate.copernicus.eu), for the period of 1950 to 2020 in a grid with a spatial resolution of 0.1° × 0.1°. These variables are the 2-meter temperature, 2-meter dew point temperature, 10-meter u and v components of the wind, and the total precipitation.

To compute the hourly FWI, the input data variables are the same as for the traditional FWI. These variables correspond to the 2-meter temperature and relative humidity, the 10-meter wind speed and the 24h total precipitation. The relative humidity is computed using the temperature and dew-point temperature following the Magnus expression (Lawrence 2005). The 24h total precipitation is always the cumulative value of the previous 24h.

The method proposed to compute the hourly FWI consists of using the usual FWI algorithm but changing the "memory" inputs (i.e., the DC, DMC and FFMC from the previous day in the daily FWI). Considering the example of **Figure 2.13** for the computation of the FWI on 03-08-2020, in the traditional FWI the inputs DC_{in}, DMC_{in} and $FFMC_{in}$ are simply equal to the values of the previous day: $DC_{in} = DC_0$, $DMC_{in} = DMC_0$ and $FFMC_{in} = FFMC_0$. The FWI indices are then calculated with weather conditions at 12h. For the case of the hourly FWI the inputs DC_{in}, DMC_{in} and $FFMC_{in}$, are instead given by:

$$DC_{in} = \alpha(t)\, DC_0 + \big(1 - \alpha(t)\big)\, DC_1 \tag{2.9}$$

$$DMC_{in} = \alpha(t)\, DMC_0 + \big(1 - \alpha(t)\big)\, DMC_1 \tag{2.10}$$

$$FFMC_{in} = \alpha(t)\, FFMC_0 + \big(1 - \alpha(t)\big)\, FFMC_1 \tag{2.11}$$

where DC_0, DMC_0 and $FFMC_0$, are the values at the most recent reference hour and DC_1, DMC_1 and $FFMC_1$ the values for one day before as represented in the example of **Figure 2.13**. The function $\alpha(t)$, using the 12h as the reference hour, is given by:

$$\alpha(t) = \begin{cases} \frac{t-12}{24}, t > 12 \\ \frac{t+12}{24}, t \leq 12 \end{cases} \tag{2.12}$$

where t is the hour from 0 to 23.

From the expression above for α, it can be observed that for $t = 12$, $\alpha = 1$ and therefore the inputs DC_{in}, DMC_{in} and $FFMC_{in}$ correspond to the values of the previous day at 12h, as in the traditional FWI, as mentioned before.

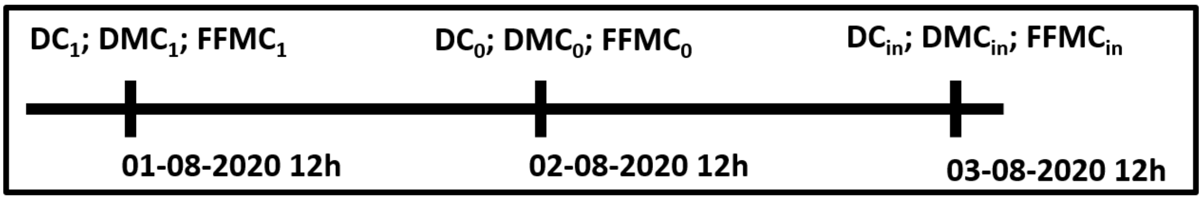

Figure 2.13. Example timeline for the definition of the input DC, DMC and FFMC for the computation of the hourly FWI.

In order to assess the relevance of the hourly FWI the correlation with the Fire Radiative Power (FRP), a proxy of fire intensity, was computed for the period of 2012 to 2019 over the study region. FRP data is produced and disseminated by the Satellite Application Facility for Land Surface Analysis (LSA SAF) (Trigo et al. 2011, Wooster et al. 2015). To select the spatial and temporal location of significant fire events to consider, burned areas derived from BA-Net (algorithm described in **section 3.2** of this thesis) were used for the same period.

Of all the fire events in the BA-Net dataset, the following selection criteria were applied:

1. The burned area must be larger than 500 ha.
2. The duration of the event, according to the burned area dataset, must be of at least 2 days.
3. FRP data must be available for at least 24 unique hours, contiguous or not.

This selection resulted in a total of 175 events. The rationale for this selection is that to better understand the relation between the hourly FWI and the FRP the fires of interest are in general large fires with enough data points to allow for computation of correlations.

To compute the Pearson correlation coefficient, and the time series shown in **section 2.4.3.2**, the median of FRP was computed for each 15-min time-step over the fire region given by the burned area dataset with a padding of 0.1° at every side of the bounding box for each event. The padding is used since the FRP data usually extends beyond the burned area due to the low spatial resolution of the sensor (about 4 km in the study region) and contamination of neighbouring pixels that may occur due to the sensor's point spread function. The 15-min FRP time-series was then converted to an hourly periodicity by averaging the values closest to each hour. For the hourly FWI, the spatial average over the event area was used. The correlation is finally computed using all the time-steps for which FRP data is available. Notice that due to the selection of events described above, the number of data points used to compute the correlation is at least 24.

For the computation of seasonal statistics presented in **section 2.4.3.1**, the year 1950 of the FWI dataset was not considered as it corresponds to the initialization year. The analysis corresponds therefore to the period 1951 to 2020.

2.4.3 Results

2.4.3.1 Climatology of the hourly FWI

To better understand the hourly variability of the FWI over the study region, the average daily cycle was computed for the period 1951 to 2020 for each season. Obtained results (**Figure 2.14**) show that, as expected, there is a seasonally variable daily cycle of FWI that is stronger in the summer months (June, July, and August) reaching a mean FWI of 29 at 16h (**Figure 2.14**, top right panel). In contrast, the winter core months (December, January, and February) show a very low mean FWI value along the day with an absolute extreme for the study period of just over 20 (**Figure 2.14**, bottom right panel). Notice these values correspond to the spatial averages of all land pixels considered within the study region.

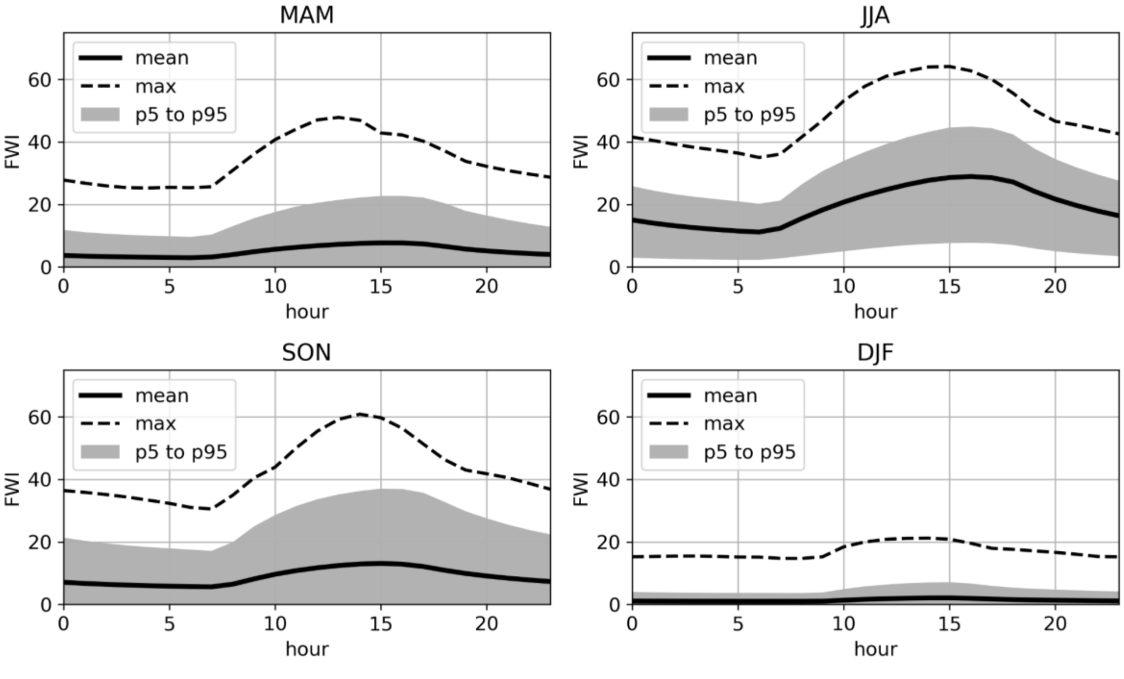

Figure 2.14. Daily cycles of FWI for each season for the period 1951 to 2020. The black solid line indicates the mean, the dashed line the absolute maximum and the grey region spans the percentiles 5 to 95.

To better understand the spatial distribution of the daily cycle of FWI, the results in **Figure 2.15** show the average hour of the daily maximum FWI over the study area for each season. The results for the summer months (**Figure 2.15**, second panel) are particularly interesting as the North-South contrast is stronger being the peak of the daily cycle at 13h in the northernmost parts of the region and increasing to 16h in parts of the interior South. It is interesting to note that in a small region in the southernmost part of Portugal the maximum occurs on average between 17h and 18h. These values contrast to the winter season where for most of the territory the average FWI daily maximum occurs at 13h to 14h. These results show that it is not possible to choose a single hour that captures on average the maximum daily FWI as this hour changes spatially as well as seasonally. It is also worth mentioning that the use of 12h UTC to compute the FWI for the region of Portugal leads to a general underestimation of the maximum daily FWI, particularly for the summer months.

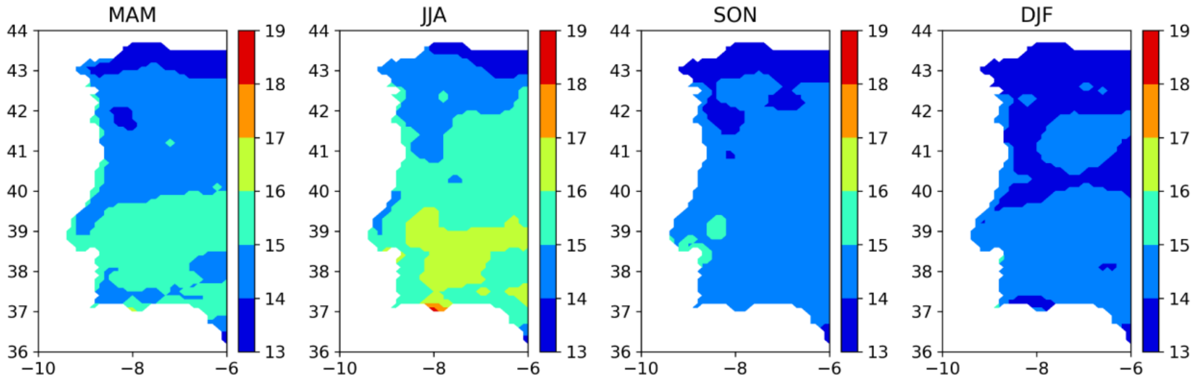

Figure 2.15. Average time of hourly FWI maxima for the period 1951 to 2020. Panels from left to right correspond to spring (March, April, May), summer (June, July, August), autumn (September, October, November) and winter (December, January, February).

Looking now for the spatial variability of FWI, **Figure 2.16** shows the average of the daily maximum FWI for each season. It is possible to observe a strong gradient from north to south, particularly in the summer months (**Figure 2.16**, JJA) where the FWI reaches on average values around 40 in the centre/south and values below 10 in the north/northwest. In the winter months (**Figure 2.16**, DJF), as mentioned before, the FWI is generally very low, being on average below 2 north of 40°N and up to 6 south of 38°N. It is worth noticing that since the average of the daily maximum FWI is computed the values are not affected by the spatial differences in the hour of the maximum (shown in **Figure 2.15**) as they would be in the traditional FWI that would correspond to computing the average on a selected hour.

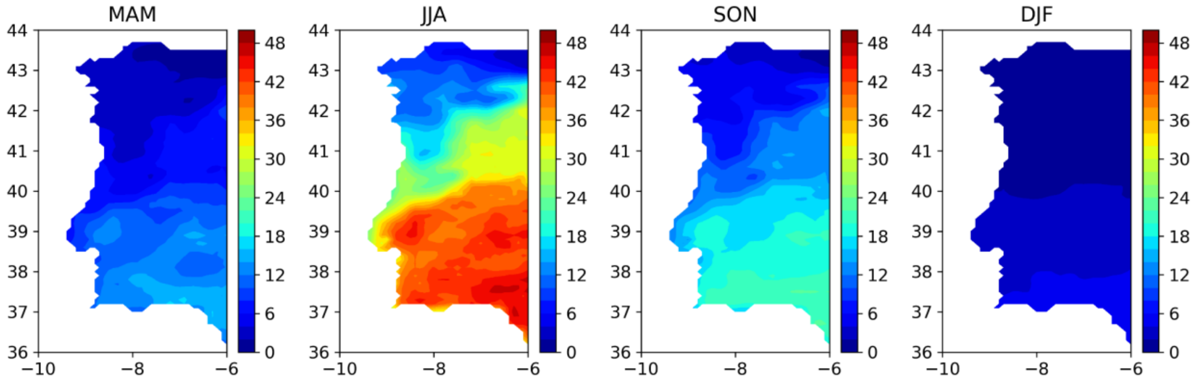

Figure 2.16. As in Figure 2.15 but for the average of the daily maximum FWI.

Another interesting spatial field to observe is relative to the absolute maximum of (hourly) FWI for each season (**Figure 2.17**). Once again, as expected, the summer months (JJA) present the highest values record in most of the region with values of FWI surpassing 100 in southern Portugal and locally reaching nearly 120.

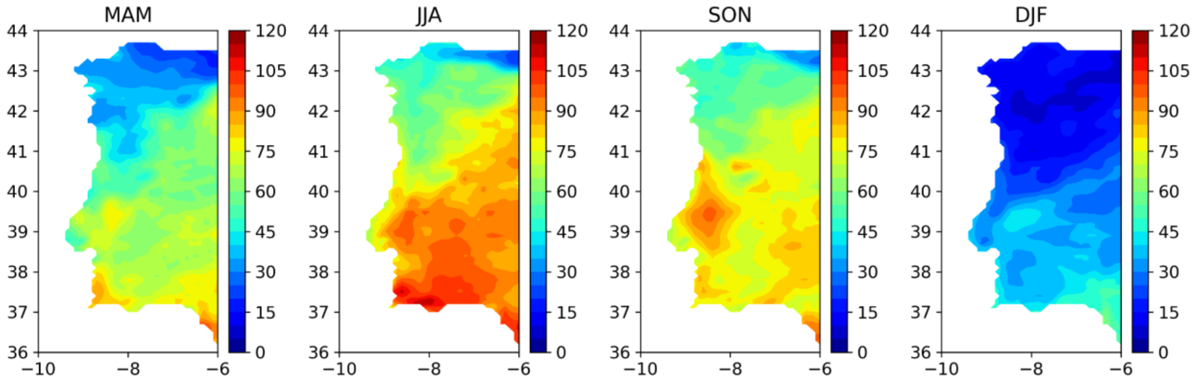

Figure 2.17. As in Figure 2.15 but for the absolute maximum of hourly FWI.

So far, the analysis shown is focused on the period from 1951 to 2020. Since this is a sufficiently long period it has been already affected by climate change in the last few decades (IPCC, 2021). Therefore, it is also worth assessing how the average FWI (shown in **Figure 2.16**) changed over time. **Figure 2.18** shows the difference in the average of maximum daily FWI from the period 1951–1980 to 1991–2020 and as it would be expected there is a general increase of FWI of as much as approximately 6 in the summer months in parts of the interior (JJA). For the spring months, the increase is smaller followed by the winter months and the autumn, where in most of the region differences are close to zero, being as low as -1.5 in parts of the South. This is the result of an increase in precipitation that translates into a decrease in the average value for the drought and fuel moisture codes (see **Figure A.1 – Figure A.5** in the appendix) which in turn leads to a slightly lower FWI.

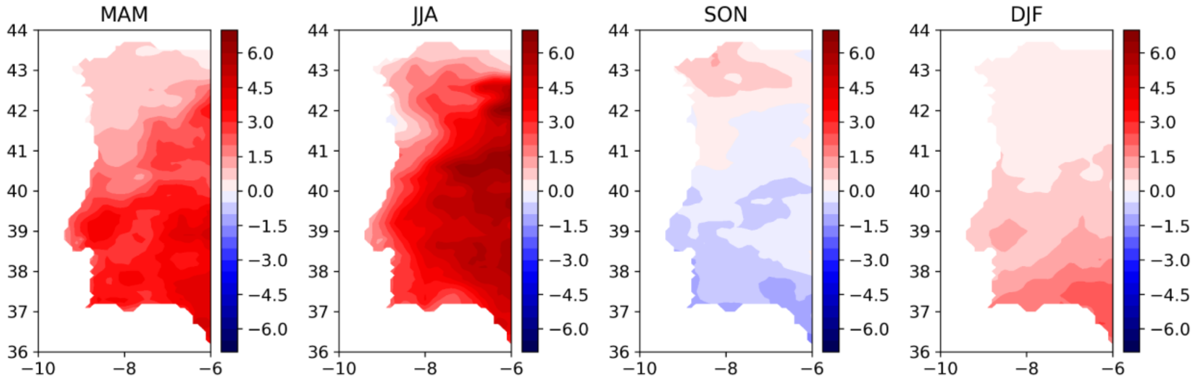

Figure 2.18. As in Figure 2.15 but for the change in FWI from 1951–1980 to 1991–2020.

2.4.3.2 Correlation with Fire Radiative Power

To better understand the practical use case for the hourly FWI, a comparison with the FRP is presented for the 175 events selected according to the methods described before. The distribution of correlations for the 175 events has an average correlation of 0.46 with the vast majority of these events (96.6%) showing a positive correlation (**Figure 2.19**).

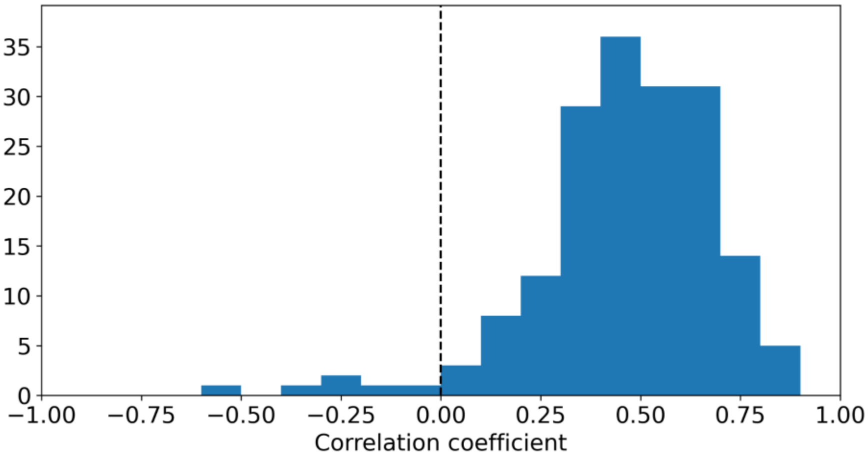

Figure 2.19. Distribution of the correlation coefficient between the hourly FWI and the corresponding hourly FRP values obtained for the 175 selected events during the period of 2012 to 2019.

For a visual interpretation of these correlations in a practical context, two well-known case studies were selected. The first corresponds to a large fire in central Portugal that occurred in late July 2017, and the second to the large Monchique fire of early August 2018 in southwest Portugal. For the first case (**Figure 2.20**), a correlation of 0.53 was obtained. As it can be seen in the figure, this fire has almost continuous FRP data observations during a 5-day period, making it an excellent example. A very clear daily cycle of FRP is observed matching generally well to the periodicity of the hourly FWI. Regarding the Monchique 2018 fire (**Figure 2.21**), a correlation of 0.61 was obtained. This fire spanned a period of about 6 days and the daily cycle of FRP is marked but not always clear. It should be noted that, for some events, using higher-resolution weather data may allow for a better interpretation of the FRP variations. In particular, for the Monchique fire, previous work has shown that the hourly FWI based on 4 km resolution forecasts maintained high values for the period of 6–8 August even during the nighttime in parts of the fire region (Pinto et al. 2018c). A comparison of the effects of the spatial resolution of the weather data in the correlations of hourly FWI and FRP is however a topic for future work.

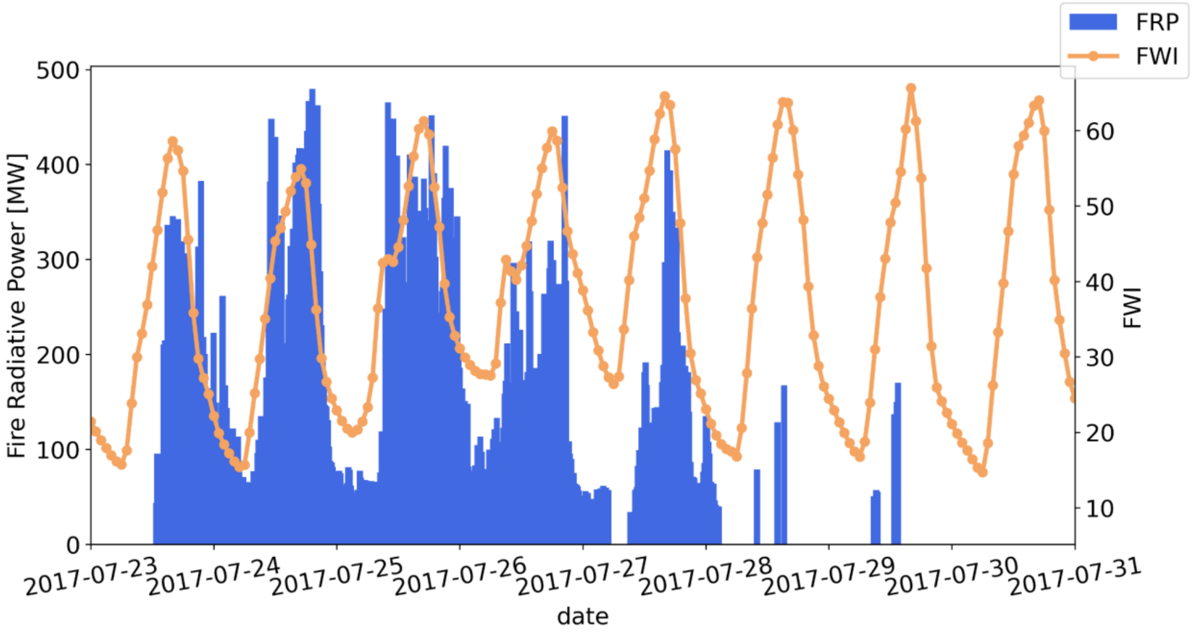

Figure 2.20. Hourly FWI and 15-min FRP for a fire in July 2017 in central Portugal.

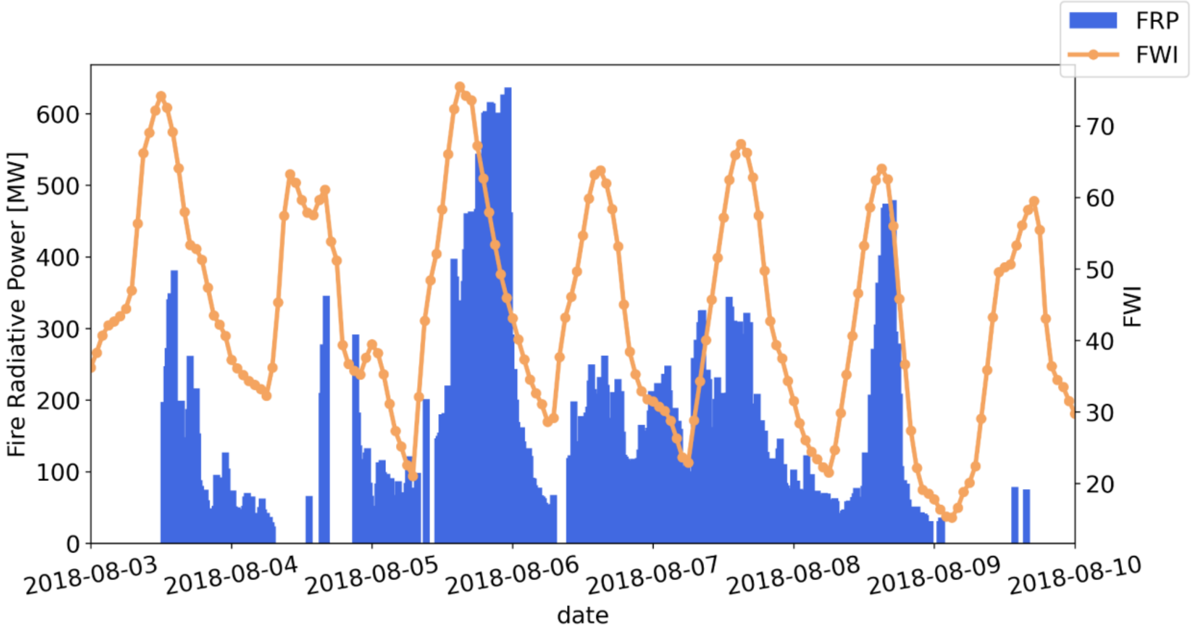

Figure 2.21. As in Figure 2.20 but for the fire of Monchique in early August 2018.

2.4.4 Conclusions

The FWI is the most widely used index to evaluate fire danger or to calibrate fire danger rating systems on a global scale. Extending this index to an hourly time scale provides additional information in the same metric that users are familiar with. This can have a positive impact in several areas such as suppression efforts for active fires, resource allocation for quick response to new ignitions, defining windows of opportunity for prescribed fire management, general research about fire behaviour and fire risk classification, and a better understanding of the local variability in the daily cycle of fire weather danger (DaCamara et al. 2018). Furthermore, the hourly FWI can potentially be combined with the extended FWI (**section 2.3** of this thesis), since the Continuous Haines Index has no "memory" components and can straightforwardly be calculated at any time of the day. The verification of these two FWI extensions combined is however a subject for future research.

3 Mapping Burned Areas using Satellite Data

3.1 Introduction

Mapping and dating burned areas using satellite data is an important topic of research for a wide range of applications from forest management (Bowman et al. 2011), assessment of wildfire impact on the ecosystems and human populations (Moritz et al. 2014), calibration of fire danger (DaCamara et al. 2014, Pinto et al. 2018a), and fire propagation models (Freire and DaCamara 2019). High-resolution fire mapping is also critical to better estimate CO_2 emissions that have been increasingly incorporated in earth system climate models (Liu et al. 2014) as well as to obtain derived datasets of individual fire metrics such as size, duration, velocity, and direction of expansion (Andela et al. 2019).

From the point of view of satellite data, the burned areas can be identified as an abrupt change in the spectral signature of a region when comparing images at different dates of acquisition. These changes are particularly prominent in the Near-Infrared (NIR) since green vegetation is very reflective in this frequency, contrasting with a burned region that will instead absorb very well the NIR radiation. As result, when a fire occurs, a spatiotemporal pattern will be visible in a sequence of satellite images that use this band of the electromagnetic spectrum. These patterns can be further enhanced with additional spectral bands such as Red that is often used in combination with NIR as part of vegetation indices such as the Normalized Differences Vegetation Index (NDVI) and the Middle-Infrared (MIR) used to detect active fires (Escuin et al. 2008, Calle and Casanova 2012). The task for the model or algorithm responsible to map the burned areas is then to identify these patterns to determine with the best possible accuracy the burned pixels and the date of burning. This task, however, can be very challenging as clouds and thick smoke can often obfuscate the patterns. Furthermore, the polar orbit satellites often used for this task, due to their lower orbit and higher spatial resolution, view each region from different angles leading to a lower effective spatial resolution (Campagnolo et al. 2016). The result is a problem of identifying spatiotemporal patterns in noisy data with degrees of noise varying for different regions and climates, particularly due to the spatial changes in cloud cover patterns (Frey et al. 2020). To make the problem even more challenging, in some regions the fire can burn only on the surface under the tree cover, making the spectral signature of the fire weaker (Johnston et al. 2018).

Over the years, several methods have been proposed to map burned areas using satellite images (Meng and Zhao 2017, Chuvieco et al. 2019). These methods can be grouped into two categories based on the spatial and temporal resolution of the sensors used to derive the product as there is a trade-off between temporal and spatial resolution. Coarse burned area products have resolutions greater than 250 meters and often daily temporal resolution, as it is the case for MODIS and VIIRS. Medium resolution products with resolutions between 10 and 80 meters have a temporal resolution of at least 5 days as it is the case for Sentinel-2 satellites. High-resolution satellites can provide data with up to less than 1 m resolution, but their data is not publicly available and therefore not widely used for these applications. Regarding coarse products, the four main global products for an extended period are the FireCCI51 (Chuvieco et al. 2018) available from 2000 to 2017 with a resolution of 250 m, the MCD64A1 Collection 6 (Giglio et al. 2018a) available from 2000 to the present with a resolution of 500 m, the Global Fire Emission Database (van der Werf et al. 2017) from 1997 to 2016 with a resolution of 0.25° and the FireCCILT10 (Otón and Pettinari 2019) that covers the period of 1982 to 2017 with a resolution of 0.25°. For medium resolution, the higher volume of data makes the problem more challenging from a computational perspective. Some solutions have been proposed to use cloud computing platforms such as the Google Earth Engine (GEE) to overcome this difficulty and generate annual medium resolution burned area maps on a global scale (Long et al. 2019). The validation of these results is however challenging as the best practice for validation of burned area products is to rely on higher resolution reference maps derived or verified by visual inspection. Another notable effort for a large and challenging area is the FireCCISFD11 (Roteta et al. 2019) developed for sub-Saharan Africa for the year 2016.

Despite all the efforts and recent advancements in methods for burned area mapping and dating, the existing methods have some limitations. Most notably, coarse burned area products often focus on spatial accuracy and give less attention to temporal accuracy and consistency. For the medium resolution products, due to the longer revisit time, it is expected that spatial accuracy should be the main focus, but the high volumes of data may limit the scope of methodologies that can be applied efficiently making it challenging to develop fully automated approaches over large areas.

In this chapter, some of the limitations of existing methods are addressed, namely a robust deep learning model is developed and trained to map daily burned areas using VIIRS and tested over several regions around the world. Furthermore, a methodology is developed for quick monitoring of burned areas with medium resolution by leveraging information from pre-mapped burned areas with coarse resolution and GEE as a tool for pre-processing and downloading of pre-fire and post-fire composites together with a Deep Learning model trained to map the burned pixels. In the last section of this chapter, the topic of short-term reconstruction and forecast of fire progression is explored and some promising results are presented.

The structure of this chapter is as follows:

- In **section 3.2** a method is presented to map and date burned areas using sequences of daily satellite images. This is achieved by defining and training a deep learning model designed to capture the spatiotemporal patterns that characterize the burned areas. This work corresponds to the paper "A deep learning approach for mapping and dating burned areas using temporal sequences of satellite images" published in the ISPRS **Journal of Photogrammetry and Remote Sensing**.
- In **section 3.3** a method is proposed to quickly map burned areas using Sentinel-2 10-meter resolution data. This is achieved by leveraging the use of a coarse resolution burned area product, the computation capabilities of Google Earth Engine to pre-process and download Sentinel-2 data, and a deep learning model trained to map the multispectral satellite data into the burned area maps. Results in this section correspond to the paper "A practical method for high-resolution burned area monitoring using Sentinel-2 and VIIRS" published in **Remote Sensing**.
- In **section 3.4** a case study is presented for the analysis of the south-eastern Australian fires of 2019–2020. BA-Net model (described in **section 3.2**) is used to map the burned areas using VIIRS 750 m and 375 m bands and results are compared with a widely used global burned area product and validated using higher-resolution reference maps of fire severity. The analysis and results of this section are new material not published or presented before.
- In **section 3.5** a method is proposed for short-term forecasting of fire progression. This is achieved by using a particle simulation driven by the meteorological conditions as summarized by the hourly enhanced FWI (based on work described in **chapter 2**) and structural variables such as topography, land cover and roads. The results presented in this section correspond to new material not published or presented before.

The main contribution of this chapter is a set of accurate and efficient methods to map burned areas and to better understand fire progression behaviour.

3.2 A deep learning approach for mapping and dating burned areas using temporal sequences of satellite images

This section presents the results published in the following article: Pinto, M. M., Libonati, R., Trigo, R. M., Trigo, I. F., & DaCamara, C. C. (2020). A deep learning approach for mapping and dating burned areas using temporal sequences of satellite images. ISPRS Journal of Photogrammetry and Remote Sensing, 160, 260-274.

Over the past decades, methods for burned areas mapping and dating from remote sensing imagery have been the object of extensive research. The limitations of current methods, together with the heavy pre-processing of input data they require, make them difficult to improve or apply to different satellite sensors. Here, we explore a deep learning approach based on daily sequences of multi-spectral images, as a promising and flexible technique that can be applied to observations with various spatial and spectral resolutions. We test the proposed model for five regions around the globe using input data from VIIRS 750 m bands resampled to a 0.01° spatial resolution grid. The derived burned areas are validated against higher resolution reference maps and compared with the MCD64A1 Collection 6 and FireCCI51 global burned area datasets. We show that the proposed methodology achieves competitive results in the task of burned areas mapping, despite using lower spatial resolution observations than the two global datasets. Furthermore, we improve the task of burned areas dating for the considered regions of study when compared with state-of-the-art products. We also show that our model can be used to map burned areas for low burned fraction levels and that it can operate in near-real-time, converging to the final solution in only a few days. The obtained results are a strong indication of the advantage of deep learning approaches for the problem of mapping and dating of burned areas and provide several routes for future research.

3.2.1 Introduction

Forest fires are a natural phenomenon highly dependent on human activities, having significant impacts on social, economic and ecological levels (Patz et al. 2000, Bowman and Johnston 2005, Driscoll et al. 2010). Mapping the fire events accurately is a problem of great importance for fire management (Bowman et al. 2011), fire danger rating and fire propagation (Freire and DaCamara 2019, Maffei and Menenti 2019), assessment of vegetation fire emissions and air quality (Langmann et al. 2009), land cover dynamics studies (Jin and Roy 2005), derivation of fire patch functional traits (Laurent et al. 2018, Andela et al. 2019) and to better understand how fire patterns are evolving in a scenario of climate change and population change (Flannigan et al. 2009, Moritz et al. 2012, Andela et al. 2017).

At present, there are four main global up-to-date products for an extended period, namely: (1) the FireCCI51 (Chuvieco et al. 2018), at 250 m resolution, available for 2000–2017; (2) the MCD64A1 Collection 6 (MCD64A1C6, Giglio et al. 2018a) at 500 m resolution, covering the period of 2000-present; (3) the Global Fire Emission Database (van der Werf et al. 2017), covering the period of 1997–2016 with 0.25° resolution; and (4) the FireCCILT10 (Otón and Pettinari 2019), recently released on its beta version, covering the period of 1982–2017 also with a 0.25° resolution.

The main underlying limitation of coarse resolution products (≥250 m) is the underestimation of burned area in regions with small and highly fragmented fires (Padilla et al. 2015, Chuvieco et al. 2019), trading off with a higher temporal resolution that allows for daily date of burning assignment. Products derived from medium resolution sensors (10–80 m) have a lower temporal resolution of about 5–18 days leading to higher uncertainty in the date of burning, a problem further enhanced if clouds are present (Roteta et al. 2019). Another notable limitation of the medium and high-resolution products is the computational cost required to process those very large volumes of data, making it challenging to create and maintain an operational product on a global scale, a limitation that may be reduced with the use of distributed cloud computing systems such as Google Earth Engine (Long et al. 2019).

Several techniques to map and date burned areas using remote sensing imagery have been proposed over the years. In general terms, the procedure underlying the MCD64A1C6 and FireCCI51 algorithms consists of creating temporal composites to capture the persistent changes, filtering low-quality pixels, and then combining this information with active fires identified using the Moderate Resolution Imaging Spectroradiometer sensor (MODIS). For FireCCI51, initial burned pixels candidates are identified, and then a growing algorithm is applied to identify pixels that are likely to have burned near the initial candidates (Chuvieco et al. 2018). For MCD64A1C6 a series of steps are then applied as described in detail by Giglio et al. (2018a), also including a region growing procedure, a common practice in traditional approaches (Bastarrika et al. 2011, Stroppiana et al. 2012, Alonso-Canas and Chuvieco 2015). Other algorithms have been proposed and tested on a regional scale. For example, Pereira et al. (2017) used One-Class Support Vector Machines to reduce the omission errors caused by the omission of active fires and avoid the need for a region growing algorithm, making the procedure simpler. However, the algorithm still relies on temporal composites to address the problem of pixel contamination by clouds or cloud shadows. The use of temporal composites is a limitation as some of the information discarded could be useful. Moreover, failing to discard cloud contaminated pixels can result in unexpected behaviour as the algorithms are designed and optimized to work with clean data.

As different sensors have different characteristics, traditional burned area mapping algorithms are often designed and refined for a particular sensor, making the adaptation to another instrument often a challenging process. Furthermore, despite the significant advances in the methodologies over the years, there are still some aspects that either require improvement or are beyond the capability of the traditional approaches. In particular, the users of burned area products would benefit from longer and consistent time-series of burned areas, a better estimation of model uncertainty (Mouillot et al. 2014) and estimation of burned area fraction and combustion completeness (Chuvieco et al. 2019). It arises, therefore, the need for a methodology that is both scalable and capable of addressing these limitations. It is within this context that we would like to stress that deep learning (LeCun et al. 2015) techniques have been gaining increasing attention over the last few years. Computer vision problems, like object detection and recognition, flourished with the use of deep Convolutional Neural Networks (Krizhevsky et al. 2012) as the main building block that enables to capture the spatial correlations in image data efficiently. On the other hand, for problems with sequence data, Recurrent Neural Networks (RNNs, Rumelhart et al. 1986) are commonly used. Several types of RNNs have been proposed to better learn longer dependencies in the data. Long Short-Term Memory (LSTM, Hochreiter and Schmidhuber 1997) have been particularly successful and are nowadays applied in numerous tasks such as speech recognition (Graves et al. 2013) and sequence to sequence models (Sutskever et al. 2014).

Recent applications to remote sensing have started to emerge (Zhang et al. 2016, Zhu et al. 2017, Kemker et al. 2018, Ma et al. 2019) for land-cover classification (Hu et al. 2015, Kussul et al. 2017, Maggiori et al. 2017, Scott et al. 2017, Marcos et al. 2018), segmentation of buildings, roads and small objects (Kampffmeyer et al. 2016, Alshehhi et al. 2017), reconstruction of missing data (Zhang et al. 2018), identification of clouds and cloud shadows (Jeppesen et al. 2019, Wieland et al. 2019) and some making use of spatiotemporal structure in sequences of satellite data (Benedetti et al. 2018, Rußwurm and Körner 2018, Pelletier et al. 2019). The problem of mapping burned areas and identifying the respective date of burning falls into the range of problems that can be addressed by these new deep learning techniques and, in turn, benefit from their inherent advantages (Reichstein et al. 2019). To our knowledge, this is the first work applying these new techniques to the problem of burned areas mapping and dating.

The approach we propose is an end-to-end model based on satellite retrieved sequences of daily images. The model uses convolutional neural networks and LSTMs with an architecture based on U-Net (Ronneberger et al. 2015). We train the model using daily top-of-atmosphere observations from Visible Infrared Imaging Radiometer Suite (VIIRS) 750 m Red, near-infrared (NIR) and middle-infrared (MIR) bands and VIIRS 375 m active fires product as inputs and using MCD64A1C6 as targets. We compare the results with MCD64A1C6 and FireCCI51 and validate them against locally derived medium resolution reference maps, subject to data availability.

Our approach addresses several of the current limitations of traditional methodologies, namely: (1) No clouds/shadows mask, filtering of lower quality images or use of temporal composites is required, making the pipeline more straightforward and avoiding errors that are often observed when applying such procedures; (2) the structure of the model is not dependent on the sensor but only on the existence of input data consisting of daily sequences of images, making it an excellent candidate to be used to produce longer time-series with the resource to Advanced Very High-Resolution Radiometer (AVHRR) aboard NOAA 7–19 satellites, dating back to 1982; and (3) the incorporation of the active fires is accomplished simply by adding a “channel” to the input data without requiring any pre-processing to avoid commission errors, also opening ground for the incorporation of further input data (e.g., land-cover, topography, solar/satellite zenith angles). It is worth noticing that to the best of our knowledge this is one of the first applications of VIIRS observations to map burned areas on a global scale.

3.2.2 Methods

3.2.2.1 Study Regions

Fires have different characteristics in different parts of the globe. In order to construct a diverse dataset, we selected five regions (**Figure 3.1**) covering California, Portugal, part of the Brazilian Cerrado (hereafter referred as Brazil), Mozambique and north Australia (hereafter referred as Australia). Australia, Mozambique and Brazil are the three main choices with very different fire characteristics among them. While Australia is characterized by large fires sizes and a high rate of expansion but a low density of ignitions, Mozambique has a very high density of ignitions but a lower fire size and rate of expansion, and Brazil figures in between the two

(Andela et al. 2019). The main motivations for including the areas of Portugal and California were the occurrence of recent tragic fires events in the past two years of 2017 (Viegas 2018) and 2018 (Gorman et al. 2019) and the author's domain knowledge about fires in Portugal resulting from previous studies (Trigo et al. 2006, DaCamara et al. 2019) and continuous monitoring of the fires during the fire season. This domain knowledge is useful for a more insightful discussion of the case studies shown in **section 3.2.3.4**.

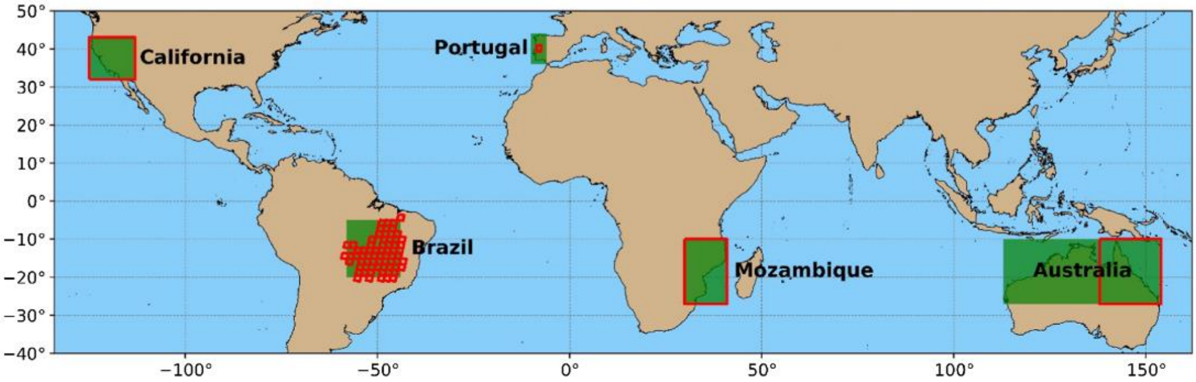

Figure 3.1. Location of the 5 study regions marked by the green rectangles, corresponding to California, Portugal, Brazil, Mozambique and Australia. Red rectangles mark regions used for validation against medium resolution reference maps. (For interpretation of the references to colour in this figure legend, the reader is referred to the web version of this article.)

3.2.2.2 Datasets

Several datasets are used in this study with different usage types, namely: for model input and target; comparisons; and validation. **Table 3.1** summarizes all the datasets used and their respective region, spatial resolution and time coverage used for this work that we now describe in the following two subsections.

3.2.2.2.1 Model Inputs and Targets

Daily images of Red, NIR and MIR reflectances from VIIRS Level 1B product for the period of 2012–2018, covering the five regions (https://ladsweb.modaps.eosdis.nasa.gov) were resampled to a regular grid of 0.01° spatial resolution using bilinear interpolation and selecting the image with lower satellite zenith angle if more than one image was available for a single day. Red and NIR reflectances correspond to bands M5 (centred at 0.672 μm) and M7 (centred at 0.865 μm). MIR reflectance is derived from MIR and longwave-infrared radiances (Kaufman and Remer, 1994, Libonati et al., 2010) corresponding to bands M12 (centred at 3.7 μm) and M15 (centred at 10.76 μm). VIIRS Active Fires data were obtained from https://firms.modaps.eosdis.nasa.gov for the five regions and interpolated to the working grid by summing Fire Radiative Power (FRP) values inside each grid cell for each day. Data is then organized as four-layer images with the three reflectance bands (Red, NIR and MIR) and the gridded Active Fires data.

As targets to train the model, we used MCD64A1C6, a global burned area dataset at 500 m spatial resolution, available at ftp://ba1.geog.umd.edu. This dataset includes the date of burning for each burned pixel and therefore allows to generate daily targets by resampling the original data to our working grid of 0.01° by computing the fraction of burned pixels inside each 0.01° grid cell for each day. The choice of MCD64A1C6 as the target for train supervision instead of FireCCI51 is due to the much smaller bias in the date of burning of MCD64A1C6 and the better spatial accuracy in general, for the regions considered over the 0.01° grid, when compared with dates of active fires and medium resolution reference maps, as discussed in **section 3.2.3**. We note that despite the problem being treated as classification, the targets are the burned area fractions (i.e., the fraction of area burned within each pixel) and not binary burned/non-burned masks. This can be thought as classification with soft labels.

Table 3.1. Description of the datasets used, regions covered, original resolution, used temporal coverage, and usage type.

Dataset	Region	Resolution (m)	Years	Usage
VIIRS Level 1B	All	750	2012–2018	Inputs
VIIRS Active Fires (Schroeder et al. 2014)	All	375	2012–2018	Inputs, Validation
MCD64A1C6 (Giglio et al. 2018a)	All	500	2012–2018	Targets, Comparison
FireCCI51 (Chuvieco et al. 2018)	All	250	2012–2017	Comparison
Landsat-8 53 scenes (Rodrigues et al. 2019)	Brazil	30	2015	Validation
FireCCISFD11 (Roteta et al. 2019)	Mozambique	10	2016	Validation
MTBS (Eidenshink et al. 2007)	California	30 (fire perimeters)	2012–2016	Validation
TERN AusCover (Goodwin and Collett 2014)	Australia	30	2014–2016	Validation
ICNF Burned Areas	Portugal	Variable	2017	Validation

Inputs and targets were cropped into 128x128 tiles with 28 pixels of overlap to reduce inaccuracies that can occur near the boundaries of the tiles due to the convolution operations applied by the model. The dataset covers the months of June to September for California and Portugal, July to October for Brazil and Mozambique and September to December for Australia. The selected months cover the most active period for each region (Giglio et al. 2006). This period was extended further for Portugal in 2017 (May to November) and California in 2018 (June to December), in order to include recent extreme fire events that occurred outside the usual fire season.

3.2.2.2.2 Intercomparisons and Validation Data

To intercompare our results, we use both MCD64A1C6, described above, and the FireCCI51 dataset, obtained from https://www.esa-fire-cci.org, that provides the date of burning for each burned pixel at 250 m resolution. As for MCD64A1C6, the FireCCI51 is resampled to the working grid considering the fraction of burned pixels inside each 0.01° grid cell for each day.

For validation, a common requirement is to use higher resolution references derived from Landsat/Sentinel imagery or other medium/high resolution source, according to the Committee on Earth Observation Satellites Calibration and Validation protocol (CEOS CalVal protocol, Boschetti et al. 2009). Due to the constraints on the availability of these burned area reference maps, several different datasets are used in this study for the validation task. For Brazil we use reference burned areas derived from 53 Landsat-8 scenes for the year of 2015, with a resolution of 30 m, matching our region of study both in time and space (**Figure 3.1**, red patches over Brazil region). These scenes are a subset of those used by Rodrigues et al. (2019), as derived from pairs of images for nearby dates, with burned area mapped for the period between those dates, following the recommendations by the CEOS CalVal protocol. For Mozambique we use the FireCCISFD11 dataset, obtained from https://www.esa-fire-cci.org, which covers Sub-Saharan Africa for the year of 2016 with 10 m resolution, derived from Sentinel-2 imagery. For California we use the MTBS dataset, obtained from https://www.mtbs.gov, which covers the United States of America, matching our study period on years 2012 to 2016 consisting of fire perimeters derived from 30 m resolution Landsat images. For Australia we use TERN AusCover burned areas dataset, obtained from http://www.auscover.org.au, covering north-east Australia (**Figure 3.1**, red rectangle over the east part of Australia region) derived from Landsat imagery with 30 m resolution and matching our study period over 2012 to 2016. We considered, however, just the years 2014 to 2016 for TERN AusCover dataset, since the quality drops for the first years as evaluated visually and in comparison with MCD64A1C6 and FireCCI51. Finally, for Portugal we use a reference map obtained from ICNF (https://www.icnf.pt), corresponding to the provisory version of 5 January 2018, selecting only the fires in Central Portugal (**Figure 3.1**, small red rectangle over Portugal region) that occurred in 2017 with source attributed to Landsat/Sentinel/Copernicus, being the most important fires mapped with resource to the medium resolution data (Landsat/Sentinel).

For the validation of the date of burning, we used VIIRS active fires because of the better detection rates of this product, compared to similar ones (Oliva and Schroeder 2015).

All high-resolution references are interpolated for the working grid resolution of 0.01° by computing the burned area fraction inside each coarse cell.

3.2.2.3 BA-Net Model

The proposed model hereafter referred to as BA-Net (from Burned Areas Neural Network), is based on U-Net architecture but with several modifications in order to adapt for the problem of temporal sequences of images. First, a 3d version of U-Net is constructed based on De Fauw et al. (2018) where it is shown that separating the spatial and temporal convolutions can achieve excellent results with a much smaller and faster model. For example, a single 3d convolution with a kernel size of 7 × 7 × 7 would have 343 parameters, while two convolutions, one with kernel size 1 × 7 × 7, followed by another with kernel size 7 × 1 × 1 only have 56 parameters. Secondly, contrary to the tasks of 3d segmentation for which 3d U-Nets are usually applied (e.g., biomedical image segmentation with 3d spatial data) the satellite data has a temporal dimension with large amounts of noise, most notably clouds. The kernel convolutions are not a natural way to learn from such noisy data, and therefore we include a unidirectional LSTM layer after the first spatial convolution, allowing the model to capture longer-term temporal dependencies in the data and to better filter the noise.

The input data consists of sequences of 64 images of size 128 × 128 and 4 data layers or "channels" (Red, NIR, MIR, Active Fires). Due to memory constraints, we use a batch size of 1, resulting in an input tensor with dimensions [1, 64, 4, 128, 128]. The output is also a sequence but only with one "channel" representing the probability that the pixel has burned.

Figure 3.2 shows the model architecture, with the characteristic encoder/decoder (green/blue modules) of U-Nets with connections between each encoder and decoder module to avoid losing information while allowing to capture higher-level structures in the data. We now describe in detail each module of **Figure 3.2**.

The ST-Conv3(LSTM) module (ST from Space and Time) consists of the layers described in **Table 3.2** (left column). The first 3d convolution is the spatial convolution, followed by Batch Normalization and a rectified linear unit (ReLU). Then, optionally (only on the first module), an LSTM layer is used. The second 3d convolution is the temporal convolution also followed by Batch Normalization and ReLU, and finally, Dropout is applied with a probability of 0.2. On the decoder part of the model (blue modules in **Figure 3.2** and central column of **Table 3.2**), the UpST-Conv3 modules (Up from "Upward" part of the model) have a similar structure but Transposed Convolutions are used instead, to do the upsampling. Note, however, that these modules receive two inputs, one from the module below (**Figure 3.2**) and the other from the module at left. These inputs are concatenated over the channels dimension. The modules at the bottom of **Figure 3.2** (S-Conv3 and UpS-Conv3) only have the spatial convolution part, and the penultimate module named (T-Conv3) only has the temporal convolution part as suggested by the adopted terminology. The final convolution is a 3d convolution with kernel size 1 × 1 × 1, used to reduce the number of channels to 1.

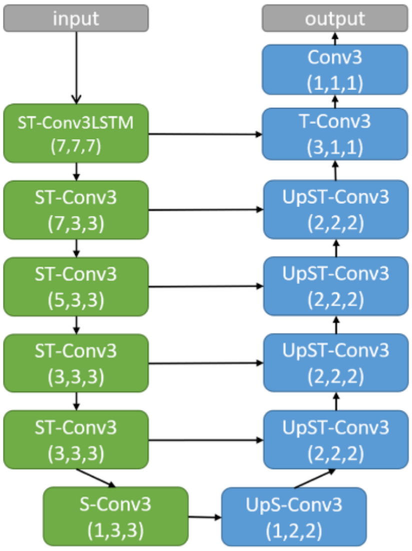

Figure 3.2. Model architecture of BA-Net showing the encoder (green modules) and decoder (blue modules) sections of the model. Black arrows represent the flow of information between individual modules. (For interpretation of the references to color in this figure legend, the reader is referred to the web version of this article.

The exact kernel sizes and strides of the convolution layers vary from module to module and are specified in

Table 3.3, together with the number of input and output channels and shape of the output of each module. On all convolution layers but the last, no bias parameters are used since these layers are followed by a batch normalization that has already a bias parameter. The padding on the convolution layers is set to be equal to the integer division of the respective kernel size by 2, ensuring that the output of the convolution has the same size (half the size) as the input if the stride is equal to one (equal to two). The choice of sequence size of (64, 128, 128), i.e., consisting only on powers of 2, is also to guarantee that these calculations hold.

We now describe the details of how BatchNorm and LSTM are used. Since we are using a batch size of 1, due to memory limitations, using a 3d BatchNorm would be unstable. As we are working with sequences of 64 images, we instead apply a 2d BatchNorm over batch and time dimensions together. We refer to this as BatchTimeNorm in **Table 3.2**. The LSTM layer is applied over the temporal dimension, to the individual time-series extracted from each pixel.

Note that as the LSTM is placed after the spatial convolution, the time-series already capture local spatial correlations of the neighbour pixels.

As shown in **Figure 3.2**, only the first ST-Conv3 module has an LSTM layer. In the ablation study, on **section 3.2.3.5**, we show that including the LSTM layer results in an improvement of the performance when compared with an identical model without the LSTM layer. The resulting model is simple and robust, having only about 3.5 million trainable parameters. For comparison, a ResNet (He et al. 2016), a typical model for image classification, has from 11 to 60 million parameters.

Table 3.2. Description of the layers constituting the ST-Conv3(LSTM) and UpST-Conv3 modules.

ST-Conv3(LSTM)	**UpST-Conv3**	**Description**
Conv3d	ConvTranspose3d	3d convolution and transposed convolution (Dumoulin and Visin 2016, Goodfellow et al. 2016)
BatchTimeNorm2d	BatchTimeNorm2d	Batch Normalization (Ioffe and Szegedy 2015) but applied over batch and time dimensions
ReLU	ReLU	Rectified Linear Unit (Nair and Hinton, 2010)
(LSTM)	-	Long Short-Term Memory (Hochreiter and Schmidhuber 1997)
Conv3d	ConvTranspose3d	-
BatchTimeNorm2d	BatchTimeNorm2d	-
ReLU	ReLU	-
Dropout3d	Dropout3d	3d Dropout (Srivastava et al. 2014)

Table 3.3. For each module of **Figure 3.2**, the number of input/output channels, convolution kernel sizes and strides and size of the output sequence is described. (*for these modules the number of input channels is the double of the output channels of the previous module because those channels are concatenated with the ones coming from the encoder as shown in **Figure 3.2**)

Module	**Input channels**	**Output channels**	**1st Conv kernel size**	**1st Conv stride**	**2nd Conv kernel size**	**2nd Conv stride**	**Output sequence size**
ST-Conv3LSTM	4	32	1, 7, 7	1, 1, 1	7, 1, 1	1, 1, 1	64, 128, 128
ST-Conv3 (1)	32	64	1, 3, 3	1, 2, 2	7, 1, 1	2, 1, 1	32, 64, 64
ST-Conv3 (2)	64	128	1, 3, 3	1, 2, 2	5, 1, 1	2, 1, 1	16, 32, 32
ST-Conv3 (3)	128	256	1, 3, 3	1, 2, 2	3, 1, 1	2, 1, 1	8, 16, 16
ST-Conv3 (4)	256	256	1, 3, 3	1, 2, 2	3, 1, 1	2, 1, 1	4, 8, 8
S-Conv	256	256	1, 3, 3	1, 2, 2	-	-	4, 4, 4
UpS-Conv	256	256	1, 2, 2	1, 2, 2	-	-	4, 8, 8
UpST-Conv3 (4)	*512	256	1, 2, 2	1, 2, 2	2, 1, 1	2, 1, 1	8, 16, 16
UpST-Conv3 (3)	*512	128	1, 2, 2	1, 2, 2	2, 1, 1	2, 1, 1	16, 32, 32
UpST-Conv3 (2)	*256	64	1, 2, 2	1, 2, 2	2, 1, 1	2, 1, 1	32, 64, 64
UpST-Conv3 (1)	*128	32	1, 2, 2	1, 2, 2	2, 1, 1	2, 1, 1	64, 128, 128
T-Conv	*64	64	3, 1, 1	1, 1, 1	-	-	64, 128, 128
Conv3	64	1	1, 1, 1	1, 1, 1	-	-	64, 128, 128

3.2.2.4 Data Augmentation

Data augmentation is an important aspect to consider when training a model in cases where data availability is limited to improve generalization and reduce overfitting (Perez and Wang

2017). It is also a good way to make the model robust to specific types of noise. In real world applications, distributions of data are usually long-tailed, meaning that some rare cases may not be sufficiently represented in the training data even if a large dataset is collected. The burned areas signature is characterized by sudden variations followed by a slow recovery. These correspond to a background pattern often covered by clouds in some regions.

To aim for better robustness and generalization, we apply the following three transformations:

1. Random brightness and contrast transformations are applied to 75% of the images. For the brightness transformation values are sampled between 0.4 and 0.6, where values below (above) 0.5 make the image darker (brighter). Contrast transformation is applied with a scale between 0.8 and 1.25 where values below (above) 1 translate to lower (higher) contrast.
2. Rectangular patches with random size and a random value, constant for the entire patch, are applied to the three first channels of the images (Red, NIR and MIR). For each image, the probability of applying patches is 0.5 with size between 5 and 50 pixels, and 1 to 5 patches, sampled from a uniform distribution.
3. Random erasing (Zhong et al. 2017) is applied with a probability of 0.5 to the Active Fires channel with size and number of patches identical to (2).

The first transformation mimics natural variability in the input images that occur due to differences in solar and satellite zenith angle. The second transformation is aimed to make the model robust to any signal that is not persistent in time, such as clouds. Finally, the random erasing of active fires is used to simulate the omission of active fires.

3.2.2.5 Implementation Details

The procedure was implemented using the fastai v1.0.50.post1 (https://fast.ai) and PyTorch v1.0.1.post2 (https://pytorch.org) libraries. We train the model using One Cycle Learning (Smith 2018) with a maximum learning rate of 0.01, Adam (Kingma and Ba 2014) optimizer and a weight decay of 0.01. We use sigmoid activation function and Binary Cross Entropy Loss, and train the model for 8 epochs defined as 2000 individual sequences each, resulting in a total train time of about 4.3 h and inference time of about 155 ms per sequence of size 64 × 4 × 128 × 128 on a NVIDIA GTX 1080 graphics card. The inference on CPU is also possible but significantly slower, with 2.7 s per sequence on an Intel Core i7-7700 CPU.

During the training phase, each sequence is sampled as follows:

1. From all images where at least 10 pixels are burned, we select one at random with reposition.
2. We select a sequence of 64 images centred at the previous selected image.
3. In case no such sequence exists (i.e., the random image is close to the beginning or end of the timeline we considered) the process is repeated until such sequence is found.

The rationale is that the model can learn faster if the samples that are given during the training are rich in burned areas.

3.2.2.6 Post-processing of Model Outputs

The model output sequences have the same size as the input sequences where each pixel has a value between 0 and 1 that can be interpreted as a probability that the pixel has burned. To extract monthly burned areas and date of burning, we follow the steps described below:

1. To generate the output for month m the model is provided with a sequence of 64 days starting on the 15th of the month $m-1$, i.e. ensuring that there are at least 15 days prior and a few more than 15 days after the month m, as represented by the 64 rectangles in **Figure 3.3**;
2. The output is sliced to the days corresponding to the month m (green rectangles in **Figure 3.3**) and both the sum of daily probabilities and the day the maximum probability occurs is computed for each pixel. Hereafter we refer to the sum of daily probabilities as the model confidence level;
3. The burned pixels are then given by all the pixels above a selected threshold and the date of burning is the corresponding day of the maximum probability obtained on step 2.

As a result, the first and last month for each year and each region are not used for validation.

For near real-time (NRT) mode, the approach is similar, but a sequence of 64 past images is selected instead with no slicing applied in step 2. For this case, the maximum probability and day of maximum are computed from the 64 days sequence.

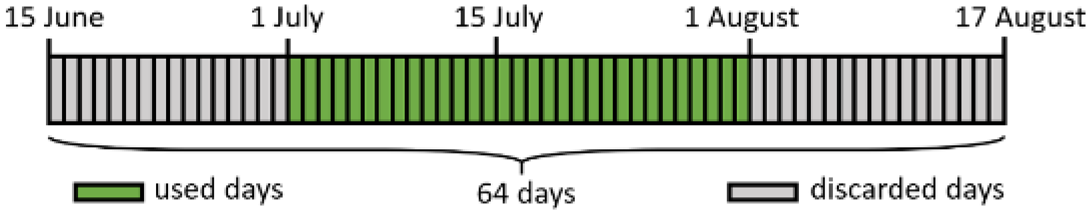

Figure 3.3. Illustration of the selection of days for the monthly product for the month of July.

3.2.2.7 Validation

In order to intercompare or validate BA-Net results with independent data not used for training, we apply Cross Validation (CV) leaving one year out each time for the training period (2012–2017), resulting in six CV folds. To evaluate the uncertainty caused by random transformations during the training of the model, for each CV fold, we train the model three times and present the average and standard deviation of the three runs, unless otherwise stated.

The spatial performance of the model is measured using Dice coefficient (also known as F1 score) and Overall Accuracy (OA), whereas the Omission Error (OE) and Commission Error (CE) are used to calibrate the products when validating against medium resolution reference data. The metrics are defined as:

$$Dice = \frac{2TP}{2TP + FP + FN} \tag{3.1}$$

$$OA = \frac{TP + TN}{TP + FP + TN + FN} \tag{3.2}$$

$$OE = \frac{FN}{FN + TP} \tag{3.3}$$

$$CE = \frac{FP}{FP + TP} \tag{3.4}$$

where TP, FP, FN and TN are the number of true positives, the number of false positives, the number of false negatives and the number of true negatives, respectively.

The validation is performed over the study period for each region but discarding the first and last month of each period as extra 15 days are required prior and after the study period to apply the post-processing described in **section 3.2.2.6**. For example, Mozambique region is covered from July to October, but the evaluation is done only for August and September. Hereafter, we refer to this subset as the evaluation period.

3.2.2.7.1 Intercomparisons and Temporal Validation

For the intercomparisons between each pair of the three products we compute the Dice coefficient, for each region, during the validation period (2012–2017), considering all the months in the evaluation period simultaneously. For the test set (2018), we compare the results of BA-Net and MCD64A1C6 with a similar approach but averaging the scores of the six CV folds. A fixed threshold of 0.5 was used to convert BA-Net confidence values to a binary burned/not burned mask, as well as for MCD64A1C6 and FireCCI51 burned area fractions on the 0.01° grid.

The dating of the burned pixels is evaluated by visual inspection of histograms of deviations between the VIIRS active fires and the date given by the product (Boschetti et al. 2010, Panisset et al. 2017, DaCamara et al. 2019), as well as by comparing the Mean Absolute Error (MAE), defined as follows

$$MAE = \frac{1}{N}\sum_{p=1}^{N}\left|D_p^{product} - D_p^{reference}\right| \tag{3.5}$$

Where $D_p^{product}$ and $D_p^{reference}$ are the reference and product julian days of burning for pixel p and N is the total number of pixels considered. This metric evaluates how close are the assigned dates of burning, on average, to the VIIRS active fires dates.

3.2.2.7.2 Validation with Reference Data and Burned Area Fraction

As some of the reference datasets available have different temporal and spatial coverages than the five regions and periods of study (**Figure 3.1**), the validation with reference data is restricted to pixels in the intersection of the reference data and the study spatial and temporal coverage. For Brazil however, as the reference data consists of 53 Landsat scenes covering a short period each, 2 days at the end of the period were added for FireCCI51, when matching the temporal range, in order to account for the bias in the date of burning. The value of 2 days was obtained by testing successive values and selecting the one achieving the best results.

The reference datasets used for validation for each region have different characteristics among them. Nevertheless, as emphasized in the CEOS CalVal protocol, all reference datasets consist of medium resolution data (i.e., higher resolution than the coarse products). As we are validating not only BA-Net but also FireCCI51 and MCD64A1C6, under the same conditions, any errors in the reference datasets will be common to three products and therefore the results can be compared.

As mentioned in the data section, all burned area datasets are resampled to the 0.01° working grid by computing the fraction of burned area inside each pixel. For a general validation of the spatial burned area patterns, we consider a burned area fraction greater than or equal to 0.5 for reference maps so that a pixel is considered as burned if it has burned 50% or more, and not burned otherwise. For BA-Net, MCD64A1C6 and FireCCI51, an optimal threshold is selected based on the following procedure:

1. For the thresholds of 0.001, 0.005, 0.01 and hereafter increasing by steps of 0.01 up to 1, omission and commission errors are computed for each product and each threshold;

2. For increasing threshold values, the omission error increases and the commission error decreases. We select the threshold for which the difference between omission and commission errors is minimal, usually corresponding to the point where the two lines cross (i.e., omission error equals commission error), the exception being if the lines never cross, resulting in a saturated threshold at either 0.001 or 1;
3. Pixels with a value greater than or equal to the optimal threshold are then considered as burned and not-burned otherwise.

To evaluate the results for different reference burned area fractions a set of thresholds ranging from 0.01 up to 0.9 are used and for each of those the same procedure as before is applied to find the set of optimal thresholds for the coarse products. It should be noted that each individual reference burned area fraction threshold (from 0.01 to 0.9) results in a set of binary reference maps that are then used to find the optimal thresholds for the three coarse products.

The resulting binary maps for the three products (after applying the optimal thresholds) are evaluated against the binary reference maps using the validation metrics. This process is repeated for each one of the reference burned area fraction thresholds ranging from 0.01 to 0.9. We also note that, for each region, the months of the same year are aggregated together but different years (when available) were processed separately (i.e., optimal thresholds are computed for each year, not for each month).

3.2.3 Results and Discussion

3.2.3.1 Spatial Intercomparisons

Results shown in **Table 3.4** correspond to the intercomparisons of the three burned area products for the cross-validation (2012–2017) and also the comparison between BA-Net and MCD64A1C6 for 2018 (test period). The comparisons that include BA-Net are the average of three runs with different random weight initialization and the values in square brackets the respective standard deviations. A fixed threshold of 0.5 was used to convert the BA-Net confidence values into binary burned area masks. The Dice values for 2012–2017 (**Table 3.4**) indicate that the BA-Net estimates are closer to MCD64A1C6, with scores above 0.8 for all regions but Mozambique. When comparing the Dice scores for the various pairs of products shown in **Table 3.4**, we find that matches between FireCCI51 and each of the two other products are very similar between them, as it should be expected due to the substantial similarity between BA-Net and MCD64A1C6. There are some fluctuations in the Dice values for the BA-

Net - MCD64A1C6 pair obtained for the cross-validation and test periods, with some regions in the test period experiencing an increase, while others show degraded values. Such variations are to be expected since the Dice score is usually higher when large fires occur, as most of the incorrectly classified pixels are often in the fire perimeters (Libonati et al. 2015). In particular, California had several large fires in 2018, while the same year in Portugal was generally mild with a single large fire, explaining the Dice score of 0.94.

Most importantly, these results show that the proposed model learns how to map burned areas with a performance level at least comparable to existing approaches using data from the VIIRS sensor resampled to about 1 × 1 km grid size. Furthermore, the methodology can be applied to data provided by any other sensor as long as its spectral channels capture the signature of wildfire in the landscape and a dataset is prepared to train the model. We also note that here we train the model from random weights initialization, however, to train on another dataset, the obtained trained weights can be used as a better initialization for a faster convergence requiring less data, a process known as transfer learning (Pan and Yang 2009).

Table 3.4. Dice coefficient for each region for the cross-validation (2012–2017) and test (2018) periods and every two pairs of the three products. In columns where BA-Net is present, the values correspond to the mean of 3 runs and the standard deviation is shown in square brackets.

Region	**2012–2017 (cross validation)**			**2018 (test)**
	BA-Net MCD64A1C6	BA-Net FireCCI51	MCD64A1C6 FireCCI51	BA-Net MCD64A1C6
California	0.884 [0.003]	0.831 [0.005]	0.832	0.906 [0.001]
Portugal	0.878 [0.008]	0.815 [0.010]	0.825	0.940 [0.001]
Brazil	0.831 [0.002]	0.761 [0.005]	0.753	0.780 [0.003]
Mozambique	0.742 [0.003]	0.614 [0.008]	0.626	0.749 [0.006]
Australia	0.886 [0.001]	0.749 [<0.001]	0.735	0.881 [0.004]

3.2.3.2 Temporal Validation

The MAE scores were computed for each region for the cross-validation (2012–2017), and the results are presented in **Table 3.5**. BA-Net achieves the lowest MAE for all regions and an overall MAE of 1.13 days, followed by MCD64A1C6 with 1.80 days. FireCCI51 shows a high bias on the date of burning with an overall MAE of 4.25 days, more than 3 times the BA-Net score. The bias existing in FireCCI51 is due to the algorithm design. Namely, the date of burning attributed is based on the three images with the lowest NIR closest to MODIS active fires, after filtering images with low quality (Chuvieco et al. 2018). The lowest NIR is usually expected to occur after the detection of active fires and therefore burning dates attributed this way are likely to have a bias as confirmed by the results shown in the right panel of **Figure 3.4**. Results for the test year (2018) are very similar to the cross-validation results (2012–2017). As mentioned before, the active fires are used for both input and validation of BA-Net but it is worth noting that the model was optimized to reproduce the MCD64A1C6 daily burned fractions and not the dates of the active fires. Therefore, the better performance of BA-Net on this task suggests that the model is making an appropriate use of the active fires information as it will be further discussed in the case studies of **section 3.2.3.4**.

Figure 3.4 shows the histograms of the difference (in days) between the detection of the active fire and the day of burn given by BA-Net, MCD64A1C6 and FireCCI51. We see that BA-Net has few negative differences, corresponding to a low rate of anticipation of the actual day of the active fire detection. The histograms confirm the overall superior performance of the BA-Net product, with very few attribution dates outside the 0–1 day range of the "true" date and matching the "true" date in 70% of the cases, compared with 45% for MCD64A1C6 and just about 5% for FireCCI51. Results for MCD64A1C6 are coherent with Giglio et al. (2018a) that reported a 44% match to the "true" date, globally, when comparing against MODIS active fires.

Table 3.5. Mean absolute error between active fires and dates of burning given by BA-Net, MCD64A1C6 and FireCCI51 for the five regions and the overall score, for the cross-validation (2012–2017) and test (2018). Values for BA-Net are the average of 3 runs for cross-validation and the average of the 6 CV folds for test with the standard deviation of the 3 model runs in square brackets. Values in bold highlight the best scoring product in each case.

	2012–2017 (cross validation)			**2018 (test)**	
Region	BA-Net	MCD64A1C6	FireCCI51	BA-Net	MCD64A1C6
California	**0.61** [<0.01]	1.03	4.88	**0.70** [0.01]	1.15
Portugal	**0.30** [<0.01]	0.87	4.43	**0.19** [<0.01]	0.43
Brazil	**0.76** [0.01]	1.17	3.49	**0.68** [0.01]	1.28
Mozambique	**2.02** [0.04]	2.85	5.39	**1.82** [0.04]	2.65
Australia	**0.39** [<0.01]	0.84	2.95	**0.39** [<0.01]	0.79
Overall	**1.13** [0.03]	1.80	4.25	**1.11** [0.03]	1.80

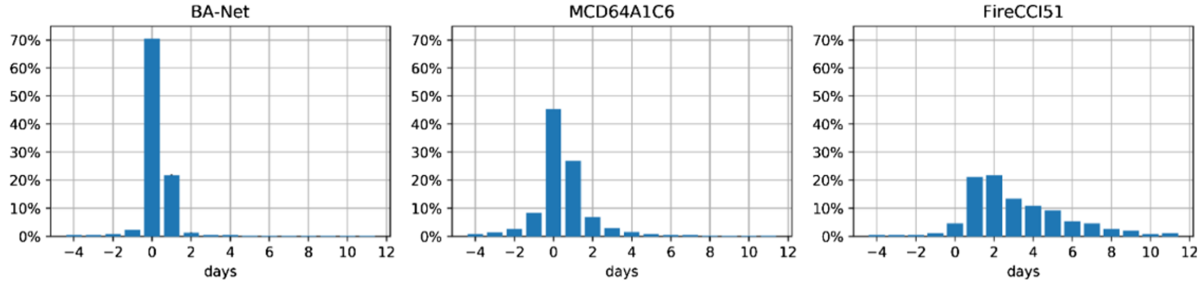

Figure 3.4. Histograms of the difference in days between the predicted date of burning and detection of active fires for BA-Net, MCD64A1C6 and FireCCI51, respectively.

3.2.3.3 Spatial Validation

The intercomparisons in **section 3.2.3.1** allowed to verify that BA-Net product is similar to MCD64A1C6 and, to a lesser extent, to FireCCI51. However, to assess the quality of a burned area product, careful validation needs to be made against higher resolution reference maps, for when they are available. In this section, we validate BA-Net, MCD64A1C6 and FireCCI51 with the independent references (as listed in **Table 3.1**, last five rows) for all the five regions. We have a particular interest in Brazil and Mozambique as they are more challenging regions due to the high density of small fires that are often not well captured by the coarse products, leading to significant underestimation of the burned area (Roteta et al. 2019). As the three coarse products are evaluated under the same conditions, concerning the same reference data, the results can then be compared to find how well BA-Net performs in relation to MCD64A1C6 and FireCCI51.

Following the procedure described in **section 3.2.2.7.2**, the optimal thresholds for the three products are selected as the ones that minimize the difference between omission and commission errors for each region and year, considering a reference burned area fraction threshold of 0.5. We note that the term burned area fraction always refer to the fraction of burned area within each 0.01° size pixel. Other metrics can be used to compute the optimal thresholds and the ideal metric will depend on the intended application. As an example, if it is more important to reduce the omission error, the metric to optimize should favour a lower omission error, trading off with a higher commission error.

Table 3.6 shows the results corresponding to the Dice coefficient for each region and year, computed for the available data, using the optimal thresholds for each of the three products. BA-Net (**Table 3.6**, third column) outperforms MCD64A1C6 (fourth column) and FireCCI51 (last column) in Australia (over 2 of the 3 years) and California (over 4 of the 5 years). For the remaining cases BA-Net scores as the second best of the three products except on Portugal where BA-Net and MCD64A1C6 score identically and very close to FireCCI51. It is also worth noticing that BA-Net is based on VIIRS 750 m bands on a 0.01° grid, whereas MCD64A1C6 and FireCCI51 are produced at 500 and 250 m resolution, respectively, and when resampled to the 0.01° grid the burned area fraction is computed, hence keeping information from the original resolution. This difference in spatial resolution makes the task harder for BA-Net, particularly for regions with the predominance of small fires (Mozambique and Brazil), but despite that BA-Net shows competitive results for Mozambique and Brazil and outperforms MCD64A1C6 and FireCCI51 in Australia and California in general. Overall (**Table 3.6**, last row), BA-Net shows a Dice of 0.678, not far from MCD64A1C6 with a Dice of 0.687 and above FireCCI51 with a Dice of 0.656. The obtained Dice score for FireCCI51, lower than MCD64A1C6 score, is coherent with the global validation performed by Chuvieco et al. (2018) that obtained a global Dice of 0.365 for FireCCI50 (the preceding version of FireCCI51), lower than 0.478 for MCD64A1C6.

Table 3.6. Dice coefficient for validation with reference maps, considering a reference burned area fraction greater than or equal to 0.5. Columns from left to right indicate the region, the year and Dice scores for BA-Net, MCD64A1C6 and FireCCI51, respectively. BA-Net scores correspond to the mean of 3 model runs, and the standard deviation is shown in brackets. Values in bold highlight the best scoring product in each case.

Region	**Year**	**BA-Net**	**MCD64A1C6**	**FireCCI51**
Australia	2014	0.820 [<0.001]	0.811	**0.828**
	2015	**0.729** [0.001]	0.722	0.719
	2016	**0.837** [0.014]	0.832	0.795
Mozambique	2016	0.582 [0.001]	**0.595**	0.557
California	2012	**0.920** [0.002]	0.898	0.890
	2013	**0.800** [0.002]	0.752	0.694
	2014	0.786 [0.008]	**0.791**	0.712
	2015	**0.798** [0.014]	0.791	0.657
	2016	**0.867** [0.005]	0.849	0.795
Portugal	2017	0.907 [0.001]	0.907	**0.910**
Brazil	2015	0.754 [0.003]	**0.756**	0.721
Overall		0.678 [0.002]	**0.687**	0.656

The overall results are strongly influenced by Mozambique where fires are in general small with a very high rate of ignitions, making it the most challenging of the five depicted regions and making the advantage for higher resolution products more prominent. To better understand how the coarse products perform for partially burned pixels, the Dice and overall accuracy are computed for reference burned area fraction thresholds other than 0.5. Again, this makes use of the procedure described in **section 3.2.2.7.2** to find the optimal thresholds for each of the three products. We note that while for MCD64A1C6 and FireCCI51 the optimal thresholds correspond to burned area fractions, for BA-Net the optimal thresholds are based on the model confidence levels for the monthly data computed as described in **section 3.2.2.6**.

Figure 3.5 shows, as an example, the comparison of BA-Net with binary reference maps for reference burned area fractions greater than or equal to 0.1, 0.5 and 0.7 respectively from left to right where green, red and blue represent true positives, omission and commission. We observe that for the fraction greater than or equal to 0.1 (left panel) the number of burned pixels (i.e., the number of pixels that burned 10% or more) increases dramatically. BA-Net performs surprisingly well in this context achieving a Dice of 0.793 when using the selected optimal threshold that balances omission and commission errors.

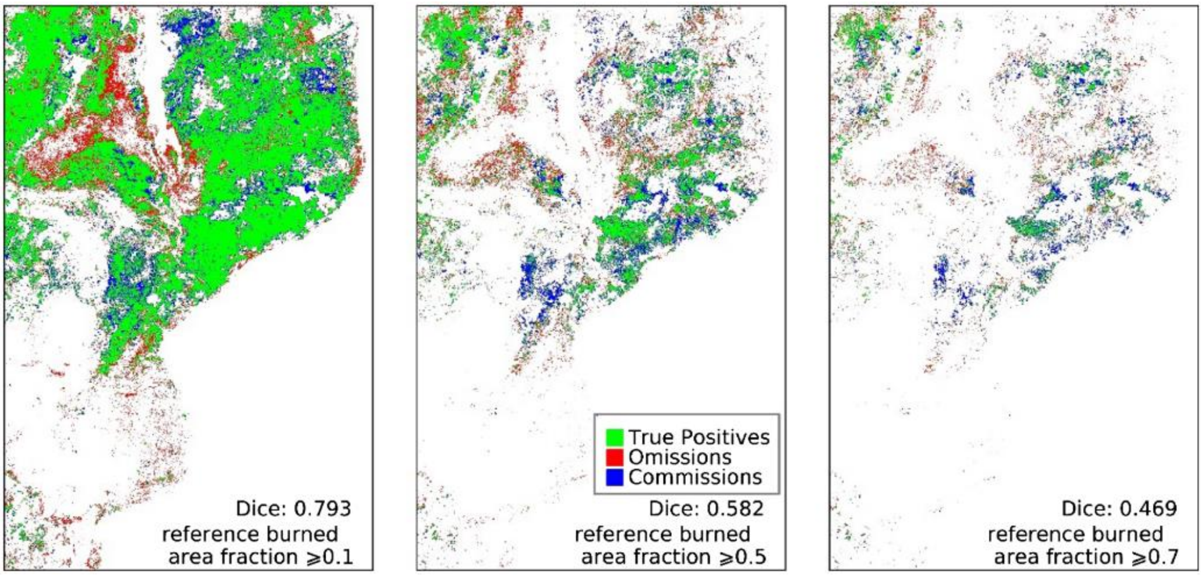

Figure 3.5. Comparison of BA-Net with reference burned area fractions greater than or equal to 0.1 (left panel), 0.5 (central panel) and 0.7 (right panel) for the region of Mozambique. Green, red and blue pixels represent true positives, omissions and commissions, respectively. For BA-Net maps correspond to the average of the 3 model runs. (For interpretation of the references to colour in this figure legend, the reader is referred to the web version of this article.)

For a more systematic evaluation of the results, we compute the validation metrics for successive reference burned area fraction thresholds, ranging from 0.01 to 0.9, for each region. We note that this procedure is the same as in **Figure 3.5** but now considering each region and a wider set of reference burned area fraction thresholds. Results are presented in **Figure 3.6** in a graphical form. The Dice score, overall accuracy and optimal thresholds are shown in the left, central and right columns of **Figure 3.6**, for each reference burned area fraction threshold and for each region – California, Portugal, Brazil, Mozambique and Australia – respectively. We note that the result obtained for each reference burned area fraction threshold can be interpreted as different classification problems: each of those cases corresponds to a (positive) classification of pixels partially burned by a fraction greater than or equal to the respective threshold.

Figure 3.6 shows that, in general, BA-Net (blue line) shows Dice scores higher than MCD64A1C6 (orange line) and FireCCI51 (green line) for lower reference burned area fraction thresholds and competitive performance otherwise. The exception is the region of California where the opposite behaviour is observed, possibly explained by the different characteristics of the reference data that consists of fire perimeters (i.e., inside the fire perimeter the burned fraction is always considered to be 1). It is worth noting that the inverse U-shaped curves often observed for the Dice score (**Figure 3.6**, left column panels) are to be expected since the task becomes harder for both lower and higher reference burned area fraction thresholds. The rationale is that the coarse resolution of the products is not sufficient to detect, as accurately, small sub-grid fires that are present in the reference maps or, conversely, to distinguish between pixels that burned almost completely.

Looking for the region of Portugal (**Figure 3.6**, second row) the scores are very similar between the three products, BA-Net showing, however, a slightly higher overall accuracy (central panel) for reference burned area fraction thresholds below 0.5. For Mozambique, (**Figure 3.6**, fourth row), BA-Net shows an increasingly better Dice for low burned area fraction thresholds up to 0.01 (left panel), with a clear advantage over MCD64A1C6 and FireCCI51. It should be noticed that the BA-Net Dice scores for the reference burned area fraction thresholds of 0.1, 0.5 and 0.7 in the fourth row of **Figure 3.6** (indicated by the three black arrows) correspond to the maps shown in **Figure 3.5**. Contrary to the Dice score, the overall accuracy increases for higher reference burned area fraction thresholds as expected since the number of burned pixels decreases, making it easier to score well on overall but harder to have a solid match to the reference maps. The opposite is true for the lower reference burned area fraction thresholds, resulting in a drop of overall accuracy. However, this drop is very slight for BA-Net that remains with an overall accuracy above 0.85, even for a reference burned area fraction threshold of 0.01, contrasting to the two other products that show an accuracy below 0.75. **Figure 3.6** third row shows the results for Brazil, corresponding to the overall score for the 53 Landsat scenes. We see that BA-Net have a similar Dice as MCD64A1C6 but surpassing it for reference burned area fraction thresholds below about 0.35, reinforcing the observation that BA-Net has a better performance for small fires. For Australia (**Figure 3.6**, last row), BA-Net outperforms MCD64A1C6 and FireCCI51 for reference burned area fraction thresholds below about 0.6 with a higher Dice score and a higher overall accuracy for reference burned area fraction thresholds between about 0.15 and 0.6.

The general improvement of BA-Net for small fractions can have a substantial impact for the estimation of the total burned area in regions where small fires prevail, and most importantly, BA-Net achieves overall competitive results in burned area mapping, even when compared with products, such as MCD64A1C6 and FireCCI51, that have the advantage of using higher spatial resolution observations. The choice of VIIRS 750 m bands instead of VIIRS 375 m bands is necessary for this discussion since otherwise it could be argued that a better dataset could be the cause of BA-Net good results. However, by using the 750 m resampled to 0.01° grid we show competitive and state-of-the-art results despite the lower resolution, corroborating the benefit of BA-Net and the deep learning framework for the problem of mapping and dating of burned areas.

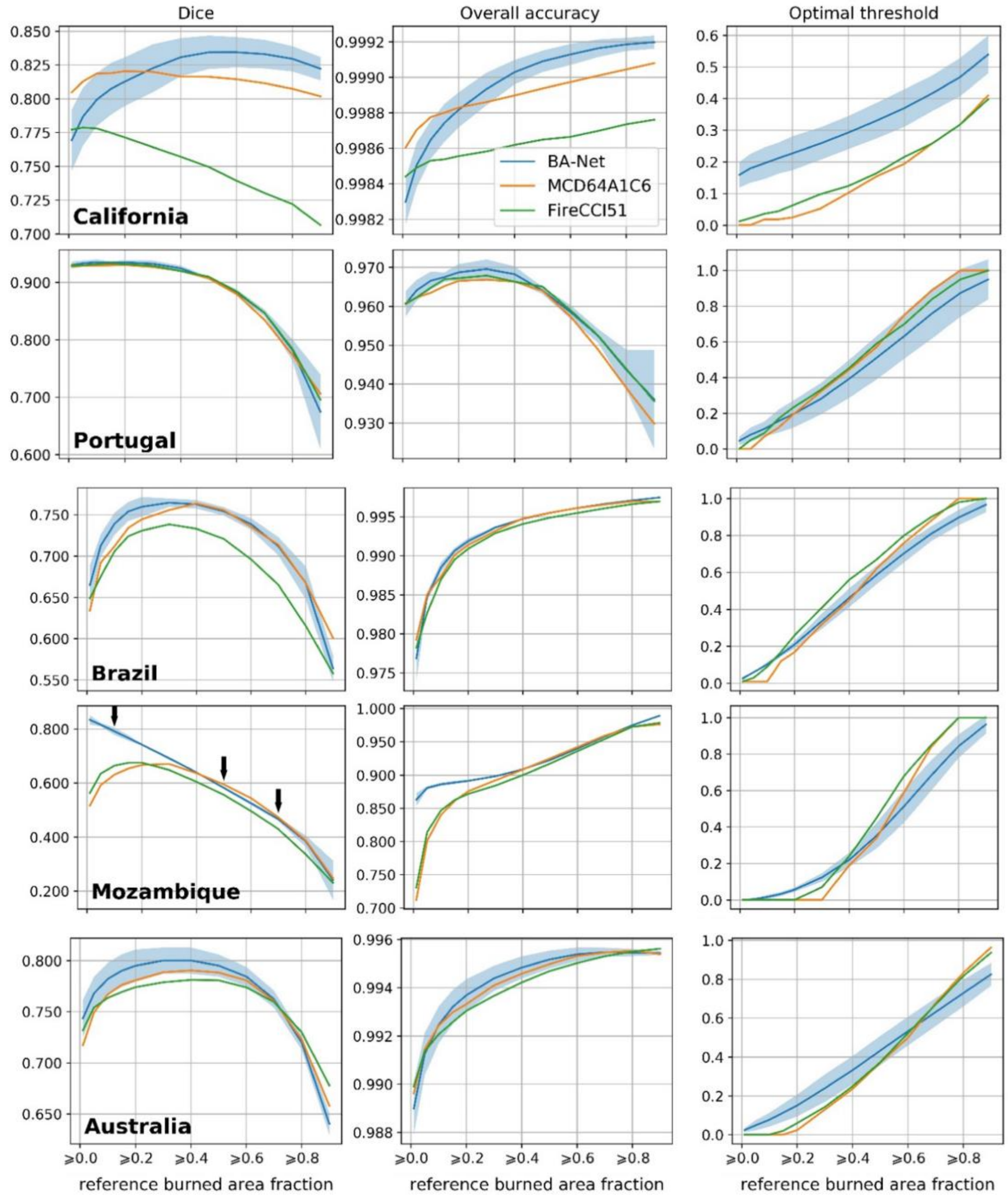

Figure 3.6. Dice, overall accuracy and optimal thresholds (left, middle, and right panels, respectively) for each reference burned area fraction for the BA-Net (blue), MCD64A1C6 (orange) and FireCCI51 (green), for the regions of California, Portugal, Brazil, Mozambique and Australia (first to last row). The shaded blue region for BA-Net corresponds to the 95% confidence interval of 3 model runs. The three black arrows indicate the Dice values corresponding to the thresholds shown in **Figure 3.5** (0.1, 0.5 and 0.7). (For interpretation of the references to colour in this figure legend, the reader is referred to the web version of this article.)

3.2.3.4 Case Studies and Near-real-time Application

To better understand the BA-Net model performance, we show case studies for two fires that occurred in Portugal. The first occurred on 15/16 October 2017 in central Portugal (Pinto et al. 2018b) and the second on 3–9 August 2018 in Algarve, southern Portugal (Rego et al. 2019). These two case studies have very distinct characteristics, which allow us to gain insight into the inner-working of BA-Net.

Figure 3.7 shows the sequence of input images (first row) corresponding to 15 to 25 October (19–20 October are not shown as VIIRS images are completely covered by clouds) in Central Portugal where the colours correspond to an RGB composite with bands Red, NIR and MIR inverted, and the active fires overlapped in red. The second and third rows (**Figure 3.7**) show the BA-Net in near-real-time (NRT) mode (i.e., only considering input data up to the event date shown on top of each panel) and in monthly mode (i.e., allowing input data after the event date), while the last two sequences show MCD64A1C6 and FireCCI51, respectively. This particular case study is very challenging, as the presence of clouds during the fire event did not allow a clear view of the surface during the first few days. Good quality images, where burned areas can be accurately identified, are available only one week after the fire events (on 23 and 24 October).

We first note (**Figure 3.7**) that BA-Net and MCD64A1C6 have similar characteristics, whereas FireCCI51 has a higher bias for the date of burning as mentioned before. Another important aspect is that active fires on 15 October (**Figure 3.7**; red dots in the 1st top panel) extend outside the burned area, resulting in commission errors appearing on BA-Net NRT on 15/16 October, as pointed by the magenta arrow on the second row. However, as the model is exposed to new images with better quality, particularly starting on 22 October, it updates the outputs according to the new information, converging rapidly to the final solution shown in the third row. This result is relevant, since if the BA-Net estimates were too influenced by (overfitting to) the active fires, then that whole region where active fires are present should be identified as burned. The evolution of the BA-Net burned areas suggests that instead, the model is able to reach a balance between the various inputs. Furthermore, the evolution of the BA-Net NRT (second row) shows that for 16 October only a few pixels are classified as burned. However, as we move forward in time, it includes more burned regions and maps the date of burning to the correct or close to the correct day, suggesting that the model "understands" the spatiotemporal correlations between the active fires and the reflectances leading to more accurate and spatially coherent dates of burning.

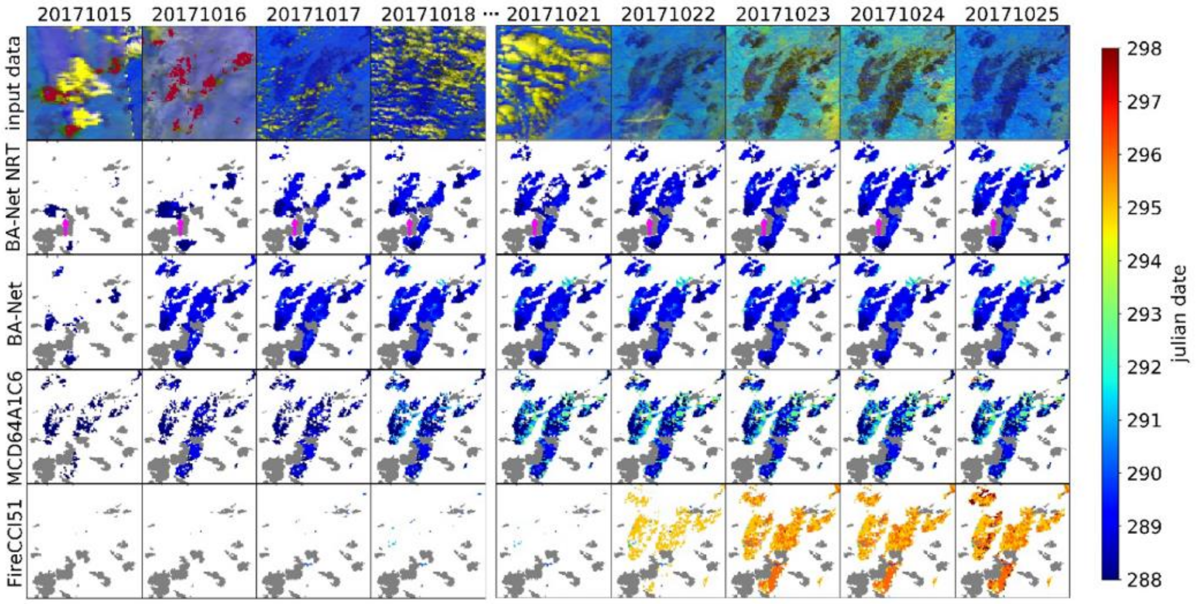

Figure 3.7. An example of 11 consecutive days, for 15 (day 288) to 25 (day 298) October for Central Portugal covering a region of about 1 × 1°. The lines from top to bottom correspond to: (1) crop of a sequence of input images represented with RGB colours corresponding to bands Red, NIR, MIR inverted and active fires overlaid in red; (2) BA-Net burned area (coloured surface) and date of burning (according to the colorbar) in NRT mode; (3) as in (2) but in monthly mode; (4) burned area (coloured surface) and date of burning (according to the colorbar) for the MCD64A1C6; (5) as in (4) but for FireCCI51. Shaded grey regions in rows 2–5 correspond to areas burned in the same year but previous to the displayed time window. (For interpretation of the references to colour in this figure legend, the reader is referred to the web version of this article.)

Looking now for the case study of August 2018, **Figure 3.8** shows the comparison between BA-Net and MCD64A1C6 final dates of burning and a high-resolution analysis adapted from a local evaluation report for this fire event (Rego et al. 2019). We can see that BA-Net dates of burning (central panel) follow a pattern close to the "true" fire progression (left panel), whereas MCD64A1C6 (right panel) shows a less realistic fire progression. These small differences can have a substantial impact for applications such as the derivation of fire patch functional traits (Laurent et al. 2018, Andela et al. 2019) such as daily fire expansion speed, direction and fire line length. The one-day delay well visible between the reference map and BA-Net is a consequence of a different definition of day as the day for BA-Net corresponds to the period between two satellite observations. In the Monchique fire, the period of higher activity and higher burned area expansion occurred mostly in the afternoon, after the satellite passage, hence the apparent delay of 1-day from the real day.

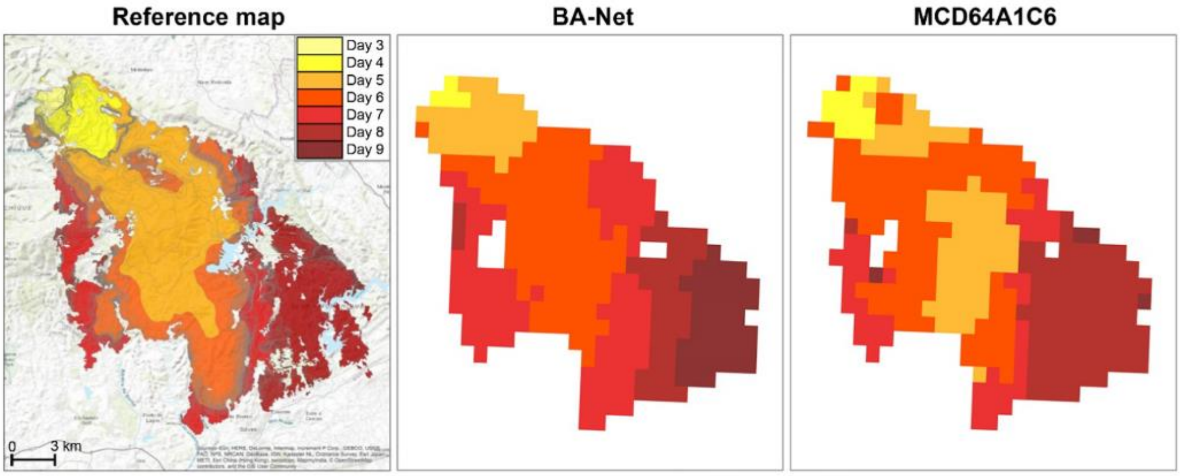

Figure 3.8. Reference burned area and dates of burning (left panel, adapted from Rego et al., 2019), BA-Net mapping (centre panel) and MCD64A1C6 mapping (right panel). All dates of burning are coloured according to the colour legend on the left panel.

3.2.3.5 Ablation Study

In this section, we test the impact of the main model design choices on the results, namely the LSTM layer and the U-Net structure. For these experiments, we train the model with the years of 2012–2017 but leaving 2015 out for validation and we report the results for 2015. This is enough to test the differences in performance using intercomparisons (**Table 3.7**) with MCD64A1C6 and validation results for Australia, California and Brazil for the year 2015 (

Table 3.8) to show that the decrease in the similarity between BA-Net and MCD64A1C6 also translates to differences with the reference data.

Table 3.7 shows that removing the LSTM or using a shallower model without the U-Net structure (i.e., following the direct path input → STConv3LSTM → T-Conv3 → Conv3 → output and removing all remaining modules) results in an overall decrease in performance as measured by the Dice coefficient, a result that is corroborated by the results in

Table 3.8. The exception being the region of California where the performance increases when compared with the reference data. This could, however, be a consequence of the different characteristics of the reference data for California as discussed before.

When using the shallower model and removing the LSTM layer simultaneously results drop further (**Table 3.7** last row,

Table 3.8 last column), corroborating the observation that LSTM layer has an important impact on the model performance.

Table 3.7. Effects on model performance (baseline) of removing the LSTM layer (w/o LSTM), removing the U-Net architecture, i.e. following a direct path input → STConv3LSTM → T-Conv3 → Conv3 → output (w/o U-Net arch) and removing both the previous two together (w/o LSTM, U-Net arch). Values for each region correspond to the Dice coefficient for the year 2015, using MCD64A1C6 as reference. Values in bold highlight the best scoring model for each region.

Model/Region	California	Portugal	Brazil	Mozambique	Australia
Baseline	**0.832** [0.011]	**0.846** [0.003]	**0.819** [0.001]	**0.727** [0.013]	**0.885** [0.001]
w/o LSTM	0.815 [0.010]	0.808 [0.002]	0.786 [0.005]	0.656 [0.005]	0.866 [0.002]
w/o U-Net	0.794 [0.003]	0.807 [0.008]	0.796 [0.001]	0.714 [0.010]	0.860 [<0.001]
w/o U-Net and LSTM	0.740 [0.004]	0.780 [0.014]	0.748 [0.003]	0.652 [0.002]	0.797 [0.003]

Table 3.8. Similar to **Table 3.7** but using the higher resolution reference maps as reference.

Region	Year	Baseline	w/o LSTM	w/o U-Net	w/o U-Net and LSTM
Australia	2015	**0.729** [0.001]	0.716 [0.003]	0.710 [0.001]	0.686 [0.003]
California	2015	0.798 [0.014]	**0.847** [0.002]	0.842 [0.001]	0.826 [0.008]
Brazil	2015	**0.754** [0.003]	0.734 [0.002]	0.735 [0.001]	0.712 [0.002]

3.2.4 Conclusions

Systematic mapping and dating of burned areas is a task of great importance for a wide range of applications, such as fire management, calibration of fire propagation models, assessment of vegetation fire emissions and air quality, land cover dynamics studies, derivation of fire patch functional traits and to better understand how the fire patterns are evolving in a scenario of climate change and population change.

Here we proposed a model capable of learning to identify and assign dates to burned areas from sequences of multi-spectral daily images retrieved from satellite without the need for cloud masking or image selection as pre-processing. The trained model provides competitive results on burned area mapping, for a reference threshold of 0.5, showing the second-best overall Dice of 0.678, not far from MCD64A1C6 with 0.687 and better than FireCCI51 with 0.656. For lower burned area fraction thresholds, BA-Net shows generally higher Dice scores than the two other products, except for the region of California where it shows instead higher Dice score for higher burned area fraction thresholds. Such behaviour is likely to be caused by the different characteristics of the reference for this region, as discussed in **section 3.2.3.3**.

For the task of dating of fire events, BA-Net shows clearly state-of-the-art results with an overall mean absolute error of 1.13 days, followed by MCD64A1C6 with 1.80 and FireCCI51 with 4.25 when validating for the 6 cross-validation years (2012–2017) using dates of the active fires as reference. The two case studies analysed in **section 3.2.3.4** corroborate these results and further show that BA-Net assigned dates of burning are consistent in space, even for difficult cases such as the fires of October in Portugal, contrary to what is observed for MCD64A1C6 and FireCCI51. The better consistency of dates of burning is a consequence of BA-Net model structure that is able to capture the spatiotemporal relations of the daily surface reflectances and active fires.

The case studies in **section 3.2.3.4** also show that BA-Net NRT converges rapidly to the final monthly product result with a rate that depends primarily on cloud coverage. The NRT product has important applications for emergency services and quick assessments of burned area. In this line, the European Forest Fire Information System (San-Miguel-Ayanz et al. 2012) has a Rapid Damage Assessment module that produces near real-time burned area maps using, however, a semi-automatic approach, that requires manual verification and correction. As BA-Net outputs converge to the final solution in a few days, we expect it to improve on this task by reducing significantly the amount of manual work needed to map the burned areas and by providing more accurate dates of burning.

In recent years deep learning has been driving important progress in many different areas, including data-driven Earth system science (Pelletier et al. 2019, Reichstein et al. 2019). Such an achievement is only possible due to the better capacity of these algorithms to extract meaningful information from large amounts of data in a computationally feasible way (Reichstein et al. 2019). Mapping and dating of burned areas with satellite retrieved imagery is the type of problem that can benefit from recent deep learning advances. The results obtained in this work are a first step towards bringing these great advances in computer vision of the recent few years to the domain of burned areas mapping with satellite imagery, a challenging problem that has been the subject of research for more than four decades (Hitchcock and Hoffer 1974). The good results obtained in this work and the prospects of a continuous increase in computational power and data availability suggest that this is a path that is worth following in years to come, given the high potential for future applications.

Despite the good results obtained we acknowledge that there are, however, several open questions. In the short-term we plan to investigate how the model performs in other regions, namely over higher latitudes, by studying burned areas in boreal forests and tundra, both covering about 33% of the global land surface (MCGuire et al. 1995, Young et al. 2017). This is an important step towards the application of this methodology to derive a global burned area product, either from VIIRS or another sensor with similar bands onboard a polar-orbiter (e.g., SLSTR onboard Sentinel-3). Similarly, we expect to test the BA-Net to coarser sensors such as AVHRR, which in turn have the potential to provide longer time-series, as well as to medium resolution sensors (10–80 m) such as Landsat-8 and Sentinel-2. The need of different thresholds for different regions/fire regimes is also a question we plan to address in future work, namely by incorporating input information suitable to explain the differences in fire regimes, such as land cover and topography. Sociocultural factors also play an important role in fire ignition patterns that may be possible to incorporate indirectly based on historical fire data.

With the aim of accelerating research on these and many other topics that may benefit from the methodology presented in this work, code, pre-trained models and datasets used to train the model are available at https://github.com/mnpinto/banet.

3.2.5 Acknowledgements

This work was partially supported by national funds through Fundação para a Ciência e a Tecnologia, Portugal (FCT) under project FireCast (PCIF/GRF/0204/2017). Miguel M. Pinto was supported by FCT through PhD grant PD/BD/142779/2018. Renata Libonati was supported by Serrapilheira Institute, Brazil (grant number SERRA-1708-15159) and Conselho Nacional de Desenvolvimento Científico e Tecnológico, Brazil (CNPQ) through grants 305159/2018-6 and 441971/2018-0.

3.2.6 Author Contributions

Miguel M. Pinto (MMP) wrote the paper, organized the data, developed the algorithms, and validated the results. Renata Libonati (RL), Ricardo M. Trigo (RMT), Isabel F. Trigo (IFT) and Carlos C. DaCamara (CCD) contributed with constructive criticism and suggestions. RL, RMT, IFT and CCD revised and edited the manuscript.

3.3 A Practical Method for High-Resolution Burned Area Monitoring Using Sentinel-2 and VIIRS

This section presents the results published in the following article: Pinto, M. M., Trigo, R. M., Trigo, I. F., & DaCamara, C. C. (2021). A Practical Method for High-Resolution Burned Area Monitoring Using Sentinel-2 and VIIRS. Remote Sensing, 13(9), 1608.

Mapping burned areas using satellite imagery has become a subject of extensive research over the past decades. The availability of high-resolution satellite data allows burned area maps to be produced with great detail. However, their increasing spatial resolution is usually not matched by a similar increase in the temporal domain. Moreover, high-resolution data can be a computational challenge. Existing methods usually require downloading and processing massive volumes of data in order to produce the resulting maps. In this work, we propose a method to make this procedure fast and yet accurate by leveraging the use of a coarse resolution burned area product, the computation capabilities of Google Earth Engine to pre-process and download Sentinel-2 10-meter resolution data, and a deep learning model trained to map the multispectral satellite data into the burned area maps. For a 1500 ha fire, our method can generate a 10-meter resolution map in about 5 min, using a computer with an 8-core processor and 8 GB of RAM. An analysis of six important case studies located in Portugal, southern France and Greece shows the detailed computation time for each process and how the resulting maps compare to the input satellite data as well as to independent reference maps produced by Copernicus Emergency Management System. We also analyse the feature importance of each input band to the final burned area map, giving further insight into the differences among these events.

3.3.1 Introduction

Wildfires are a natural hazard with important impacts on ecosystems and human populations (e.g., Pausas et al. 2008, Bowman et al. 2017). Mediterranean Europe is regularly affected by wildfires, a trend that is poised to increase according to the range of climate change scenarios (Turco et al. 2018, Ruffault et al. 2020). Monitoring the areas burned by wildfires with high resolution is of paramount importance for damage assessment and forest management (Fernandez-Manso et al. 2016, Hislop et al. 2018), and fire danger and propagation forecasts (Freire et al. 2019). Burned area products can be derived based on ground observations or satellite data, often presenting significant differences at the end of the fire season (Loepfe et al. 2011, Mangeon et al. 2015). The latter have the advantage of allowing for a consistent analysis over space and time and have therefore been used extensively over the past decades (Chuvieco et al. 2019). Furthermore, the importance of satellite observations will keep growing as more satellite data are available with increasingly higher resolution.

Polar-orbiting satellites are usually the choice for developing burned area products due to their higher spatial resolution and global coverage (Chuvieco et al. 2019). Recently, several global burned area products have been proposed using data from Moderate Resolution Imaging Spectroradiometer (MODIS) (Chuvieco et al. 2018, Giglio et al. 2018a) and Visible Infrared Imaging Radiometer Suite (VIIRS) (**section 3.2** of this thesis). These products, despite having a coarse resolution (250–1000 m), provide daily coverage allowing for near-real-time applications and better robustness to the presence of clouds. The coarse resolution is however a limitation for applications where the fine details of the burned areas are important or to accurately estimate the total burned area at the end of the season, a basic metric that can still present significant differences depending on the methods used (Humber et al. 2018, Roteta et al. 2019). Aiming towards higher resolution products, Landsat satellites have been extensively used to map burned areas with up to 30 m resolution (e.g., Bastarrika et al. 2011, Stroppiana et al. 2012, Hawbaker et al. 2017) and an 8-day revisit period with two satellites. Sentinel-2 satellites (Drusch et al. 2012) go a step further with a spatial resolution up to 10 m and a revisit period of 5 days, considering Sentinel-2A and Sentinel-2B, the latter operating since early 2017. This higher spatial resolution and better temporal coverage make Sentinel-2 a great choice to map burned areas since 2017, as already shown by several studies (e.g., Roteta et al. 2019, Filipponi et al. 2019).

Traditional approaches for mapping burned areas with Sentinel-2 or Landsat data are often based on a two-step approach, where candidate pixels are first selected based on active fires data and spectral indices, followed by a refinement step to balance and reduce the commission and omission errors (Roteta et al. 2019). In some approaches, it is also common to use a region growing algorithm where the initial candidate points are used as seeds and new candidates are included with awareness of the neighbouring pixels (Bastarrika et al. 2011). A detailed overview of the historical methods for mapping burned areas can be found in Chuvieco et al. 2019.

Deep learning techniques have been gaining increasing attention over the recent years following the increase in computational capability. Most notably, the use of Graphical

Processing Units (GPUs) has enabled a very fast development and improvement of computer vision techniques. Applications for burned areas mapping have started to emerge for daily burned areas mapping and dating using VIIRS (**section 3.2** of this thesis), as well as for higher resolution data using Sentinel-1 (Ban et al. 2020) and Sentinel-2 (Knopp et al. 2020). Deep learning techniques present interesting advantages, namely: optimization can be done with batches of data, making the training process computationally feasible; the convolutional neural network structure can efficiently capture the spatial context of neighbouring pixels; the inference step, after the model is trained, is very efficient and highly parallelizable.

One important limitation of existing algorithms for mapping burned areas with medium to high-resolution data is the computational cost and storage required. Even if deep learning techniques reduce the cost of processing the data, just the acquisition and pre-processing of data for an extended period and region can be very slow and challenging for regular desktop or laptop computers. To mitigate this problem, we propose a modular methodology for a faster monitoring of burned areas with 10 m resolution. The method explores the storage and processing capacity of the Google Earth Engine (GEE, Gorelick et al. 2017) for data pre-processing and acquisition, and a deep learning model trained to map the burned areas using previously downloaded pre-fire and post-fire composites. The sequence of steps in our approach consists of: (1) using BA-Net model (**section 3.2** of this thesis) to produce coarse burned areas maps using VIIRS 375 m bands; (2) splitting the detected burned areas into individual events; (3) downloading pre-fire and post-fire Sentinel-2 composites of red, near-infrared (NIR) and shortwave-infrared (SWIR) only for the regions enclosing the fires of interest, making use of the GEE functionalities to create the pre-fire and post-fire composites; (4) using a deep learning model optimized to generate 10 m burned areas using as inputs the Sentinel-2 data and the coarse burned area map derived from VIIRS.

The proposed approach can be used for fast monitoring of wildfires as BA-Net model allows for daily updates and Sentinel-2 data are available every 5 days if there is no occlusion by clouds in the burned region. As we will show, the procedure can generate a 10 m resolution burned map for a 1500 hectares fire event in about 5 min overhead time (assuming the coarse mask for the event is already routinely generated and provided) on a regular personal computer, including the download time of the Sentinel-2 data required.

The main objectives of this work are three-fold: (1) To develop a fast and robust tool for quick post-fire assessment, as soon as clean data are available; (2) to allow for a more detailed analysis of historical fires, particularly those with intricate borders between burned and unburned pixels within large fires, and (3) to make the methodology available as a Python package ready to be used.

In line with the third goal of this work, the Python package and pretrained models necessary to apply our methodology are available at https://github.com/mnpinto/FireHR, accessed on 14 April 2021.

3.3.2 Data and Methods

Our study focused on Mediterranean Europe and, since we were working with Sentinel-2A and Sentinel-2B satellites, we were restricted to data from the 2017 fire season onwards. However, in 2017 Portugal's fire season accounts for a total burned area of about 500,000 hectares, representing more than 50% of the total burned area in the EU for that year (San-Miguel-Ayanz et al. 2018, Turco et al. 2019). Therefore, there was an unusually high amount of data for that year alone that could be used to train and evaluate our model for 10 m resolution burned areas as described in **section 3.3.2.4**. The pipeline for the approach we propose is illustrated in **Figure 3.9** and described in detail in **sections 3.3.2.1 to 3.3.2.5**.

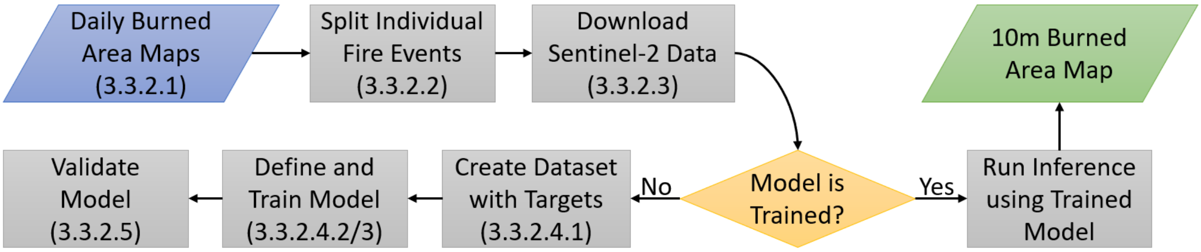

Figure 3.9. Pipeline to generate the 10 m resolution burned areas. Numbers in parenthesis indicate the paper's subsection describing the process.

3.3.2.1 Daily Burned Areas Using BA-Net

BA-Net (**section 3.2** of this thesis) is a deep learning model trained to map and date burned areas using sequences of daily satellite images derived from VIIRS sensors. We used the BA-Net Python library version 0.6 (pypi.org/project/banet/0.6.0, accessed on 14 April 2021) to generate the burned area products with 0.001° resolution (about 100 m) for the time periods and regions described in **Table 3.9** and delimited in **Figure 3.10** by green rectangles.

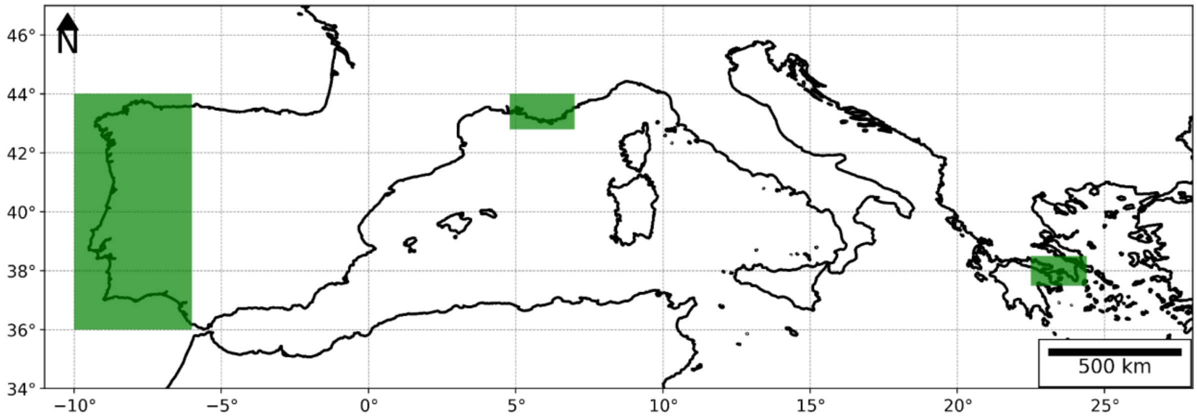

Figure 3.10. Green rectangles delimit the regions of study described in **Table 3.9**.

Table 3.9. Study regions details.

Region Name	Bounding Box	Time	Use
Western Iberia	36.0 to 44.0º N 10.0 to 6.0º W	June to October 2017 and August 2018	Train/Test
French Riviera	42.8 to 44.0º N 4.8 to 7.0º E	July 2017	Test
Attica Greece	37.5 to 38.5º N 22.5 to 24.4º E	July 2018	Test

3.3.2.2 Split Individual Fire Events

A common method to split individual fire events is flood fill (Archibald et al. 2009, Nogueira et al. 2016, Laurent et al. 2018) in which neighbouring burned pixels with an identical or sequential date of burning are aggregated to identify the individual burned patches. This method is, however, computationally expensive, particularly for large regions with large fires, and even more if implemented in high-level programming languages (e.g., Python). In order to make the pipeline fast and efficient in Python, we developed the *fire_split* library (https://github.com/mnpinto/fire_split, accessed on 14 April 2021) that makes use of the very efficient *ndimage.label* function from SciPy library (Virtanen et al. 2020), that split non overlapping patches, enhanced with functionality to allow for a spatial buffer and temporal separation of the events.

The method consists of the following steps:

1. Create a buffer around the burned pixels using kernel convolution with kernel size 2x2 pixels;
2. Use ndimage.label function to split the fires spatially without taking into account the temporal component;
3. Remove fire events smaller than 25 pixels;

4. For each retained event, look at the dates of burning and split the event every time the temporal distance is greater than 2 days;
5. For each newly separated event run *ndimage.label* to separate events that may have been previously connected by a third one;
6. Remove again fire events smaller than 25 pixels if any are present after the temporal split.

The value of 2x2 pixels for the kernel size of the spatial buffer corresponds to a minimum separation distance of about 4 pixels at the 0.001° spatial resolution and was set to be close to, but higher than the original 375 m resolution of the VIIRS data. As for the temporal separation, the value of 2 days was set in order to have good discrimination of the dense number of fires that occurred in western Iberia in 2017, but still giving enough margin to account for the uncertainty in the date of burning of BA-Net, which is smaller than 2 days for more than 90% of the pixels (**section 3.2** of this thesis). The minimum size selected of 25 pixels corresponds to about 25 hectares, a number that is close to about 2 pixels at the original 375 m resolution of the data. In the *fire_split* Python library, all these parameters can be adjusted by the user.

3.3.2.3 Sentinel-2 Composites Using Google Earth Engine

Google Earth Engine (GEE) Python API can be used to select, pre-process and download data automatically using a Python script. In fact, in a recent work, Long et al. 2019 proposed a global annual burned area mapping tool based on GEE and Landsat images. Our approach significantly differs, as we only use GEE as a pre-processing and data acquisition tool at single event level. In this regard, our method is designed as a tool either for quick post-fire assessment or for a detailed analysis of historical fires. The quick post-fire assessment can be performed as soon as clean Sentinel-2 data are available, i.e., less than 6-days if the following overpass finds clear sky conditions.

Our approach consists in downloading two composites of multispectral images for each event, one corresponding to dates before the fire, and the other immediately after the fire. These images include Sentinel-2 Level-1C (reference code on GEE: COPERNICUS/S2) bands Red (B4), NIR (B8) and SWIR2 (B12). In order to obtain images that are usually free of clouds we computed the median of all available images within the two months prior and after the fire. The Python code we provide has additional options for the pre-processing of the composites, namely, a maximum cloud coverage level can be set to filter cleaner images or the number of images (n) with the least cloud cover fraction could be selected, where n can be set by the user.

This pre-processing process, regardless of the option used, is very fast since it was performed on GEE platform. We only download the two (pre-fire and post-fire) composited images for the region of each fire event of interest, as defined with the method described in **section 3.3.2.2**. Furthermore, as there was a maximum total request size for each download request, we split each fire region into 32×32 pixel tiles that are downloaded individually and then stitched together into the full region image. For the near-real-time monitoring of the fires using our Python code, the post-fire time window can be shortened to select a single image that will be available in less than 6-days after the event, following the best revisit time using both Sentinel-2A and Sentinel-2B. In this case, if clouds and shadows or dense smoke plumes are present over the burned region, the results will be compromised. This is a limitation of any near-real-time application for burned areas.

We note that this approach can also be applied to Landsat data to study events prior to mid-2015 (the date Sentinel 2A became operational). We plan to add this functionality to the Python package in a future update.

3.3.2.4 Model and Training

To generate the 10 m burned area maps from Sentinel-2 data and the coarse mask derived from VIIRS data, we used a deep learning model that is defined and trained for such purpose. This sequence of processes (see **Figure 3.9**) is described in detail in **sections 3.3.2.4.1 to 3.3.2.4.3**.

3.3.2.4.1 Create Dataset

To train the model we prepared a dataset consisting of events for western Iberia (see **Table 3.9**). For each event, the Sentinel-2 data was downloaded using the procedure described in **section 3.3.2.3**. Since the model training requires batches of data with identically-sized images and the total size is limited by the 8 GB memory of the GPU used for training, large images were cropped into 512x512 tiles, corresponding to regions of about 5x5 km. Smaller-sized images were interpolated to fill-in the full 512x512 tiles.

To train the model with supervision we also needed target data. To generate the targets, we used a semi-automatic approach making use of the pre-fire to post-fire differences of the Normalized Burned Ratio (NBR), a widely used metric to map burned area and estimate burn severity (e.g., Cocke et al. 2005, Miller and Thode 2007, Quintano et al. 2018). The approach consisted of the following steps:

1. NBR was computed for each event using the expression NBR = (NIR − SWIR) / (NIR + SWIR);
2. The difference between prefire and postfire NBR (dNBR) was computed;
3. The median dNBR was then computed inside and outside the coarse burned mask, using the BA-Net product;
4. The dNBR threshold to define the burned region was defined for each event as the mean point between the two medians of step 3;
5. The resulting mask was cleaned using the method described in **section 3.3.2.2** with a spatial buffer of 10 pixels, a minimum pixel size of 100 and keeping only the burned regions representing at least 10% of the total burned area of each event. The choice of the buffer size, minimum pixel size and the 10% criteria was done by visual interpretation with the goal of removing any existing noise around the main burned patch;
6. Finally, each mask was evaluated visually, together with dNBR data, and events looking “unnatural” were discarded.

This procedure resulted in 3188 input/target pairs of data.

We note that the target masks do not need to be absolutely accurate since the deep learning models, like the one we used (described in the next section), are robust to some degree of random noise (Rolnick et al. 2017). Indeed, during optimization, the model learned how to link the input data to the burned area maps consistently among the training samples, reflecting the spectral patterns associated with burned areas. We stress that users of our Python package do not need to repeat this process as the pre-trained models are provided together with the code.

3.3.2.4.2 Define Model

The deep learning model defined to tackle this problem is represented in **Figure 3.11** where numbers in parenthesis indicate the number of input features (left) and the number of output features (right). The ConvLayer is a 2D convolution operation with kernel-size 3x3 and no bias term, followed by a 2D batch normalization (Ioffe et al. 2015) and a Rectified Linear Unit (ReLU, Nair et al. 2010) activation. The rationale for the ConvLayer is that the convolution operation captures local contextual information of close neighbouring pixels, followed by a normalization step that ensures that the data distribution remains with an average close to zero and standard deviation close to one to stabilize the training process in multi-layer models, and finally, the rectified linear unit is a commonly used activation function, consisting of setting all negative values to zero and in turn giving the model its non-linear characteristic. The ChannelLinear layer applies a 1D linear layer to the channel dimension (i.e., without awareness of the spatial relation of the pixels) followed by a 1D batch normalization and a ReLU activation. The rationale for the ChannelLinear layers is to combine the features at a pixel level, without any spatial awareness. This allows the model to learn non-linear combinations of the spectral features. For instance, the model could learn a spectral index with characteristics similar to the dNBR described in **section 3.3.2.4.1**, but since the parameters are learned they result in an optimized index with a 64-dimensional representation, since the number of output features for the second ChannelLinear layer is 64.

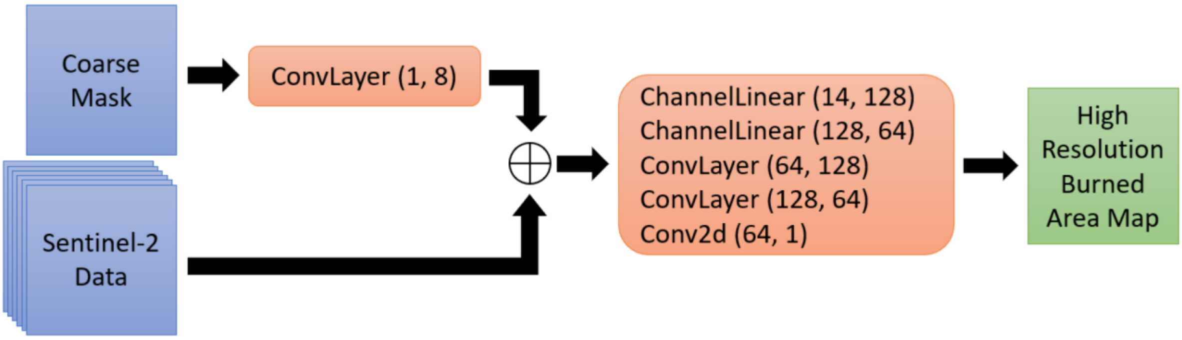

Figure 3.11. Diagram representing the model pipeline. Blue, orange, and green boxes represent inputs, neural network modules and outputs, respectively. The ⊕ symbol indicates that features are concatenated on the channel dimension. Numbers in parenthesis indicate the number of input (**left**) and output (**right**) features for the respective neural network layer.

The Coarse Mask in **Figure 3.11** is the BA-Net (**section 3.2** of this thesis) burned area map interpolated to the same projection and spatial resolution as the Sentinel-2 data and after applying a spatial moving average filter with a kernel size of 101x101 pixels (about 1x1 km) to soften the edges of the coarse mask. The output of the ConvLayer (small orange box in **Figure 3.11**) is then concatenated with the 6 input channels of the high-resolution data, corresponding to the Red, NIR and SWIR before and after the fire. The resulting tensor has a size of [batch-size, 14, 512, 512], where the batch-size is constrained by the GPU memory as will be covered in the next subsection. The layers in the large orange block in **Figure 3.11** are then applied sequentially resulting in the high resolution burned area as output, a tensor with size [batch-size, 1, 512, 512].

We also note that by allowing the model to learn an optimal combination of the input bands we can then gain some insight on which input feature has the most impact on the final result, as we will discuss in **section 3.3.3**.

3.3.2.4.3 Train Model

The model was trained using a NVIDIA GTX 1080 GPU. For training, the data were randomly split into a train and validation set with 80/20 ratio, making sure the test events were not in the train set, in order to evaluate if the model was generalizing properly. The model was trained with mixed precision (Micikevicius et al. 2017) using iterative upscaling starting with 20 epochs at 128x128 image size and batch-size of 64, followed by 20 epochs at 256x256 image size and batch-size of 16, and finally by 20 epochs at the 512x512 original image size and batch-size of 8. Starting with a smaller image size and large batch-size allowed for better stability at the beginning of training, as Batch Normalization is known to be less stable for smaller batch-sizes (Wu et al. 2018). For each scale level a one-cycle learning rate schedule (Smith 2018) was used with a maximum learning rate of 0.01 for the first cycle at 128x128 scale and dividing the maximum learning rate by the same factor as the batch-size was decreased for the two following cycles, at 256x256 and 512x512 scales respectively. The Adam optimizer (Kingma and Ba 2014) was used with a weight decay of 0.001. Image augmentations were used to increase the diversity of the dataset, as it is common practice in computer vision applications (Shorten et al. 2019). The augmentations used were the eight dihedral transformations, brightness, contrast, rotation and wrapping using the default parameters of fastai library (Howard and Gugger 2020). For a general overview of practical deep learning techniques, we recommend fastai open online courses (https://www.fast.ai, accessed on 14 April 2021).

3.3.2.5 Validation of the Six Case Studies

For the validation of the six case studies, we used burned area maps produced by the Copernicus Emergency Management Service (CEMS). The CEMS provides on-demand detailed information for several types of emergency situations, including wildfires. The service was activated for all of the six case studies we selected and therefore detailed maps of the burned areas are available. **Table 3.10** describes the details for each CEMS event. For most cases, CEMS used SPOT-6-7 1.5 m resolution data. For the “Attica Greece 2” event, CEMS used the higher resolution (0.5 m) Pleiades-1A-1B data to produce the burned area maps. We note, however, that these maps were generated as a quick response to emergency activations and that their level of detail and accuracy may have varied significantly, being dependent on the quality of the source images and on the presence of clouds and/or smoke partially obstructing the view.

Table 3.10. Description of the CEMS validation data for the six test regions.

FireID	CEMS ID	Source Name	Source Resolution	Published Time (UTC)
Portugal 1	EMSR207	SPOT-6-7/Other	1.5 m/Other	2017-06-22 19:56:12
Portugal 2	EMSR303	SPOT-6-7	1.5 m	2018-08-10 17:00:48
French Riviera 1	EMSR214	SPOT-6	1.5 m	2017-07-31 14:58:03
French Riviera 2	EMSR214	SPOT-6	1.5 m	2017-07-28 19:16:39
Attica Greece 1	EMSR300	SPOT-6-7	1.5 m	2018-07-30 17:28:17
Attica Greece 2	EMSR300	Pleiades-1A-1B	0.5 m	2018-07-26 16:38:00

For a general overview of the comparison between the two products we also computed the Commission Error (CE, equation 3.4), Omission Error (OE, equation 3.3) and Dice coefficient (equation 3.1), considering the CEMS maps as the reference. These are common metrics used to evaluate burned area products (e.g., Padilla et al. 2015, Roteta et al. 2019). The rationale for these metrics is that CE (OE) represents the fraction of false positives (negatives) over all predicted (reference) positives and the Dice (also known as F1 score) corresponds to the harmonic mean of precision and recall.

3.3.3 Results

3.3.3.1 Computation Benchmark

In this section, we will present the results and performance benchmarks for six case studies that took place in the three Mediterranean boxes considered (see **Figure 3.10** and **Table 3.9**). For all the computation benchmarks, an Intel i7-7700 CPU or a NVIDIA GTX 1080 GPU were used, running on a machine with 32 GB of RAM. After training the model with the procedure described in **section 3.3.2.4.3**, resulting Dice coefficient for the validation set was 0.97.

The first step in our pipeline, the production of the coarse masks using the BA-Net model, can take up to several hours, depending on the size of the region of study and also on the spatial resolution selected for the product. For the benchmark of the BA-Net model, we refer to Pinto et al. 2020a. Regarding the computational cost to split the fires, the process took about 1 second for French Riviera and Attica Greek regions, since the number of fires was very small. For the western Iberia region, it took about 7 min for 2017 and 2 min for 2018.

The performance benchmarks for the data acquisition and computation of the burned area maps for the six case studies are shown in **Table 3.11**. We did not include the time to produce the coarse masks in our performance benchmark, since we are only interested in evaluating the overhead time of generating the 10 m resolution maps. We assume that the coarse product is already routinely generated and provided. The most time-consuming step corresponds to the GEE download process. This step takes less than about 5 min for fires up to about 1500 ha size and, for larger fires, the time increases as expected, since the volume of data to download is significantly larger. Nevertheless, for the largest of the six case studies, a fire with 42,333 ha in central Portugal, the data were downloaded in less than an hour on average. Fires larger than 20,000 ha are rare in Mediterranean Europe and most often only occur in Portugal. The inference time to compute the high resolution burned area map is short, particularly if using a GPU (**Table 3.11** sixth column) which even for the largest fire took less than a minute to compute. For fires under 1500 ha, this step takes 1–2 s on the GPU and about 3 to 6 times more on the CPU. For example, for the 1344 ha fire with ID "French Riviera 2" (**Table 3.11** row 5), the inference time on CPU was 11 s.

Table 3.11. Benchmark results for the six test regions. Computation times are the average of seven runs for all cases but GEE Download Time, that corresponds to the average of three runs on different days.

FireID	Sentinel-2 Image Size	Sentinel-2 Data Size on Disk	GEE Download Time	Inference Time (CPU)	Inference Time (GPU)	Burned Area (ha)
Portugal 1	4733 x 4732	300 MB	51 min	152 s	50 s	42333
Portugal 2	3419 x 3418	161 MB	25 min	76 s	21 s	23868
French Riviera 1	870 x 881	9 MB	3 min	5 s	1 s	489
French Riviera 2	1315 x 1327	19 MB	4 min	11 s	2 s	1344
Attica Greece 1	2262 x 2260	62 MB	13 min	32 s	7 s	4363
Attica Greece 2	1093 x 1081	16 MB	4 min	7 s	1 s	1232

3.3.3.2 Feature Importance

To better understand the results and the trained model we computed the relative importance of each input band to the final result (**Figure 3.12**). The relative importance was measured as the decrease in Dice score of the output when the input band in x-axis was randomly shuffled compared to the score when the unchanged input data were used. When shuffling the data, water pixels were masked out to avoid mixing land and water pixels. We can see that, in general, the NIR and SWIR were the most important features (**Figure 3.12**), particularly, the post-fire NIR and SWIR followed by the pre-fire SWIR. The pre-fire NIR and coarse mask followed with a small importance variation among the six case studies, and finally, the least important feature was the red, particularly the pre-fire red. Looking in more detail at the three dominant features (post-fire SWIR and NIR and pre-fire SWIR), there were noticeable differences among the case studies. For example, while for the "Portugal 1" case the post-fire NIR was the most important feature, for the "Attica Greece 1" case, the post-fire SWIR and NIR showed the highest importance, followed by the pre-fire SWIR. There are several factors that could explain these differences. For example, a fire occurring earlier in a fire season, as is the case for "Portugal 1" event, is more likely to show a stronger drop in NIR as the vegetation is usually not as dry as later in the season. It is also worth noting that our feature importance reflects the spatial variability of the features. If the fire occurs in a perfectly uniform forest region, shuffling the pre-fire features have no impact on the result. In fact, we see that the pre-fire bands, particularly the SWIR were also important, meaning that the location of the burned shape could be to some extent identified before the fire, something that is expected especially for the fires in forest-urban interface regions where the forest-urban delimitation is usually clear in the pre-fire images.

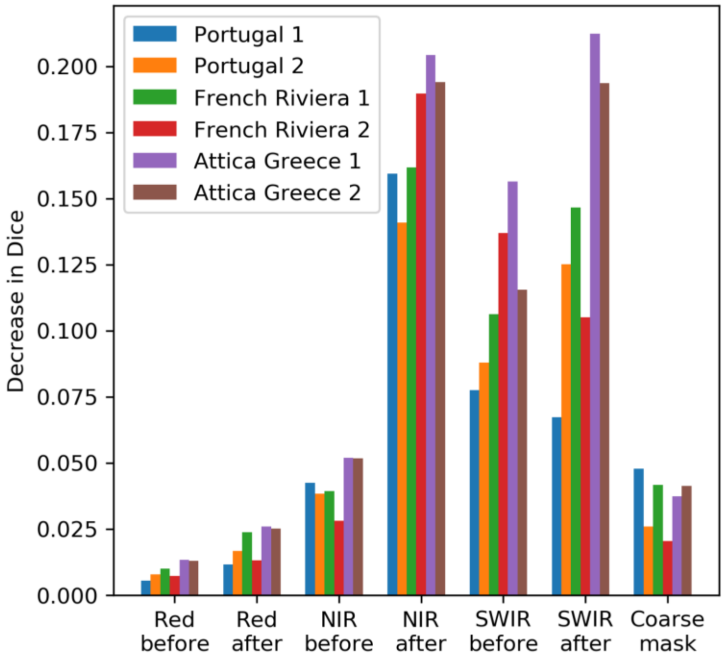

Figure 3.12. Feature importance for each input channel measured before and after the fire (x-axis) and per fire event (indicated by the top label).

3.3.3.3 Case Studies

In this section we look in detail to the six case studies, comparing our product with the CEMS maps to obtain further insight into the performance of our model. **Table 3.12** summarizes the three metrics described in **section 3.3.2.5** for each case study. Overall, the agreement between the products is very good with a Dice coefficient greater than 0.92 for all but one event.

Table 3.12. Evaluation metrics for the six test regions considering the CEMS product as the reference.

FireID	Commission Error	Omission Error	Dice
Portugal 1	0.034	0.097	0.933
Portugal 2	0.016	0.122	0.928
French Riviera 1	0.074	0.065	0.931
French Riviera 2	0.072	0.047	0.941
Attica Greece 1	0.007	0.225	0.870
Attica Greece 2	0.059	0.093	0.924

Figure 3.13 and **Figure 3.14** show the two case studies for Portugal that took place in 2017 and 2018, respectively. The first fire event (**Figure 3.13**) occurred in June 2017 in central Portugal and led tragically to a death toll of 64 people (Pinto et al. 2018b) and a total burned area of 42,333 ha. The second event (**Figure 3.14**) occurred in August 2018 in southwest Portugal, with a total burned area of 23,868 ha and mobilizing up to about 1400 firefighters and 14 aircraft and leading to 41 people injured and millions of euros of economic losses (DaCamara et al. 2019).

Figure 3.13a suggests an overall good accuracy, which was confirmed by a Dice score of 0.933 (**Table 3.12**, first row). The white patch on the northeast part of the burned area corresponds to a region not mapped by the CEMS and therefore was not considered for the computation of the evaluation metrics. Regarding the large easternmost red patch, we visually confirmed, using the Sentinel-2 data, that it corresponds to a burned region, but it was one of the latest regions to burn, likely after the CEMS analysis data, thus explaining the difference. On the remaining of the burned region (**Figure 3.13a**) we see that most differences lay in small patches within the burned region, which CEMS map attributed to burned contrary to our classification. To get some insight, we looked in detail at one of these patches (identified by a magenta square in **Figure 3.13a**) in **Figure 3.13** panels (a) to (e). Looking at panels (b) and (c), corresponding to true colour view median composites for the periods before and after the fire, respectively, we see, although not very clearly, that the green regions in panel (e) had a shift in colour from dark green to dark brown. The false colour composite in panel (d) makes it easier to appreciate this difference. Furthermore, we note that the southernmost section of this burned area was mapped with higher detail by CEMS and **Figure 3.13a** shows that the agreement between the two maps is stronger thereby suggesting that most of the differences are in part based on the detail of the analysis or the criteria for regions with a low burn severity as we will further discuss later.

Figure 3.14 shows once again a very good overall accuracy for the second case study, with a Dice coefficient of 0.928. After the green, the blue colour is the most common in **Figure 3.14a**, corresponding to regions where CEMS map assigns pixels as burned contrary to our product. The zoomed region in panels (b) to (e) shows an interesting detail with narrow burned patches captured by our product as well as by CEMS map. It is worth noting that some of the CEMS maps provide burn severity grading but since these varied among the cases, we opted to include all severity grades. As our product does not map different levels of burn severity it is expected that differences may be more frequent in low severity burn regions where the spectral difference in pre-fire to post-fire images was small, as is the case in the example presented in **Figure 3.14**.

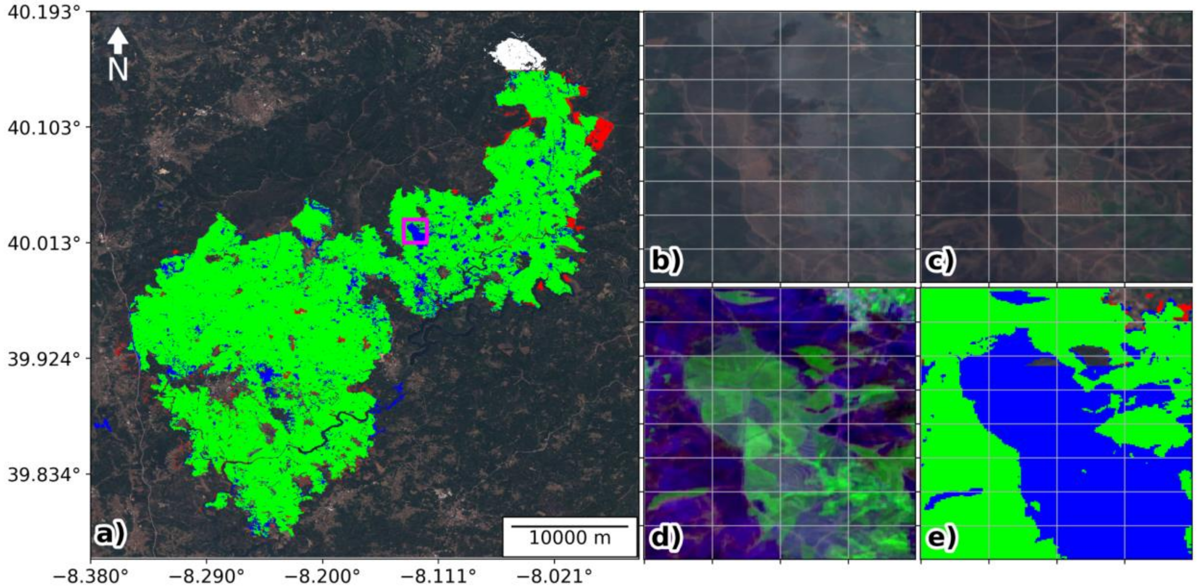

Figure 3.13. Visual analysis of "Portugal 1" fire. Panel (**a**) shows the true colour satellite view for the selected fire region together with the burned area maps derived in this study and by CEMS: green represents the pixels where both products agree; red represent burned pixels identified by this study and not by CEMS; blue corresponds to burned pixels identified by CEMS and not in this study; white pixels correspond to burned pixels outside the CEMS mapping window. Panels (**b**–**e**) correspond to the zoomed region indicated by the magenta square in panel (**a**); panels (**b**,**c**) represent the true colour view for the median composite before and after the fire, respectively; panels (**d**,**e**) show the false colour composite of pre/post-fire differences in red, NIR and SWIR and the zoomed view of panel (**a**) map, respectively.

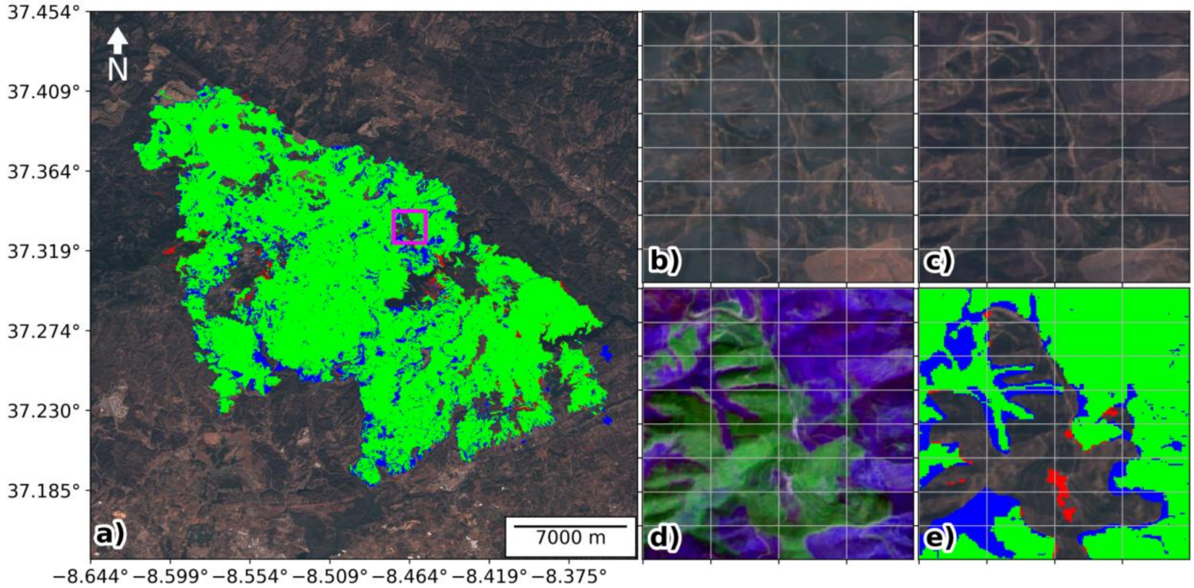

Figure 3.14. Visual analysis of "Portugal 2" fire. See **Figure 3.13** for panel descriptions.

Figure 3.15 and **Figure 3.16** show the two cases for the French Riviera in July 2017. These two fires represented a total of 489 and 1344 ha of burned area, respectively, and despite being much smaller in size compared to the examples of Portugal, they led to significant socio-economic impacts, forcing the evacuation of more than 10,000 people, according to the local press. The agreement between our product and the CEMS maps was again very good with a Dice coefficient of 0.931 and 0.941 for each case, respectively. The zoomed view in **Figure 3.15** and **Figure 3.16** b–e panels shows that the discrepancies between the two maps are mostly in the margins between burned and unburned regions. These small differences are to be expected when comparing products obtained from different satellite sensors, particularly if the raw data have different spatial resolution or view angles.

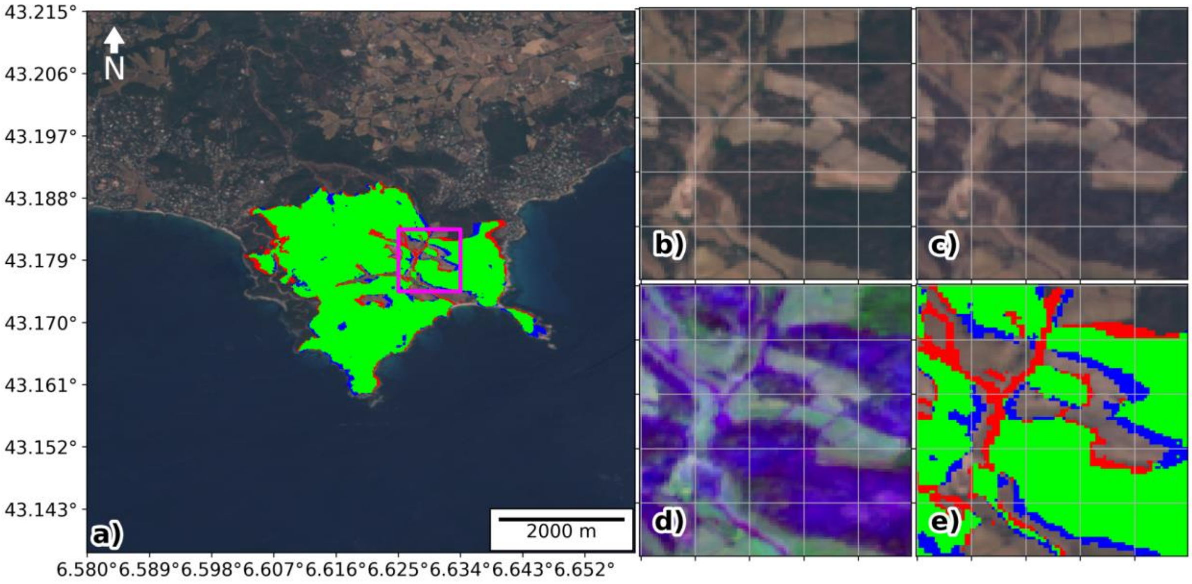

Figure 3.15. Visual analysis of "French Riviera 1" fire. See **Figure 3.13** for panel descriptions.

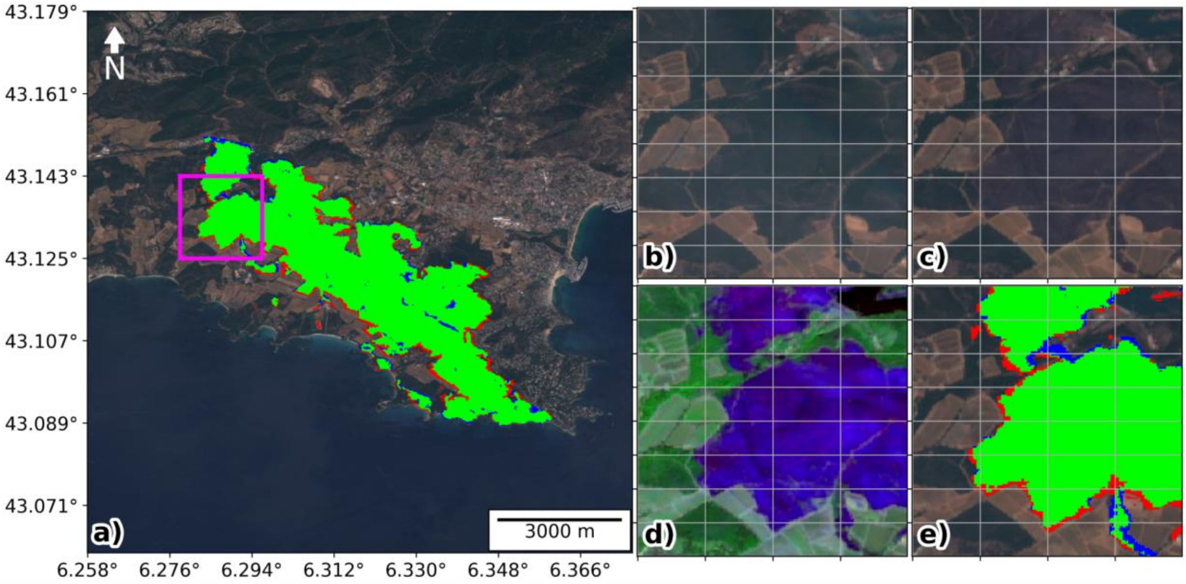

Figure 3.16. Visual analysis of "French Riviera 2" fire. See **Figure 3.13** for panel descriptions.

Figure 3.17 and **Figure 3.18** show the two cases for Attica, Greece in July 2018. The total burned area for these events was 4363 and 1232 ha, respectively. The location of the fires in wildland-urban interfaces, together with extreme weather conditions, led to the tragic outcome of 102 fatalities (Lagouvardos et al. 2019). For these two cases, we obtained a Dice coefficient of 0.870 and 0.924, respectively. Starting with the first case (**Figure 3.17**) where the discrepancy between our product and the CEMS maps was the largest of all other five case studies considered here, we first note that there is a large blue patch in the western side of the burned area, i.e., a burned scar identified by CEMS maps, contrary to our product. By visually inspecting post-fire Sentinel-2 images we found no evidence for that patch to be burned. It is most likely that this was misclassified by CEMS due to the presence of clouds in the region as observed in the CEMS data for this case study (see **Table 3.10**). Looking now at the zoomed region on **Figure 3.17** panels (b) to (e) we can see that scattered burned patches with sectors that may have burned with low or negligible severity, since in several parts they still appear in dark green colour in the post-fire true colour composite (panel c). This example illustrates well what we already mentioned in the previous case studies. Looking now at **Figure 3.18** we start by noting that the small white patch on the west side of the burned area is outside the region mapped by CEMS and was therefore not considered to compute the evaluation metrics (**Table 3.12**, last row). Focusing now on the zoomed region a high number of small gaps are clearly observed. These correspond to small clusters of houses in the path of the fire and it is, therefore, a challenging case to map the burned area. We note that for this case the CEMS used data from Pleiades-1A-1B that has a source resolution of 0.5 m. The good agreement between our product and the CEMS is an indication that our methodology can be applied not only for wildland regions but also to more challenging wildland-urban interfaces with as good accuracy, reflecting that the deep learning model described in **section 3.3.2.4.2** successfully learned the spectral patterns associated with the burned areas.

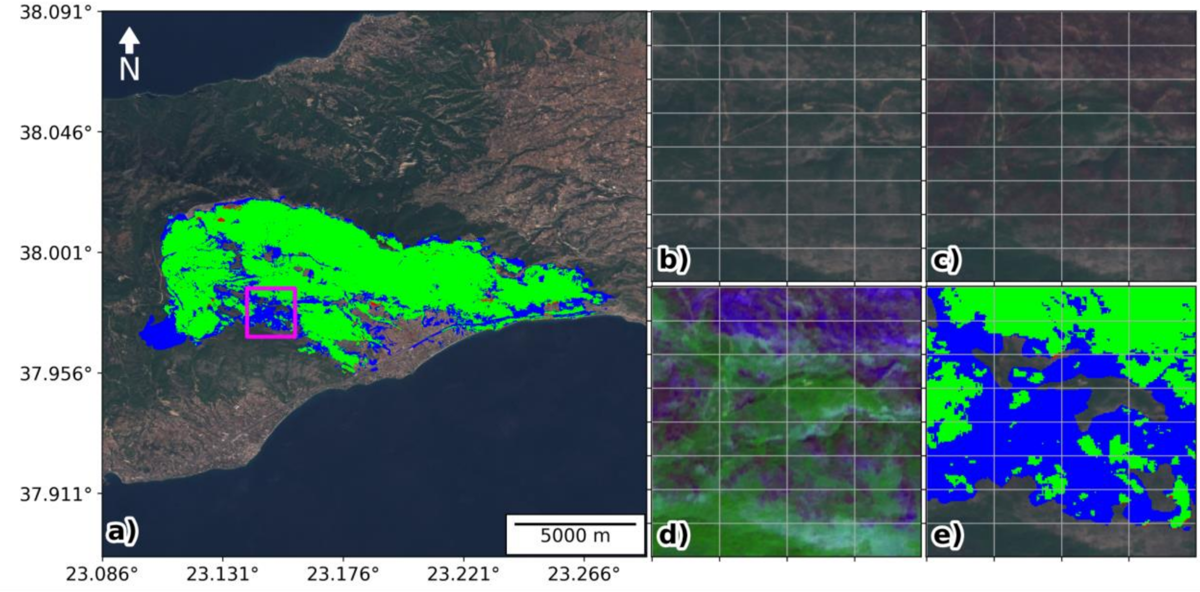

Figure 3.17. Visual analysis of “Attica Greece 1” fire. See **Figure 3.13** for panel descriptions.

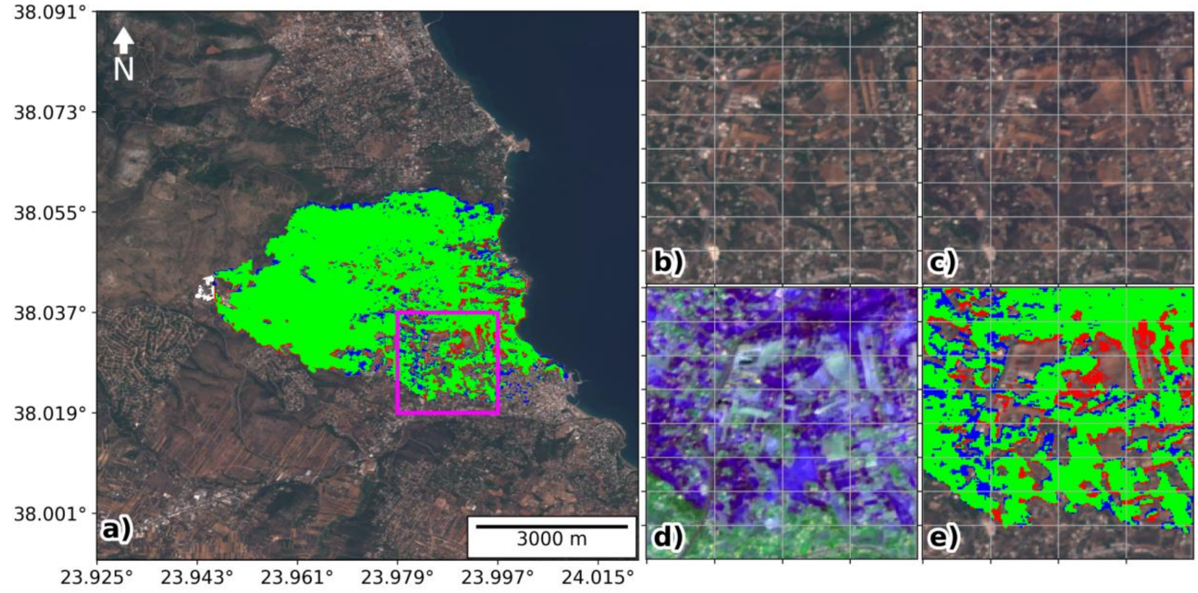

Figure 3.18. Visual analysis of “Attica Greece 2" fire. See **Figure 3.13** for panel descriptions.

3.3.4 Discussion

The target data used to train the model are produced with a semi-automatic method and do not correspond to the ground truth, since such reference data do not exist. Often a higher resolution product is used as reference to evaluate the performance of burned area products (Boschetti et al. 2009), however, data with a resolution higher than 10 m are usually not available or difficult to obtain. Therefore, the validation is restricted to the six case studies selected, for which the CEMS burned area maps are available (**Table 3.10**). Nevertheless, since the main goal of this work is to provide a fast and practical method (and yet accurate and robust) for quick monitoring of the burned regions, the comparison with CEMS is very relevant.

Regarding the input data, the coarse mask used in our pipeline is not restricted to be produced by BA-Net model. For instance, it can be manually produced based on ground observations or based on other coarse burned area products. However, the BA-Net product provides daily updates and a state-of-the-art accuracy in the date of burning, making it, to the best of our knowledge, the most appropriate choice for near-real-time applications, when compared to other fully automated products, such as MCD64A1 Collection 6 burned area product (Giglio et al. 2018a) that can only be produced with at least one month delay. For the higher resolution data, the use of GEE to create the composites and download data at the event level is a major improvement in download time, storage, and processing requirements. This contrasts with the algorithm for near-real-time mapping of burned areas using Sentinel-2 proposed by Pulvirenti et al. 2020 for Italy where data is processed at a country level.

Most existing methods for computation of high resolution burned areas are based on indices combining two or more spectral bands, usually Red, NIR and MIR or SWIR, as well as their pre-fire to post-fire difference (e.g., Escuin et al. 2007, Miller et al. 2007, Libonati et al. 2011). In our approach, we used a deep learning model that, instead, learns an optimal non-linear combination of pre-fire and post-fire Red, NIR and SWIR. Furthermore, the convolutional layers that follow allow the model to learn some spatial correlations between neighbouring pixels, instead of considering each pixel individually. This is an important component for burned area identification. Traditional algorithms to map burned areas often rely on a grid expansion method to account for the spatial factor (e.g., Stroppiana et al. 2012). We also note that our deep learning model has about 160,000 parameters, a number that is relatively small for this type of model. This results in lower memory requirements and faster computation. For instance, typical model architectures for image segmentation, like the U-Net architecture used by Knopp et al. 2020, usually have at least millions to tens of millions of parameters. Our smaller model trades off with a lower field of vision (i.e., it can only take into account close neighbouring pixels in the convolutional layers) but we note that: (1) the coarse mask we use as input was generated with a larger model (BA-Net, Pinto et al. 2020a) and therefore the task of the model we defined for this work (**Figure 3.11**) has already a spatial guideline; (2) in the identification of burned areas, the pre-fire to post-fire changes in reflectance are the dominant signal and therefore a very large field of vision is unlikely to be necessary for most situations. This contrasts with other applications of computer vision, where large complex objects need to be identified.

The two main limitations of the methodology proposed are: (1) very small fires may not be captured by the coarse burned area product used as input; (2) for regions where cloud cover is very frequent it may take longer to have clear sky images and therefore the near-real-time mapping is compromised for these situations. These limitations can possibly be addressed in future works by combining multiple input sensors in a single model, in particular through the inclusion of Synthetic Aperture Radar data that is capable of penetrating clouds and smoke (Ban et al. 2020). Finally, future research on high resolution burned areas would benefit from detailed ground or drone observations for calibration and validation of the models. This is particularly relevant to generate very high resolution burned severity maps where information at single tree scale may be relevant.

3.3.5 Conclusions

Forest fires have long been part of the Mediterranean landscape and will continue to be so in the future. Climate change only worsens this problem as the meteorological conditions for severe fires become more and more likely in a warming scenario (Turco et al. 2018, Ruffault et al. 2020). In this context, having the tools for a timely high-resolution assessment of the burned areas is of paramount importance. Satellite data are now openly available allowing anyone to access high-quality data. Powerful computational tools, such as the Google Earth Engine (GEE), make the visualization and processing of high volumes of data feasible. Our proposed method corresponds to a fast and yet reliable tool, suited for monitoring of burned areas with 10m resolution, leveraging the functionalities of GEE as a data acquisition and pre-processing tool to obtain input data to then feed to a deep learning model that outputs the burned area map. This methodology can generate a burned map for a 1500 ha fire in about 5 min, using about 25 MB of storage on disk and running inference on a computer with an 8-core processor and 8 GB of RAM. This is important for researchers, forest managers, or any entity interested in studying or evaluating the impacts of wildland fires. We showed in this work, six case studies as examples of the application of the proposed methodology. A visual evaluation of the maps produced by our model and the validation using maps produced by the CEMS shows how our model successfully captures the fine details of the burned areas that cannot be observed in coarse-resolution products. This is especially noticeable in fires occurring in wildland-urban interfaces where the fine spatial resolution is decisive to identify small clusters of houses. By using a deep learning model that maps the pre-fire and post-fire Red, NIR and SWIR bands, together with the coarse resolution mask, to the final 10 m resolution burned map, we can then study how each input band affects the result on the trained model. The results show that, as expected, the NIR and SWIR bands are the most important spatial features. On average post-fire NIR shows the highest importance, followed by post-fire SWIR, pre-fire SWIR and pre-fire NIR. There are however differences among the case studies that are likely due to the spatial and temporal context in which the fire occurred. Finally, this work is a step towards a fully automated procedure to produce high resolution burned areas in near-real-time over an extended region with a feasible computational cost. Once again, the code to our methodology is provided as a Python package, ready to apply to new cases, at https://github.com/mnpinto/FireHR, accessed on 14 April 2021.

3.3.6 Acknowledgements

This work was in part supported by Fundação para a Ciência e a Tecnologia, Portugal (FCT) under project FireCast (PCIF/GRF/0204/2017). Miguel M. Pinto was supported by FCT through the PhD grant PD/BD/142779/2018. Ricardo M. Trigo contribution was partially supported with funding from the European Union (EU) and in-kind funding from FCiências.ID/FCUL within the frame of the ERANET "European Research Area for Climate Services—ERA4CS" 2016 Call (INDECIS—ERA4CS—GA 690462).

3.3.7 Author Contributions

Miguel M. Pinto (MMP) wrote the paper, organized the data, developed the algorithms, and validated the results. Ricardo M. Trigo (RMT), Isabel F. Trigo (IFT) and Carlos C. DaCamara (CCD) contributed with constructive criticism and suggestions. RMT, IFT and CCD revised and edited the manuscript.

3.4 South-eastern Australian Fires of 2019–2020

3.4.1 Introduction

The 2019-2020 fire season in south-eastern Australia was unusually severe with about 7 million hectares burned between September 2019 and March 2020 causing extensive ecological and humanitarian damage (Filkov et al. 2020, Collins et al. 2021). It is estimated that these fires were likely the largest affecting the region in more than 150 years (Bowman et al. 2020). Moreover, these extreme fires occurred within a context of an unprecedented multi-year drought lasting since 2017 (King et al. 2020) which is in line with climate change trends that suggest an increase in fire risk over the region (Harris et al. 2018, Lewis et al. 2020).

As discussed in more detail in the introductory section of this chapter, mapping and dating burned areas is an important task for a range of applications such as forest management, calibration of fire danger and fire progression models, estimation of CO_2 emissions and to estimate event-level metrics such as the size, duration and speed of the fire progression.

In this section, the south-eastern Australia fires are used as a case study for: 1) comparison of BA-Net 1000m (based on VIIRS 750 m inputs) and MCD64A1 Collection 6 (Giglio et al. 2018a) products; and 2) testing BA-Net using the VIIRS 375 m bands interpolated to a resolution of about 100 m. The objective of this experiment is twofold: first, to evaluate how BA-Net performs for these important mega-fires over south-eastern Australia in comparison with MCD64A1 C6 that is a global product of reference continuously being updated; secondly, to test the generalization of the pretrained BA-Net model using the VIIRS 375 m bands as inputs instead of the 750 m bands used for training and discuss future improvement possibilities.

3.4.2 Data and Methods

The case study focuses on the south-eastern Australia region, spanning the latitudes -26° to -39° and the longitudes 146° to 154° over the period of August 2019 to April 2020. The BA-Net model (described in **section 3.2** of this thesis) was used to compute the burned areas interpolated to a 0.01° x 0.01° grid (about 1000 m) using VIIRS 750 m bands as input data as in the original work. For the product using VIIRS 375 m bands, the same model is used but a few modifications in the methodology were required. For instance, the input data consisting of Red and NIR reflectances correspond to bands I1 (centred at 0.64 μm) and I2 (centred at 0.865 μm) and MIR reflectance is derived from MIR and longwave-infrared radiances corresponding to bands I4 (centred at 3.74 μm) and I5 (centred at 11.45 μm). Moreover, regarding the VIIRS active fires product that is part of the inputs for BA-Net, the point data was first mapped onto a 0.01° x 0.01° grid, computing the sum of the fire radiative power inside each grid cell, as in the original methodology and then interpolated to the working resolution of 0.001° x 0.001° (about 100 m), the same resolution used for the input reflectances in this case. This extra step for the pre-processing of the VIIRS active fires ensures that there is no significant shift in the data distribution when compared to the data used to train the model. The two BA-Net products are hereafter referred to as BA-Net 1000 m and BA-Net 100 m, respectively. Regarding the MCD64A1 Collection 6 burned area product, data is downloaded following the instructions in the user guide (Giglio et al. 2018b) and all three products (BA-Net 1000m, BA-Net 100m and MCD64A1 C6) were interpolated to the 0.001° x 0.001° grid for easier comparison.

The validation of the spatial accuracy of the three products was performed using reference maps of fire severity obtained from the Australian Department of Agriculture, Water and the Environment (AUS GEEBAM) obtained for the states of New South Wales, Victoria and Australian Capital Territory. These maps were derived based on visual interpretation of Sentinel-2 false colour composites and provide a classification ranging from 1 to 5 where 1 means “No data”, 2 translates to unburned and 3 to 5 correspond to increasing levels of severity. The pixels classified as “no data” correspond to regions located outside the Australian National Indicative Aggregated Fire Extent Dataset (NIAFED) or the National Vegetation Information System as well as categories not representing native vegetation. Pixels classified as unburned, correspond to regions where little or no change was observed between the pre-fire and post-fire images. The reference maps were also interpolated to the 0.001° x 0.001° grid in order to perform the pixel-level accuracy assessment. The evaluation metric used to evaluate the accuracy of the products was the Dice score (equation 3.1). The performance of the products was then evaluated for different thresholds for the case of BA-Net products since the confidence level ranging from 0 to 1 is used. A comparison using different thresholds for fire severity was also performed to gain further insight into the characteristics of the three products.

3.4.3 Results

The resulting burned area maps produced by the BA-Net model using VIIRS 375m bands interpolated to a 0.001° x 0.001° grid are shown in **Figure 3.19** where the confidence level (left) and date of burning (right) are represented (see **section 3.2.2.6**). Besides the impressive extent of the burned areas, it is also worth noticing that while some of the burned areas show a gradual progression (right panel of **Figure 3.19**) others occurred within just a few days, particularly those located in the southernmost part of the region. This observation can also be made by looking at the daily burned area bar graph shown in **Figure 3.20** where we can see that the most extreme days in terms of total burned area were close to the New Year, reaching circa 500 thousand hectares mapped (twice) in a single day, corresponding predominantly to the fires in the southernmost part of the country near the frontier between the states of Victoria and New South Wales.

Figure 3.21 shows the visual comparison between the three products and the reference map, discarding pixels classified as “no data”. Green colour corresponds to pixels where the product and the reference map agree, while red and blue correspond to the false positives and false negatives, respectively. Overall, the three products have good accuracy, particularly for the mid and southern sectors, closer to the border between Victoria and New South Wales states. The northern sector reveals less accurate results with relatively large red patches present in all three products. However, MCD64A1 (right panel) presents slightly more false negatives (blue) and BA-Net 100 m (centre panel) shows several small red spots distributed across the study region. A closer inspection of the northernmost burned patch (see **Figure 3.22** and **Figure 3.23**) suggests that the commission errors of the products compared to the reference map may correspond to areas that burned but are not mapped in the reference map. For instance, the VIIRS active fires and Himawari derived Fire Radiative Power provided by the Copernicus Atmosphere Monitoring Service (CAMS) show patterns that, by visual inspection, appear to match BA-Net and MCD64A1 products better than the reference map (**Figure 3.22** bottom panels). The Sentinel-2 comparison for July 2019 and January 2020 (**Figure 3.23**) shows that most of the forest areas (dark green in the left panel) burned during this period (dark brown in the right panel). Moreover, by visual inspection of the Sentinel-2 true colour maps and the reference burned area map, it appears that there are some discrepancies that corroborate the analysis of active fire and FRP data, suggesting that the main large-scale differences between the products and the reference map result from different mapping criteria and not from limitations of the products.

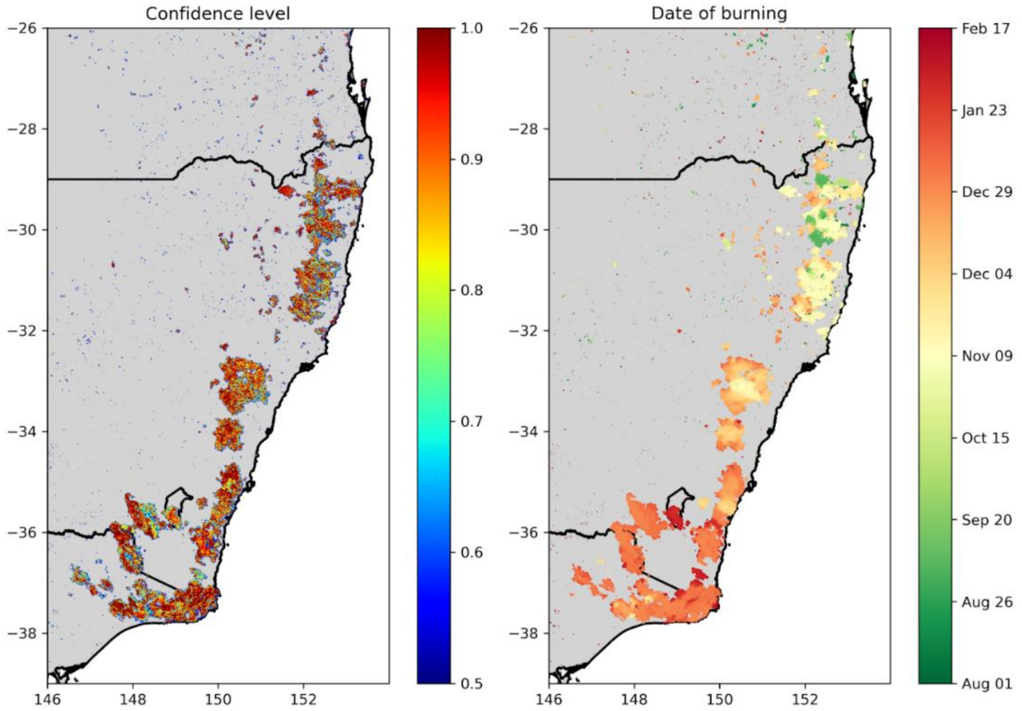

Figure 3.19. Maps of confidence level (left) and date of burning (right) obtained.

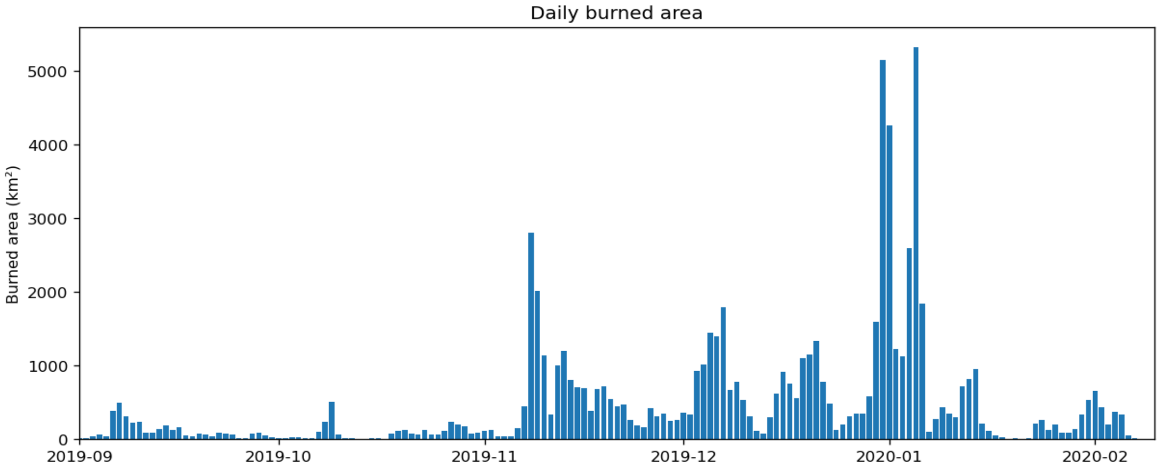

Figure 3.20. Daily burned area during the study period.

The Dice score results for each product are shown in **Figure 3.24** left panel for various thresholds. For MCD64A1 C6, however, since binary data was used, all pixels with a value greater than zero, after the interpolation, are considered as burned and therefore the green line in **Figure 3.24** left panel is perfectly horizontal. The right panel shows how the maximum Dice score varies when changing the threshold for the fire severity map and we note that BA-Net 1000 m and 100 m products show very similar performances (with different optimal thresholds), while MCD64A1 C6 slightly outperforms BA-Net products when only High and Very High severity regions are considered, suggesting that BA-Net is more sensitive to lower severity regions. Most importantly, for the Dice score considering Low/Moderate class and higher, BA-

Net 1000 m and 100 m products outperform MCD64A1 C6 classification even if a default threshold of 0.5 is used (**Figure 3.24** left panel). It is worth noting that the threshold that results in a maximum Dice for BA-Net 100 m is higher than for BA-Net 1000 m (**Figure 3.24** left panel) and this is consistent with the observation regarding the small red spots observed for BA-Net 100 m scattered across the study region that can be in part reduced by choosing a higher threshold. It is not clear if these areas were evaluated for the reference map, however, it has been observed (based on BA-Net 100 m data for the Iberian Peninsula that are not part of this case study) that BA-Net 100 m sometimes identifies burned pixels associated to cultivated regions where active fires are also detected. This suggests that BA-Net 100 m may benefit from a fine-tuning or inclusion of information about the land cover to better distinguish between agricultural and wildfire as the finer resolution of VIIRS 375 m bands is more sensitive to small burned areas. In this regard, it is worth noting that, contrary to BA-Net, the MCD64A1 C6 product uses land cover classification data that may give it some advantage to filter agricultural fires.

It is also worth noting that the difference in resolution between BA-Net 1000 m and BA-Net 100 m products cannot be well appreciated in **Figure 3.21** due to its large spatial extent but a closer look at the northernmost section of the study region shows the expected increase in detail due to the higher resolution of the input data (see **Figure 3.22** top panels).

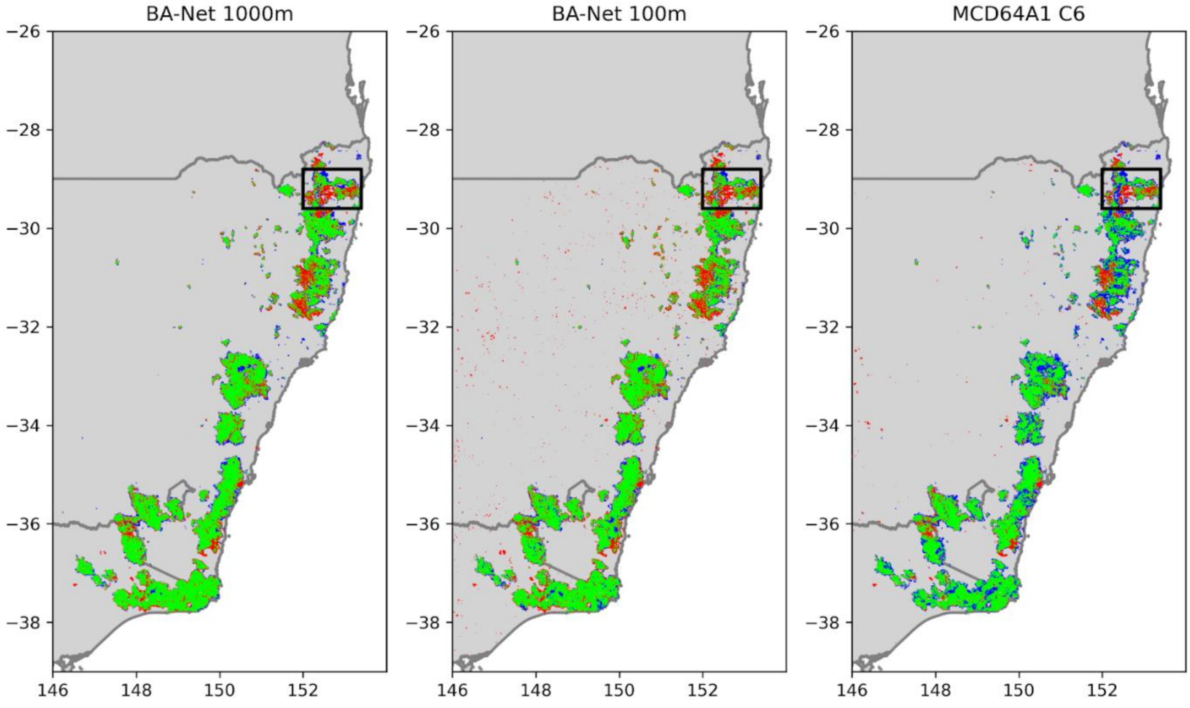

Figure 3.21. Visual comparison of BA-Net 1000m (left), BA-Net 100m (centre) and MCD64A1 C6 (right) with a reference map derived from Sentinel-2 data. Green, red and blue correspond to true positives, false positives and false negatives, respectively. The black rectangle marks a region analysed in more detail in **Figure 3.22**.

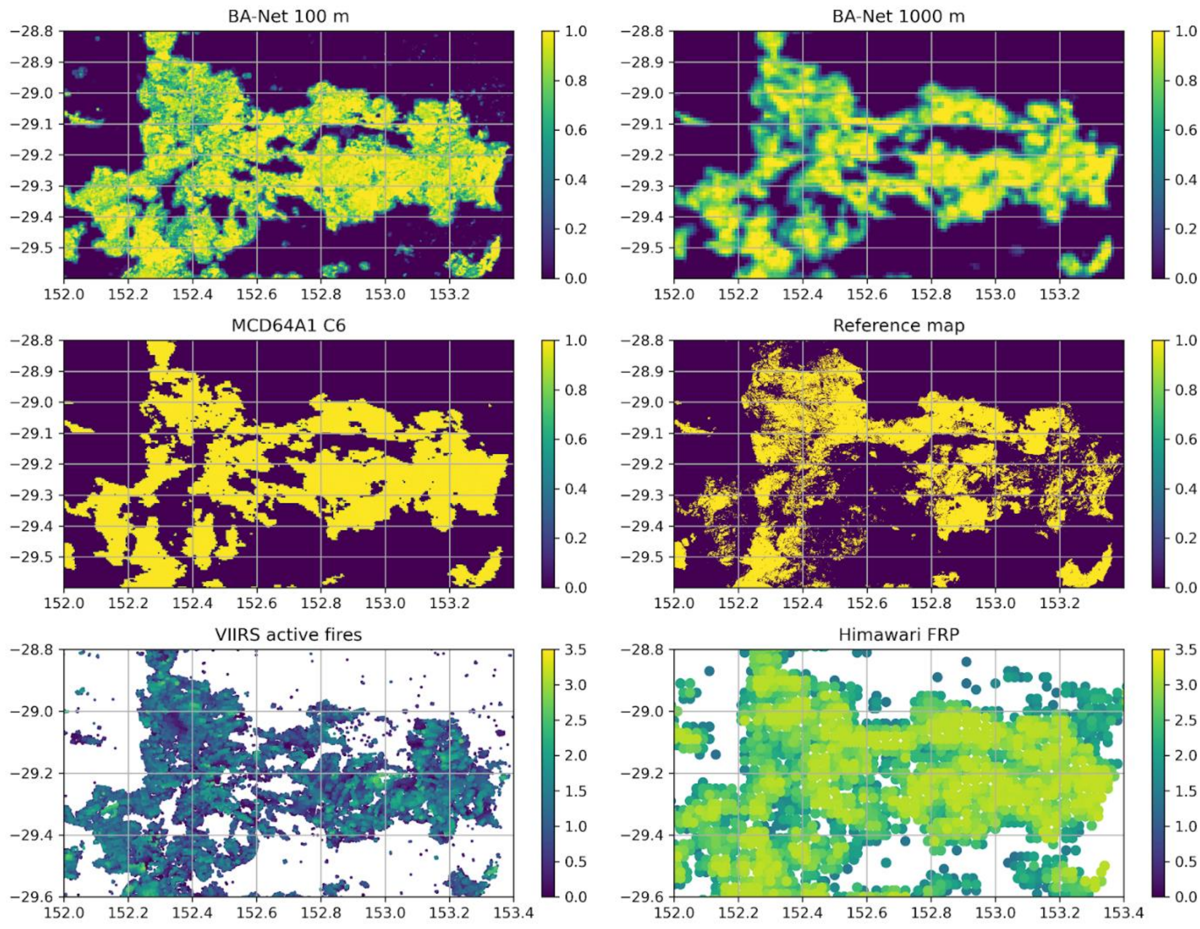

Figure 3.22. Detailed visual comparison of BA-Net 100m and BA-Net 1000m (top row), MCD64A1 C6 and the reference map derived from Sentinel-2 data (middle row) and VIIRS active fires and Himawari derived Fire Radiative Power (FPR) (bottom row) for the northernmost burned section in New South Wales. The colour range indicates the confidence level for BA-Net products and the log10(FRP) for the active fires and FRP (where FRP is in megawatts). The reference map considers pixels with at least Low/Moderate fire severity grade, as "burned". The size of the circles in the scatter plot on the bottom right panel roughly represents the coarser spatial resolution on this sensor.

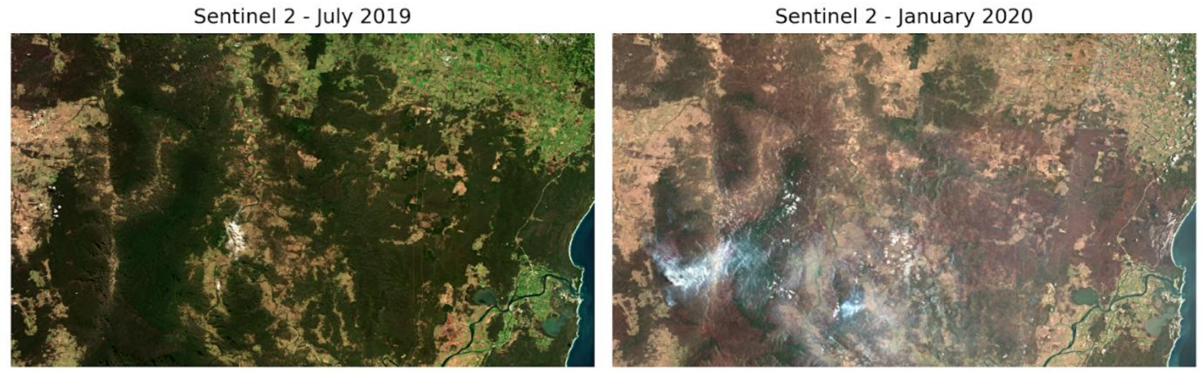

Figure 3.23. Sentinel true colour images for before (left) and after (right) the fires in the same region as shown in **Figure 3.22**.

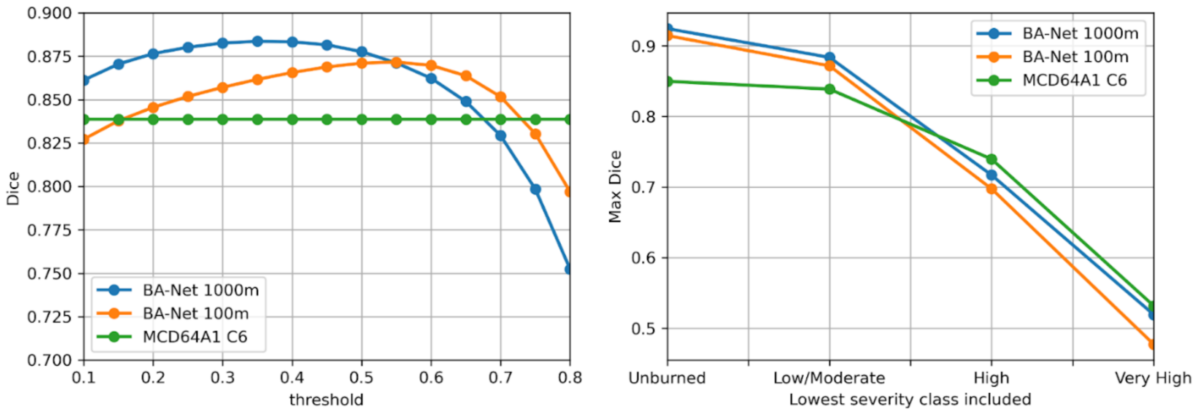

Figure 3.24. Dice scores for varying thresholds (left panel) and maximum Dice for different thresholds of fire severity (right panel) for the BA-Net 1000m (blue), BA-Net 100m (orange) and MCD64A1 C6 (green) using as reference the Sentinel-2 derived burned area maps.

3.4.4 Conclusions

Overall, the BA-Net products appear to provide slightly better accuracy for mapping the south-eastern Australia fires when compared with MCD64A1 Collection 6 product. The use of the higher resolution VIIRS bands (375 m) allows to better identify small fires and more intricate details but overall, for the case study presented, the original BA-Net product, derived from VIIRS 750 m bands, showed a slight advantage when validated against the reference data available. This is mostly due to the small false positives scattered over the study region in the BA-Net 100 m product. Evaluating the exact cause of this behaviour is beyond the goal of this case study but observations of BA-Net 100 m data for the Iberian Peninsula (not shown) suggest that those can occur within agricultural regions where sudden changes in reflectance are accompanied by active fire observations. It is also observed that MCD64A1 accuracy approximates and even surpasses BA-Net accuracy if Low/Moderate severity fire classes in the reference fire map are not considered as burned. Overall, these results suggest that a fine-tuning of BA-Net 100 m and incorporation of land cover data could improve the results by reducing the false positives in agricultural regions. For future work, it would also be of interest to investigate if changing the BA-Net output to derive fire severity classifications can provide additional useful information. Semi-supervised learning is another relevant topic for future research with the goal of reducing the amount of labelled data required to train the models.

3.5 Short-term forecasting of fire progression

3.5.1 Introduction

The capacity to forecast the short-term fire progression is important for monitoring the evolution of active fires in near-real-time. In particular, it allows for the proper planning of firefighting operations, such as assessment of the impact of fuel-breaks, and mitigation of the risks to the populations that may be caught in the fire path (Cohen and Etienne 2002, Freire et al. 2019, Mutthulakshmi et al. 2020). The direction and speed of fire line propagation critically depends on several meteorological variables, as well as the characteristics of the region such as topography and land cover types including artificial surfaces and water bodies (Rothermel et al. 1972). The existence and location of natural (e.g. rivers) or manmade (e.g. roads, power lines) features can also play an important role as they can act, not only as a fire-barrier, but also facilitate the fast access of fire fighters and heavy equipment to reach the fire or strategical locations to create artificial fuel-breaks (Laschi et al. 2019).

As discussed in more detail in the introductory section of this thesis (section 1.4), over the years several types of methods to address this problem have been considered (Sullivan 2009a, 2009b, 2009c). In this work, it is proposed an approach inspired by cellular automata, intended to frame the fire simulation as a partially supervised reinforcement learning problem. Reinforcement learning is a branch of machine learning in which one or more agents take a set of actions in an environment aiming to maximize some reward function (Sutton and Barto, 2018). In supervised learning with neural networks, the model and loss functions need to be differentiable, and every input corresponds to an output that can be compared with a target, allowing then to train the model parameters by backpropagation techniques (Alpaydin 2020). In the case of reinforcement learning, the aim is to find, by trial and error, the set of operations (i.e., the model), which achieves the best performance evaluated by a reward function. This, in turn, can make the problem more challenging to optimize than a supervised learning one. However, it must be also stressed that it allows to address problems that could be otherwise very difficult (Dulac-Arnold et al. 2019). To test the approach for fire simulation, a simple model is defined with a set of 6 parameters to be optimized for the task of forecasting the next 12h of fire progression based on reconstructions of large real fire events that occurred in Portugal during the period of 2012 to 2020. The optimization strategy used is based on the Cross-Entropy Method (Rubinstein 1997, De Boer et al. 2005) that has shown to be useful in many different optimization problems over the years (e.g.: Szita and Lörincz 2006, Botev and

Kroese 2011, Zhang et al. 2014), often combined with additional improvements to make the process more efficient (Wen and Topcu 2018, Pinneri et al. 2020). The result is a prediction of fire spread as probability maps based on the ensemble of parameters obtained for individual forecast tasks.

In the following sections the data and methods are presented (**section 3.5.2**), followed by the results (**section 3.5.3**) and the conclusions and comments regarding future improvements (**section 3.5.4**).

3.5.2 Data and Methods

This study focuses on roughly the western half of the Iberia region, delimited by the latitudes of 36° to 44° and by the longitudes of -10° to -6° during the period of 2012 to 2020. For the burned areas the BA-Net 100 m was applied, following the approach described in **section 3.2** and incorporating the modifications described in **section 3.4** regarding the use of the higher resolution bands of VIIRS. Following the procedure described in **section 3.3,** the individual fire events were identified from the BA-Net maps and the 10 m resolution burned areas computed based on Sentinel-2 data for all events greater than 2500 ha. Topography data was obtained from SRTM Digital Elevation Data Version 4 dataset (Jarvis et al. 2008) using Google Earth Engine. Both 10 m burned areas and topography maps were resampled to the 100 m BA-Net grid. The hourly Fire Weather Index (FWI) was computed using ERA5-Land weather data at the original grid of 0.1° x 0.1°, following the methodology described in **section 2.4**. As for the Continuous Haines Index (CHI) ERA5 pressure levels data was obtained corresponding to the temperature at 700 and 850 hPa and dew point temperature at 850 hPa. The hourly enhanced FWI (FWIe) was then computed following the methodology proposed in **section 2.3**. VIIRS active fire data points were also mapped to each event. For the land cover, the CORINE 2012 and 2018 datasets were used for fires in the period of 2012–2017 and 2018–2020, respectively. **Table 3.13** lists the datasets used, as well as their native spatial resolution and references. Finally, a dataset of the national road network was obtained for continental Portugal. This procedure resulted in a dataset with 82 events.

All data were interpolated to the working grid of 0.001° x 0.001° (about 100 m). Regarding the land cover, the original 45 classes were aggregated into urban areas (1 to 11), agriculture (12 to 22), forest (23 to 25), shrubs and grass (26 to 29) and “noburn” (30 to 45). For the FWIe and slope gradient data, the multiplicative scaling factors of 1/50 and 1/100 were applied, respectively, to ensure that the different variables are roughly on the same scale. Note that classical data standardization techniques could have been used instead, but due to the characteristics of the optimization process (**section 3.5.2.3**), a significant difference in the result would not be expected and hence the option of using a scaling factor for simplicity.

Table 3.13. Overview of the data used to create the dataset of events.

Name	**Data resolution**	**Reference**
BA-Net 100 m burned areas	375 m	Pinto et al. 2020a (section 3.2) and section 3.4.
FireHR 10 m burned areas	10 m	Pinto et al. 2021 (section 3.4)
SRTM Digital Elevation Data Version 4	90 m	Jarvis et al. 2008
Hourly enhanced Fire Weather Index	11 km	Pinto et al. 2020b (section 2.2) and section 2.4.
CORINE Land Cover	100 m	Copernicus Land Monitoring Servie (land.copernicus.eu/pan-european/corine-land-cover, last access 2022-01-30)
Portuguese National Road Network	NA	Portuguese National Road Network (dados.gov.pt/pt/datasets/rede-rodoviaria-nacional, last access 2022-01-30)

3.5.2.1 Reconstruction of fire progression

In order to generate reconstructions of the fire progression to use as a reference for the forecasting models, the active fire derived from VIIRS/NPP (VIIRS on-board Suomi National Polar-orbiting Partnership) data were interpolated to fill the entire burned area for each event. Note that the active fire data is available twice a day and, since 2018, FRP from VIIRS on-board JPSS-1 (Joint Polar Satellite System - 1) data is also available. Both satellites, NPP and JPSS-1, shared the same equator crossing time and, therefore, the difference in observing times between the two is usually small. Nevertheless, for the reconstruction of the events since 2018, data from both satellites have been used, as the additional information can slightly improve the results. For the interpolation of the point data to fill the entire burned area, the finite differences solution of the diffusion equation in two dimensions was used. The procedure consists of the following steps:

1. The base image $M_0 = M_0(x, y)$ is defined by applying a spatial buffer of 3 pixels around each VIIRS active fire coordinate, where the date of burning is assigned to the pixels in M_0 which are within the buffer region and the value 0 is assigned elsewhere. The date of burning is assigned as the decimal day of year (i.e.: the time of the day is encoded as the respective fraction of the day, for example, the 12h of day 200 are encoded as 200.5).
2. Iteratively apply the following update rule for each sequential integer $n \in [0, 100000]$:

$$M_{n+1}(x, y) = M_n(x, y) + \alpha\big(w * M_n(x, y)\big), \qquad \forall(x, y)\ \ s.t.\ M_0(x, y) = 0 \tag{3.6}$$

where α was set to 0.2 (it can be shown that the numerical solution is only stable for smaller than or equal to 0.25, e.g., Epperson (2021)) and the operator (*) indicates a convolution of the image M_n with the kernel w that corresponds to the discrete Laplacian operator defined as:

$$w = \begin{bmatrix} 0 & 1 & 0 \\ 1 & -4 & 1 \\ 0 & 1 & 0 \end{bmatrix} \tag{3.7}$$

3. Apply the update rule of the previous point for 100 additional iterations but removing the constraint $M_0(x, y) = 0$. These final steps without the constraint are intended to act as a smooth filter. Note that in some cases there is an overlap of active fires with consecutive observation dates that would lead to roughness in the reconstruction map within those regions.

The resulting image, after applying the procedure described above, is a smooth representation of the fire progression that is necessarily more accurate nearby VIIRS active fire observations, with uncertainty increasing for pixels located further away. It is worth noticing that, in the absence of any obstruction that makes the active fire undetected by the satellite, it is expected that the error in the date of burning should be generally smaller than the period between two consecutive observations of about 12h.

Additionally, of the 82 events described before, a manual selection was performed to remove any events in which the reconstruction may not be adequate due to limited observations or other factors (e.g., burned areas resulting from multiple smaller events without a clear direction of progression). This resulted in the removal of 17 events, and the establishment of a final set of 65 events that will be used for the experiments described in the following sections.

3.5.2.2 Simulation Environment

The fire simulation works as a particle system driven by a changing velocity vector field. The particles represent the fire line and the velocity vector field, $\vec{V} = \vec{V}(t, x, y)$, represents the parametrizations that define the speed and direction that the fire line should move based on the weather variables and accounting also for the terrain slope, land cover, road network and the position of the fire line itself.

The velocity vector field is defined as:

$$\vec{V} = \left(w_1\vec{W} + w_2\vec{S} + w_3\vec{G}\right) \times FWIe \times LandCover \tag{3.8}$$

where $\vec{W} = \vec{W}(t,x,y)$ is the wind vector field, $\vec{S} = \vec{S}(x,y)$ the slope vector field defined as the gradient of the terrain height map, $\vec{G} = \vec{G}(t,x,y)$ is the negative of the fire line gradient (i.e.: arrows point from pixels with active fire particles to pixels not burned), $FWIe = FWIe(t,x,y)$ represents the enhanced Fire Weather Index and $LandCover = LandCover(c,x,y)$ is an embedding for land cover classes (c) defined as

$$LandCover(c,x,y) = \begin{cases} 0 \; if \; c \in [1,2] \\ w_4 \; if \; c = 3 \\ w_5 \; if \; c = 4 \\ w_6 \; if \; c = 5 \end{cases} \tag{3.9}$$

where $c = 1$ corresponds to "noburn" class, $c = 2$ urban areas, $c = 3$ agricultural areas, $c = 4$ to shrublands and grasslands and $c = 5$ to forest areas. The scalar values $w_1, w_2, w_3, w_4, w_5, w_6$ are the learnable parameters of the model.

An epoch of the fire simulation for a given time t in hours consists of the following steps:

1. A set of particles are randomly sampled from pixels where the active fire matrix has values greater than 0.1.
2. The velocity vector field (equation 3.8) is computed.
3. For each particle, it is assigned the velocity vector of the respective pixel.
4. Next, the particle position is updated following the rule $p(t + \Delta t) = p(t) + \vec{V}(\mathrm{t})\Delta\mathrm{t}$, where p represents the x and y coordinates of the particle and $\Delta t = \frac{1}{steps\; per\; epoch}$ the time step.
5. The value of the active fire matrix in newly burned pixels is set to 1. Optionally, for longer forecast times, a decay rate could be used to simulate pixels where the fire is extinct.

After the epoch is complete, the fire particles are mapped to the working grid to define the updated active fire matrix and matrix with dates of burning given by the simulation. To efficiently find the grid positions of every particle, since the grid is represented with integer coordinates, and the particle floating-point values, the conversion is performed by adding 0.5 to the particle coordinates, truncating the values to integer and the result is therefore the position of the particle in the grid that can be used to sample the velocities for each particle (step 3 of the process described before).

For the results presented in **section 3.5.3**, the variable steps per epoch is set to 1 so that $\Delta t = 1$, meaning that a time-step of 1h is used. Note that for fast-moving fires the velocity can be such that the particle will cross multiple grid points and therefore choosing a large Δt does not limit the speed the fire line can travel. Nevertheless, the methodology is defined so that it allows reducing the Δt in future iterations if beneficial to improve the accuracy of the simulations.

3.5.2.3 Model training and evaluation

The optimization strategy used is based on the Cross-Entropy Method (Rubinstein 1997, De Boer et al. 2005) and the performance of the model during training is evaluated using the Dice score (equation 3.1). During training, the 65 selected events are split into 12h intervals so that the task is always to predict the next 12h following a starting point along the fire duration. For each event and for each 12h period the training process consists of the following steps:

1. An ensemble of 50 random parametrizations (population size) is randomly initialized sampling from a uniform distribution in the interval [0, 1] for parameters w_1, w_2 and w_3 and in the interval [0, 10] for parameters w_4, w_6 and w_6. Note that the population size was empirically selected to balance between diversity in the population and computational cost (i.e., larger population size corresponds to higher diversity but also higher computational cost).
2. The simulation runs for each of the 50 parameter sets and for the number of iterations necessary to achieve the 12h forecast duration (12 iterations with $\Delta t = 1$h).
3. The performance of each simulation in comparison to the reference map is calculated using the Dice score as defined in equation 3.1.
4. A new set of 50 parameterizations are generated from a normal distribution with the mean and standard deviation of the top 20% best performing parameter sets (the so-called elite-set).
5. The procedure is then repeated until the set of parametrizations converges (i.e.: the standard deviation will decrease as a maximum is approached in the optimization landscape) and the average performance of the elite-set approaches the performance of the best model in the population. This number is referred to as the number of iterations or epochs and it was set to 20 based on visual inspection of the performance metrics during the optimization.

The set of optimal parameters for each 12h slice of each event is stored as a member of the ensemble. The result after running this process for the 65 events and 12h slices of each event is an ensemble of 380 parameterizations. Note that several of the events have durations that can exceed 24h, resulting in several 12h slices for the same event.

During the forecast or evaluation phase, the simulation is computed for every parametrization of the ensemble excluding the parametrizations of the respective event. The resulting ensemble of progression maps is used to define a probability map for the expected fire progression over the 12h that follows the starting time.

The validation of the forecasted progression based on the probability maps is performed using the SoftDice (Sudre et al. 2017) defined as:

$$SoftDice = \frac{2\sum_{ij} x_{ij} y_{ij}}{\sum_{ij}\left(x_{ij} + y_{ij}\right)} \tag{3.10}$$

where x is the probability map and y the binary target map. Note that, similarly to the Dice, for two binary maps, if the prediction is perfect (i.e.: $x = y$), then equation (3.10) yields $SoftDice = 1$ since $y^2 = y$ for a binary variable. The SoftDice is computed for each 12h forecast period for each of the 65 events. The overall event score is then defined as the average of the 12h forecasts.

3.5.3 Results

Applying the methodology described in **section 3.5.2.1** the reconstruction of dates of burning is performed for the 65 events. **Figure 3.25** shows an example comparing BA-Net 100 m (left) dates of burning, the active fires map with a spatial buffer (centre) and the reconstruction (right). Note that there are some regions with no active fire observations in the central panel that are populated in the reconstruction map, as intended. In general, the reconstruction map is also smoother than the active fire map in regions where active fires were observed as the last 100 steps of the interpolation methodology (described in **3.5.2.1**), thus working as a spatial smoothing filter. Note that for the matrix shown in the central panel of **Figure 3.25**, whenever pixels with overlapping active fires with different dates were observed within the spatial buffer, the earliest date was selected.

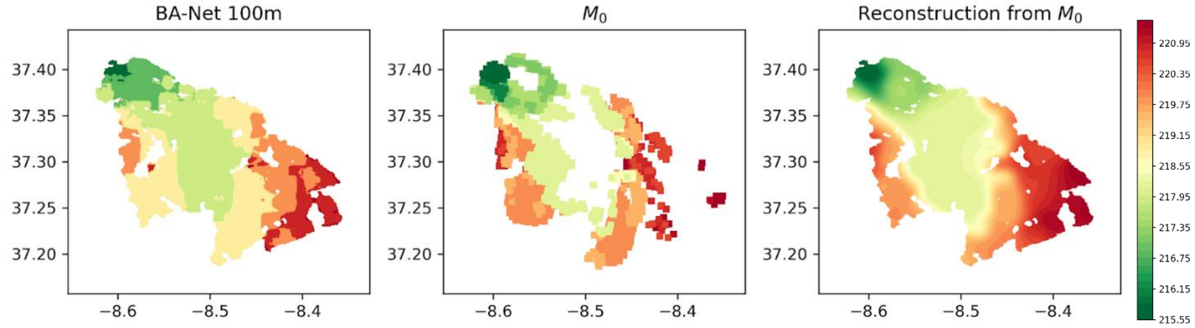

Figure 3.25. Dates of burning for the Monchique fire 2018 in south Portugal. Panels from left to right correspond to BA-Net 100 m product, the active fires with a spatial buffer, and the reconstruction using the method proposed in **section 3.5.2.1**.

Following the procedure described in **section 3.5.2.3**, the ensemble of 380 parametrizations was obtained and the corresponding histograms with the distributions of these parameters can be observed in **Figure 3.26**. Note that despite the first three parameters being initialized within the range [0, 1] and the remaining within the range [0, 10], in some simulations the optimal value was found outside that range as the optimization process does not define an upper bound to the parameter values. It is also worth observing that the forest, shrub and cultivated histograms in **Figure 3.26** (bottom row) should be interpreted as a combined effect of land cover class and the FWIe. Nonetheless, the results show that, on average, the weight for cultivated areas is smaller, followed by shrub and grass and by forest areas with average weights of 1.82, 2.93 and 2.98, respectively. This result is consistent with observations of energy released by fires in different vegetation types (Pinto et al. 2018a).

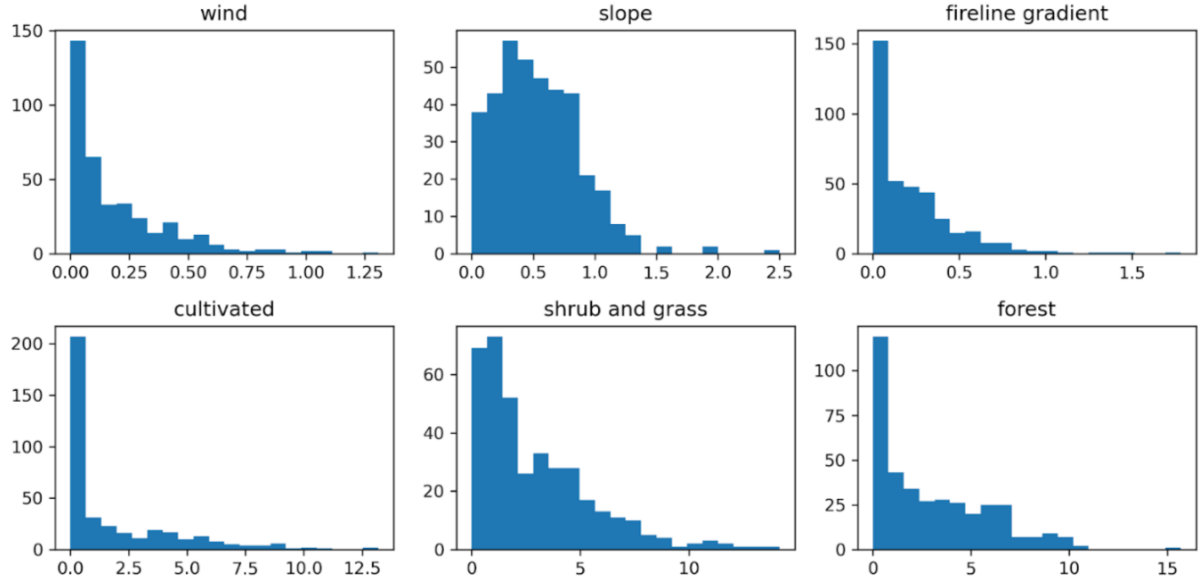

Figure 3.26. Parameter distributions for wind, slope, fire line gradient and the three vegetation categories considered (forest, shrub and cultivated) respectively as indicated above each subplot.

Using the ensemble of 380 parametrizations applied to each event (excluding the parametrizations optimized for the respective event), probability maps for the 12h forecasted fire progression are obtained for each case. The distribution of the average SoftDice score of the 65 events is shown in **Figure 3.27** with an average SoftDice of 0.24 and most events ranging between 0.1 and 0.4.

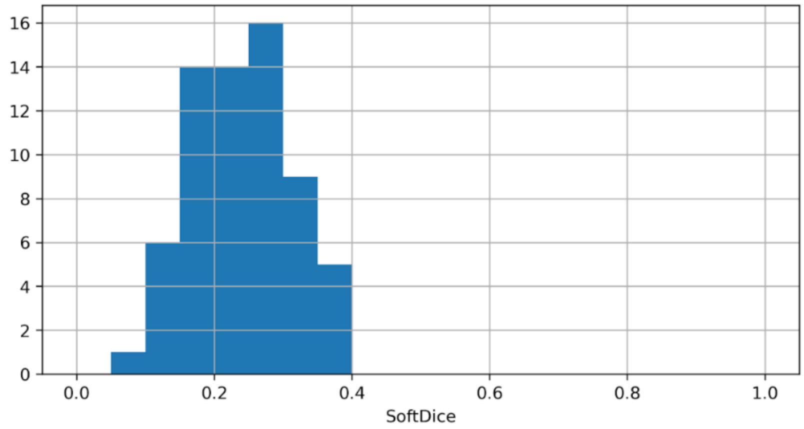

Figure 3.27. Histogram of SoftDice scores for the 65 events.

To better understand the performance of the model, three case studies are now presented. The first case study (**Figure 3.28**) corresponds to a 12h period of the 2012 Tavira fire in south Portugal, an event with a SoftDice score of 0.43. Note that the probability map (left panel) suggests that the fire will move roughly southward, being likely to burn an extensive region, since the 25% to 50% ensemble member probabilities (light green colour) suggest the extension of the burned area for more than 70 grid points southward (about 7 km). Furthermore, some of the ensemble members spread so far that they reach the limit of the study area. The reconstruction of the fire progression during this period (**Figure 3.28**, right panel) shows that indeed the fire expanded southwards, however the fire line split apart into two main branches and the right branch expanded more to the right (East) than forecasted by most of the members of the ensemble.

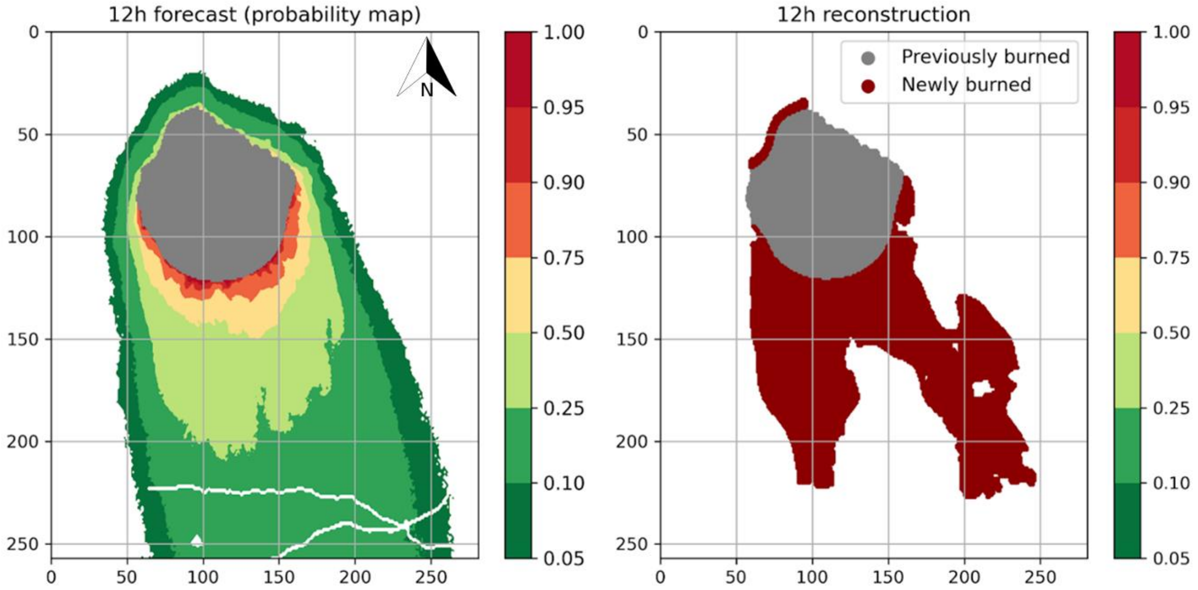

Figure 3.28. Probability map for the 12h burned area forecast (left) and reconstruction for the same period for part of the 2012 Tavira fire event in south Portugal.

For the next case study, corresponding to a large fire in the centre of Portugal in 2017 that lasted several days, the starting point of the fire is presented in **Figure 3.29**. Some of the ensemble members predict the burned area to extend further than 150 grid points (~15 km) and the observations show that indeed the fire extended quite far and in a narrow band, suggesting that it was strongly wind-driven. However, the fire progressed more to the East than forecasted resulting in a SoftDice score of just 0.14. The difference is likely explained by the real wind direction not matching exactly the wind given in the reanalysis. This is a limitation of any fire simulation model, and the problem can potentially be reduced by allowing for an uncertainty parameter applied to the input data. A real-time application of this method to assess fire progression would necessarily need to make use of numerical weather forecast fields, which generally provide fields with higher spatial resolution than ERA5 reanalysis. As an example, ECMWF currently provides forecasts with a spatial resolution of about 8 km together with an ensemble run at ~16 km resolution. Both are likely to represent local features in a more realistic way than ERA5 or ERA5-Land (forced with ERA5) near-surface wind fields, while the ensemble may be considered for uncertainty characterization.

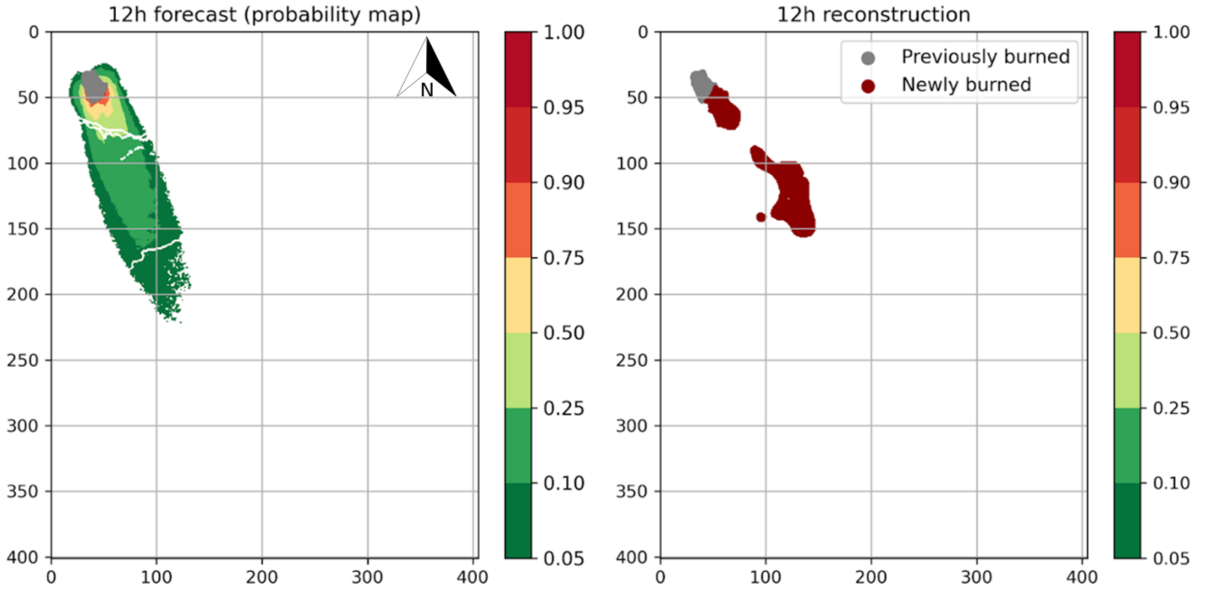

Figure 3.29. As in **Figure 3.28** but for the start of a large fire in the centre of Portugal in July 2017.

The third case study corresponds to part of the Monchique 2018 fire in south Portugal (**Figure 3.30**) with a SoftDice of 0.41. An interesting observation, in this case, is the role played by “noburn” pixels such as water bodies and roads. In particular, looking at the white region within the forecast probability map in **Figure 3.30**, near the point (200, 150), it is clear that only faster-moving fire lines in the ensemble were able to cross to the other side of the water body. This is an interesting aspect of using a particle-based approach for the expansion of the fire as fast-moving fire can cross multiple cells.

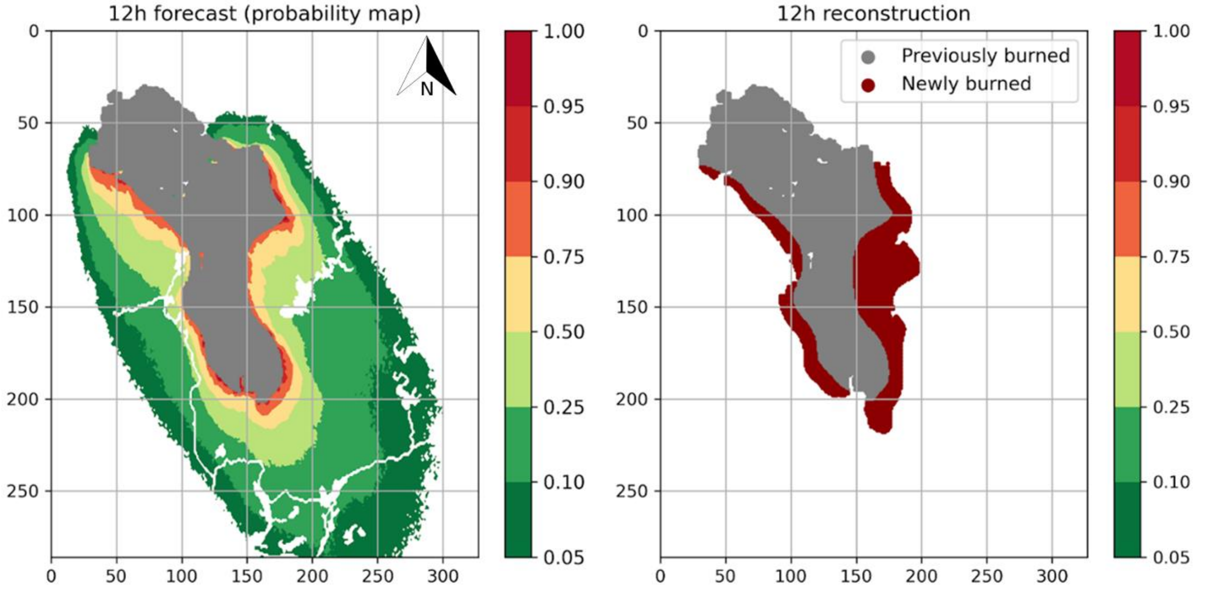

Figure 3.30. As in **Figure 3.28** but for part of the Monchique 2018 fire in south Portugal.

3.5.4 Conclusions and future work

Overall, the results presented in this section show that the developed fire simulation model is able to successfully learn the basic characteristics of the fire progression, namely how the wind direction drives the fire, how different wind speeds lead to more extended narrow fire lines and how different land covers affect the speed of the fire line. An average SoftDice of 0.24 was obtained for the 65 events considered. These results are encouraging as the basis for future work, since it is necessary to acknowledge that there are several important limitations in the current version of this work. For instance, no information about tree height or density is given, the ERA5-Land near-surface variables were linearly interpolated to the working 100 m resolution grid, and no information about fuel loads was provided. These variables are commonly used in fire simulation models and, without them, the results are certainly limited, therefore a comparison with widely used models such as FARSITE (Finney 1998) is not possible at the current state of this work. Nevertheless, the results obtained suggest that the proposed approach is promising and, despite the need for further development, it has been shown that a model with a very limited number of input variables can provide useful scenarios of fire progression.

For future work, it is expected that solving some of the data limitations described should improve the results and further suggest new aspects of improvement. In particular, WindNinja software can be used to interpolate the wind to a fine resolution accounting for the continuity and momentum conservation and slope wind (Wagenbrenner et al. 2016). Finer land cover inputs, based on higher resolution satellite data such as Sentinel-2 (10 m resolution) are also a promising direction for improvement. Ideally, LIDAR high-resolution data mapping detailed tree cover and height (Kwak et al. 2017) would be the best option, although the availability of such data is currently limited. From the optimization side, the use of a larger dataset could be beneficial, particularly if more complex models are to be tested. Larger models could also require better training strategies.

4 Final Remarks and Future Work

4.1 Final Remarks

The increasing availability of remote sensing data opens ground to new research opportunities to address a wide range of problems. The advance of technology at a fast pace provides us with new computational devices capable of processing very large volumes of data retrieved from satellite sensors orbiting the Earth. New machine learning and deep learning techniques further allow to achieve new state-of-the-art results in many problems such as pattern recognition. It is in this context that a large fraction of the work presented in this thesis was developed and the solutions proposed can be used to leverage these new innovations and to provide products that are useful and usable.

Chapter 2 of this thesis covered the general topic of meteorological fire danger. The work described in **section 2.2**, the analysis of the meteorological conditions behind two extreme fire events in central Portugal in 2017, provided insight into the combined use of the Fire Weather Index (FWI) and the Continuous Haines Index (CHI) that is a measure of atmospheric conditions that may be favourable to convective fires. This observation set the rationale for the work developed in **section 2.3**, where FWI and CHI were combined into an enhanced FWI. FWIe was constructed using the fire radiative power observed by MSG satellite as the variable to fit Generalized Pareto distributions used to define the new enhanced FWI (in a way that preserves the meaning of the values in terms of the probability of a fire becoming very intense). In **section 2.4** another important limitation of the standard FWI was addressed, namely, a formulation is proposed to extend the daily FWI to be computed on an hourly basis while maintaining compatibility with the former. This extension is important to evaluate the change in fire danger throughout the day as a result of the changing weather conditions.

Chapter 3 of this thesis covered the topic of burned area mapping and fire progression forecasting. **Section 3.2** presents a methodology that allows to map the daily progression of burned areas using, as input, sequences of VIIRS data sampled over a 1 km spatial grid, tested in several regions around the globe and resulting in state-of-the-art results for the task it was proposed. This was possible in part thanks to a deep learning model developed for the task, based on model architectures that have been proven successful in other areas of research. Another challenge in burned area mapping stems from a more intensive use of medium or high-resolution data, as the large volume of data poses some computational challenges and even more so if downloading large volumes of data from a remote server is required. To address this problem, in **section 3.3**, a general methodology was proposed to leverage the cloud computational capabilities of Google Earth Engine to select and pre-process data at an event level, reducing the volume of data required to download. The downloaded data is then processed using a deep learning model that combines the coarse mask, resulting from **section 3.2** work, with the Sentinel-2 10 m input data, to provide burned area maps with 10 m resolution for large fire events in a quick and computationally efficient way from the user standpoint. In **section 3.4**, the results of the BA-Net model described in **section 3.2** are further explored for the case study of the large fires that took place in eastern Australia in the outstanding fire season of 2019–2020. In particular, it is proposed the use of the higher resolution bands of VIIRS (375 m) and results are compared for both models (BA-Net 1000 m and BA-Net 100 m) as well as to the MCD64A1 Collection 6 product and validated using a reference map derived from medium resolution data.

Section 3.5 proposed a methodology for short-term forecasting of fire progression that is inspired by the widely used cellular automata framework but, in this case, with the problem framed as a reinforcement learning task, where the parametrizations that define the fire progression are learned based on the reconstruction of large events over Portugal. This method allows to train an ensemble of predictors that in turn can be used to generate probability maps that forecast the fire progression for a 12h period.

Most of the novel scientific results presented in this thesis have been published in international peer-reviewed scientific journals (**section 2.3**, **section 3.2**, **section 3.3**) and a conference book chapter publication (**section 2.2**):

- **Section 2.2:** Pinto, M. M., Hurduc, A., Trigo, R. M., Trigo, I. F., and DaCamara, C. C., 2018: The extreme weather conditions behind the destructive fires of June and October 2017 in Portugal, in Advances in Forest Fire Research 2018, Ed. Imprensa da Universidade de Coimbra.
- **Section 2.3:** Pinto, M. M., DaCamara, C. C., Hurduc, A., Trigo, R. M., & Trigo, I. F. (2020). Enhancing the fire weather index with atmospheric instability information. Environmental Research Letters, 15(9), 0940b7.
- **Section 3.2:** Pinto, M. M., Libonati, R., Trigo, R. M., Trigo, I. F., & DaCamara, C. C. (2020). A deep learning approach for mapping and dating burned areas using temporal sequences of satellite images. ISPRS Journal of Photogrammetry and Remote Sensing, 160, 260-274.

- **Section 3.3:** Pinto, M. M., Trigo, R. M., Trigo, I. F., & DaCamara, C. C. (2021). A Practical Method for High-Resolution Burned Area Monitoring Using Sentinel-2 and VIIRS. Remote Sensing, 13(9), 1608.

Furthermore, the following peer-reviewed publication was not presented in this thesis as the work was developed prior to the onset of my doctoral program

- Pinto, M. M., DaCamara, C. C., Trigo, I. F., Trigo, R. M., & Turkman, K. F. (2018). Fire danger rating over Mediterranean Europe based on fire radiative power derived from Meteosat. Natural Hazards and Earth System Sciences, 18(2), 515-529.

This publication provides the first insights into using the fire radiative power derived from MSG as covariates of Generalized Pareto distributions to assess probabilities of exceedance of predefined thresholds of energy released by the fires, an idea that was used and further extended in the work presented in **section 2.3**.

In line with a goal of making the methodologies accessible and usable, code has been made available to make easy to use the models and methods described in the three peer-reviewed articles (**sections 2.3**, **3.2** and **3.3** of this thesis). These packages can be found at the following addresses, respectively:

- https://github.com/mnpinto/FWIe (last accessed on 2022-02-25)
- https://github.com/mnpinto/banet/tree/v0.6 (last accessed on 2022-02-25)
- https://github.com/mnpinto/FireHR (last accessed on 2022-02-25)

Overall, I am confident that the results obtained and presented in this thesis provide a significant contribution to the remote sensing and wildfires scientific community, while opening interesting paths for future research on the topics described.

4.2 Future Work

Regarding the topic of fire danger, the enhancements of FWI to incorporate atmospheric instability information and to be computed at an hourly timescale unleash new research opportunities. Namely, towards a better understanding of how fire weather danger patterns are changing in a climate change scenario and to define more accurate fire danger classifications. These types of products are very useful for a wide range of users such as forest managers, firefighters, civil protection, as well as individuals and companies that perform activities in forest regions that involve fire or have the risk of causing accidental fire ignitions.

For the topic of mapping burned areas, the deep learning approaches presented, particularly the method described in **section 3.2** for mapping the daily progression of burned areas using sequences of satellite images, set a new path for the task. The use of this type of model provides several important advantages over traditional approaches. One important advantage is that it is straightforward to adapt to other satellite sensors with spectral bands in the same range (namely Red, NIR and MIR combined with active fires data), simply requiring a dataset of the new sensor for fine-tuning the model. Another advantage is that the method proposed in **section 3.2** does not require any cloud and smoke filter as the neural network is capable of learning the underlying pattern of burned areas ignoring the noise in the images. This reduces the problem of inheriting potential inaccuracies from the cloud mask to the burned area product. It also reduces the requirement of having a cloud mask product developed and validated for that particular satellite sensor before being able to develop a burned area product. This type of method is also computationally efficient for inference as they are highly parallelizable, particularly if a GPU can be used. The improved temporal consistency of the burned area maps generated with the method described in **section 3.2** can further lead to future research on the topics of deriving statistics and parameters regarding individual fire events, as well as any study for which the fine temporal accuracy of the burned areas is important.

For the general problem of mapping burned areas, future work directions to improve the temporal and spatial accuracy of the products may involve the fusion of multiple sensors with distinct spatial resolutions and possibly combining with synthetic aperture radar (e.g. Sentinel-1) sensors that can penetrate clouds and smoke, providing important information that is particularly relevant in regions with frequent cloud coverage. Semi-supervised methods for training deep neural networks are also a path to explore as the task of creating accurate human labelled burned area targets is very time-consuming.

Finally, regarding the work on fire progression, the results presented in **section 3.5** are just a starting point for the methodology proposed. Several steps can be taken to further develop the methods and improve the accuracy of the models. Namely, the inclusion of medium and high-resolution data to account for variables such as tree height, fine-grained land cover type, and estimated biomass available as fuel for the fire to burn. Another aspect of potential improvement is to use a larger dataset extended over several regions around the world and a finer temporal reconstruction of the events that may be possible to obtain by combining multiple satellite sensors such as VIIRS and Sentinel-3 that have different equator crossing times (see **Table 1.1**).

Overall, fire danger forecasting, mapping burned areas and forecasting the fire progression are intimately connected and improvements in one of the topics can lead to improvements in the others. Over time I expect the boundaries between these three topics to gradually dissipate as new artificial intelligence techniques, combined with better datasets, will make them converge into a more holistic approach to manage wildfires throughout their different stages, allowing: an effective risk assessment, a consistent management of fire propagation and fire fighting, and the assessment of post-fire impacts and fire recovery.

5 References

Abatzoglou, J. T., Williams, A. P., & Barbero, R. **(2019)**. Global emergence of anthropogenic climate change in fire weather indices. *Geophysical Research Letters*, *46*(1), 326-336. DOI: 10.1029/2018GL080959.

Alonso-Canas, I. & Chuvieco, E. **(2015)**. Global burned area mapping from ENVISAT-MERIS and MODIS active fire data. *Remote Sens. Environ. 163*, 140–152. DOI: 10.1016/j.rse.2015.03.011.

Alpaydin, E. **(2020)**. Introduction to machine learning. *MIT press.*

Alshehhi, R., Marpu, P.R., Woon, W.L. Dalla & Mura, M. **(2017)**. Simultaneous extraction of roads and buildings in remote sensing imagery with convolutional neural networks. *ISPRS J. Photogramm. Remote Sens. 130*, 139–149. DOI: 10.1016/j.isprsjprs.2017.05.002.

Amatulli, G., Camia, A., & San-Miguel-Ayanz, J. **(2013)**. Estimating future burned areas under changing climate in the EU-Mediterranean countries. *Science of the total environment*, *450*, 209-222. DOI: 10.1016/j.scitotenv.2013.02.014.

Amraoui, M., Pereira, M. G., DaCamara, C. C., & Calado, T. J. **(2015)**. Atmospheric conditions associated with extreme fire activity in the Western Mediterranean region. *Science of the total environment*, *524*, 32-39. DOI: 10.1016/j.scitotenv.2015.04.032.

Andela, N., Morton, D.C., Giglio, L., Chen, Y., Van Der Werf, G.R., Kasibhatla, P.S., DeFries, R.S., Collatz, G.J., Hantson, S., Kloster, D., Bachelet, M., Forrest, G., Lasslop, F., Li, S., Mangeon, J.R., Melton, C., Yue, C. & Randerson, D. **(2017)**. A human-driven decline in global burned area. *Science 356 (6345)*, 1356–1362. DOI: 10.1126/science.aal4108.

Andela, N., Morton, D.C., Giglio, L., Paugam, R., Chen, Y., Hantson, S., van der Werf, G.R. & Randerson, J.T. **(2019)**. The Global Fire Atlas of individual fire size, duration, speed and direction. *Earth Syst. Sci. Data 11 (2)*, 529–552. DOI: 10.5194/essd11-529-2019.

Anderson, T. W., & Darling, D. A. **(1952)**. Asymptotic theory of certain" goodness of fit" criteria based on stochastic processes. *The annals of mathematical statistics*, 193-212.

Archibald, S., & Roy, D. P. **(2009, July)**. Identifying individual fires from satellite-derived burned area data. In *2009 IEEE International Geoscience and Remote Sensing Symposium* (Vol. 3, pp. III-160). IEEE. DOI: 10.1109/IGARSS.2009.5417974.

Arnell, N. W., Freeman, A., & Gazzard, R. **(2021)**. The effect of climate change on indicators of fire danger in the UK. *Environmental Research Letters*, *16*(4), 044027. DOI: 10.1088/1748-9326/abd9f2.

AUS GEEBAM **(2020, July)**: Australian Google Earth Engine Burnt Area Map – A Rapid, National Approach to Fire Severity Mapping. *Department of Agriculture, Water and the Environment*, Canberra.

Baatz, R., Hendricks Franssen, H. J., Euskirchen, E., Sihi, D., Dietze, M., Ciavatta, S., Fennel, K., Beck, H., De Lannoy, G., Pauwels, V. R. N., Raiho, A., Montzka, C., Williams, M., Mishra, U., Poppe, C., Zacharias, S., Lausch, A., Samaniego, L., Van Looy, K., Bogena, H., Adamescu, M., Mirtl, M., Fox, A., Goergen, K., Naz, B. S., Zeng, Y. & Vereecken, H. **(2021)**. Reanalysis in Earth system science: Toward terrestrial ecosystem reanalysis. Reviews of Geophysics, 59(3), e2020RG000715. DOI: 10.1029/2020RG000715.

Balch, J. K., Abatzoglou, J. T., Joseph, M. B., Koontz, M. J., Mahood, A. L., McGlinchy, J., Cattau, M. E. & Williams, A. P. **(2022)**. Warming weakens the night-time barrier to global fire. Nature, 602(7897), 442-448. DOI: 10.1038/s41586-021-04325-1.

Ban, Y., Zhang, P., Nascetti, A., Bevington, A.R. & Wulder, M.A. **(2020)**. Near Real-Time Wildfire Progression Monitoring with Sentinel-1 SAR Time Series and Deep Learning. *Sci. Rep. 10*. DOI: 10.1038/s41598-019-56967-x.

Bastarrika, A., Chuvieco, E. & Martín, M.P. **(2011)**. Mapping burned areas from Landsat TM/ETM+ data with a two-phase algorithm: Balancing omission and commission errors. Remote Sens. Environ. 115 (4), 1003–1012. DOI: 10.1016/j.rse.2010.12.005.

Bedia, J., Herrera, S., Camia, A., Moreno, J. M., & Gutiérrez, J. M. **(2014)**. Forest fire danger projections in the Mediterranean using ENSEMBLES regional climate change scenarios. *Climatic Change*, *122*(1), 185-199. DOI: 10.1007/s10584-013-1005-z.

Benedetti, P., Ienco, D., Gaetano, R., Ose, K., Pensa, R.G. & Dupuy, S. **(2018)**. M3Fusion: a deep learning architecture for multiscale multimodal multitemporal satellite data fusion. *IEEE J. Sel. Top. Appl. Earth Obs. Remote Sens. 11 (12),* 4939–4949. 10.1109/JSTARS.2018.2876357.

Boschetti, L., Roy, D.P. & Justice, C.O. **(2009)**. International Global Burned Area Satellite Product Validation Protocol. Part I – production and standardization of validation reference data, https://lpvs.gsfc.nasa.gov/PDF/BurnedAreaValidationProtocol.pdf (accessed 2 March, 2022).

Boschetti, L., Roy, D.P., Justice, C.O. & Giglio, L. **(2010)**. Global assessment of the temporal reporting accuracy and precision of the MODIS burned area product. *Int. J. Wildl. Fire 19 (6)*, 705–709. DOI: 10.1071/WF09138.

Botev, Z. I., & Kroese, D. P. **(2011)**. The generalized cross entropy method, with applications to probability density estimation. Methodology and Computing in Applied Probability, 13(1), 1-27. DOI: 10.1007/s11009-009-9133-7.

Bowman, D. M. & Johnston, F. H. **(2005)**. Wildfire smoke, fire management, and human health. EcoHealth 2 (1), 76–80. DOI: 10.1007/s10393-004-0149-8.

Bowman, D. M., Balch, J., Artaxo, P., Bond, W. J., Cochrane, M. A., D'Antonio, C. M., DeFries, R., Johnston, F. H., Keeley, J. E., Krawchuk, M. A., Kull, C. A., Mack, M., Moritz, M. A., Pyne, S., Roos, C. I., Scott, A. C., Sodhi, N. S., Swetnam, T. W. & Whittaker, R. **(2011)**. The human dimension of fire regimes on Earth. *J. Biogeogr. 38 (12)*, 2223–2236. DOI: 10.1111/j.1365-2699.2011.02595.x.

Bowman, D. M., Williamson, G. J., Abatzoglou, J. T., Kolden, C. A., Cochrane, M. A., & Smith, A. **(2017)**. Human exposure and sensitivity to globally extreme wildfire events. *Nature ecology & evolution*, *1*(3), 1-6. DOI: 10.1038/s41559-016-0058.

Bowman, D., Williamson, G., Yebra, M., Lizundia-Loiola, J., Pettinari, M. L., Shah, S., Bradstock, R. & Chuvieco, E. **(2020)**. Wildfires: Australia needs national monitoring agency. *Nature 584*, 188-191. DOI: 10.1038/d41586-020-02306-4.

Brown, T., Leach, S., Wachter, B., & Gardunio, B. **(2020)**. The extreme 2018 northern California fire season. *Bulletin of the American Meteorological Society, 101*(1), S1-S4. DOI: 10.1175/BAMS-D-19-0275.1.

Bureau of Meteorology **(2019)**. Special Climate Statement 72—Dangerous Bushfire Weather in Spring 2019. Melbourne, Bureau of Meteorology.

Calle, A., & Casanova, J. L. **(2012)**. Forest fires and remote sensing. Earth Observation. *IntechOpen*. Rijeka, Croatia.

Campagnolo, M. L., Sun, Q., Liu, Y., Schaaf, C., Wang, Z., & Román, M. O. **(2016)**. Estimating the effective spatial resolution of the operational BRDF, albedo, and nadir reflectance products from MODIS and VIIRS. *Remote Sensing of Environment*, 175, 52-64. DOI: 10.1016/j.rse.2015.12.033.

Cardil, A., & Molina, D. M. **(2015)**. Factors causing victims of wildland fires in Spain (1980–2010). *Human and Ecological Risk Assessment: An International Journal*, *21*(1), 67-80. DOI: 10.1080/10807039.2013.871995.

Castro, R., & Chuvieco, E. **(1998)**. Modeling forest fire danger from geographic information systems. *Geocarto International*, 13(1), 15-23. DOI: 10.1080/10106049809354624.

Cheney, P., & Sullivan, A. (Eds.). **(2008)**. Grassfires: fuel, weather and fire behaviour. *Csiro Publishing*. Collingwood, Australia.

Chuvieco, E., Lizundia-Loiola, J., Pettinari, M.L., Ramo, R., Padilla, M., Tansey, K., Mouillot, F., Laurent, P., Storm, T., Heil, A., Plummer, S. **(2018)**. Generation and analysis of a new global burned area product based on MODIS 250 m reflectance bands and thermal anomalies. *Earth Syst. Sci. Data 10 (4)*, 2015–2031. DOI: 10.5194/essd-10-2015-2018.

Chuvieco, E., Mouillot, F., van der Werf, G.R., San Miguel, J., Tanasse, M., Koutsias, N., García, M., Yebra, M., Padilla, M., Gitas, I., Heil, A., Hawbaker, T.J. & Giglio, L. **(2019)**. Historical background and current developments for mapping burned area from satellite Earth observation. *Remote Sens. Environ. 225*, 45–64. DOI: 10.1016/j.rse.2019.02.013.

Chuvieco, E., Aguado, I., Salas, J., García, M., Yebra, M., & Oliva, P. **(2020)**. Satellite remote sensing contributions to wildland fire science and management. *Current Forestry Reports*, *6*(2), 81-96. DOI: 10.1007/s40725-020-00116-5.

Cocke, A. E., Fulé, P. Z., & Crouse, J. E. **(2005)**. Comparison of burn severity assessments using Differenced Normalized Burn Ratio and ground data. *International Journal of Wildland Fire*, *14*(2), 189-198. DOI: 10.1071/WF04010.

Coen, J. L., Cameron, M., Michalakes, J., Patton, E. G., Riggan, P. J., & Yedinak, K. M. **(2013)**. WRF-Fire: coupled weather–wildland fire modeling with the weather research and forecasting model. Journal of Applied Meteorology and Climatology, 52(1), 16-38. DOI: 10.1175/JAMC-D-12-023.1.

Cohen, M., Rigolot, E., & Etienne, M. **(2002)**. Modelling fuel distribution with cellular-automata for fuel-break assessment. VIEGAS, DX, 304(316), 72.

Collins, L., Griffioen, P., Newell, G., & Mellor, A. **(2018)**. The utility of Random Forests for wildfire severity mapping. Remote Sensing of Environment, 216, 374-384. DOI: 10.1016/j.rse.2018.07.005.

Collins, L., Bradstock, R. A., Clarke, H., Clarke, M. F., Nolan, R. H., & Penman, T. D. **(2021)**. The 2019/2020 mega-fires exposed Australian ecosystems to an unprecedented extent of high-severity fire. Environmental Research Letters, 16(4), 044029. DOI: 10.1088/1748-9326/abeb9e.

DaCamara, C. C., Calado, T. J., Ermida, S. L., Trigo, I. F., Amraoui, M., & Turkman, K. F. **(2014)**. Calibration of the Fire Weather Index over Mediterranean Europe based on fire activity retrieved from MSG satellite imagery. *International Journal of Wildland Fire, 23*(7), 945-958. DOI: 10.1071/WF13157.

DaCamara, C. C., Trigo, R. M., Pinto, M. M., Nunes, S. A., Trigo, I. F., Gouveia, C. M., & Rainha, M. **(2018)**. CeaseFire: a website to assist fire managers in Portugal. *Imprensa da Universidade de Coimbra*. Coimbra, Portugal.

DaCamara, C.C., Libonati, R., Pinto, M.M. & Hurduc, A. **(2019)**. Near-and middle-infrared monitoring of burned areas from space. in satellite information classification and interpretation. IntechOpen. DOI: 10.5772/intechopen.82444.

De Boer, P. T., Kroese, D. P., Mannor, S., & Rubinstein, R. Y. **(2005)**. A tutorial on the cross-entropy method. Annals of operations research, 134(1), 19-67. DOI: 10.1007/s10479-005-5724-z.

De Fauw, J., Ledsam, J.R., Romera-Paredes, B., Nikolov, S., Tomasev, N., Blackwell, S., Askham, H., Glorot, X., O’Donoghue, B., Visentin, D., van den Driessche, G., Lakshminarayanan, B., Meyer, C., Mackinder, F., Bouton, S., Ayoub, K., Chopra, R., King, D., Karthikesalingam, A., Hughes, C.O., Raine, R., Hughes, J., Sim, D.A., Egan, C., Tufail, A., Montgomery, H., Hassabis, D., Rees, G., Back, T., Khaw, P.T., Suleyman, M., Cornebise, J., Keane, P.A., Ronneberger, O. **(2018)**. Clinically applicable deep learning for diagnosis and referral in retinal disease. *Nat. Med. 24 (9)*, 1342. DOI: 10.1038/s41591-018-0107-6.

De Haan, L., Ferreira, A., & Ferreira, A. **(2006)**. Extreme value theory: an introduction (Vol. 21). New York: Springer.

de Zea Bermudez, P., & Kotz, S. **(2010)**. Parameter estimation of the generalized Pareto distribution—Part II. *Journal of Statistical Planning and Inference*, 140(6), 1374-1388. DOI: 10.1016/j.jspi.2008.11.020.

Dee, D. P., Uppala, S.M., Simmons, A. J., Berrisford, P., Poli, P., Kobayashi, S., Andrae, U., Balmaseda, M. A., Balsamo, G., Bauer, P., Bechtold, P., Beljaars, A. C. M., van de Berg, L., Bidlot, J., Bormann, N., Delson, C., Dragani, R., Fuentes, M., Geer, A. J., Haimberger, L., Healy, S. B., Hersbach, H., Hólm, E. V., Isaksen, L., Kallberg, P., Köhler, M., Matricardi, M., McNally, A. P., Monge-Sanz, B. M., Morcrette, J-J., Park, B-K., Peubey, C., de Rosnay, P., Tavolato, C., Thépaut, J-N. & Vitart F. **(2011)**. The ERA-Interim reanalysis: Configuration and performance of the data assimilation system. *Quarterly Journal of the Royal Meteorological Society 137*, 553–597. DOI: 10.1002/qj.828.

Deeming, J. E., Burgan, R. E., and Cohen, J. D. **(1977)**. The National Fire-Danger Rating System – 1978. USDA Forest Service Gen. Technical Report INT-39, Ogden, Utah, USA.

Driscoll, D.A., Lindenmayer, D.B., Bennett, A.F., Bode, M., Bradstock, R.A., Cary, G.J., Clarke, M.F., Dexter, N., Fensham, R., Friend, G., Gill, M., James, S., Kay, G., Keith, D.A., MacGregor, C., Russell-Smith, J., Salt, D., Watson James, J.E.M., Williams, R.J., York, A. **(2010)**. Fire management for biodiversity conservation: key research questions and our capacity to answer them. *Biol. Conserv. 143 (9)*, 1928–1939. DOI: 10.1016/j.biocon.2010.05.026.

Di Giuseppe, F., Pappenberger, F., Wetterhall, F., Krzeminski, B., Camia, A., Libertá, G., & San Miguel, J. **(2016)**. The potential predictability of fire danger provided by numerical weather prediction. *Journal of Applied Meteorology and Climatology*, 55(11), 2469-2491. DOI: 10.1175/JAMC-D-15-0297.1.

Di Gregorio, S., Filippone, G., Spataro, W., & Trunfio, G. A. **(2013)**. Accelerating wildfire susceptibility mapping through GPGPU. Journal of Parallel and Distributed Computing, 73(8), 1183-1194. DOI: 10.1016/j.jpdc.2013.03.014.

Dulac-Arnold, G., Mankowitz, D., & Hester, T. **(2019)**. Challenges of real-world reinforcement learning. arXiv preprint arXiv:1904.12901.

Dumoulin, V. & Visin, F. **(2016)**. A guide to convolution arithmetic for deep learning. arXiv preprint arXiv:1603.07285.

Drusch, M., Del Bello, U., Carlier, S., Colin, O., Fernandez, V., Gascon, F., Hoersch, B., Isola, C., Laberinti, P., Martimort, P., Meygret, A., Spoto, F., Sy, O., Marchese, F., Bargellini, P. **(2012)**. Sentinel-2: ESA's optical high-resolution mission for GMES operational services. *Remote Sens. Environ. 120*, 25–36. DOI: 10.1016/j.rse.2011.11.026.

Eidenshink, J., Schwind, B., Brewer, K., Zhu, Z. L., Quayle, B., Howard, S. **(2007)**. A project for monitoring trends in burn severity. Fire ecology 3 (1), 3–21. DOI: 10.4996/fireecology.0301003.

Ellis, T. M., Bowman, D. M., Jain, P., Flannigan, M. D., & Williamson, G. J. **(2021)**. Global increase in wildfire risk due to climate driven declines in fuel moisture. *Global change biology*. DOI: 10.1111/gcb.16006.

Epperson, J. F. **(2021)**. An introduction to numerical methods and analysis. John Wiley & Sons.

Escuin, S., Navarro, R., & Fernandez, P. **(2007)**. Fire severity assessment by using NBR (Normalized Burn Ratio) and NDVI (Normalized Difference Vegetation Index) derived from LANDSAT TM/ETM images. *International Journal of Remote Sensing*, *29*(4), 1053-1073. DOI: 10.1080/01431160701281072.

Fernandes, P. M., Barros, A. M., Pinto, A., & Santos, J. A. **(2016)**. Characteristics and controls of extremely large wildfires in the western Mediterranean Basin. *Journal of Geophysical Research:* Biogeosciences, 121(8), 2141-2157. DOI: 10.1002/2016JG003389.

Fernandes, P. M. **(2019)**. Variation in the Canadian fire weather index thresholds for increasingly larger fires in Portugal. Forests, 10(10), 838. DOI: 10.3390/f10100838.

Fernandez-Manso, A., Quintano, C., & Roberts, D. A. **(2016)**. Burn severity influence on post-fire vegetation cover resilience from Landsat MESMA fraction images time series in Mediterranean forest ecosystems. *Remote Sensing of Environment*, *184*, 112-123. DOI: 10.1016/j.rse.2016.06.015.

Field, R. D., Spessa, A. C., Aziz, N. A., Camia, A., Cantin, A., Carr, R., de Groot, W. J., Dowdy, A. J., Flannigan, M. D., Manomaiphiboon, K., Pappenberger, F., Tanpipat, V. & Wang, X. **(2015)**. Development of a global fire weather database. *Natural Hazards and Earth System Sciences*, 15(6), 1407-1423. DOI: 10.5194/nhess-15-1407-2015.

Filipponi, F. **(2019)**. Exploitation of Sentinel-2 Time Series to Map Burned Areas at the National Level: A Case Study on the 2017 Italy Wildfires. *Remote Sens. 11*, 622. DOI: 10.3390/rs11060622.

Filkov, A. I., Ngo, T., Matthews, S., Telfer, S., & Penman, T. D. **(2020)**. Impact of Australia's catastrophic 2019/20 bushfire season on communities and environment. Retrospective analysis and current trends. *Journal of Safety Science and Resilience*, 1(1), 44-56. DOI: 10.1016/j.jnlssr.2020.06.009.

Finney, M. A. **(1998)**. FARSITE, Fire Area Simulator--model development and evaluation (No. 4). *US Department of Agriculture, Forest Service*, Rocky Mountain Research Station.

Flannigan, M.D., Krawchuk, M.A., de Groot, W.J., Wotton, B.M., Gowman, L.M. **(2009)**. Implications of changing climate for global wildland fire. *Int. J. Wildl. Fire 18 (5),* 483–507. DOI: 10.1071/WF08187.

Freire, J.G. & DaCamara, C.C. **(2019)**. Using cellular automata to simulate wildfire propagation and to assist in fire management. *Nat. Hazards Earth Syst. Sci. 19 (1),* 169–179. DOI: 10.5194/nhess-19-169-2019.

Frey, R. A., Ackerman, S. A., Holz, R. E., Dutcher, S., & Griffith, Z. **(2020)**. The continuity MODIS-VIIRS cloud mask. Remote Sensing, 12(20), 3334. DOI: 10.3390/rs12203334.

Fujita, T. T. **(1985)**. The Downburst: Microburst and Macroburst. SMRP Research Paper 210, 112.

Ghisu, T., Arca, B., Pellizzaro, G., & Duce, P. **(2015)**. An improved cellular automata for wildfire spread. *Procedia Computer Science*, 51, 2287-2296. DOI: j.procs.2015.05.388.

Giglio, L., Van der Werf, G.R., Randerson, J.T., Collatz, G.J., Kasibhatla, P. **(2006)**. Global estimation of burned area using MODIS active fire observations. Atmos. Chem. Phys. 6 (4), 957–974. DOI: 10.5194/acp-6-957-2006.

Giglio, L., Boschetti, L., Roy, D.P., Humber, M.L., Justice, C.O. **(2018a)**. The Collection 6 MODIS burned area mapping algorithm and product. Remote Sens. Environ. 217, 72–85. DOI: 10.1016/j.rse.2018.08.005.

Giglio, L., Boschetti, L., Roy, D., Hoffmann, A. A., Humber, M., & Hall, J. V. **(2018b)**. Collection 6 modis burned area product user's guide version 1.2. NASA EOSDIS Land Processes DAAC: Sioux Falls, SD, USA.

Goodfellow, I., Bengio, Y. & Courville, A. **(2016)**. Deep Learning. MIT Press. deeplearningbook.org.

Goodwin, N.R. & Collett, L.J. **(2014)**. Development of an automated method for mapping fire history captured in Landsat TM and ETM+ time series across Queensland, Australia. Remote Sens. Environ. 148, 206–221. DOI: 10.1016/j.rse.2014.03.021.

Gorelick, N., Hancher, M., Dixon, M., Ilyushchenko, S., Thau, D. & Moore, R. **(2017)**. Google Earth Engine: Planetary-scale geospatial analysis for everyone. *Remote Sens. Environ. 202*, 18–27. DOI: 10.1016/j.rse.2017.06.031.

Gorman, C., Feng, Y., Chambers, J., Stapp, J. **(2019)**. Camp fire processed landsat 8 images, pre-fire, during-fire, post-fire. environmental system science data infrastructure for a virtual ecosystem. *Next-Gen. Ecosyst. Experim. (NGEE) Trop*. DOI: 10.15485/1512511.

Graham, A. M., Pringle, K. J., Pope, R. J., Arnold, S. R., Conibear, L. A., Burns, H., Rigby, R., Borchers-Arriagada, N., Butt, E. W., Kiely, L., Reddington, C., Spracklen, D. V., Woodhouse, M. T., Knote, C. & McQuaid, J. B. **(2021)**. Impact of the 2019/2020 Australian megafires on air quality and health. GeoHealth, 5(10), e2021GH000454. DOI: 10.1029/2021GH000454.

Graves, A., Mohamed, A.R. & Hinton, G. **(2013)**. Speech recognition with deep recurrent neural networks. In: 2013 IEEE International Conference on Acoustics, Speech and Signal Processing, Vancouver, BC, Canada, 26–31 May, pp. 6645–6649. DOI: 10.1109/ICASSP.2013.6638947.

Grimshaw, S. D. **(1993)**. Computing maximum likelihood estimates for the generalized Pareto distribution. *Technometrics*, 35(2), 185-191. DOI: 10.2307/1269663.

Haines, D. A. **(1988)**. A lower atmospheric severity index for wildland fires. *Natl Weather Dig. 13*, 23–7.

Harris, R. M., Beaumont, L. J., Vance, T. R., Tozer, C. R., Remenyi, T. A., Perkins-Kirkpatrick, S. E., Mitchell, P. J., Nicotra, A. B., McGregor, S., Andrew, N. R., Letnic, M., Kearney, M. R., Wernberg, T., Hutley, L. B., Chambers, L. E., Fletcher, M.-S. Keatley, M. R., Woodward, C. A., Williamson, G., Duke, N. C. & Bowman, D. M. J. S. **(2018)**. Biological responses to the press and pulse of climate trends and extreme events. *Nature Climate Change*, 8(7), 579-587. DOI: 10.1038/s41558-018-0187-9.

Hawbaker, T.J., Vanderhoof, M.K., Beal, Y.J., Takacs, J.D., Schmidt, G.L., Falgout, J.T., Williams, B., Fairaux, N.M., Caldwell, M.K., Picotte, J.J., Howard, S. M., Stitt, S. & Dwyer, J. L. **(2017)**. Mapping burned areas using dense time-series of Landsat data. *Remote Sens. Environ. 198*, 504–522. DOI: 10.1016/j.rse.2017.06.027.

Haynes, K., Short, K., Xanthopoulos, G., Viegas, D., Ribeiro, L. M., & Blanchi, R. **(2020)**. Wildfires and WUI fire fatalities. In: Manzello, Samuel L., ed. Encyclopedia of Wildfires and Wildland-Urban Interface (WUI) Fires. Cham, Switzerland: Springer. 16 p. DOI: 10.1007/978-3-319-51727-8_92-1.

He, K., Zhang, X., Ren, S. & Sun, J. **(2016)**. Deep residual learning for image recognition. In: Proceedings of the IEEE Conference on Computer Vision and Pattern Recognition, Las Vegas, NV, USA, 27–30 June, pp. 770–778. DOI: 10.1109/CVPR.2016.90.

Hersbach, H., Bell, B., Berrisford, P., Hirahara, S., Horányi, A., Muñoz-Sabater, J., Nicolas, J., Peubey, C., Radu, R., Schepers, D., Simmons, A., Soci, C., Abdalla, S., Abellan, X., Balsamo, G., Bechtold, P., Biavati, G., Bidlot, J., Bonavita, M., Chiara, G., Dahlgren, P., Dee, D., Diamantakis, M., Dragani, R., Flemming, J., Forbes, R., Fuentes, M., Geer, A., Haimberger, L., Healy, S., Hogan, R. J., Hólm, E., Janisková, M., Keeley, S., Laloyaux, P., Lopez, P., Lupu, C., Radnoti, G., Rosnay, P., Rozum, I, Vamborg, F., Villaume, S. & Thépaut, J. N. **(2020)**. The ERA5 global reanalysis. Quarterly Journal of the Royal Meteorological Society, 146(730), 1999-2049. DOI: 10.1002/qj.3803.

Hislop, S., Jones, S., Soto-Berelov, M., Skidmore, A., Haywood, A., & Nguyen, T. H. **(2018)**. Using landsat spectral indices in time-series to assess wildfire disturbance and recovery. *Remote sensing*, *10*(3), 460. DOI: 10.3390/rs10030460.

Hitchcock, H.C. & Hoffer, R.M. **(1974)**. Mapping a recent forest fire with ERTS-1 MSS data. 3rd Remote sensing of earth resources. *In: Third Conference on Earth and Information Analysis System*. Tullahoma, TN, 25–27 March, vol. 3. pp. 449–461.

Hochreiter, S. & Schmidhuber, J. **(1997)**. Long short-term memory. *Neural Comput. 9 (8)*, 1735–1780. DOI: 10.1162/neco.1997.9.8.1735.

Howard, J., & Gugger, S. **(2020)**. Fastai: a layered API for deep learning. *Information*, *11*(2), 108. DOI: 10.3390/info11020108.

Hu, F., Xia, G.S., Hu, J. & Zhang, L. **(2015)**. Transferring deep convolutional neural networks for the scene classification of high-resolution remote sensing imagery. *Remote Sens. 7 (11)*, 14680–14707. DOI: 10.3390/rs71114680.

Humber, M. L., Boschetti, L., Giglio, L., & Justice, C. O. **(2019)**. Spatial and temporal intercomparison of four global burned area products. *International Journal of Digital Earth*, *12*(4), 460-484. DOI: 10.1080/17538947.2018.1433727.

Ioffe, S., & Szegedy, C. **(2015, June)**. Batch normalization: Accelerating deep network training by reducing internal covariate shift. In *International conference on machine learning* (pp. 448-456). PMLR.

IPCC, **(2014)**: Climate Change 2014. Synthesis Report. Contribution of Working Groups I, II and III to the Fifth Assessment Report of the Intergovernmental Panel on Climate Change ed Core Writing Team, R. K. Pachauri and L. A. Meyer (Geneva, Switzerland: IPCC) p 151.

IPCC, **(2021)**: Climate Change 2021: The Physical Science Basis. Contribution of Working Group I to the Sixth Assessment Report of the Intergovernmental Panel on Climate Change [Masson-Delmotte, V., P. Zhai, A. Pirani, S.L. Connors, C. Péan, S. Berger, N. Caud, Y. Chen, L. Goldfarb, M.I. Gomis, M. Huang, K. Leitzell, E. Lonnoy, J.B.R. Matthews, T.K. Maycock, T. Waterfield, O. Yelekçi, R. Yu, and B. Zhou (eds.)]. Cambridge University Press. In Press.

IPMA **(2017)** Boletim Climatológico outubro 2017 Portugal continental. Instituto Português do Mar e da Atmosfera. (Lisbon).

Jain, P., Castellanos-Acuna, D., Coogan, S. C., Abatzoglou, J. T., & Flannigan, M. D. **(2021)**. Observed increases in extreme fire weather driven by atmospheric humidity and temperature. *Nature Climate Change*, 1-8. DOI: 10.1038/s41558-021-01224-1.

Jarvis, A., H.I. Reuter, A. Nelson & E. Guevara. **(2008)**. Hole-filled SRTM for the globe Version 4, available from the CGIAR-CSI SRTM 90m Database: https://srtm.csi.cgiar.org.

Jeppesen, J. H., Jacobsen, R. H., Inceoglu, F. & Toftegaard, T. S. **(2019)**. A cloud detection algorithm for satellite imagery based on deep learning. *Remote Sens. Environ. 229*, 247–259. DOI: 10.1016/j.rse.2019.03.039.

Jin, Y. & Roy, D.P. **(2005)**. Fire-induced albedo change and its radiative forcing at the surface in northern Australia. *Geophys. Res. Lett. 32 (13)*. DOI: 10.1029/2005GL022822.

Johnston, J. M., Johnston, L. M., Wooster, M. J., Brookes, A., McFayden, C., & Cantin, A. S. **(2018)**. Satellite detection limitations of sub-canopy smouldering wildfires in the North American boreal forest. Fire, 1(2), 28. DOI: 10.3390/fire1020028.

Jones, M. W., Smith, A., Betts, R., Canadell, J. G., Prentice, I. C., & Le Quéré, C. **(2020)**. Climate change increases risk of wildfires. *ScienceBrief Review*, *116*, 117.

Kampffmeyer, M., Salberg, A. B. & Jenssen, R. **(2016)**. Semantic segmentation of small objects and modeling of uncertainty in urban remote sensing images using deep convolutional neural networks. *In: Proceedings of the IEEE Conference on Computer Vision and Pattern Recognition Workshops*, Las Vegas, NV, USA, 26 June–1 July, pp. 1–9. DOI: 10.1109/CVPRW.2016.90.

Kaufman, Y.J. & Remer, L.A. **(1994)**. Detection of forests using mid-IR reflectance: an application for aerosol studies. *IEEE Trans. Geosci. Remote Sens. 32 (3)*, 672–683. DOI: 10.1109/36.29798.

Kemker, R., Salvaggio, C. & Kanan, C. **(2018)**. Algorithms for semantic segmentation of multispectral remote sensing imagery using deep learning. *ISPRS J. Photogramm. Remote Sens. 145*, 60–77. DOI: 10.1016/j.isprsjprs.2018.04.014.

King, A. D., Pitman, A. J., Henley, B. J., Ukkola, A. M., & Brown, J. R. **(2020)**. The role of climate variability in Australian drought. Nature Climate Change, 10(3), 177-179. DOI: 10.1038/s41558-020-0718-z.

Kingma, D.P., & Ba, J. **(2014)**. Adam: A method for stochastic optimization. arXiv preprint arXiv:1412.6980.

Knopp, L., Wieland, M., Rättich, M., & Martinis, S. **(2020)**. A deep learning approach for burned area segmentation with Sentinel-2 data. Remote Sensing, 12(15), 2422. DOI: 10.3390/rs12152422.

Koutsias, N., & Karteris, M. **(1998)**. Logistic regression modelling of multitemporal Thematic Mapper data for burned area mapping. International Journal of Remote Sensing, 19(18), 3499-3514. DOI: 10.1080/014311698213777.

Krikken, F., Lehner, F., Haustein, K., Drobyshev, I., & van Oldenborgh, G. J. **(2021)**. Attribution of the role of climate change in the forest fires in Sweden 2018. *Natural Hazards and Earth System Sciences*, *21*(7), 2169-2179. DOI: 10.5194/nhess-21-2169-2021.

Krizhevsky, A., Sutskever, I., & Hinton, G.E. **(2012)**. Imagenet classification with deep convolutional neural networks. In: Advances in Neural Information Processing Systems, Lake Tahoe, Nevada, 3–6 December, pp. 1097–1105.

Kumar, S., Getirana, A., Libonati, R., Hain, C., Mahanama, S. & Andela, N. **(2022)**. Changes in land use enhance the sensitivity of tropical ecosystems to fire-climate extremes. *Scientific Reports*, 12, 964. DOI: 10.1038/s41598-022-05130-0.

Kussul, N., Lavreniuk, M., Skakun, S., & Shelestov, A. **(2017)**. Deep learning classification of land cover and crop types using remote sensing data. *IEEE Geoscience and Remote Sensing Letters*, 14(5), 778-782. DOI: 10.1109/LGRS.2017.2681128.

Kwak, D. A., Lee, W. K., Lee, J. H., Biging, G. S., & Gong, P. **(2007)**. Detection of individual trees and estimation of tree height using LiDAR data. *Journal of Forest Research*, 12(6), 425-434. DOI: 10.1007/s10310-007-0041-9.

Lagouvardos, K., Kotroni, V., Giannaros, T. M., & Dafis, S. **(2019)**. Meteorological conditions conducive to the rapid spread of the deadly wildfire in eastern Attica, Greece. *Bulletin of the American Meteorological Society*, 100(11), 2137-2145. DOI: 10.1175/BAMS-D-18-0231.1.

Langmann, B., Duncan, B., Textor, C., Trentmann, J., & van der Werf, G.R. **(2009)**. Vegetation fire emissions and their impact on air pollution and climate. *Atmos. Environ. 43 (1)*, 107–116. DOI: 10.1016/j.atmosenv.2008.09.047.

Laschi, A., Foderi, C., Fabiano, F., Neri, F., Cambi, M., Mariotti, B., & Marchi, E. **(2019)**. Forest road planning, construction and maintenance to improve forest fire fighting: a review.

Croatian Journal of Forest Engineering: Journal for Theory and Application of Forestry Engineering, 40(1), 207-219.

Laurent, P., Mouillot, F., Yue, C., Ciais, P., Moreno, M.V., & Nogueira, J.M. **(2018)**. FRY, a global database of fire patch functional traits derived from space-borne burned area products. Sci. Data 5, 180132. DOI: 10.1038/sdata.2018.132.

Lawrence, M. G. **(2005)**. The relationship between relative humidity and the dewpoint temperature in moist air: A simple conversion and applications. Bulletin of the American Meteorological Society, 86(2), 225-234. DOI: 10.1175/BAMS-86-2-225.

Lecina-Diaz, J., Alvarez, A., & Retana, J. **(2014)**. Extreme fire severity patterns in topographic, convective and wind-driven historical wildfires of Mediterranean pine forests. PloS one, 9(1), e85127. DOI: 10.1371/journal.pone.0085127.

LeCun, Y., Bengio, Y., & Hinton, G. **(2015)**. Deep learning. nature, 521(7553), 436-444. DOI: 10.1038/nature14539.

Lewis, S. C., Blake, S. A., Trewin, B., Black, M. T., Dowdy, A. J., Perkins-Kirkpatrick, S. E., King, A. D., & Sharples, J. J. **(2020)**. Deconstructing factors contributing to the 2018 fire weather in Queensland, Australia. Bull. Am. Meteorol. Soc., 101, 115S-S121. DOI: 10.1175/BAMS-D-19-0144.1.

Li, H. **(2014)**. Geostationary satellites collocation (pp. 99-195). Berlin, Germany: Springer.

Libonati, R., DaCamara, C.C., Pereira, J.M.C., Peres, L.F. **(2010)**. Retrieving middle-infrared reflectance for burned area mapping in tropical environments using MODIS. Remote Sens. Environ. 114 (4), 831–843. DOI: 10.1016/j.rse.2009.11. 018.

Libonati, R., DaCamara, C. C., Pereira, J. M. C., & Peres, L. F. **(2011)**. On a new coordinate system for improved discrimination of vegetation and burned areas using MIR/NIR information. *Remote Sensing of Environment*, *115*(6), 1464-1477. DOI: 10.1016/j.rse.2011.02.006.

Libonati, R., DaCamara, C.C., Setzer, A.W., Morelli, F., Melchiori, A.E. **(2015)**. An algorithm for burned area detection in the Brazilian Cerrado using 4 µm MODIS imagery. Remote Sens. 7 (11), 15782–15803. DOI: 10.3390/rs71115782.

Liu, Y., Goodrick, S., & Heilman, W. **(2014)**. Wildland fire emissions, carbon, and climate: Wildfire–climate interactions. Forest Ecology and Management, 317, 80-96. DOI: 10.1016/j.foreco.2013.02.020.

Loepfe, L., Lloret, F., & Román-Cuesta, R. M. **(2012)**. Comparison of burnt area estimates derived from satellite products and national statistics in Europe. *International journal of remote sensing, 33*(12), 3653-3671. DOI: 10.1080/01431161.2011.631950.

Long, T., Zhang, Z., He, G., Jiao, W., Tang, C., Wu, B., Zhang, X., Wang, G., & Yin, R., **(2019)**. 30 m resolution global annual burned area mapping based on landsat images and google earth engine. *Remote Sens. 11 (5),* 489. DOI: 10.3390/rs11050489.

Ma, L., Liu, Y., Zhang, X., Ye, Y., Yin, G., Johnson, B.A. **(2019)**. Deep learning in remote sensing applications: a meta-analysis and review. *ISPRS J. Photogramm. Remote Sens. 152,* 166–177. DOI: 10.1016/j.isprsjprs.2019.04.015.

Maffei, C., & Menenti, M. **(2019)**. Predicting forest fires burned area and rate of spread from pre-fire multispectral satellite measurements. *ISPRS J. Photogramm. Remote Sens. 158*, 263–278. DOI: 10.1016/j.isprsjprs.2019.10.013.

Maggiori, E., Tarabalka, Y., Charpiat, G., & Alliez, P. **(2017)**. Convolutional neural networks for large-scale remote-sensing image classification. IEEE Trans. Geosci. Remote Sens. 55 (2), 645–657. DOI: 10.1109/TGRS.2016.2612821.

Maini, A. K., & Agrawal, V. **(2014)**. Weather satellites. *In: Satellite Technology: Principles and Applications*. Wiley Telecom. 577-613. DOI: 10.1002/9781118636459.ch12.

Mangeon, S., Field, R., Fromm, M., McHugh, C., & Voulgarakis, A. **(2016)**. Satellite versus ground-based estimates of burned area: A comparison between MODIS based burned area and fire agency reports over North America in 2007. *The Anthropocene Review, 3*(2), 76-92. DOI: 10.1177/2053019615588790.

Maranghides, A., Link, E., Hawks, S., Wilson, M., Brewer, W., Brown, C., Vihnaneck, B., & Walton, W. D. **(2021)**. A Case Study of the Camp Fire–Fire Progression Timeline Appendix C. Community WUI Fire Hazard Evaluation Framework. DOI: 10.6028/NIST.TN.2135sup.

Marcos, D., Volpi, M., Kellenberger, B., & Tuia, D. **(2018)**. Land cover mapping at very high resolution with rotation equivariant CNNs: Towards small yet accurate models. *ISPRS J. Photogramm. Remote Sens. 145,* 96–107. DOI: 10.1016/j.isprsjprs. 2018.01.021.

McArthur, A. G. (1967) Fire Behaviour in Eucalypt Forests. Commonwealth Australia Forest and Timber Bureau Leaflet Number 107 (Canberra: Australian Capital Territory).

McCaw, L., Marchetti, P., Elliott, G., & Reader, G. **(2007)**. Bushfire weather climatology of the Haines Index in southwestern Australia. Australian Meteorological Magazine, 56(2).

McElhinny, M., Beckers, J. F., Hanes, C., Flannigan, M., & Jain, P. **(2020)**. A high-resolution reanalysis of global fire weather from 1979 to 2018–overwintering the Drought Code. Earth System Science Data, 12(3), 1823-1833. DOI: 10.5194/essd-12-1823-2020.

McGuire, A.D., Melillo, J.M., Kicklighter, D.W., & Joyce, L.A. **(1995)**. Equilibrium responses of soil carbon to climate change: empirical and process-based estimates. J. Biogeogr. 785–796. DOI: 10.2307/2845980.

McRae, R. H., Sharples, J. J., Wilkes, S. R., & Walker, A. **(2013)**. An Australian pyro-tornadogenesis event. Natural Hazards, 65(3), 1801-1811. DOI: 10.1007/s11069-012-0443-7.

Meng, R., & Zhao, F. **(2017)**. Remote sensing of fire effects: A review for recent advances in burned area and burn severity mapping. *Remote Sensing of Hydrometeorological Hazards*, 261-283.

Micikevicius, P., Narang, S., Alben, J., Diamos, G., Elsen, E., Garcia, D., Ginsburg, B., Houston, M., Kuchaiev, O., Venkatesh, G., & Wu, H. **(2017)**. Mixed precision training. arXiv preprint arXiv:1710.03740.

Miller, J. D., & Thode, A. E. **(2007)**. Quantifying burn severity in a heterogeneous landscape with a relative version of the delta Normalized Burn Ratio (dNBR). *Remote Sensing of Environment*, *109*(1), 66-80. DOI: 10.1016/j.rse.2006.12.006.

Milletari, F., Navab, N., & Ahmadi, S. A. **(2016, October)**. V-net: Fully convolutional neural networks for volumetric medical image segmentation. In 2016 fourth international conference on 3D vision (3DV) (pp. 565-571). IEEE. DOI: 10.1109/3DV.2016.79.

Mills, G. A., & McCaw, L. **(2010)**. *Atmospheric stability environments and fire weather in Australia: extending the Haines index. Centre for Australian Weather and Climate Research*. CAWCR technical report 20. (Melbourne, Australia)

Molina-Terrén, D. M., Xanthopoulos, G., Diakakis, M., Ribeiro, L., Caballero, D., Delogu, G. M., Viegas, D. X., Silva, C. A., & Cardil, A. **(2019)**. Analysis of forest fire fatalities in southern Europe: Spain, Portugal, Greece and Sardinia (Italy). International journal of wildland fire, 28(2), 85-98. DOI: 10.1071/WF18004.

Moreira, N., Silva, A., Novo, I., Rio, J., Pinto, P., Correia, S., Barbosa, S., & Cota, T. **(2017)** Condições meteorológicas associadas ao incêndio de Pedrógão Grande de 17 junho 2017. Instituto Português do Mar e da Atmosfera. (Lisbon).

Moritz, M.A., Parisien, M.A., Batllori, E., Krawchuk, M.A., Van Dorn, J., Ganz, D.J., & Hayhoe, K. **(2012)**. Climate change and disruptions to global fire activity. Ecosphere 3 (6), 1–22. DOI: 10.1890/ES11-00345.1.

Moritz, M. A., Batllori, E., Bradstock, R. A., Gill, A. M., Handmer, J., Hessburg, P. F., Leonard, J., McCaffrey, S., Odion, D. C., Schoennagel, T., & Syphard, A. D. **(2014)**. Learning to coexist with wildfire. Nature, 515(7525), 58-66. DOI: 10.1038/nature13946.

Mouillot, F., Schultz, M.G., Yue, C., Cadule, P., Tansey, K., Ciais, P., & Chuvieco, E. **(2014)**. Ten years of global burned area products from spaceborne remote sensing—a review: analysis of user needs and recommendations for future developments. *Int. J. Appl. Earth Obs. Geoinf. 26*, 64–79. DOI: 10.1016/j.jag.2013.05.014.

Muñoz-Sabater, J., Dutra, E., Agustí-Panareda, A., Albergel, C., Arduini, G., Balsamo, G., Boussetta, S., Choulga, M., Harrigan, S., Hersbach, H., Martens, B., Miralles, D., Piles, M., Rodríguez-Fernández, N. J., Zsoter, E., Buontempo, C., & Thépaut, J. N. **(2021)**. ERA5-Land: A state-of-the-art global reanalysis dataset for land applications. Earth System Science Data, 13(9), 4349-4383. DOI: 10.5194/essd-13-4349-2021.

Mutthulakshmi, K., Wee, M. R. E., Wong, Y. C. K., Lai, J. W., Koh, J. M., Acharya, U. R., & Cheong, K. H. **(2020)**. Simulating forest fire spread and fire-fighting using cellular automata. Chinese Journal of Physics, 65, 642-650. DOI: 10.1016/j.cjph.2020.04.001.

Nair, V. & Hinton, G.E. **(2010)**. Rectified linear units improve restricted boltzmann machines. In: ICML-10 Proceedings of the 27th International Conference on Machine Learning, Haifa, Israel, 21–24 June, pp. 807–814.

Navon, I. M. **(2009)**. Data assimilation for numerical weather prediction: a review. Data assimilation for atmospheric, oceanic and hydrologic applications, 21-65.

Ndalila, M. N., Williamson, G. J., Fox-Hughes, P., Sharples, J., & Bowman, D. M. **(2020)**. Evolution of a pyrocumulonimbus event associated with an extreme wildfire in Tasmania, Australia. Natural Hazards and Earth System Sciences, 20(5), 1497-1511. DOI: 10.5194/nhess-20-1497-2020.

Nesterov, V. **(1949)**. Combustibility of the Forest and Methods for its Determination, USSR State Industry Press, Moscow, USSR.

Neyman, J., & Pearson, E. S. **(1933)**. IX. On the problem of the most efficient tests of statistical hypotheses. Philosophical Transactions of the Royal Society of London. Series A, Containing Papers of a Mathematical or Physical Character, 231(694-706), 289-337.

Nogueira, J. M., Ruffault, J., Chuvieco, E., & Mouillot, F. **(2017)**. Can we go beyond burned area in the assessment of global remote sensing products with fire patch metrics?. *Remote Sensing, 9*(1), 7. DOI: 10.3390/rs9010007.

Nusrat, I., & Jang, S. B. **(2018)**. A comparison of regularization techniques in deep neural networks. Symmetry, 10(11), 648. DOI: 10.3390/sym10110648.

Oliva, P., & Schroeder, W. **(2015)**. Assessment of VIIRS 375 m active fire detection product for direct burned area mapping. Remote Sens. Environ. 160, 144–155. DOI: 10.1016/j.rse.2015.01.010.

Otón, G., & Pettinari, M.L. **(2019)**. ESA CCI ECV Fire Disturbance: D3.3.4 Product User Guide – LTDR, version 1.0. Available at: climate.esa.int/media/documents (last accessed 2022-03-03).

Padilla, M., Stehman, S.V., Ramo, R., Corti, D., Hantson, S., Oliva, P., Alonso-Canas, I., Bradley, A.V., Tansey, K., Mota, B., Pereira, J.M., & Chuvieco, E. **(2015)**. Comparing the accuracies of remote sensing global burned area products using stratified random sampling and estimation. Remote Sens. Environ. 160, 114–121. DOI: 10. 1016/j.rse.2015.01.005.

Pan, S. J., & Yang, Q. **(2009)**. A survey on transfer learning. IEEE Trans. Knowl. Data Eng. 22 (10), 1345–1359. DOI: 10.1109/TKDE.2009.191.

Panisset, J., DaCamara, C.C., Libonati, R., Peres, L.F., Calado, T.J., & Barros, A. **(2017)**. Assigning dates and identifying areas affected by fires in Portugal based on MODIS data. *Anais da Academia Brasileira de Ciências 89 (3)*, 1487–1501. DOI: 10.1590/0001-3765201720160707.

Patz, J. A., Engelberg, D., Last, J. **(2000)**. The effects of changing weather on public health. *Annu. Rev. Public Health 21 (1)*, 271–307. DOI: 10.1146/annurev. publhealth.21.1.271.

Pausas, J. G., & Vallejo, V. R. **(1999)**. The role of fire in European Mediterranean ecosystems. In Remote sensing of large wildfires (pp. 3-16). Springer, Berlin, Heidelberg. DOI: 10.1007/978-3-642-60164-4_2.

Pausas, J. G., Llovet, J., Rodrigo, A., & Vallejo, R. **(2008)**. Are wildfires a disaster in the Mediterranean basin?–A review. *International Journal of wildland fire, 17*(6), 713-723. DOI: 10.1071/WF07151.

Peace, M., Charney, J., & Bally, J. **(2020)**. Lessons Learned from Coupled Fire-Atmosphere Research and Implications for Operational Fire Prediction and Meteorological Products

Provided by the Bureau of Meteorology to Australian Fire Agencies. *Atmosphere*, 11(12), 1380. DOI: 10.3390/atmos11121380.

Pelletier, C., Webb, G.I., & Petitjean, F. **(2019)**. Temporal convolutional neural network for the classification of satellite image time series. *Remote Sens. 11* (5), 523. DOI: 10.3390/rs11050523.

Pereira, A., Pereira, J., Libonati, R., Oom, D., Setzer, A., Morelli, F., Machado-Silva, F., & De Carvalho, L.M.T. **(2017)**. Burned area mapping in the Brazilian Savanna using a oneclass support vector machine trained by active fires. *Remote Sens. 9* (11), 1161. DOI: 10.3390/rs9111161.

Pereira, M. G., Calado, T. J., DaCamara, C. C., & Calheiros, T. **(2013)**. Effects of regional climate change on rural fires in Portugal. *Climate research*, 57(3), 187-200. DOI: 10.3354/cr01176.

Pereira, M. G., Malamud, B. D., Trigo, R. M., & Alves, P. I. **(2011)**. The history and characteristics of the 1980–2005 Portuguese rural fire database. Natural Hazards and Earth System Sciences, 11(12), 3343-3358. DOI: 10.5194/nhess-11-3343-2011.

Perez, L., Wang, & J. **(2017)**. The effectiveness of data augmentation in image classification using deep learning. arXiv preprint arXiv:1712.04621.

Pickands III, J. **(1975)**. Statistical inference using extreme order statistics. the Annals of Statistics, 119-131. DOI: 10.1214/aos/1176343003.

Pinneri, C., Sawant, S., Blaes, S., Achterhold, J., Stueckler, J., Rolinek, M., & Martius, G. **(2020)**. Sample-efficient cross-entropy method for real-time planning. arXiv preprint arXiv:2008.06389.

Pinto, M. M., DaCamara, C. C., Trigo, I. F., Trigo, R. M., & Turkman, K. F. **(2018a)**. Fire danger rating over Mediterranean Europe based on fire radiative power derived from Meteosat. Natural Hazards and Earth System Sciences, 18(2), 515-529. DOI: 10.5194/nhess-18-515-2018.

Pinto, M. M., Hurduc, A., Trigo, R. M., Trigo, I. F., & DaCamara, C. C. **(2018b)**. The extreme weather conditions behind the destructive fires of June and October 2017 in Portugal. *Imprensa da Universidade de Coimbra*. Coimbra, Portugal.

Pinto, M. M., DaCamara, C. C., Trigo, I. F. & Trigo, R. M. **(2018c)**. Forecasting hourly Fire Weather Index: an application to Portugal. *A previsão numérica do tempo em Portugal: "estado da arte e novos desafios"* IPMA, 26-27 novembro 2018.

ipma.pt/export/sites/ipma/bin/docs/publicacoes/meteo.prev/PNT2018-C11.pdf (last accessed 2022-03-03)

Pinto, M. M., Libonati, R., Trigo, R. M., Trigo, I. F., & DaCamara, C. C. **(2020a)**. A deep learning approach for mapping and dating burned areas using temporal sequences of satellite images. *ISPRS Journal of Photogrammetry and Remote Sensing*, 160, 260-274. DOI: 10.1016/j.isprsjprs.2019.12.014.

Pinto, M. M., DaCamara, C. C., Hurduc, A., Trigo, R. M., & Trigo, I. F. **(2020b)**. Enhancing the fire weather index with atmospheric instability information. Environmental Research Letters, 15(9), 0940b7. DOI: 10.1088/1748-9326/ab9e22.

Pinto, M. M., Trigo, R. M., Trigo, I. F., & DaCamara, C. C. **(2021)**. A Practical Method for High-Resolution Burned Area Monitoring Using Sentinel-2 and VIIRS. Remote Sensing, 13(9), 1608. DOI: 10.3390/rs13091608.

Potter, B. **(2018)**. The Haines Index–it's time to revise it or replace it. International journal of wildland fire, 27(7), 437-440. DOI: 10.1071/WF18015.

Pulvirenti, L., Squicciarino, G., Fiori, E., Fiorucci, P., Ferraris, L., Negro, D., Gollini, A., Severino, M., & Puca, S. **(2020)**. An automatic processing chain for near real-time mapping of burned forest areas using sentinel-2 data. *Remote Sensing*, *12*(4), 674. DOI: 10.3390/rs12040674.

Quintano, C., Fernández-Manso, A., & Fernández-Manso, O. **(2018)**. Combination of Landsat and Sentinel-2 MSI data for initial assessing of burn severity. *International journal of applied earth observation and geoinformation*, *64*, 221-225. DOI: 10.1016/j.jag.2017.09.014.

Rego, F.C., Fernandes, P., Silva, J.S., Azevedo, J., Moura, J.M., Oliveira, E., Cortes, R., Viegas, D.X., Caldeira, D., & Santos, F.D. **(2019)**. Avaliação do Incêndio de Monchique. Technical Report. Observatório Técnico Independente, Assembleia da República, Lisboa, Portugal.

Reichstein, M., Camps-Valls, G., Stevens, B., Jung, M., Denzler, J., & Carvalhais, N. **(2019)**. Deep learning and process understanding for data-driven Earth system science. Nature 566 (7743), 195. DOI: 10.1038/s41586-019-0912-1.

Ribeiro, L. M., Viegas, D. X., Almeida, M., McGee, T. K., Pereira, M. G., Parente, J., Xanthopoulos, G., Leone, V., Delogu, G. M., & Hardin, H. **(2020)**. Extreme wildfires and disasters around the world: Lessons to be learned. In Extreme wildfire events and disasters (pp. 31-51). Elsevier. DOI: 10.1016/B978-0-12-815721-3.00002-3.

Roberts, G., & Wooster, M. J. **(2014)**. Development of a multi-temporal Kalman filter approach to geostationary active fire detection & fire radiative power (FRP) estimation. Remote sensing of environment, 152, 392-412. DOI: 10.1016/j.rse.2014.06.020

Rodrigues, J.A., Libonati, R., Pereira, A.A., Nogueira, J.M., Santos, F.L., Peres, L.F., Rosa, A.S., Schroeder, W., Pereira, J.M.C., Giglio, L., Trigo, I.F., & Setzer, A.W. **(2019)**. How well do global burned area products represent fire patterns in the Brazilian Savannas biome? An accuracy assessment of the MCD64 collections. *Int. J. Appl. Earth Obs. Geoinf. 78*, 318–331. DOI: 10.1016/j.jag.2019.02.010.

Rolnick, D., Veit, A., Belongie, S., & Shavit, N. **(2017)**. Deep learning is robust to massive label noise. *arXiv preprint arXiv:1705.10694*.

Ronneberger, O., Fischer, P., & Brox, T. **(2015, October)**. U-net: Convolutional networks for biomedical image segmentation. In International Conference on Medical image computing and computer-assisted intervention (pp. 234-241). Springer, Cham.

Roteta, E., Bastarrika, A., Padilla, M., Storm, T., & Chuvieco, E. **(2019)**. Development of a Sentinel-2 burned area algorithm: generation of a small fire database for sub-Saharan Africa. Remote Sens. Environ. 222, 1–17. DOI: 10.1016/j.rse.2018.12.011.

Rothermel, R. C. **(1972)**. A mathematical model for predicting fire spread in wildland fuels (Vol. 115). Intermountain Forest & Range Experiment Station, Forest Service, US Department of Agriculture.

Rubinstein, R. Y. **(1997)**. Optimization of computer simulation models with rare events. European Journal of Operational Research, 99(1), 89-112. DOI: 10.1016/S0377-2217(96)00385-2.

Rumelhart, D.E., Hinton, G.E., & Williams, R.J. **(1986)**. Learning representations by backpropagating errors. Cogn. Model. 5 (3), 1. DOI: 10.1038/323533a0.

Ruffault, J., Curt, T., Moron, V., Trigo, R. M., Mouillot, F., Koutsias, N., Pimont, F., Martin-StPaul, N., Barbero, R. Dupuy, J. L., Russo, A. & Belhadj-Khedher, C. **(2020)**. Increased likelihood of heat-induced large wildfires in the Mediterranean Basin. *Scientific reports*, *10*(1), 1-9. DOI: 10.1038/s41598-020-70069-z.

Rußwurm, M., & Körner, M. **(2018)**. Multi-temporal land cover classification with sequential recurrent encoders. *ISPRS Int. J. Geo-Inf. 7 (4)*, 129. DOI: 10.3390/ijgi7040129.

San-Miguel-Ayanz, J., Carlson, J. D., Alexander, M., Tolhurst, K., Morgan, G., Sneeuwjagt, R., & Dudley, M. **(2003)**. Current methods to assess fire danger potential. *In Wildland fire* *danger estimation and mapping: The role of remote sensing data* (pp. 21-61). DOI: 10.1142/9789812791177_0002.

San-Miguel-Ayanz, J., Schulte, E., Schmuck, G., Camia, A., Strobl, P., Liberta, G., Giovando, C., Boca, R., Sedano, F., Kempeneers, P., McInerney, D., Withmore, C., Oliveira, S.S., Rodrigues, M., Durrant, T., Corti, P., Oehler, F., Vilar, L., & Amatulli, G. **(2012)**. Comprehensive monitoring of wildfires in Europe: the European forest fire information system (EFFIS). *In: Approaches to Managing Disaster-Assessing Hazards, Emergencies and Disaster Impacts*. IntechOpen. DOI: 10.5772/28441.

San-Miguel-Ayanz, J., Durrant, T., Boca, R., Libertà, G., Branco, A., De Rigo, D., Ferrari, D., Maianti, P., Vivancos, T. A., Costa, H., Lana, F., Löffler, P., Nuijten, D., Ahlgren, A. C., & Leray, T. **(2018)**. Forest Fires in Europe, Middle East and North Africa 2017. *Publications Officer of the European Union. doi*, *10*, 663443.

Sánchez-Benítez, A., García-Herrera, R., Barriopedro, D., Sousa, P. M. & Trigo, R. M. **(2018)**. June 2017: The Earliest European Summer Mega-heatwave of Reanalysis Period. *Geophysical Research Letters 45(4)*, 1955-1962. DOI: 10.1002/2018GL077253.

Schnapf, A. **(1982)**. The development of the TIROS global environmental satellite system. Meteorological Satellites-Past, Present, and Future, 7.

Schroeder, W., Oliva, P., Giglio, L., & Csiszar, I.A. **(2014)**. The New VIIRS 375 m active fire detection data product: algorithm description and initial assessment. *Remote Sens. Environ. 143*, 85–96. DOI: 10.1016/j.rse.2013.12.008.

Scott, G.J., England, M.R., Starms, W.A., Marcum, R.A., & Davis, C.H. **(2017)**. Training deep convolutional neural networks for land–cover classification of high-resolution imagery. *IEEE Geosci. Remote Sens. Lett. 14 (4)*, 549–553. DOI: 10.1109/ LGRS.2017.2657778.

Sharples, J. J., Cary, G. J., Fox-Hughes, P., Mooney, S., Evans, J. P., Fletcher, M. S., Fromm, M., Grierson, P. F., & Baker, P. **(2016)**. Natural hazards in Australia: extreme bushfire. *Climatic Change*, 139(1), 85-99. DOI: 10.1007/s10584-016-1811-1.

Shorten, C., & Khoshgoftaar, T. M. **(2019)**. A survey on image data augmentation for deep learning. *Journal of big data*, *6*(1), 1-48. DOI: 10.1186/s40537-019-0197-0.

Showstack, R. **(2013)**. Landsat 5 to be decommissioned. *American Geophysical Union*. DOI: 10.1002/2013EO020003.

Simpson, C. C., Pearce, H. G., Sturman, A. P., & Zawar-Reza, P. **(2014)**. Behaviour of fire weather indices in the 2009–10 New Zealand wildland fire season. *International Journal of Wildland Fire*, *23*(8), 1147-1164. DOI: 10.1071/WF12169.

Sinelnikov, V., Kuznetsov, V., & Alpert, S. **(2014)**. Sputnik 1 and the first satellite ionospheric experiment. 40th COSPAR Scientific Assembly, 40, C0-2.

Skamarock, W. C., Klemp, J. B., Dudhia, J., Gill, D. O., Liu, Z., Berner, J., Wang, W., Powers, J. G., Duda, M. G., Barker, D. M., & Huang, X. Y. **(2019)**. A description of the advanced research WRF model version 4. National Center for Atmospheric Research: Boulder, CO, USA, 145, 145.

Smith, L. N. **(2018)**. A disciplined approach to neural network hyper-parameters: Part 1–Learning rate, batch size, momentum, and weight decay. arXiv preprint arXiv:1803. 09820.

Sousa, F. A., dos Reis, R. J., & Pereira, J. C. **(2012)**. Simulation of surface fire fronts using fireLib and GPUs. Environmental Modelling & Software, 38, 167-177. DOI: 10.1016/j.envsoft.2012.06.006.

Srivastava, N., Hinton, G., Krizhevsky, A., Sutskever, I., & Salakhutdinov, R. **(2014)**. Dropout: a simple way to prevent neural networks from overfitting. J. Mach. Lear. Res. 15 (1), 1929–1958.

Stroppiana, D., Bordogna, G., Carrara, P., Boschetti, M., Boschetti, L., & Brivio, P.A. **(2012)**. A method for extracting burned areas from Landsat TM/ETM+ images by soft aggregation of multiple Spectral Indices and a region growing algorithm. *ISPRS J. Photogramm. Remote Sens. 69*, 88–102. DOI: 10.1016/j.isprsjprs.2012. 03.001.

Sudre, C. H., Li, W., Vercauteren, T., Ourselin, S., & Jorge Cardoso, M. **(2017)**. Generalised dice overlap as a deep learning loss function for highly unbalanced segmentations. *In Deep learning in medical image analysis and multimodal learning for clinical decision support* (pp. 240-248). Springer, Cham. DOI: 10.1007/978-3-319-67558-9_28.

Sullivan, A. L. **(2009a)**. Wildland surface fire spread modelling, 1990–2007. 1: Physical and quasi-physical models. International Journal of Wildland Fire, 18(4), 349-368. DOI: 10.1071/WF06143.

Sullivan, A. L. **(2009b)**. Wildland surface fire spread modelling, 1990–2007. 2: Empirical and quasi-empirical models. International Journal of Wildland Fire, 18(4), 369-386. DOI: 10.1071/WF06142.

Sullivan, A. L. **(2009c)**. Wildland surface fire spread modelling, 1990–2007. 3: Simulation and mathematical analogue models. International Journal of Wildland Fire, 18(4), 387-403. DOI: 10.1071/WF06144.

Sutskever, I., Vinyals, O., & Le, Q.V. **(2014)**. Sequence to sequence learning with neural networks. In: Advances in Neural Information Processing Systems, Montreal, Canada, 8–13 December, pp. 3104–3112.

Sutton, R. S., & Barto, A. G. **(2018)**. Reinforcement learning: An introduction. MIT press.

Szita, I., & Lörincz, A. **(2006)**. Learning Tetris using the noisy cross-entropy method. Neural computation, 18(12), 2936-2941. DOI: 10.1162/neco.2006.18.12.2936.

Tatli, H., & Türkeş, M. **(2014)**. Climatological evaluation of Haines forest fire weather index over the Mediterranean Basin. *Meteorological Applications*, *21*(3), 545-552. DOI: 10.1002/met.1367.

Trigo, I. F., Dacamara, C. C., Viterbo, P., Roujean, J. L., Olesen, F., Barroso, C., Camacho-de-Coca F., Carrer, D., Freitas, S. C., García-Haro, J., Geiger, B., Gellens-Meulenberghs, F., Ghilain, N., Meliá, J., Pessanha, L., Siljamo, N., & Arboleda, A. **(2011)**. The satellite application facility for land surface analysis. *International Journal of Remote Sensing*, 32(10), 2725-2744. DOI: 10.1080/01431161003743199.

Trigo, R.M., Pereira, J.M., Pereira, M.G., Mota, B., Calado, T.J., DaCamara, C.C., & Santo, F.E. **(2006)**. Atmospheric conditions associated with the exceptional fire season of 2003 in Portugal. Int. J. Climatol. 26 (13), 1741–1757. DOI: 10.1002/joc. 1333.

Trouet, V., Taylor, A. H., Carleton, A. M., & Skinner, C. N. **(2009)**. Interannual variations in fire weather, fire extent, and synoptic-scale circulation patterns in northern California and Oregon. *Theoretical and Applied Climatology*, *95*(3), 349-360. DOI: 10.1007/s00704-008-0012-x.

Turco, M., Rosa-Cánovas, J. J., Bedia, J., Jerez, S., Montávez, J. P., Llasat, M. C., & Provenzale, A. **(2018)**. Exacerbated fires in Mediterranean Europe due to anthropogenic warming projected with non-stationary climate-fire models. *Nature communications*, *9*(1), 1-9. DOI: 10.1038/s41467-018-06358-z.

Turco, M., Jerez, S., Augusto, S., Tarín-Carrasco, P., Ratola, N., Jiménez-Guerrero, P., & Trigo, R. M. **(2019)**. Climate drivers of the 2017 devastating fires in Portugal. *Scientific reports*, *9*(1), 1-8. DOI: 10.1038/s41598-019-50281-2.

Uppala, S., Simmons, A., Dee, D., Kållberg, P., & Thépaut, J. N. **(2008)**. Atmospheric reanalyses and climate variations. In Climate variability and extremes during the past 100 years (pp. 103-117). Springer, Dordrecht. DOI: 10.1007/978-1-4020-6766-2_6.

Van Der Werf, G.R., Randerson, J.T., Giglio, L., Van Leeuwen, T.T., Chen, Y., Rogers, B.M., Mu, M., van Marle, M.J.E., Morton, D.C., Collatz, G.J., Yokelson, R.J., & Kasibhatla, P.S. **(2017)**. Global fire emissions estimates during 1997–2016. *Earth Syst. Sci. Data 9*, 697–720. DOI: 10.5194/essd-9-697-2017.

Van Wagner, C. E. **(1974)** Structure of the Canadian Forest Fire Weather Index (Ontario: Environment Canada, Forestry Service) 1333 vol.

Van Wagner, C. E. **(1987)**. Development and structure of the Canadian forest fire weather index system. Canadian Forestry Service. Forestry technical report, 35, 37.

Vasilakos, C., Kalabokidis, K., Hatzopoulos, J., Kallos, G., & Matsinos, Y. **(2007)**. Integrating new methods and tools in fire danger rating. International Journal of Wildland Fire, 16(3), 306-316. DOI: 10.1071/WF05091.

Vaughan, W. W., & Johnson, D. L. **(1994)**. Meteorological Satellites—The Very Early Years, Prior to Launch of TIROS-1. Bulletin of the American Meteorological Society, 75(12), 2295-2302. DOI: 10.1175/1520-0477(1994)075<2295:MSVEYP>2.0.CO;2.

Viegas, D.X. **(2018)**. Wildfires in Portugal. *Fire Res. 2 (1).* DOI: 10.4081/fire. 2018.52.

Viegas, D. X., Bovio, G., Ferreira, A., Nosenzo, A., & Sol, B. **(1999)**. Comparative study of various methods of fire danger evaluation in southern Europe. *International Journal of wildland fire*, 9(4), 235-246. DOI: 10.1071/WF00015.

Virtanen, P., Gommers, R., Oliphant, T. E., Haberland, M., Reddy, T., Cournapeau, D., Burovski, E., Peterson, P. Weckesser, W., Bright, J., van der Walt, S. J., Brett, M., Wilson, J., Millman, K. J., Mayorov, N., Nelson, A. R. J., Jones, E., Kern, R., Larson, E., Carey, C. J., Polat, I., Feng, Y., Moore, E. W., VanderPlas, J., Laxalde, D., Perktold, J., Cimrman, R., Henriksen, I., Quintero, E. A., Harris, C. R., Archibald, A. M., Ribeiro, A. H., Pedregosa, F., van Mulbregt, P., & SciPy 1.0 Contributors **(2020)**. SciPy 1.0: fundamental algorithms for scientific computing in Python. *Nature methods*, 17(3), 261-272. DOI: 10.1038/s41592-019-0686-2.

Vitolo, C., Di Giuseppe, F., Krzeminski, B., & San-Miguel-Ayanz, J. **(2019)**. A 1980–2018 global fire danger re-analysis dataset for the Canadian Fire Weather Indices. Scientific data, 6(1), 1-10. DOI: 10.1038/sdata.2019.32.

Wagenbrenner, N. S., Forthofer, J. M., Lamb, B. K., Shannon, K. S., & Butler, B. W. **(2016)**. Downscaling surface wind predictions from numerical weather prediction models in complex terrain with WindNinja. Atmospheric Chemistry and Physics, 16(8), 5229-5241. DOI: 10.5194/acp-16-5229-2016.

Wang, Y., Anderson, K. R., & Suddaby, R. M. **(2015)**. Updated source code for calculating fire danger indices in the Canadian Forest Fire Weather Index System. *Information Report NOR-X-424*. Canadian Forest Service, Northern Forestry Centre. Edmonton, Canada.

Wen, M., & Topcu, U. **(2018)**. Constrained cross-entropy method for safe reinforcement learning. Advances in Neural Information Processing Systems, 31.

Werth, P., & Ochoa, R. **(1993)**. The evaluation of Idaho wildfire growth using the Haines Index. *Weather and Forecasting*, *8*(2), 223-234.

Wieland, M., Li, Y. & Martinis, S. **(2019)**. Multi-sensor cloud and cloud shadow segmentation with a convolutional neural network. Remote Sens. Environ. 230, 111203. DOI: 10.1016/j.rse.2019.05.022.

Wilks, D. S. **(2011)**. *Statistical methods in the atmospheric sciences* (Vol. 100). Academic press.

Winkler, J. A., Potter, B. E., Wilhelm, D. F., Shadbolt, R. P., Piromsopa, K., & Bian, X. **(2007)**. Climatological and statistical characteristics of the Haines Index for North America. International Journal of Wildland Fire, 16(2), 139-152. DOI: 10.1071/WF06086.

Wooster, M. J., Roberts, G., Freeborn, P. H., Xu, W., Govaerts, Y., Beeby, R., He, J., Lattanzio, A., Fisher, D., & Mullen, R. **(2015)**. LSA SAF Meteosat FRP products–Part 1: Algorithms, product contents, and analysis. *Atmospheric Chemistry and Physics*, 15(22), 13217-13239. DOI: 10.5194/acp-15-13217-2015

Wotton, B. M. **(2009)**. Interpreting and using outputs from the Canadian Forest Fire Danger Rating System in research applications. *Environmental and Ecological Statistics*, *16*(2), 107-131. DOI: 10.1007/s10651-007-0084-2.

Wu, Y., & He, K. **(2018)**. Group normalization. In *Proceedings of the European conference on computer vision (ECCV)* (pp. 3-19).

Young, A.M., Higuera, P.E., Duffy, P.A., & Hu, F.S. **(2017)**. Climatic thresholds shape northern high-latitude fire regimes and imply vulnerability to future climate change. Ecography 40 (5), 606–617. DOI: 10.1111/ecog.02205.

Zayan, M. A., & Eltohamy, F. (2008, March). Orbits Design for Remote Sensing Satellite. In *2008 IEEE Aerospace Conference* (pp. 1-9). IEEE. DOI: 10.1109/AERO.2008.4526494.

Zhang, L., Zhang, L., & Du, B. **(2016)**. Deep learning for remote sensing data: A technical tutorial on the state of the art. IEEE Geoscience and remote sensing magazine, 4(2), 22-40. DOI: 10.1109/MGRS.2016.2540798.

Zhang, Q., Yuan, Q., Zeng, C., Li, X., & Wei, Y. **(2018)**. Missing data reconstruction in remote sensing image with a unified spatial–temporal–spectral deep convolutional neural network. IEEE Trans. Geosci. Remote Sens. 56 (8), 4274–4288. DOI: 10. 1109/TGRS.2018.2810208.

Zhang, Q., Ge, L., Zhang, R., Metternicht, G. I., Du, Z., Kuang, J., & Xu, M. **(2021)**. Deep-learning-based burned area mapping using the synergy of Sentinel-1&2 data. Remote Sensing of Environment, 264, 112575. DOI: 10.1016/j.rse.2021.112575.

Zhang, W., Wang, H., Hartmann, C., Weber, M., & Schütte, C. **(2014)**. Applications of the cross-entropy method to importance sampling and optimal control of diffusions. SIAM Journal on Scientific Computing, 36(6), A2654-A2672. DOI: 10.1137/14096493X.

Zhong, Z., Zheng, L., Kang, G., Li, S., & Yang, Y. **(2017)**. Random erasing data augmentation. arXiv preprint arXiv:1708.04896.

Zhu, X.X., Tuia, D., Mou, L., Xia, G.S., Zhang, L., Xu, F., & Fraundorfer, F. **(2017)**. Deep learning in remote sensing: a comprehensive review and list of resources. *IEEE Geosci. Remote Sens. Mag. 5 (4)*, 8–36. DOI: 10.1109/MGRS.2017. 2762307.

A. Annexes I

Table A.1. 15 -fold average and standard deviation (in square brackets) for the parameters a, b, c and d of equations (2.5) and (2.6).

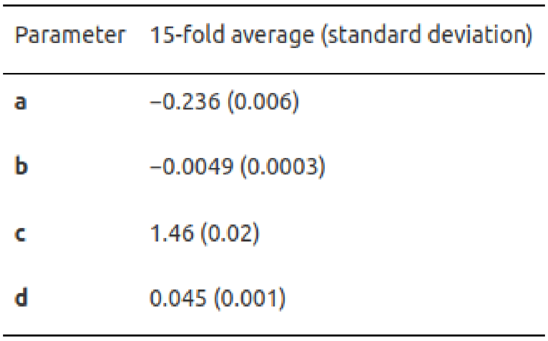

Parameter	15-fold average (standard deviation)
a	−0.236 (0.006)
b	−0.0049 (0.0003)
c	1.46 (0.02)
d	0.045 (0.001)

Table A.2. As in **Table A.1**, but for parameters e, f, g, h, i, j, k and l of equations (2.7) and (2.8).

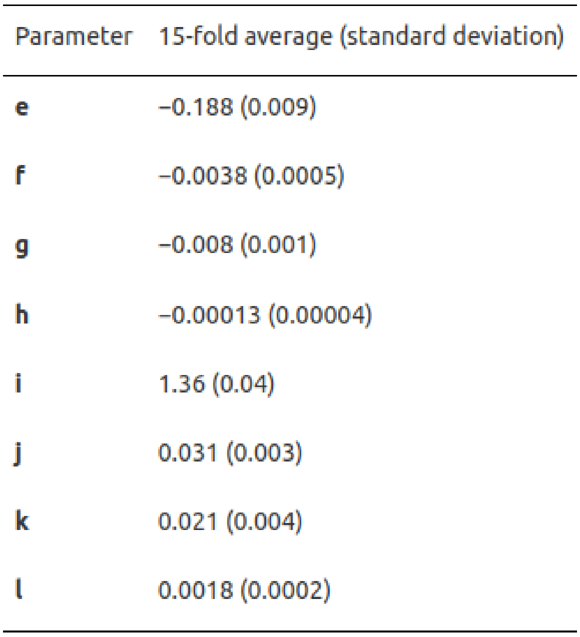

Parameter	15-fold average (standard deviation)
e	−0.188 (0.009)
f	−0.0038 (0.0005)
g	−0.008 (0.001)
h	−0.00013 (0.00004)
i	1.36 (0.04)
j	0.031 (0.003)
k	0.021 (0.004)
l	0.0018 (0.0002)

Table A.3. FWIe values for the FWI/CHI pairs.

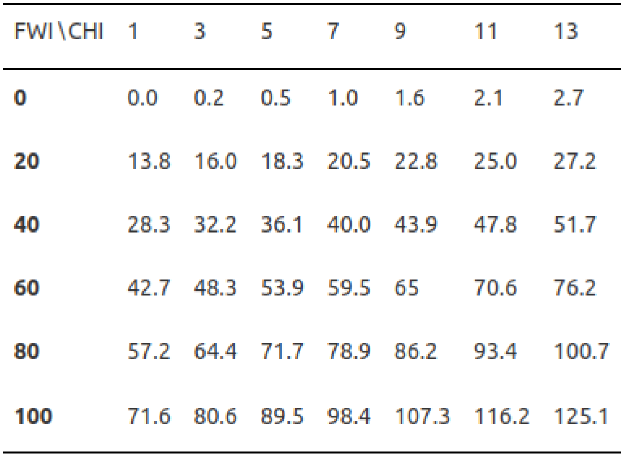

FWI \ CHI	1	3	5	7	9	11	13
0	0.0	0.2	0.5	1.0	1.6	2.1	2.7
20	13.8	16.0	18.3	20.5	22.8	25.0	27.2
40	28.3	32.2	36.1	40.0	43.9	47.8	51.7
60	42.7	48.3	53.9	59.5	65	70.6	76.2
80	57.2	64.4	71.7	78.9	86.2	93.4	100.7
100	71.6	80.6	89.5	98.4	107.3	116.2	125.1

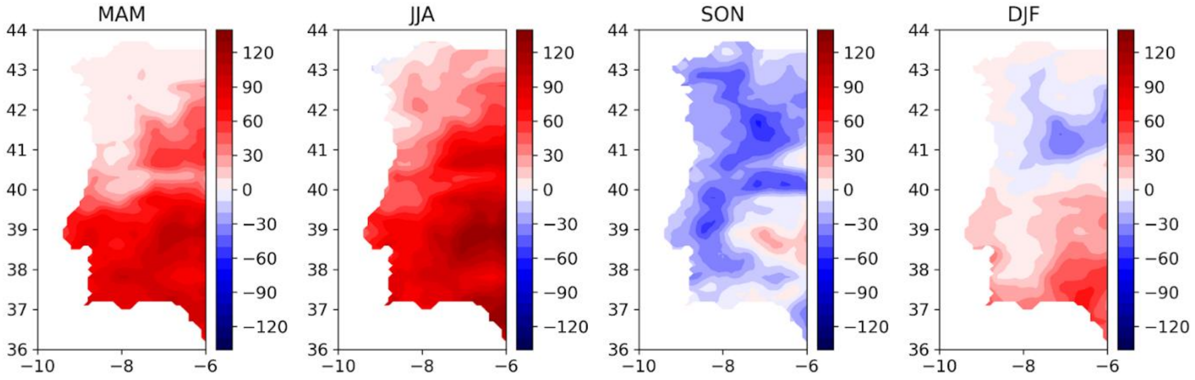

Figure A.1. As in **Figure 2.18** but for the Drought Code (DC).

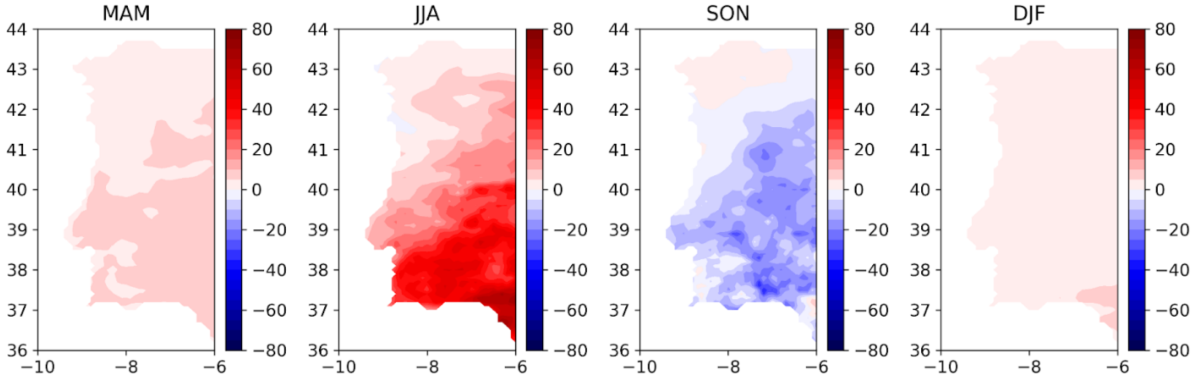

Figure A.2. As in **Figure 2.18** but for the Duff Moisture Code (DMC).

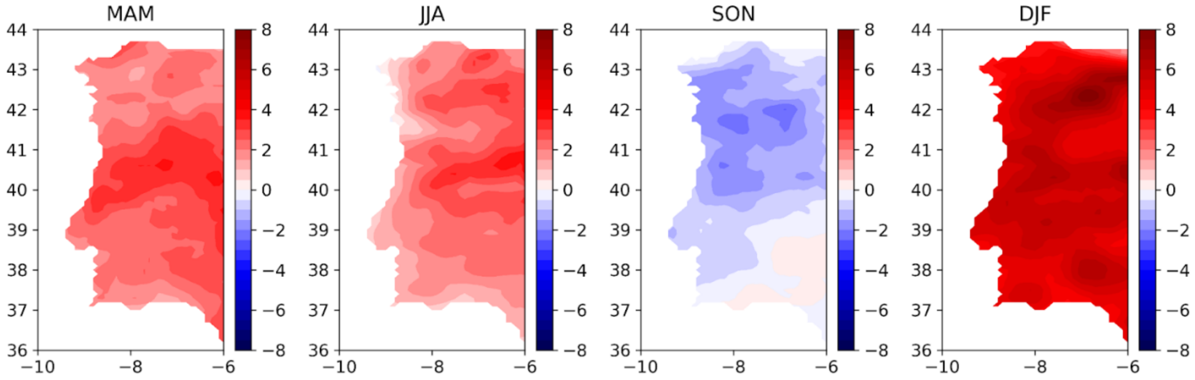

Figure A.3. As in **Figure 2.18** but for the Fine Fuel Moisture Code (FFMC).

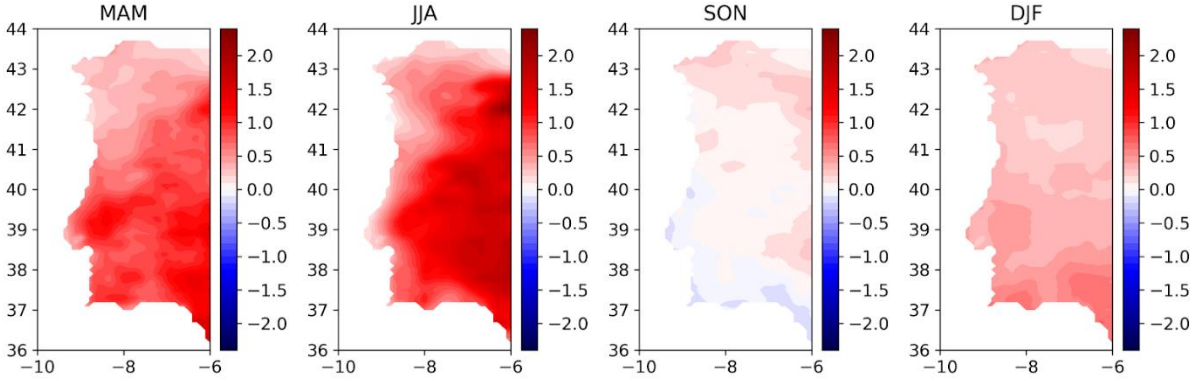

Figure A.4. As in **Figure 2.18** but for the Initial Spread Index (ISI).

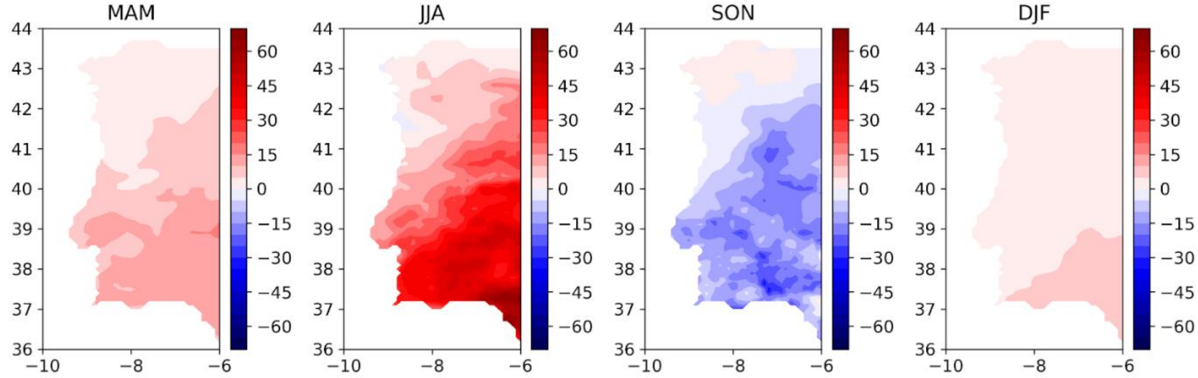

Figure A.5. As in **Figure 2.18** but for the Build-up Index (BUI).

B. Annexes II

This section includes the transcription of the following book chapter that I co-authored: DaCamara, C. C., Libonati, R., ***Pinto, M. M.****, & Hurduc, A. (2019). Near-and Middle-Infrared Monitoring of Burned Areas from Space. In Satellite Information Classification and Interpretation. London, UK: IntechOpen.*

Near-and Middle-Infrared Monitoring of Burned Areas from Space

Abstract

We describe a methodology to discriminate burned areas and date burning events that use a burn-sensitive (V, W) index system defined in near-/mid-infrared space. Discrimination of burned areas relies on a monthly composite of minimum of W and on the difference between this composite and that of the previous month. The rationale is to identify pixels with high confidence of having burned and aggregate new burned pixels on a contextual basis. Dating of burning events is based on the analysis of time series of W, and searching for the day before maximum temporal separability is achieved. The procedure is applied to the fire of Monchique, a large event that took place in the southwest of Portugal in August 2018. When the obtained pattern of burned pixels is compared against a reference map, the overall accuracy is larger than 99%; the commission and omission errors are lower than 5 and 10%, respectively; and the bias and the Dice coefficient are above 0.95 and 0.9, respectively. Differences between estimated dates of burning and reference dates derived from remote-sensed observations of active fires show a bias of 0.03 day and a root mean square difference of 0.24 day.

Keywords

Burned area, dates of burning, (V, W) index system, VIIRS sensor, Monchique fire (Portugal)

1. Introduction

Vegetation fires have significant direct and indirect impacts on all components of the Earth system, including the anthroposphere. They are a source of greenhouse gases, aerosols, and trace gases to the atmosphere [1, 2, 3]; they induce modifications in most radiative forcing terms [4, 5] and disturb the radiative budget and cloud microphysics [6, 7]; they lead to changes in soil properties [8] and in the hydrological cycle [9, 10, 11]; they play a key role in biodiversity reduction, loss of genetic diversity, forest ecosystem functioning [12, 13], and land use/cover dynamics [14, 15, 16]; and they cause damages to human health [17, 18] and have adverse effects on public health and economy [19].

A thorough understanding of spatial and temporal patterns of burned area (BA) by wildfires is therefore of fundamental importance when assessing either climate or anthropogenic influences on the Earth system [20, 21]; when addressing a very wide range of subjects that include the fields of atmospheric physics and chemistry, ecology, agriculture and forestry, hydrology, biology, sociology, and economy; and when defining climate, environment, and health policies [22, 23, 24, 25, 26]. When specifically focusing on fire management that comprises fire prevention, fire presuppression, and fire suppression measures, reliable information about the extent, location, and time of occurrence of BA is of high added value [25]. Accurate BA information is also crucial to land and fire decision-makers, as well as to research groups and ecologists, government agencies, and NGOs when implementing environmental policies aiming to reduce socioeconomic impacts from vegetation fires on ecosystems and people [27].

The use of remotely sensed information for BA detection is well established, and there is a consensus about its usefulness from global down to regional levels [28, 29, 30, 31, 32]. Spaceborne sensors are a cost-effective way to map vegetation fires and the unique source of information for large areas with limited access at regional and global scales and for continuous monitoring over time [33, 34]. Over the last decades, several initiatives have been carried out to generate global and regional long-term maps of BA using remote sensing. These include, among others, (1) the 1-km L3JRC product, covering the period from April 2000 to March 2007, produced from SPOT VEGETATION data [35]; (2) the 1-km GLOBCARBON BA product, spanning the period April 1998–December 2007, derived from SPOT VEGETATION, Along Track Scanning Radiometer (ATSR-2), and Advanced ATSR (AATSR) imagery using a combination of mapping algorithms [36]; (3) the MCD45 [37] and MCD64A1 [30] BA products derived by NASA using data collected by the Moderate Resolution Imaging Spectroradiometer (MODIS); (4) the Global Fire Emissions Database (GEFD) initiative that consists in monthly BA estimates aggregated at 0.5° spatial resolution, covering the period from July 1996 to mid-2009 using four satellite data sets [38]; (5) the AQM-MODIS product [39] that was derived for Brazil and consists in monthly maps of BA at 1 km spatial resolution from 2000 up to the present; (6) the global burned area algorithm based on Medium Resolution Imaging Spectrometer (MERIS) reflectance and MODIS hotspots from 2006 to 2008 [29]; and (7) the recent global burned area product based on MODIS bands with a spatial resolution of 250 m [40].

Remote-sensed detection of burned vegetation makes use of spectral bands that are sensitive to spectral changes induced by fire events [41], namely, those associated to the deposit of char and ash on the surface and the change or destruction of vegetation structure [33]. Spectral indices have revealed to be the most appropriate to uncover changes in the radiometric signals of surfaces in operational applications [42], and a large variety of spectral indices for burned area discrimination have been developed in the last decades using a variety of techniques and different spectral bands, such as the red (R, about 0.6–0.7 μm), the near infrared (NIR, about 0.7–1.3 μm), the shorter short-wave infrared (SSWIR, about 1.3–1.9 μm), and the longer short-wave infrared (LSWIR, about 1.9–2.5 μm). Developed approaches include, among others, the Burned Area Index (BAI) [43] based on R and NIR and its improved version BAIM [44] based on NIR and LSWIR, the NIR and LSWIR-based Normalized Burn Index (NBI) [45], the Normalized Burn Ratio (NBR) [46] and derived indices from the latter [47, 48, 49, 50, 51], and the Mid-Infrared Burned Index (MIRBI) [52] based on SSWIR and LSWIR.

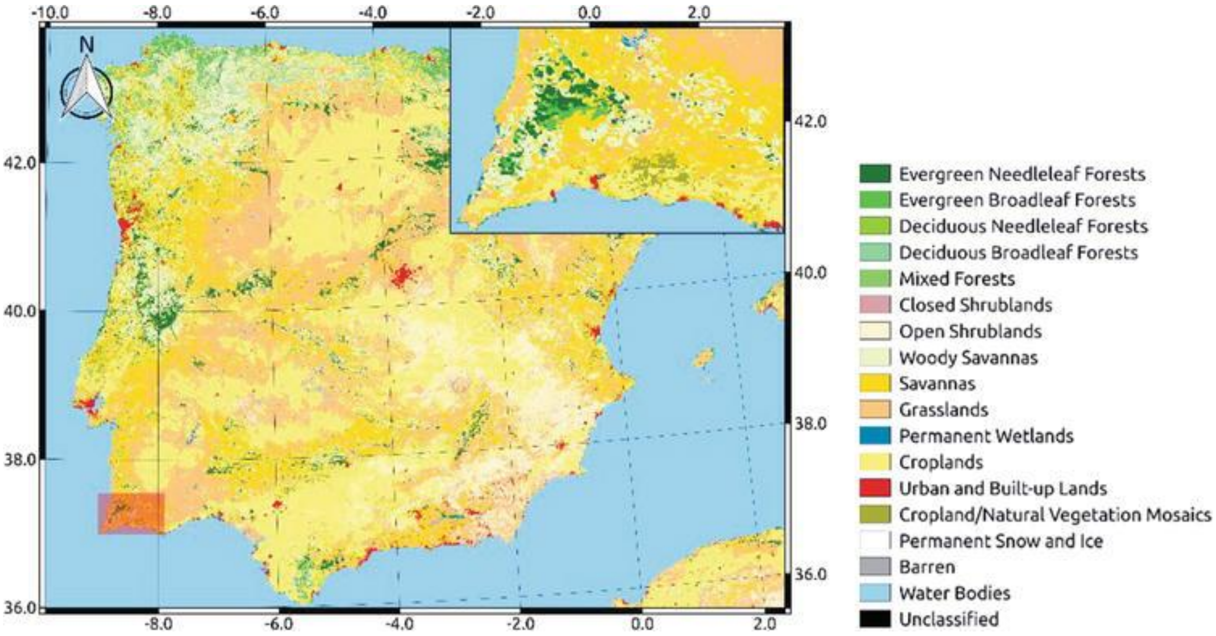

Figure 1. Land cover map of the Iberian Peninsula showing the geographical location (shaded rectangular area) and a zoom (top right box) of the study area near the southern coast of Portugal (source of land cover data: Modis collection 6 global land cover, https://lpdaac.usgs.gov/sites/default/files/public/product_documentation/mcd12_user_guide_v6.pdf).

A burn-sensitive vegetation index system, the so-called (V, W) system, has also been defined on the NIR/MIR space with the aim of optimally discriminating burned vegetation [53, 54].

Here we present and discuss the use of the (V, W) index system to design an automated algorithm aiming at both mapping burned area and dating the associated burning events. As an example of application, the procedure is applied to the fire of Monchique, a large event that took place in the southwest of Portugal in August 2018 (Figure 1).

Table 1. Contingency table for pixels classified as burned versus unburned.

Classification map	Reference map		
	Burned	Unburned	
Burned	a	b	$a + b$
Unburned	c	d	$c + d$
	$a + c$	$b + d$	$a + b + c + d$

The fire of Monchique started on August 3 about noon and was not dominated until August 9. The fire resulted in about 27,000 hectares of burned area, 41 people injured and millions of euros in economic losses. By the second day of the event, about 700 firefighters and 11 aerial resources were fighting the fire, and this number kept increasing up to about 1400 firefighters and 14 aerial resources. The fire occurred within a context of very high temperatures and intense and highly variable winds in terrain with difficult access and high accumulation of biomass.

2. Data and pre-processing

Input data to the algorithms to compute (V, W) consist of top-of-the-atmosphere (TOA) values of middle-infrared (MIR) and thermal-infrared (TIR) radiances and of near-infrared (NIR) reflectance, as acquired by the Visible Infrared Imaging Radiometer Suite (VIIRS) instrument on board of the joint NASA/NOAA Suomi National Polar-Orbiting Partnership (Suomi-NPP) satellite [55]. VIIRS data were reprojected onto a geographical grid of 0.0045° in latitude by 0.0059° in longitude, corresponding to about 500 m in spatial resolution. Data over Portugal, covering the period of July and August 2018, were extracted from the VIIRS/NPP Level 1B 375 m product [56] and correspond to bands I2 (NIR, centered at 0.865 μm), I4 (MIR, centered at 3.74 μm), and I5 (TIR, centered at 11.45 μm).

Geolocation data, as well as land/sea mask and solar and view angle information for each VIIRS tile, were obtained from the VIIRS geolocation product (VIIRS/NPP Imagery Resolution Terrain-Corrected Geolocation). Values of MIR reflectance were then computed using VIIRS bands I4 (MIR) and I5 (TIR) radiances [57]. All images acquired at solar zenith angles (SZA) greater than 55° were rejected, and, when more than one image was available for the same day, the image selected was the one with the lowest solar zenith angle (SZA). Images used as input to the algorithm for burned area discrimination were further restricted to those with view zenith angles (VZA) not exceeding 45° in order to prevent large distortions in pixel size [53].

Information about active fire data was obtained from the VIIRS 375 m Active Fire product [58]. Finally, radiative power data were obtained from the fire radiative power (FRP) product developed by the Land Surface Analysis Satellite Application Facility (LSA SAF); this product is derived from data acquired by the Spinning Enhanced Visible and Infrared Imager (SEVIRI) onboard Meteosat Second Generation (MSG) series of EUMETSAT geostationary satellites [59].

A reference map of burned area in the study region was derived from geospatial information provided by the Rapid Mapping products of the Copernicus Emergency Management Service (EMS) [60]. The Copernicus EMS service was activated by the Portugal National Authority for Civil Protection on August 5 at 16:11 UTC (reference code EMSR303). We used the Delineation Map provided as of August 10 that has an estimated geometric accuracy of 5 m or better, derived by visual interpretation from Sentinel-2 and SPOT satellite observations.

3. Methods

3.1 Simplified (V, W)

Specially designed to discriminate burned areas, the (V, W) burn-sensitive vegetation index system is defined in a transformed MIR/NIR space that allows enhancing the spectral information about burned vegetation [53]. The transformed space is framed by the following two coordinates: (1) the distance, η, of each point in MIR/NIR space to a predefined convergence point, representative of a given target (e.g., a totally burned surface) and (2) the difference, ξ, between the respective MIR and NIR reflectance of each point. The coordinates η and ξ are accordingly defined as

$$\eta = \sqrt{(\rho_{MIR} - \rho_{MIR}^{0})^2 + (\rho_{NIR} - \rho_{NIR}^{0})^2} \qquad (Eq.1)$$

$$\xi = \rho_{MIR} - \rho_{NIR} \qquad (Eq.2)$$

where ρ_{MIR} and ρ_{NIR} represent values of reflectance in MIR and NIR and $(\rho_{MIR}^{0}, \rho_{NIR}^{0})$ are the coordinates of an ideally totally burned pixel.

Values of ρ^0_{MIR} and ρ^0_{NIR} for a given sensor may be estimated by the upper (lower) bound of reflectivity in MIR (NIR) for a large sample of recently burned pixels. To estimate these values for the VIIRS sensor, we used a sample of burned regions for several fires in central Portugal that occurred in 2017. Obtained estimates are $\rho^0_{MIR} = 0.29$ and $\rho^0_{NIR} = 0.06$.

The coordinate system (V, W) is then defined in the MIR/NIR space such that the following properties are met: (1) the V coordinate has a very small dispersion for pixels associated to surfaces containing organic matter and (2) the W coordinate increases with increasing water content of vegetated surfaces. Burned vegetation is characterized by very low values of W and by a sharp decrease of W following a fire event [53], both characteristics being especially conspicuous in monthly minimum composites of W and of differences of W between a given month and the previous one (Figure 2). In turn, non-vegetated surfaces like clouds and water bodies are characterized by low values of V.

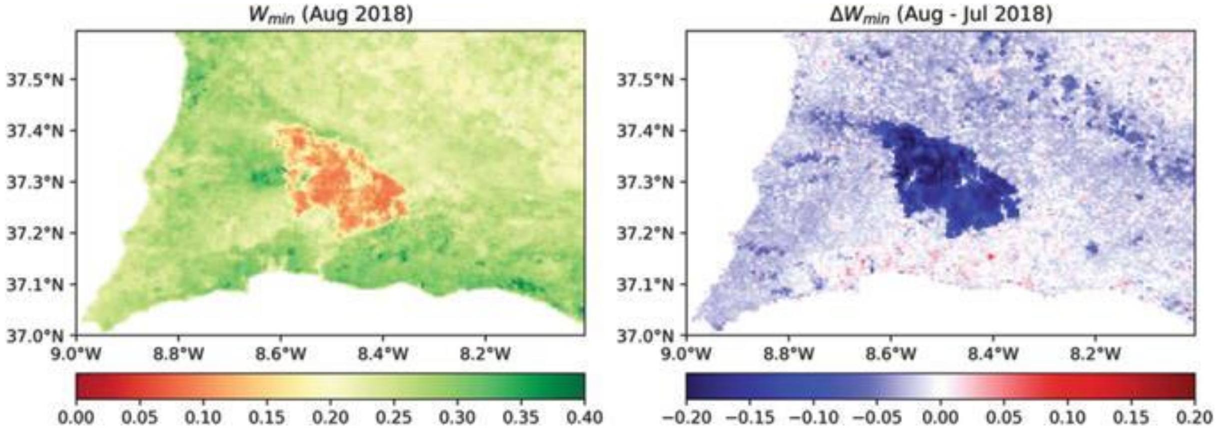

Figure 2. Spatial distribution over the study area of the minimum composite of W_{min} for August 2018 (left panel) and of the difference of minimum composites of W_{min} between August and July 2018 (right panel).

Unlike VI3 [57] and GEMI3 [33], the (V, W) index system has the advantage of not having been heuristically derived; however, unlike traditional indices that rely on simple algebraic expressions and are easy to implement by users, the computation of (V, W) is laborious, involving iterative methods and numerical computation of line integrals [53]. This disadvantage is circumvented by using the following approximation that is valid in a subdomain of the MIR/NIR space where the majority of observed values are located [54]:

$$V = \frac{(0.16 - 0.71\xi)}{\eta} \qquad (Eq. 3)$$

$$W = 1.1\eta \qquad (Eq. 4)$$

3.2 Discrimination of burned areas

Discrimination of burned areas for a given month is based on a procedure that uses as inputs a monthly composite of minimum of W and the difference between this minimum composite and that of the previous month together with locations of all identified hotspots during the considered month [39].

The rationale is first to identify burned pixels with high confidence of being burned and then use these points as seeds in a growing algorithm that will identify other burned pixels on a contextual basis and aggregate them as new seed points. Several studies [39, 61] have pointed out that the vast majority of hotspots are located inside or in the neighborhood of a burned area and that the number of burned pixels that are not close to a hotspot is low.

As suggested by results shown in Figure 2, the first seed points are therefore pixels characterized by (1) a low value of the monthly minimum composite of index W and (2) a sharp decrease in that minimum compared to the previous month.

Burned pixels are also expected to be outliers in respect to the statistical distribution pixels where no hotspots were identified. Commonly used in classification problems, the Mahalanobis distance is a measure of the distance of a point to a given distribution in units of the standard deviation in the direction to the point to the mean [62]. The square of the Mahalanobis distance in a p-dimensional space has a chi-square distribution with p degrees of freedom, a result that may be used to find outliers in a dataset [63].

Identification of burned pixels is accordingly performed in the following three steps:

- First step: Let W_{min} and ΔW_{min} be the values for a given pixel of the monthly composite of minimum W and of the difference between this composite and that of the previous month; the pixel is considered as burned if all three following conditions are met:
    - $W_{min} \leq T_1$, where T_1 is a predefined threshold.
    - $\Delta W_{min} \leq T_2$, where T_2 is a predefined threshold.
    - The pixel lies outside the ellipse defined in the two-dimensional space (W_{min}, ΔW_{min}) that corresponds to a predefined percentile of the Mahalanobis distance computed using pixels where no hotspots were identified; given that only pixels in the quadrant with lower W_{min} and ΔW_{min} should be considered as burned, a given pixel is considered as burned if the Mahalanobis distance is above the predefined percentile (e.g., percentile 95) and values of W_{min} and ΔW_{min} are

sufficiently low, that is, below another predefined percentile (e.g., percentile 10, for both quantities).

- Second step: Let each pixel classified as burned in the previous step be considered as a seed point. For each seed point, a 5×5 buffer matrix is defined centered on it, and let N be the number of seed points inside it. If $N \geq 3$, let $\widehat{W}_{min}$ and δW_{min} be the mean and the mean absolute deviation of W for these pixels. Let W^{*}_{min} and ΔW^{*}_{min} be the values of W_{min} and ΔW_{min} for a pixel inside the 5×5 buffer matrix that is not a seed point. This pixel is classified as burned and becomes a new seed point if all two following conditions are met:
    - $W^{*}_{min} < 0$
    - $\Delta W^{*}_{min} \leq \widehat{W}_{min} + \delta W_{min}$
- Third step: The previous step is repeated until no more seed points are generated.

3.3 Dating burned events

For each burned pixel identified by the algorithm above described, the date of burning is estimated by analyzing the time series of W for that pixel and searching for the day where maximum temporal separability is achieved [64]. For most cases, time series of W present daily fluctuations of rather small amplitude (Figure 3) which allows identifying the day when the burning event took place by the significant decrease in W following the event. The day of burning may accordingly be identified as the one that maximizes the following index of temporal separability [65]:

$$S = \frac{2(\mu_b - \mu_a)}{\sigma_a + \sigma_b} \qquad (Eq.5)$$

where μ_a (σ_a) are the values of the mean (standard deviation) of index W of that pixel for a pre-specified number k of images starting at a given instant in time and μ_b (σ_b) are the respective values for the same k number of images before that instant in time. The time series of W is scanned by two juxtaposed windows of fixed length k, and index S is computed for every available day (Figure 3). The burning event is considered to have taken place in the day prior to the date when S is maximized.

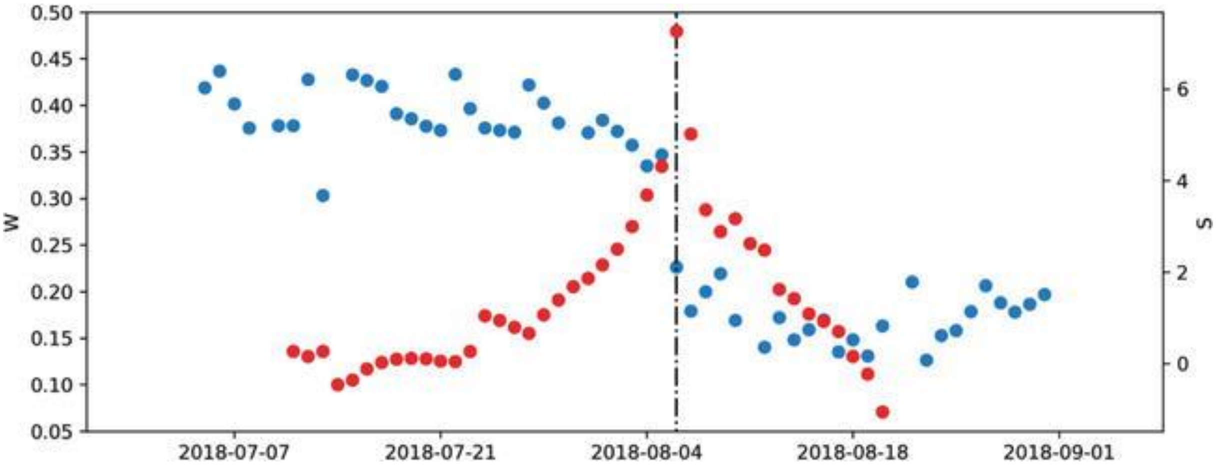

Figure 3. Time series of indices W (blue dots, left vertical scale) and S (red dots, right vertical scale) for a pixel located inside the burned scar. The vertical black dashed line indicates the day of maximum S (Eq. (5)).

3.4 Validation procedures

3.4.1 Discrimination of burned areas

The Monchique BA was validated against the data obtained from the Copernicus Emergency Management Service (EMSR303) that is used as the reference map. The quality of the classification map was assessed based on five verification measures derived from contingency tables [39]: overall accuracy (OA), omission error (OE), commission error (CE), bias (B), and Dice coefficient (DC). These verification measures are defined in Table 2. The agreement between the BA scar and the reference map is measured by the OA, a high value of OA reflecting a high accuracy in the classification. OE and CE are used to assess the discriminative power of the classifier. The bias should be close to one when burning events are not overestimated/underestimated. Finally, DC measures the similarity between the reference and the classification maps by overlapping the classified burned pixels to the "truly burned" pixels in the reference map.

Table 2. Accuracy (OA), omission error (OE), commission error (CE), bias (B), and dice coefficient (DC), with a, b, c, and d as defined in Table 1.

OA	OE	CE	B	DC
$\frac{a+d}{a+b+c+d}$	$\frac{c}{a+c}$	$\frac{b}{a+b}$	$\frac{a+b}{a+c}$	$\frac{2a}{2a+b+c}$

Since the reference map has a higher resolution than the classification map, the former was projected onto the 500 m resolution grid of the latter by computing the burned fraction inside each coarser pixel. The pixel was then considered as burned if the fraction of burned area was greater than 0.5.

3.4.2 Dating burned events

Validation of estimated dates of burning was made against data of radiative power from the FRP product developed by the LSA SAF [59]. This product, together with three other active fire products derived from SEVIRI imagery, was compared against active fire data collected by the MODIS sensor, and results obtained showed a higher detection rate of active fire pixels than the other products [66]. Albeit presenting a coarser resolution of about 4 km in the study region, the repeat cycle of 15 min by the SEVIRI instrument allows for a much better temporal resolution than when comparing against VIIRS or MODIS active fires that have only two samples per day. Furthermore, the VIIRS active fires at 375 m resolution were already used in the algorithm to discriminate burned areas and therefore should not be used for validation purposes. The estimated date of each pixel classified as burned was compared to the date of observation of the nearest SEVIRI pixel where a hotspot was identified. Obtained differences between the dates of the burning of the classified burned pixels and the dates of hotspots identified by the SEVIRI instrument were then used to assess the performance of the dating methodology.

4. Example of application

The above-described procedure was applied to the study region in the southwest of Portugal in order to discriminate burned pixels during the Monchique fire episode and then estimate the respective date of burning.

As described in Sections 3.1 and 3.2, the identification of burned areas in the study region relies on monthly minimum composites of W for August (Figure 2, left panel) and of differences between the minimum composite of August and that of July (Figure 2, right panel), hereby referred to as W_{min} and ΔW_{min}, respectively. Both composites were obtained from daily values of W as derived from reflectance values of MIR and NIR from all available VIIRS images with SZA not exceeding 55° and VZA not exceeding 45°.

When values of W_{min} and ΔW_{min} for all pixels over the study region are represented in a scatter plot (Figure 4), two clusters may be identified: (1) one that is formed by a dense cloud with a large number of points that mostly spread over the subarea of the plot that is lower bounded by percentile 10 of the distribution of W_{min} (identified in the plot by the orange-dashed horizontal line) and left bounded by percentile 10 of the distribution of ΔW_{min} (identified by the orange-dashed vertical line) and (2) a second cluster that is composed of a less dense cloud with a lower number of points that occupy the subarea that is upper bounded by percentile 10 of the distribution of W_{min} and right bounded by percentile 10 of the distribution of ΔW_{min}.

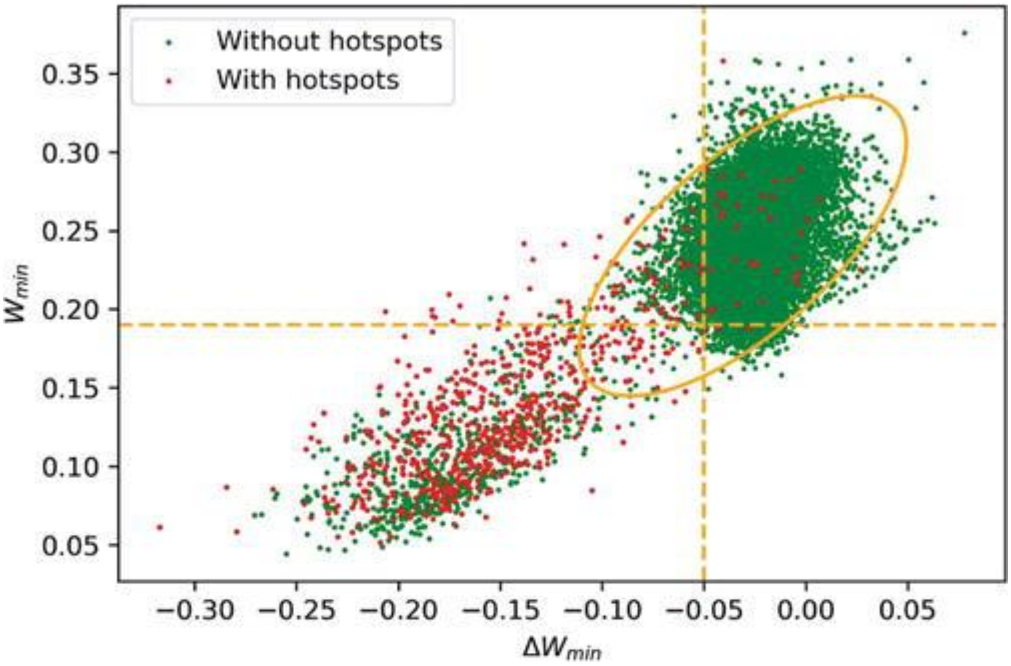

Figure 4. W_{min} (August 2018) versus ΔW_{min} (difference between August and July 2018). Red (green) dots indicate pixels with (without) hotspots associated. The orange ellipse represents percentile 95 of the Mahalanobis distance, and the horizontal (vertical) orange-dashed line represents percentile 10 of the distribution of W_{min} (ΔW_{min}).

The second cluster, formed by points with low values of both W_{min} and ΔW_{min}, is therefore likely to be associated to burned pixels. Moreover, also as to be expected in case of burned surfaces, the second cluster contains a very large fraction of pixels where hotspots were identified from the VIIRS Active Fire product (plotted as red dots). However, there are points (plotted as green dots) in the second cluster that are not associated to any hotspot, and there are also points in the first cluster that are associated to a hotspot, despite the fact that the large values of both W_{min} and ΔW_{min} are not consistent with the characteristic signature of a burned pixel. Both situations are to be expected, since (1) a pixel may burn with no active fire having been spotted by VIIRS (e.g., because of cloud or smoke screening, or because the burning took place between passages of the satellite) and (2) an identified active fire may have originated a burned area that represents a small fraction of the area of the pixel, and therefore the radiometric signature is not strong enough to be detected. Both difficulties may be circumvented in part by selecting a set of pixels with high confidence of being burned as seed points to feed into a growing algorithm.

As discussed in Section 3.2 (first step of the algorithm), seed points are defined as pixels belonging to a region of the space (W_{min}, ΔW_{min}) where there is a high confidence that points are associated to burned pixels. Taking into account the above-discussed features presented by the distribution of points in the scatter plot (Figure 4), seed points were defined according to the following criteria:

- W_{min} < percentile 10 of W_{min}.
- ΔW_{min}< percentile 10 of ΔW_{min}.
- Points (W_{min}, ΔW_{min}) must lie outside the ellipse representing percentile 95 of the Mahalanobis distance computed with all pixels not associated to any hotspot.

Once seed points were identified, new burned pixels were then iteratively aggregated following the procedure described in Section 3.2 (second and third steps of the algorithm).

Results obtained are shown in Figure 5 that also provides a comparison with the reference map that was obtained from information derived from the Copernicus EMS (EMSR303). There is an overall agreement between the downscaled higher-resolution reference map and the map generated by the proposed algorithm. Deviations from the reference map, either in the form of commission or omission errors, are located along the borders of the scar and are likely to be due to small errors in geolocation or of partially burned pixels that were differently classified (as burned or unburned) by the proposed algorithm and the downscaled reference map.

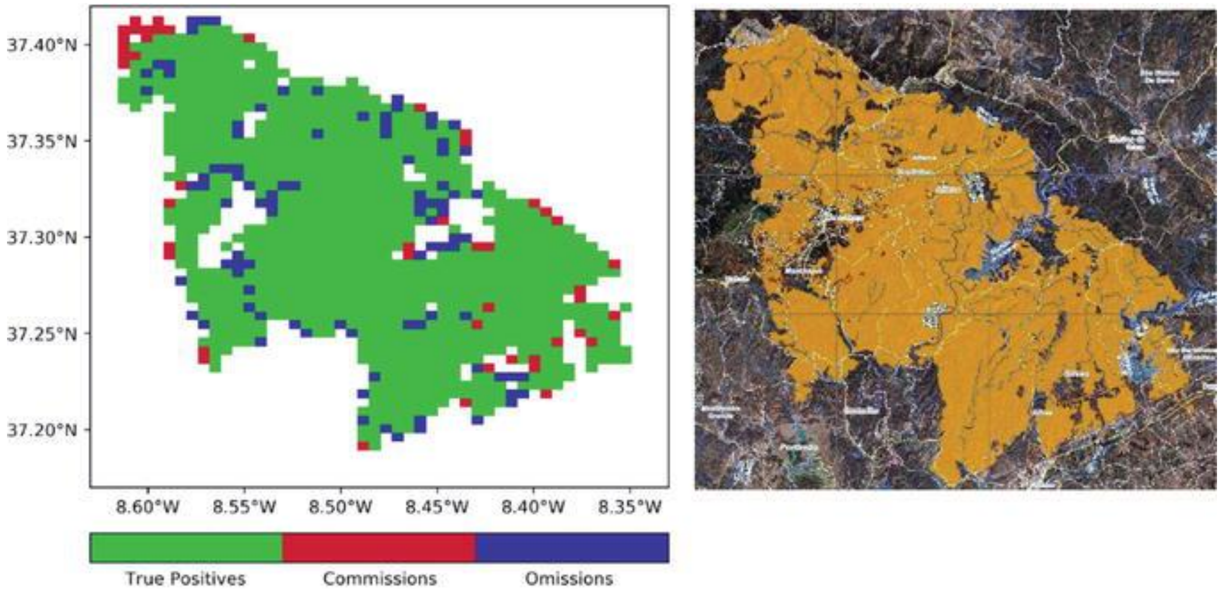

Figure 5. Burned pixels (left panel) from the proposed algorithm and reference map (right panel) from Copernicus EMS (EMSR303). True positives, commission errors, and omission errors are colored in green, red, and blue, respectively.

The overall quality of the proposed algorithm in discriminating the burned pixels associated to the Monchique fire episode reflects on values of the contingency table that compares results from the proposed algorithm with those from the reference map from Copernicus EMS (Table 3) as well as on the five verification measures derived from the obtained contingency table (Table 4). The number of commission errors (45) and the number of omission errors (94) are one order of magnitude lower than the number of match ups (979). In turn, the overall accuracy is larger than 99%, the commission error is lower than 5%, and the omission error is lower than 10%; the bias is above 0.95, and the Dice coefficient is above 0.9.

Table 3. As in Table 1 but with values obtained for the scar that resulted from the Monchique fire event of August 2018.

BA scar	Reference map		
	Burned	Unburned	
Burned	979	45	1026
Unburned	94	21357	21451
	1073	21404	22477

Table 4. As in Table 2 but with the metrics derived from Table 3.

OA	OE	CE	B	DC
99.4%	8.8%	4.6%	0.96	0.93

Following the procedure described in Section 3.3, estimates were obtained of the date of burning for all pixels that were classified as burned within the study region. Results obtained (Figure 6, left panel) show a propagation from NW to SE, forming a pattern that is very similar to the one derived from the dates of detection of hotspots by the SEVIRI instrument (Figure 6, right panel). The agreement between the latter dates and the estimates by the proposed dating algorithm reflects on the obtained histogram of differences that has the null value of differences as the modal frequency, closely followed by a delay of 1 day in the estimates, such that about 70% of the pixels classified as burned have differences in the dates of less than ±1 day. When considering the distribution of differences as a whole, there is a bias of −0.03 day and a root mean square difference of 0.24 day, both values pointing out the very good overall agreement between estimates from the proposed algorithm and the reference dates derived from SEVIRI (Figure 7).

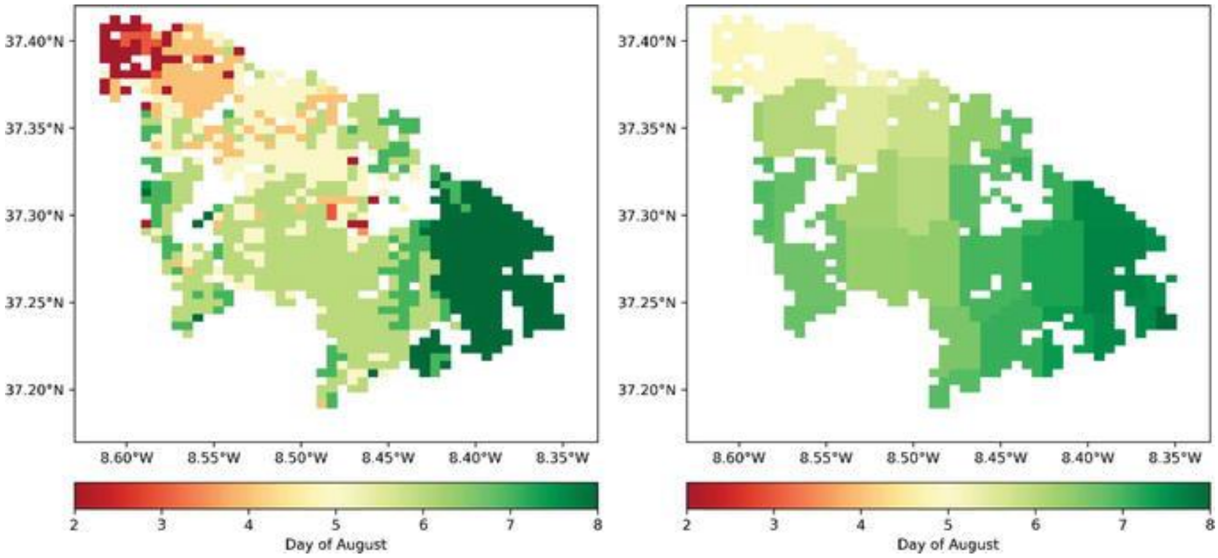

Figure 6. Dates of burning as obtained from the proposed dating algorithm (left panel) and as derived from dates of observation of hotspots by the SEVIRI instrument (right panel).

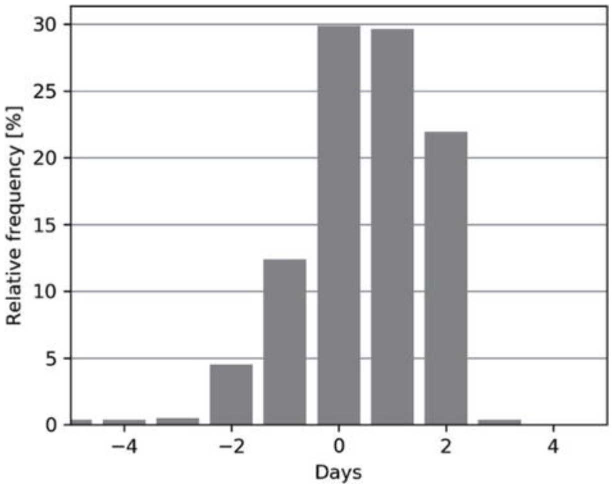

Figure 7. Histogram of difference between dates assigned by the proposed methodology and dates derived from hotspots identified by the SEVIRI instrument.

Results obtained using a similar procedure over the whole territory of Portugal for August and September 2005, one of the worst severe years in terms of burned area, [64] present an overall accuracy of 95.6% and commission and omission errors of 66.5 and 37.1%, respectively. However, the study encompasses a period of 2 months and a much wider area, covering a very large number of scars, and not a single one as in the present study. Regarding the estimated days of burning, 75% of estimated dates in the same study [64] presented deviations less than ±5 days from dates derived from hotspots identified by MODIS.

5. Conclusions

Using TOA values of MIR and TIR radiances and NIR reflectance from VIIRS 375m imagery, a set of optimal indices, V and W, were used to discriminate burned areas and to assign dates to every burned pixel. The ability of V to discriminate between vegetated and non-vegetated surfaces may be used to build up composites of W free from contamination by clouds, whereas the low values of W associated to burned surfaces suggest generating composites of minimum values of W to discriminate burned areas. Adopting this rationale, and in line with previous work [39, 64], discrimination of burned areas was performed using values (W_{min}) of a monthly composite of minimum of W and values (ΔW_{min}) of differences between that composite and the one of the previous month. First seed points are identified as the pixels that (1) are outliers in respect to pixel where no hotspots were identified, (2) present low values of W_{min} characteristic of burning event, and (3) are associated to negative values of ΔW_{min}, indicating a decrease of W_{min} that is expected to occur after a burning event. New burned pixels are then successively aggregated using a seeded region-growing algorithm that starts with the previously identified seed points.

The algorithm was applied to the Monchique fire episode, a large event that occurred in southwestern Portugal during August 2018. The discriminative power of the algorithm was validated against the scar identified by Copernicus EMS303. Results obtained show that the (V, W) algorithm is suited to discriminate burned area over a mainland Portugal, supported by the good agreement, with a Dice coefficient of 0.933, between the burned area scar and the reference map. The commission and omission errors have values of 9 and 5%, respectively. Estimated dates of burning, obtained through analysis of time series of values of W, were compared against times of observation of hotspots obtained from the SEVIRI FRP product. About 70% of the estimated dates presented deviations of 1 day or less.

The development of reliable algorithms to discriminate and date burned areas is crucial for a better understanding of the biosphere-atmosphere interactions, for estimating burning emissions, for future projections of fire regime, and for mitigation and adaptation actions in Portugal, which is recurrently affected by severe fire events. In particular, accurate estimates of the date of burning are crucial when considering fire regime modeling, due to the constraint imposed by biomass availability into the spread of fire, and are also important for reducing uncertainties in biomass burning emissions [34]. The recent VIIRS sensor will allow the development of new burned area products at high spatial resolution, continuing and enhancing the imaging of the Earth initiated by the Advanced Very High-Resolution Radiometer

(AVHRR) and the MODIS instruments. The present work represents a first attempt to assess the potential of using VIIRS imagery to identify burnt scars in Portugal. Results obtained in this work and in related previous ones pave the way to the generation of a long-term series of burned area maps containing accurate information about the extent, location, and time of occurrence of vegetation fires.

Acknowledgments

This research is supported by FAPESP/FCT Project Brazilian Fire-Land-Atmosphere System (BrFLAS) (FCT 2015/01389-4 and FAPESP/1389/2014) and by the EUMETSAT Land Surface Analysis Satellite Application Facility (LSA SAF). Research by Renata Libonati was funded by Serrapilheira Institute (grant number Serra-1708-15159) and supported by Centro de Estudos Florestais (CEF) of the University of Lisbon, a research unit funded by FCT (UID/AGR/00239/2013). Research by Miguel M. Pinto was supported by FCT through PhD grant PD/BD/142779/2018. Research by Alexandra Hurduc was supported by a grant in the framework of Project "Reabilitação das Áreas Queimadas na Freguesia de Alvares," financed by donation of Observador on time SA.

Conflict of interest

The authors declare they have no conflicts of interest.

References

1. Dentener F, Kinne S, Bond T, Boucher O, Cofala J, Generoso S, et al. Emissions of primary aerosol and precursor gases in the years 2000 and 1750 prescribed data-sets for AeroCom. Atmospheric Chemistry and Physics. 2006;6:4321-4344. DOI: 10.5194/acp-64321-2006
2. Zhang J, Webster J, Powers RF, Mills J. Reforestation after the fountain fire in northern California: An untold success story. Journal of Forestry. 2008;106:425-430. DOI: 10.1093/jof/106.8.425
3. van Leeuwen W, Casady G, Neary D, Bautista S, Alloza J, Carmel J, et al. Monitoring post-wildfire vegetation response with remotely sensed time series data in Spain, USA and Israel. International Journal of Wildland Fire. 2010;19:75-93. DOI: 10.1071/WF08078

4. Bowman DMJS, Balch JK, Artaxo P, Bond WJ, Carlson JM, Cochrane MA, et al. Fire in the Earth system. Science. 2009;324(5926):481-484. DOI: 10.1126/science.1163886
5. Storelvmo T, Leirvik T, Lohmann U, Phillips PC, Wild M. Disentangling greenhouse warming and aerosol cooling to reveal Earth’s climate sensitivity. Nature Geoscience. 2016;9(4):286. DOI: 10.1038/ngeo2670
6. Andreae MO, Rosenfeld D, Artaxo P, Costa AA, Frank GP, Longo KM, et al. Smoking rain clouds over the Amazon. Science. 2004;303:1337-1342. DOI: 10.1126/science.1092779. DOI: 10.1126/science.1092779
7. Lohmann U, Rotstayn L, Storelvmo T, Jones A, Menon S, Quaas J, et al. Total aerosol effect: Radiative forcing or radiative flux perturbation? Atmospheric Chemistry and Physics. 2010;10(7):3235-3246. DOI: 10.5194/acp-10-3235-2010
8. Certini G. Effects of fire on properties of forest soils: A review. Oecologia. 2005;143(1):1-10. DOI: 10.1007/s00442-004-1788-8
9. Rosenfeld D. TRMM observed first direct evidence of smoke from forest fires inhibiting rainfall. Geophysical Research Letters. 1999;26(20):3105-3108. DOI: 10.1029/1999GL006066
10. Menon S, Hansen J, Nazarenko L, Luo Y. Climate effects of black carbon aerosols in China and India. Science. 2002;297:2250-2253. DOI: 10.1126/science.1075159
11. Koren I, Kaufman YJ, Remer LA, Martins JV. Measurement of the effect of Amazon smoke on inhibition of cloud formation. Science. 2004;303:1342-1345. DOI: 10.1126/science.1089424
12. Fisher B, Turner RK, Morling P. Defining and classifying ecosystem services for decision making. Ecological Economics. 2009;68(3):643-653. DOI: 10.1016/j.ecolecon.2008.09.014
13. Driscoll D, Lindenmayer D, Bennett AF, Bode M, Bradstoc RA, Cary G, et al. Fire management for biodiversity conservation: Key research questions and our capacity to answer them. Biological Conservation. 2010;143(9):1928-1939. DOI: 10.1016/j.biocon.2010.05.026
14. Sellers PJ, Bounoua L, Collatz GJ, Randall DA, Dazlich DA, Los SO, et al. Comparison of radiative and physiological effects of doubled atmospheric CO2 on climate. Science. 1996;271:1402-1406. DOI: 10.1126/science.271.5254.1402
15. Jin Y, Roy DP. Fire-induced albedo change and its radiative forcing at the surface in northern Australia. Geophysical Research Letters. 2005;32:L13401. DOI: 10.1029/2005GL022822

16. Lambin EF, Geist HJ. Land-Use and Land-Cover Change. Local Processes and Global Impacts. Berlin: Springer Science & Business Media; 2008. p. WP6319
17. Bowman DMJS, Johnston FH. Wildfire smoke, fire management, and human health. EcoHealth. 2005;2(1):76-80. DOI: 10.1007/s10393-004-0149-8
18. Fowler CT. Human health impacts of forest fires in the southern United States: A literature review. Journal of Ecological Anthropology. 2003;7(1):39-63. DOI: 10.5038/2162-4593.7.1.3
19. Patz JA, Engelberg D, Last J. The effects of changing weather on public health. Annual Review of Public Health. 2000;21(1):271-307. DOI: 10.1146/annurev.publhealth.21.1.271
20. Bowman D. Wildfire science is at a loss for comprehensive data. Nature. 2018;560:7. DOI: 10.1038/d41586-018-05840-4
21. Andela N, Morton DC, Giglio L, Chen Y, Van Der Werf GR, Kasibhatla PS, et al. A human-driven decline in global burned area. Science. 2017;356:1356-1362. DOI: 10.1126/science.aal4108
22. Flannigan MD, Krawchuk MA, de Groot WJ, Wotton BM, Gowman LM. Implications of changing climate for global wildland fire. International Journal of Wildland Fire. 2009;18(5):483-507. DOI: 10.1071/WF08187
23. Langmann B, Duncan B, Textor C, Trentmann J, van der Werf GR. Vegetation fire emissions and their impact on air pollution and climate. Atmospheric Environment. 2009;43(1):107-116. DOI: 10.1016/j.atmosenv.2008.09.047
24. Kochi I, Donovan GH, Champ PA, Loomis JB. The economic cost of adverse health effects from wildfire-smoke exposure: A review. International Journal of Wildland Fire. 2010;19(7):803-817. DOI: 10.1071/WF09077
25. Bowman DM, Balch J, Artaxo P, Bond WJ, Cochrane MA, D’Antonio CM, et al. The human dimension of fire regimes on Earth. Journal of Biogeography. 2011;38(12):2223-2236. DOI: 10.1111/j.1365-2699.2011.02595.x
26. Johnston FH, Henderson SB, Chen Y, Randerson JT, Marlier M, DeFries RS, et al. Estimated global mortality attributable to smoke from landscape fires. Environmental Health Perspectives. 2012;120(5):695. DOI: 10.1289/ehp.1104422
27. Pacheco AP, Claro J, Fernandes PM, de Neufville R, Oliveira TM, Borges JG, et al. Cohesive fire management within an uncertain environment: A review of risk handling and decision support systems. Forest Ecology and Management. 2015;347:1-17. DOI: 10.1016/j.foreco.2015.02.033

28. Nogueira J, Ruffault J, Chuvieco E, Mouillot F. Can we go beyond burned area in the assessment of global remote sensing products with fire patch metrics? Remote Sensing. 2016;9(1):7. DOI: 10.3390/rs9010007
29. Alonso-Canas I, Chuvieco E. Global burned area mapping from ENVISAT-MERIS and MODIS active fire data. Remote Sensing of Environment. 2015;163:140-152. DOI: 10.1016/j.rse.2015.03.011
30. Giglio L, Boschetti L, Roy DP, Humber ML, Justice CO. The collection 6 MODIS burned area mapping algorithm and product. Remote Sensing of Environment. 2018;217:72-85. DOI: 10.1016/j.rse.2018.08.005
31. Pereira AA, Pereira J, Libonati R, Oom D, Setzer AW, Morelli F, et al. Burned area mapping in the Brazilian savanna using a one-class support vector machine trained by active fires. Remote Sensing. 2017;9(11):1161. DOI: 10.3390/rs9111161
32. Kasischke ES, French NHF, Harrell P, Christensen NL Jr, Ustin SL, Barry D. Monitoring of wildfires in boreal forests using large area AVHRR NDVI composite image data. Remote Sensing of Environment. 1993;45:61-71
33. Pereira JMC. A comparative evaluation of NOAA/AVHRR vegetation indices for burned surface detection and mapping. IEEE Transactions on Geoscience and Remote Sensing. 1999;37(1):217-226. DOI: 10.1109/36.739156
34. Mouillot F, Schultz MG, Yue C, Cadule P, Tansey K, Ciais P, et al. Ten years of global burned area products from spaceborne remote sensing—A review: Analysis of user needs and recommendations for future developments. International Journal of Applied Earth Observation and Geoinformation. 2014;26:64-79. DOI: 10.1016/j.jag.2013.05.014
35. Tansey K, Gregoire JM, Defourny P, Leigh R, Pekel JFO, van Bogaert E, et al. A new, global, multi-annual (2000-2007) burnt area product at 1 km resolution. Geophysical Research Letters. 2018;35:1. DOI: 10.1029/2007GL031567
36. Plummer S, Arino O, Simon M, Steffen W. Establishing an earth observation product service for the terrestrial carbon community: The GLOBCARBON initiative. Mitigation and Adaptation Strategies for Global Change. 2006;11:97-111. DOI: 10.1007/s11027-006-1012-8
37. Roy DP, Boschetti L, Justice CO, Ju J. The collection 5 MODIS burned area product: Global evaluation by comparison with the MODIS active fire product. Remote Sensing of Environment. 2008;112:3690-3707. DOI: 10.1016/j.rse.2008.05.013

38. Giglio L, Randerson JT, van der Werf GR, Kasibhatla PS, Collatz GJ, Morton DC, et al. Assessing variability and long-term trends in burned area by merging multiple satellite fire products. Biogeosciences. 2010;7:1171-1186. DOI: 10.5194/bg-7-1171-2010
39. Libonati R, DaCamara CC, Setzer AW, Morelli F, Melchiori AE. An algorithm for burned area detection in the Brazil Cerrado using 4 μm MODIS imagery. Remote Sensing. 2015;7:15782-15803. DOI: 10.3390/rs71115782
40. Chuvieco E, Lizundia-Loiola J, Pettinari ML, Ramo R, Padilla M, Mouillot F, et al. Generation and analysis of a new global burned area product based on MODIS 250 m reflectance bands and thermal anomalies. Earth System Science Data Discussions. 2018;512:1-24. DOI: 10.5194/essd-2018-46
41. Trigg S, Flasse S. Characterising the spectral-temporal response of burned savannah using in situ spectroradiometry and infrared thermometry. International Journal of Remote Sensing. 2000;21:3161-3168. DOI: 10.1080/01431160050145045
42. Verstraete MM, Pinty M. Designing optimal spectral indexes for remote sensing applications. IEEE Transactions on Geoscience and Remote Sensing. 1996;(5):1254-1265. DOI: 10.1109/36.536541
43. Isabel MDPM. Cartografía e inventario de incendios forestales en la Península Ibérica a partir de imágenes NOAA-AVHRR. Universidad de Alcalá de Henares; 1999
44. Martín MP, Gómez I, Chuvieco E. Performance of a burned-area index (BAIM) for mapping Mediterranean burned scars from MODIS data. In: Proceedings of the 5th International Workshop on Remote Sensing and GIS Applications to Forest Fire Management: Fire Effects Assessment. Paris: Universidad de Zaragoza, GOFC GOLD, EARSeL; 2005. pp. 193-198
45. Alleaume S, Hely C, Le Roux J, Korontzi S, Swap RJ, Shugart HH, et al. Using MODIS to evaluate heterogeneity of biomass burning in southern African savannahs: A case study. International Journal of Remote Sensing. 2005;26:4219-4237. DOI: 10.1080/01431160500113492
46. USGS. Product Guide: Landsat surface reflectance-derived spectral indices [Internet]. 2007. Available from: https://landsat.usgs.gov/sites/default/files/documents/si_product_guide.pdf [Accessed: October 28, 2018]

47. Loboda T, O'Neal KJ, Csiszar I. Regionally adaptable dNBR-based algorithm for burned area mapping from MODIS data. Remote Sensing of Environment. 2007;109:429-442. DOI: 10.1016/j.rse.2007.01.017
48. Miller JD, Yool SR. Mapping forest post-fire canopy consumption in several overstory types using multi-temporal Landsat TM and ETM data. Remote Sensing of Environment. 2002;82(2-3):481-496. DOI: 10.1016/S0034-4257(02)00071-8
49. Boer MM, Macfarlane C, Norris J, Sadler RJ, Wallace J, Grierson PF. Mapping burned areas and burn severity patterns in SW Australian eucalypt forest using remotely-sensed changes in leaf area index. Remote Sensing of Environment. 2008;112:4358-4396. DOI: 10.1015/j.rse.2008.08.005
50. Miller JD, Thode AE. Quantifying burn severity in a heterogeneous landscape with a relative version of the delta normalized burn ratio (dNBR). Remote Sensing of Environment. 2007;109:66-80. DOI: 10.1016/j.rse.2006.12.006
51. Bastarrika A, Chuvieco E, Martín MP. Mapping burned areas from Landsat TM/ETM+ data with a two phase algorithm: Balancing omission and commission errors. Remote Sensing of Environment. 2011;105:1003-1012. DOI: 10.1016/j.rse.2010.12.005
52. Trigg S, Flasse S. An evaluation of different bi-spectral spaces for discriminating burned shrub-savannah. International Journal of Remote Sensing. 2001;22(13):2641-2647. DOI: 10.1080/01431160110053185
53. Libonati R, DaCamara CC, Pereira JMC, Peres LF. On a new coordinate system for improved discrimination of vegetation and burned areas using MIR/NIR information. Remote Sensing of Environment. 2011;114:831-843. DOI: 10.1016/j.rse.2011.02.006
54. DaCamara CC, Libonati R, Ermida SL, Calado TJ. A user-oriented simplification of the (V, W) burn-sensitive vegetation index system. IEEE Geoscience and Remote Sensing Letters. 2016;13(12):1822-1826. DOI: 10.1109/LGRS.2016.2614319
55. NASA. Data Product User Guide for Suomi-National Polar-Orbiting Partnership (S-NPP) Sounder Science Investigator-led Processing System (SIPS) Advanced Technology Microwave Sounder (ATMS) Level 1B Products [Internet]. 2017. Available from: https://docserver.gesdisc.eosdis.nasa.gov/repository/Mission/SNPP_Sounder/3.3_ScienceDataProductDocumentation/3.3.4_ProductGenerationAlgorithms/ATMS_Readme_Vers_1_20170508.pdf [Accessed: October 28, 2018]
56. NASA. Visible Infrared Imaging Radiometer Suite (VIIRS) 375 m & 750 m Active Fire Detection Data Sets Based on NASA VIIRS Land Science Investigator Processing

System (SIPS) Reprocessed Data—Version 1 [Internet]. 2017. Available from: https://lpdaac.usgs.gov/sites/default/files/public/product_documentation/vnp14_user_guide_v1.3.pdf [Accessed: October 28, 2018]

57. Kaufman YJ, Remer LA. Detection of forests using MID-IR reflectance: An application for aerosol studies. IEEE Transactions on Geoscience and Remote Sensing. 1994;32:672-683. DOI: 10.1109/36.297984
58. Schroeder W, Oliva P, Giglio L, Csiszar IA. The new VIIRS 375 m active fire detection data product: Algorithm description and initial assessment. Remote Sensing of Environment. 2014;143:85-96. DOI: 10.1016/j.rse.2013.12.008
59. Wooster MJ, Roberts G, Freeborn PH, Xu W, Govaerts Y, Beeby R, et al. LSA SAF Meteosat FRP products—Part 1: Algorithms, product contents, and analysis. Atmospheric Chemistry and Physics. 2015;15(22):13217-13239. DOI: 10.5194/acp-15-13217-2015
60. Copernicus. Emergency Management Service [Internet]. 2018. Available from: http://emergency.copernicus.eu/ [Accessed: October 28, 2018]
61. Hantson S, Padilla M, Cort D, Chuvieco E. Strengths and weaknesses of MODIS hotspots to characterize global fire occurrence. Remote Sensing of Environment. 2013;131:152-159. DOI: 10.1016/j.rse.2012.12.004
62. Mahalanobis PC. On the generalised distance in statistics. Proceedings of the National Institute of Sciences of India. 1936;2(1):49-55
63. Wilks DS. Statistical Methods in the Atmospheric Sciences. Vol. 100. Oxford: Academic Press; 2006. 676 pp
64. Panisset J, DaCamara CC, Libonati R, Peres LF, Calado TJ, Barros A. Assigning dates and identifying areas affected by fires in Portugal based on MODIS data. Anais da Academia Brasileira de Ciências. 2017;89(3):1487-1501. DOI: 10.1590/0001-3765201720160707
65. Giglio L, Loboda T, Roy DP, Quayle B, Justice CO. An active-fire based burned area mapping algorithm for the MODIS sensor. Remote Sensing of Environment. 2009;113:408-420. DOI: 10.1016/j.rse.2008.10.006
66. Roberts G, Wooster MJ, Xu W, Freeborn PH, Morcrette JJ, Jones L, et al. LSA SAF Meteosat FRP products—Part 2: Evaluation and demonstration for use in the Copernicus Atmosphere Monitoring Service (CAMS). Atmospheric Chemistry and Physics. 2015;15:13241-13267. DOI: 10.5194/acp-15-13241-2015